UNIVERSITY of CALIFORNIA
Santa Barbara

A New Method for Measuring Black Hole Masses in Active Galaxies: Modeling the Broad Line Region Using Reverberation Mapping Data

A dissertation submitted in partial satisfaction of the
requirements for the degree of

Doctor of Philosophy

in

Physics

by

Anna K. Pancoast

Committee in charge:

Professor Tommaso Treu, Chair
Professor Omer Blaes
Professor Andy Howell

September 2015

The dissertation of Anna K. Pancoast is approved:

Professor Omer Blaes

Professor Andy Howell

Professor Tommaso Treu, Chair

August 2015

A New Method for Measuring Black Hole Masses in Active Galaxies: Modeling the Broad Line Region Using Reverberation Mapping Data

Anna K. Pancoast

For Peter and Iris.

Acknowledgments

The last six years have been some of the most rewarding and fulfilling of my life, due in large part to the exceptional people I have had the pleasure to work and play with while at UCSB. First and foremost I have to thank my husband Peter for his unwavering support, editing skills, and companionship on many work trips to far away places. You've made graduate school *literally* the best! I also have to thank my daughter Iris who has been the most good-natured baby a parent could hope for while trying to finish their dissertation. Iris, my thesis baby, your curiosity continues to amaze me and remind me what being a scientist is all about.

I also must thank my parents, who told me I could do anything I set my mind to do. Mom, thank you for telling me to find time for a creative outlet, no matter how busy I am. Dad, thank you for telling me all about what I realize now was atomic physics when I was little; it made car rides so much fun, even if your plan to make me into a chemist failed. And to my sister Ingrid, seeing you go after your dreams gives me the courage not to give up on mine.

Living in Santa Barbara would involve fewer BBQs, carved pumpkins, and chocolate Guinness cakes without Jen, Rachel, Christine, Karina, and Genevieve. You have reminded me that I'm not alone when the going gets tough and, perhaps equally important, of the big wide world outside academia.

Co-leaders of Women in Physics, Jen, Karina, Genevieve, Stacy, Kimberly, Netta, Charlotte, and Lia, it has been an absolute pleasure working with you to make UCSB Physics the best department it can be; you are some of the most inspiring physicists I

know.

Anna and Ale, my fellow A-team members, you have been phenomenal Treu group buddies. I can't imagine office mates more encouraging and helpful than you. Let's celebrate leap day again sometime soon.

Vardha, thank you for your mentorship and for teaching me almost everything I know about observing. I will miss our trips to Hawaii and Lick, some of the best memories I have of graduate school.

Brendon, thank you for being such an ace collaborator over the last six years. I continue to learn so much from you.

Finally, a huge thank you to my adviser, Tommaso, for providing the perfect environment for me to flourish in graduate school. With your encouragement and guidance I am exactly where I always hoped I would be.

Curriculum Vitae

Anna Pancoast

Education

2015	Ph.D. in Physics, University of California, Santa Barbara
2012	M.A. in Physics, University of California, Santa Barbara
2009	B.A. in Physics and Astronomy, Haverford College

Professional Experience

2009-2015	Graduate Research Assistant, Department of Physics, University of California, Santa Barbara
Spring 2010	Teaching Assistant, University of California, Santa Barbara
2008-2009	Undergraduate student researcher, Haverford College
Summer 2007	Undergraduate student researcher, Haverford College

First Author Publications

Pancoast, A.; Brewer, B. J.; Treu, T.; Park, D.; Barth, A. J.; Bentz, M. C.; Woo, J.-H. "Modeling reverberation mapping data II: dynamical modeling of the Lick AGN Monitoring Project 2008 dataset", Monthly Notices of the Royal Astronomical Society, 445, 3073 (2014)

Pancoast, A.; Brewer, B. J.; Treu, T. "Modeling reverberation mapping data I: improved geometric and dynamical models and comparison with cross-correlation results", Monthly Notices of the Royal Astronomical Society, 445, 3055 (2014)

Pancoast, A. et al. (36 co-authors), "The Lick AGN Monitoring Project 2011: Dynamical Modeling of the Broad-line Region in Mrk 50", The Astrophysical Journal, 754, 49 (2012)

Pancoast, A.; Brewer, B. J.; Treu, T. "Geometric and Dynamical Models of Reverberation Mapping Data", The Astrophysical Journal, 730, 139 (2011)

Pancoast, A.; Sajina, A.; Lacy, M.; Noriega-Crespo, A.; Rho, J. "Star Formation and Dust Obscuration in the Tidally Distorted Galaxy NGC 2442", The Astrophysical Journal, 723, 530, (2010)

Fellowships and Awards

2015 - 2019	Einstein Fellowship and Institute for Theory and Computation Fellowship, Harvard-Smithsonian Center for Astrophysics
Fall 2014	Dean's Fellowship, University of California, Santa Barbara
2009-2014	National Science Foundation Graduate Research Fellowship, University of California, Santa Barbara
2009-2010	Graduate Assistance in Areas of National Need Fellowship, University of California, Santa Barbara

Abstract

A New Method for Measuring Black Hole Masses in Active Galaxies: Modeling the Broad Line Region Using Reverberation Mapping Data

by

Anna K. Pancoast

Measuring the masses of supermassive black holes in active galactic nuclei (AGN) allows us to trace their evolution over cosmic time and understand how black holes coevolve with their host galaxies. We present a new technique to measure black hole masses and constrain the structure of the broad line region in AGN using reverberation mapping data. We begin by developing a simply parameterized phenomenological model of the broad line region geometry and dynamics and apply this model to high-quality reverberation mapping data for six AGN from the Lick AGN Monitoring Project 2008 and 2011 datasets. The results of this analysis provide the most precise AGN black hole masses from reverberation mapping to date and the first detailed constraints on the geometry and dynamics of the broad line region emission. Specifically, we find that the shape of the broad line region is generally a close to face-on thick disk with preferential emission from the far side, and that the dynamics range from inflow to near-circular orbits. In addition, we present photometric AGN light curves using image subtraction for the Lick AGN Monitoring Project 2011 dataset as a first step towards modeling the broad line region in a larger sample of AGN.

Contents

Chapter 1

Introduction: Measuring black hole masses in active galactic nuclei

1.1 Active galactic nuclei

The immense luminosities observed in active galactic nuclei (AGN), or quasars, are thought to be powered by accretion onto supermassive ($M_{\rm BH} \sim 10^6 - 10^{10}$) black holes residing at the center of most galaxies (Lynden-Bell & Rees 1971). We describe the evidence for astrophysical supermassive black holes in Section 1.1.1, we discuss the role of AGN in galaxy evolution in Section 1.1.2, and we summarize the standard model for the structure of AGN in Section 1.1.3.

1.1.1 Supermassive black holes

Black holes are singularities in space-time where the mass is concentrated at a single point, causing physical quantities, such as the density, to diverge there. However, divergence at the singularity is shielded from view because at some radius light is unable to escape from the black hole and thus we cannot observe the behavior of a test particle as it reaches the point of divergence. Since a full treatment of the general relativity

of black holes is beyond the scope of this introduction, we will focus only on the two characteristics of black holes that influence the work presented in Chapter 4: the size of the event horizon and the gravitational redshift of photons traveling out of the black hole gravitational potential well.

For the simple case of a nonrotating time-steady black hole, we work in the Schwarzschild metric to calculate the effects of the black hole's gravity on photons or test particles. The natural unit of length in this picture is the gravitational radius $r_g = GM/c^2$, where G is the gravitational constant, c is the speed of light, and M is the black hole mass. The g_{rr} element of the Schwarzschild metric diverges at the radius:

$$r_{\rm schw} = \frac{2GM}{c^2} = 2r_g \tag{1.1}$$

called the Schwarzschild radius, although physical quantities measured in the local frame do not diverge until the location of the singularity is reached at $r = 0$. The Schwarzschild radius marks a special point at which photons, even when directed radially outward away from the black hole, cannot escape. This defines the event horizon of the black hole.

The second characteristic of black holes that we make use of is the gravitational redshift of photons emitted from near the black hole. If a photon is emitted at a wavelength $\lambda_{\rm emit}$ near a black hole and observed at a point less deep in the gravitational potential well of the black hole, r, the observed wavelength $\lambda_{\rm obs}$ will be greater by the factor:

$$\lambda_{\rm obs} = \lambda_{\rm emit} \frac{1}{\sqrt{1 - \frac{r_{\rm schw}}{r}}}. \tag{1.2}$$

This means that events happening closer to the black hole appear to take longer when observed from further away, and thus the frequency of light is also reduced.

While the theory of Schwarzschild black holes has existed since the early 1900s (Schwarzschild 1916), it took another fifty years before supermassive black holes were invoked to explain the first bright, high-redshift (for the time), quasars (Salpeter 1964; Lynden-Bell 1969; Lynden-Bell & Rees 1971). The next step was looking for the dynamical signatures of quiescent supermassive black holes in local galaxies, where those signatures could possibly be resolved (see the reviews by Kormendy & Richstone 1995; Kormendy & Ho 2013). Nowhere did this work as successfully as the Galactic center, where ground-based high-resolution images track the orbits of individual stars around our Galaxy's supermassive black hole, Sgr A* (for a review see Genzel et al. 2010).

1.1.2 Active galactic nuclei and galaxy evolution

With the ability to outshine their host galaxy, AGN can be observed at high redshifts as luminous quasars. While rare (see the review by Brandt & Alexander 2015), with the active accretion phase lasting only $\sim 10^8$ years (e.g. Kelly et al. 2010), these luminous beacons provide the means to study the evolution of black holes and the largest gravitationally bound structures, galaxies and clusters, over cosmic time.

In the early Universe, the discovery of AGN at high redshifts with large black hole masses (e.g. Volonteri & Bellovary 2012; De Rosa et al. 2014) constrains the mechanisms by which primordial gas fragments to form the first stars and black holes. At later times, the masses of black holes and their host galaxies are found to be tightly correlated, suggesting some form of feedback where black hole growth influences the star formation rate. In the local Universe, where black hole masses can be measured by spatially resolving

the kinematics of gas or stars within the black hole's gravitational sphere of influence (see the review by Ferrarese & Ford 2005), the black hole mass is found to correlate with many properties of the host galaxy, including the velocity dispersion of the host galaxy bulge (the $M - \sigma_*$ relation, Ferrarese & Merritt 2000; Gebhardt et al. 2000). Black hole feedback also plays an important role in galaxy groups and clusters, where powerful radio emission from AGN jets prevents the intra-cluster gas from forming expected, yet unobserved, cooling flows (see the review by Fabian 2012).

Due to the strong influence of black holes on galaxy evolution, much work has focused on measuring their masses and accretion rates from the early Universe to the present (e.g. Kelly & Shen 2013). The closest, generally non-active, black holes (with the exception of NGC 3227 and NGC 4151, Davies et al. 2006; Hicks & Malkan 2008; Onken et al. 2014), where the gravitational sphere of influence can still be spatially resolved, provide black hole masses without accretion rates. At greater distances, however, black holes are identified by active accretion as AGN and both their masses and accretion rates can be measured. Since the black hole gravitational sphere of influence cannot be spatially resolved, the kinematics of gas around the black hole are resolved in the time domain using the reverberation mapping technique (Blandford & McKee 1982; Peterson 1993) described in Section 1.2.

1.1.3 The standard model of active galactic nuclei

The basic structure of AGN is described by the standard model that explains the range of AGN observational signatures as arising from differences in viewing angle of the

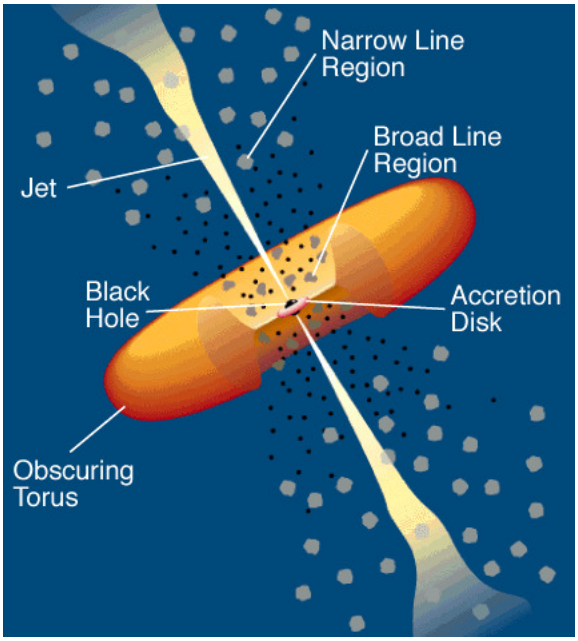

Figure 1.1: Illustration of the standard model of AGN from Urry & Padovani (1995). Copyright PASP, reprinted with permission of the author.

observer and whether the AGN hosts a jet (Antonucci 1993; Urry & Padovani 1995; Netzer 2015). In the standard model, the black hole is surrounded by an accretion disk that is the source of ionizing continuum photons, as illustrated in Figure 1.1. Possibly coincident and outside the accretion disk is the broad line region (BLR), at a distance from the black hole of $\sim 10^{14} - 10^{16}$ m or $\sim 10^4$ gravitational radii (Wandel et al. 1999; Kaspi et al. 2000; Bentz et al. 2006, 2013), from which broad lines with widths of $1000 - 25,000$ km s^{-1} are emitted. The emission lines are broadened due to the high velocities of the emitting gas orbiting around the black hole. Starting at the dust sublimation radius, the BLR turns into the dusty obscuring torus that hides the BLR from observers behind the torus. The narrow line region, at greater distances from the black hole and lower gas densities, is the source of narrow emission lines. In this model, AGN with both broad and narrow emission lines are viewed at a face-on inclination angle with respect to the dusty torus

and AGN with only narrow emission lines are viewed through the dusty torus, blocking the broad line region from sight.

Despite this general picture of AGN structure, the detailed properties of gas in the different regions are not well understood. Of particular interest are the geometry and dynamics of gas in the BLR, since the broad emission lines are used to measure the black hole mass. Analysis of the broad emission lines in the optical and ultraviolet (UV) suggests that the temperature of the gas in the BLR is $\sim 10^4\,\mathrm{K}$ and the gas is fairly dense, with an electron density greater than $10^9 \mathrm{cm}^{-3}$ (for a review on BLR physics see Peterson 2006). However, whether the gas is distributed in clumps or smooth filaments is still unknown, since confinement and creation of discreet BLR clouds are still open questions (e.g. Laor et al. 2006, and references therein). The best constraints on the geometry and dynamics of the BLR come from reverberation mapping studies, described in Section 1.2, including the typical radius of BLR gas from the central source of ionizing photons (e.g. Peterson et al. 2004), radial stratification of the emission from different broad lines (e.g. Bentz et al. 2010a), and signatures of both inflowing and outflowing gas (e.g. Grier et al. 2013b).

1.2 Reverberation mapping

Outside the local Universe, black hole masses in AGN are measured using the reverberation mapping technique (Blandford & McKee 1982; Peterson 1993; Peterson et al. 2004; Peterson 2014). Reverberation mapping works by monitoring the response of broad line emission to changes in the AGN ionizing photon flux from the accretion disk. The

time lag, τ, between changes in the ionizing photon flux and the echo of these changes in the broad line flux provides a measurement of the size of the BLR, assuming the ionizing photons come from close to the black hole. The velocity of gas in the BLR, v, is measured from the width of the doppler-broadened broad emission lines, which, together with the time lag, gives the black hole mass:

$$M_{\rm BH} = f\frac{c\tau v^2}{G}. \tag{1.3}$$

G is the gravitational constant and c is the speed of light, which converts the time lag into a distance. The dimensionless factor f of order unity, called the virial coefficient, incorporates the information about the geometry and dynamics of the BLR. Currently an average value of f is used for the full reverberation mapped sample of ~ 60 AGN (Bentz & Katz 2015), where the average value is measured by aligning the $M - \sigma_*$ relation for reverberation mapped AGN with the $M - \sigma_*$ relation for local quiescent galaxies with black hole masses measured by resolving the gravitational sphere of influence (Onken et al. 2004; Collin et al. 2006; Woo et al. 2010; Greene et al. 2010a; Graham et al. 2011; Park et al. 2012a; Woo et al. 2013; Grier et al. 2013a). Using an average value of f introduces the largest source of uncertainty in individual reverberation mapped black hole mass measurements on the order of ~ 0.4 dex (e.g. Park et al. 2012a). This uncertainty can only be reduced by measuring the value of f for individual AGN by constraining the geometry and dynamics of the BLR gas.

Most reverberation mapping campaigns have focused on the rest-frame optical spectrum of AGN, using the optical AGN continuum as a proxy for the true ionizing photon flux and the Balmer broad emission lines, specifically Hα and Hβ (e.g. Peterson et al.

2004; Bentz et al. 2009b; Denney et al. 2010; Barth et al. 2011a; Grier et al. 2012; Barth et al. 2015). The Hβ line is especially robust for measuring black hole masses because of its proximity to the narrow [O III] $\lambda\lambda$4959, 5007 doublet, which allows for robust flux inter-calibration of the spectra. However, in high redshift AGN, the rest-frame UV is shifted into the observed optical with a different set of broad emission lines, where the two most widely used are Mg II λ2798 and C IV λ1549. A handful of studies have focused on low-redshift AGN in the rest-frame UV using the *International Ultraviolet Explorer* and the *Hubble Space Telescope* (*HST*) to monitor the Mg II λ2798 and C IV λ1549 lines along with the AGN UV continuum (see De Rosa et al. 2015, and references therein). The black hole mass is measured consistently between different emission lines, suggesting that the BLR gas is a robust tracer of the black hole gravitational potential over a range in radius, since more highly ionized broad emission lines are emitted from closer to the black hole (e.g. Peterson & Wandel 2000; Kollatschny et al. 2001; Bentz et al. 2010a).

One of the most useful results to come from reverberation mapping of local AGN in the optical is the relation between the BLR radius, r, for the Hβ broad emission line and the AGN optical luminosity, L (the $r - L$ relation, e.g. Bentz et al. 2006, 2009a, 2013). Using the $r - L$ relation, the black hole mass can be measured from a single spectrum or 'single epoch', since the AGN luminosity gives the size of the BLR in place of a full reverberation mapping dataset and the broad line width gives the velocity of the BLR gas (e.g. Vestergaard & Peterson 2006). Single epoch black hole mass measurements have made it possible to quickly and cheaply measure black hole masses for AGN at any redshift, although the uncertainties from applying an $r - L$ relation derived for Hβ at low redshift to AGN at high redshift using different broad emission lines are not completely

understood (e.g. Richards et al. 2011; Shen & Liu 2012; Denney et al. 2013). A better understanding of BLR structure and how it might change with different emission lines, AGN luminosity, and black hole mass is needed to fully address this issue.

New high-quality datasets have allowed for more detailed analysis of reverberation mapping data that, in addition to providing a black hole mass measurement, also constrains the structure of the BLR (Bentz et al. 2010b; Brewer et al. 2011a; Pancoast et al. 2012; Grier et al. 2013b; Pancoast et al. 2014b; Skielboe et al. 2015). Much of this analysis has focused on recovering the shape of the transfer function that maps response of the broad line flux to changes in the AGN continuum as a function of wavelength, λ, and time lag. In terms of the transfer function $\Psi(\tau, \lambda)$, the emission line flux, $f_{\rm line}$, as a function of time, t, and wavelength is given by:

$$f_{\rm line}(t, \lambda) \propto \int \Psi(\tau, \lambda) f_{\rm cont}(t - \tau) d\tau \tag{1.4}$$

where $f_{\rm cont}$ is the AGN continuum flux. Many methods have been developed for recovering the transfer function, including deconvolution using Fourier transforms (Blandford & McKee 1982), regularized linear inversion (Vio et al. 1994; Krolik & Done 1995; Done & Krolik 1996; Skielboe et al. 2015), and inversion of the integral equation using maximum entropy techniques (Skilling & Bryan 1984; Krolik et al. 1991; Horne et al. 1991; Horne 1994). Recently, the use of maximum entropy techniques has seen the most application and suggests a diversity in BLR structure (Bentz et al. 2010a; Grier et al. 2013b). Unfortunately, the transfer function must still be interpreted using a model for the BLR, motivating the development of a direct modeling approach for reverberation mapping data as described in Chapter 2.

Another recent improvement in reverberation mapping analysis is the treatment of the AGN continuum light curve in the UV or optical. Traditional reverberation mapping analysis involves calculating the cross-correlation function between the broad emission line flux and the AGN continuum light curves, which assumes minimal information about the AGN system (Peterson et al. 2004). However, studies of AGN variability in large samples show that, on the timescales of reverberation mapping data of daily cadence or longer, AGN variability can be modeled as a damped random walk or continuous-time first-order autoregressive process (CAR(1), Kelly et al. 2009; Kozłowski et al. 2010; MacLeod et al. 2010; Zu et al. 2013). On shorter timescales, recent Kepler monitoring of AGN shows that the power spectrum steepens, reducing variability compared to a CAR(1) model (Mushotzky et al. 2011; Carini & Ryle 2012; Edelson et al. 2014; Kasliwal et al. 2015). Zu et al. (2011) use a CAR(1) model for AGN continuum variability and a top-hat transfer function to calculate time lags for reverberation mapping data, significantly decreasing the uncertainties in the inferred time lags. Similarly, Skielboe et al. (2015) improve upon the method of regularized linear inversion to infer the BLR transfer function by incorporating a model for AGN continuum variability that is equivalent to the CAR(1) model. As described in Chapter 2, a model equivalent to CAR(1) is also at the heart of the the direct BLR modeling approach.

The structure of this thesis is as follows. In Chapter 2, we present a new method to analyze high-quality reverberation mapping data by modeling the data directly using a geometric and dynamical model for the BLR. In Chapter 3, we apply this new BLR modeling method to data for Mrk 50 from the Lick AGN Monitoring Project 2011 dataset. In Chapter 4, we improve upon the BLR modeling technique, adding more flexibility to

the model of the BLR, and comparing the inferred BLR sizes to the results from standard cross-correlation function analysis using simulated data. In Chapter 5, we apply the improved BLR model to five AGN from the LAMP 2008 dataset. Finally, in Chapter 6, we present photometry using image subtraction for the LAMP 2011 sample as a first step towards BLR modeling.

Chapter 2

Modeling the broad line region I: Method

This chapter was published as Pancoast, A.; Brewer, B. J.; Treu, T. "Geometric and Dynamical Models of Reverberation Mapping Data", The Astrophysical Journal, 730, 139 (2011) and is included here with minor formatting adjustments.

Our method of analyzing reverberation mapping data simplifies the process of obtaining a transfer function and then interpreting the result using different models. We compare reverberation mapping data directly with models of the broad line region, obtaining uncertainty estimates as well as allowing for model selection. Once we have found models and model parameters that fit the data, we can easily compute the transfer function and average time-lag. Our goal is to constrain the geometry and kinematics of the BLR and provide an internally consistent factor for the black hole mass. We note that the traditionally determined average time-lag is exactly equivalent to a model where the BLR is a face-on ring of a given radius (response = δ-function) or a spherical shell (response = step function). This implicit assumption drives the inference on the average lag and its result, as we will show in this chapter.

We consider two types of reverberation mapping data sets: velocity-unresolved, where there is a time series of the continuum flux and a time series of the integrated line flux,

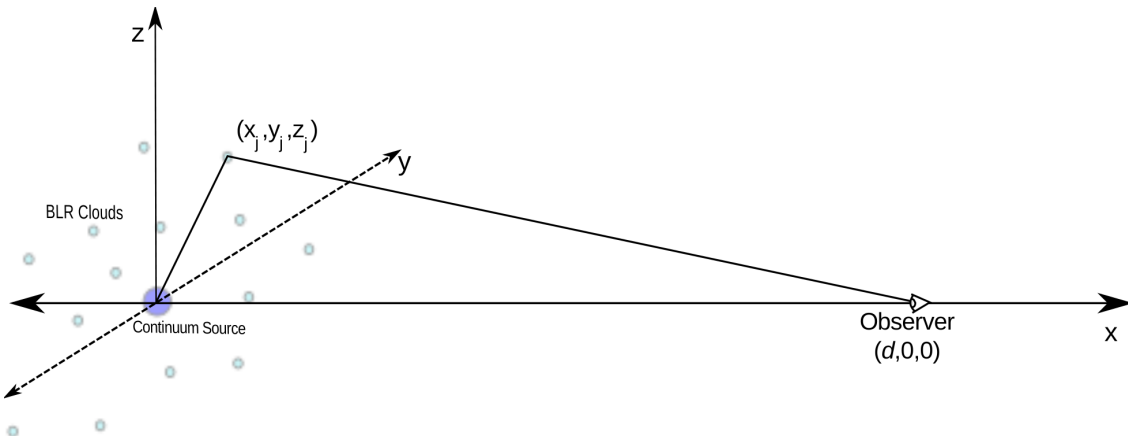

Figure 2.1: BLR clouds around the central ionizing source (central engine). The extra path length the light must travel from the central engine to the BLR cloud and then to the observer is the cause of the delayed response of the line flux.

and velocity-resolved, where the data consist of a continuum flux time series, and a series of entire line spectra as a function of time.

This chapter is organized as follows. In § 2.1 we define and describe the physical problem. In § 2.2 we outline our methods in the formalism of Bayesian probability theory and describe the algorithms we use to compare reverberation mapping data to mock data created from a model of the BLR. In § 2.3 we test our method using simple models of the BLR and show that we are able to recover the parameter values of our test systems. Finally, in § 2.4, we summarize our conclusions. Flux units throughout the chapter are arbitrary, but computed consistently within our method.

2.1 The physical picture

Throughout this chapter, we assume a simple model for the BLR, described as follows. The AGN is defined to be at $(0, 0, 0)$, and the observer is at $(d, 0, 0)$. We model the

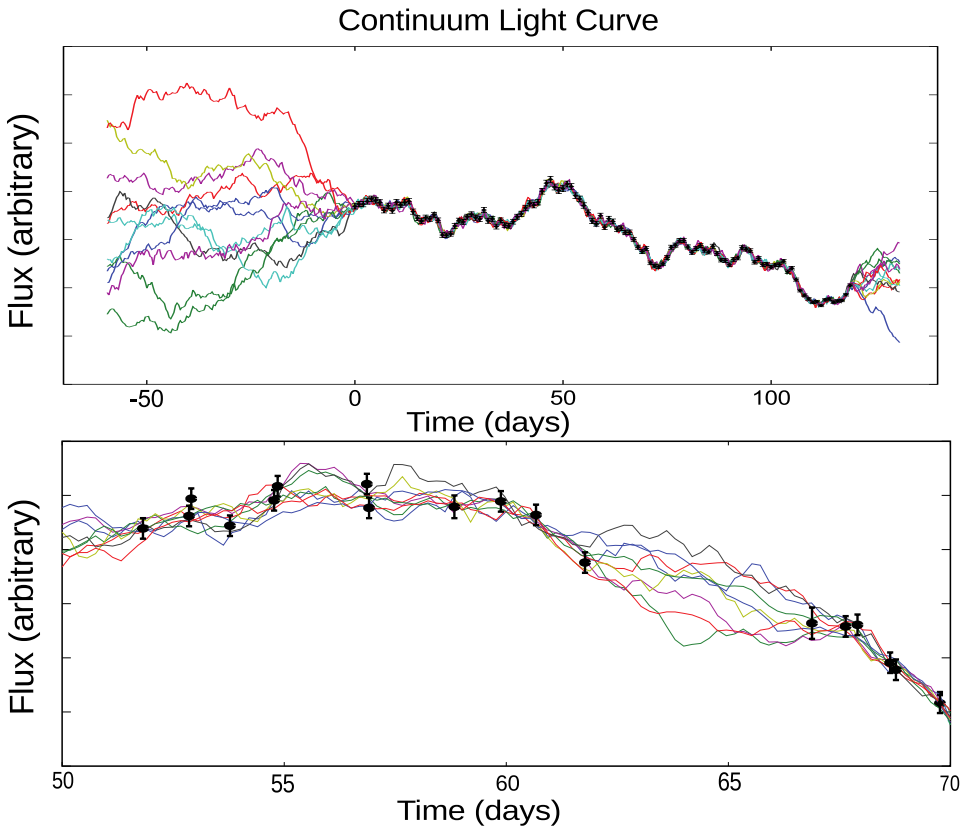

Figure 2.2: Simulated continuum emission datapoints with examples of the continuum interpolated using gaussian processes. The dispersion of the lines represents the uncertainty of the recovered light curve. As expected the uncertanty is greatest where there are no data points. The top panel shows the simulated data used throughout this chapter, whereas the bottom panel shows an example with gaps in the data. Our procedure takes into account the amount of information available and therefore the recovered light curve suffers from a larger uncertainty during the gaps.

distribution of BLR gas by defining the gas density profile $\rho(x, y, z)$, assumed to be normalized such that

$$\int_V \rho(x, y, z)\, dV = 1 \tag{2.1}$$

where $dV = dx\, dy\, dz$ and V is all of space. We assume that the gas absorbs the ionizing radiation, but is not self-shielding, so that gas at larger radii is still illuminated. It should be noted that our approach is fully general and can support more complex models of the optical properties of the BLR, as well as its geometry and dynamics.

2.1.1 Velocity-unresolved reverberation mapping

If the continuum flux varies with time according to $f_{\rm cont}(t)$, then the total line flux as a function of time is given by

$$f_{\rm line}(t) = A \int_V f_{\rm cont}(t - l(x, y, z))\rho(x, y, z)\, dV \tag{2.2}$$

where $l(x, y, z)$ is the *lag*, or time delay, associated with BLR gas at position (x, y, z), and A is a response coefficient. The lag l for each position is simply the excess light travel time from taking a path starting at $(0, 0, 0)$ that travels to some gas at (x, y, z), where the light is absorbed and reemitted as line emission, and that finally travels to the observer, relative to a direct path straight from the AGN to the observer:

$$l(x, y, z) = \left(\sqrt{x^2 + y^2 + z^2}\right. \tag{2.3}$$

$$\left. + \sqrt{(x - d)^2 + y^2 + z^2} - d\right) /c \tag{2.4}$$

For any case of interest, $d \gg \sqrt{x^2 + y^2 + z^2}$, and therefore this is well approximated by:

$$l(x, y, z) \approx \left(\sqrt{x^2 + y^2 + z^2} - x\right) /c \tag{2.5}$$

which is the formula adopted throughout this chapter. See Figure 2.1 for an illustration of this model.

Note that Equation 2.2 is a special case of the general equation

$$f_{\rm line}(t) = A \int \Psi(\tau) f_{\rm cont}(t-\tau)\, d\tau \tag{2.6}$$

where $\Psi(t)$ is the so-called *transfer function*, which gives the response of the line flux to a delta-function pulse in the continuum flux[1]. Thus, for any particular system, if we can infer the density of BLR clouds throughout space, we can automatically deduce the corresponding transfer function:

$$\Psi(\tau) = \int_V \delta\left(\tau - l(x,y,z)\right) \rho(x,y,z)\, dV \tag{2.7}$$

The meaning of this equation is that each location in space contributes to the transfer function at the value of the location's lag, with the size of the contribution being proportional to the amount of gas at that location.

2.1.2 Velocity-resolved reverberation mapping

Now suppose that the BLR gas is in motion, such that the system can be described by a time-invariant distribution function g defined over the phase space of a single particle:

$$g(x,y,z,v_x,v_y,v_z) = \rho(x,y,z) g(v_x,v_y,v_z|x,y,z) \tag{2.8}$$

The motion of the gas along the line of sight is assumed to affect the wavelength of reemitted light, but its distribution function is assumed to be time invariant and therefore

[1]For readers more familiar with image analysis, the transfer function is analogous to a PSF.

does not vary during the observing campaign. Then the emission line profile at time t will be a function of the line of sight velocity, $v_{\rm los}$:

$$f_{\rm line}(v_{\rm los}, t) = A \int_{v_y, v_z} \int_V f_{\rm cont}(t - l(x, y, z)) \tag{2.9}$$

$$\times g(x, y, z, v_x, v_y, v_z)\, dx\, dy\, dz\, dv_y\, dv_z \tag{2.10}$$

where $v_{\rm los}$ is in the x direction. This is the velocity-resolved equivalent of Equation 2.2.

2.2 Method

Our method for constraining the geometry and kinematics of the BLR is an application of Bayesian Inference (Sivia & Skilling 2006). In general, to infer parameters θ from data D, we begin by assigning a prior probability distribution $p(\theta)$ describing our initial uncertainty about the parameters. Sampling distributions $p(D|\theta)$ are also assigned to describe our uncertainty about how the data are related to the parameters. Once specific data $D = D^*$ are obtained, our updated state of knowledge about the parameters is described by the posterior distribution, given by Bayes' rule:

$$p(\theta|D = D^*, I) \propto p(\theta|I) p(D|\theta, I)|_{D=D^*} \tag{2.11}$$

Here I is any background information we have about the problem. In complex problems, where θ consists of a large number of parameters, Monte Carlo methods are used to produce random samples from the posterior distribution for θ. Methods such as Nested Sampling (Brewer et al. 2011a) can also provide the normalization constant for the posterior, known as the evidence, which is the key quantity for comparing the entire model with an alternative (Sivia & Skilling 2006).

In our method, the parameters θ to be inferred are those describing the spatial profile of the BLR gas, and the continuous continuum flux, $f_{\rm cont}(t)$. Since it is impossible to represent a continuum in a computer, we instead infer $f_{\rm cont}(t)$ evaluated at 500 time points, covering a time interval larger than the continuum data. The continuum modeling technique is described in detail in the next section.

Throughout this chapter, both the continuum flux and line flux timeseries are considered part of the dataset D:

$$D = \{\mathbf{y}_{\rm line}, \mathbf{y}_{\rm continuum}\} \tag{2.12}$$

The prior information consists of the times at which the line flux and continuum flux are measured, $\mathbf{t}$ and the error bars on the line flux and continuum flux measurements, $\boldsymbol{\sigma}$:

$$I = \{(\mathbf{t}, \boldsymbol{\sigma})_{\rm line}\,, (\mathbf{t}, \boldsymbol{\sigma})_{\rm continuum}\} \tag{2.13}$$

The likelihood function is chosen to be Gaussian, centered around the model-predicted line flux timeseries:

$$p(D|\theta) = \prod_{i=1}^{n} \frac{\exp\left[-\frac{1}{2}\left(\frac{y_{i,\rm line} - m_i(\theta)}{(\kappa\sigma_i)}\right)^2\right]}{(\kappa\sigma_i)\sqrt{2\pi}} \tag{2.14}$$

where κ is a "noise boost" parameter to account for the presence of unknown systematic effects not included in the reported error bars, such as those due to flux calibration, wavelength calibration, and continuum subtraction.

Once the posterior distribution is obtained, many different algorithms are available for exploring it and computing summaries such as marginal distributions for parameters. We have implemented our model with two methods, the first is Metropolis-Hastings, a Markov-Chain Monte Carlo (MCMC) algorithm, which provides samples from the posterior PDF for the model parameters. The second is Diffusive Nested Sampling (Brewer

et al. 2011a), which provides samples from the posterior PDF *and* an estimate of the evidence value for the model. Although the evidence calculation makes the second algorithm significantly slower than the first, Diffusive Nested Sampling is much faster than alternative MCMC-based implementations of Nested Sampling (Brewer et al. 2011a). The results presented here to test the method use the MCMC algorithm, while the Diffusive Nested Sampling algorithm is used to apply the method to real reverberation mapping data (Brewer et al. 2011b).

2.2.1 Continuum interpolation

In order to create a mock line flux time series to compare with the data, it is necessary to interpolate between the continuum flux datapoints. Linear interpolation is the simplest approach, but it does not provide an estimate of the uncertainty in the interpolation, suggesting that we know precisely the value of the continuum $f(t)$ at all times between the measured datapoints. If we want to obtain reliable uncertainties in our results, we should acknowledge the uncertainty introduced by the interpolation process.

To account for this, we consider the entire continuum function $f_{\rm cont}(t)$ to be an unknown parameter to be inferred from the data. The prior distribution for $f_{\rm cont}(t)$ is a Gaussian Process (MacKay 2003; Rasmussen & Williams 2006), which is a convenient class of probability distributions over function space. Given a mean function $\mu(t)$ and a covariance function $C(t_1, t_2)$, the probability distribution for the function value f at any finite set of times is a multivariate Gaussian:

$$p(\mathbf{f}|\mu, C) = \frac{1}{\sqrt{(2\pi)^n \det \mathbf{C}}} \exp\left(-\frac{1}{2}(\mathbf{f}-\boldsymbol{\mu})^T \mathbf{C}^{-1} (\mathbf{f}-\boldsymbol{\mu})\right) \tag{2.15}$$

where μ is a vector of means at the relevant time-points, and $\mathbf{C}$ is the covariance matrix, obtained by evaluating the covariance function at the relevant times. In the reverberation mapping problem, $f_{\rm cont}(t)$ is constrained by *two* data sets: the continuum measurements, and the line measurements. We parameterize the covariance function and mean function with four hyperparameters: μ (the long-term mean), σ (the long-term standard deviation), τ (typical timescale of variations) and α (a smoothness parameter between 1 and 2), such that the mean function is a constant $\mu(t) = \mu$ and the covariance function is

$$C(t_1, t_2) = \sigma^2 \exp\left[-\left(\frac{|t_2 - t_1|}{\tau}\right)^{\alpha}\right] \tag{2.16}$$

The posterior distribution function for $f(t)$ given some continuum data (but not the line data) is shown in Figure 2.2. Note that outside the areas where we have data, the uncertainty gets large, but in areas where the data are well sampled, the uncertainty in the interpolation is small. We keep track of $f(t)$ at 500 times, both slightly preceding and following the data. Further interpolation between these 500 points is linear. 500 continuum parameters is sufficient to render the distance between continuum flux points much smaller than the maximum monitoring cadence, allowing us to resort to linear interpolation only on scales not probed by the data. We change the 500 parameters in the same way as the model parameters, with every new proposal for the continuum function related to the one before. The function $f(t)$ can be parameterized by 500 variables with standard normal priors, which are converted to $f(t)$ values by multiplication with the Cholesky decomposition of $\mathbf{C}$. We note that our Gaussian Process method for interpolation, in the special case $\alpha = 1$, is equivalent to the method of Zu et al. (2011), apart from computational details. $\alpha = 1$ has also been used in detailed studies of quasar variability

(e.g. MacLeod et al. 2010).

2.2.2 Creating mock and simulated data

Given the phase-space density for the BLR gas and the continuous continuum light curve, we can easily create a mock line flux timeseries by adding together the line flux from all the gas, which is proportional to the continuum flux at the respective lag of the gas. The resulting mock line flux timeseries can then be compared to the reverberation mapping data and does not depend on the kinematics of the gas. If we include the velocity information of the gas, we can create a mock spectrum for each point in the timeseries. In order to create a mock spectrum, we make a histogram weighted on flux of the amount of gas with a given velocity using the same velocity resolution as the data. We then convolve the histogram with a gaussian whose width is defined by a combination of thermal broadening and instrumental resolution. The mock spectrum can then be compared to the reverberation mapping spectral data and depends on the kinematics of the gas.

2.3 Illustration and tests using simple models

In order to illustrate our method, we have developed simple models of the BLR region geometry and dynamics. As this method is fully general, it is also possible to implement more complex models within the framework described so far. We showcase these simple models by creating simulated data with known true parameter values in our models. This allows us to test our code as well as to explore the accuracy and precision of

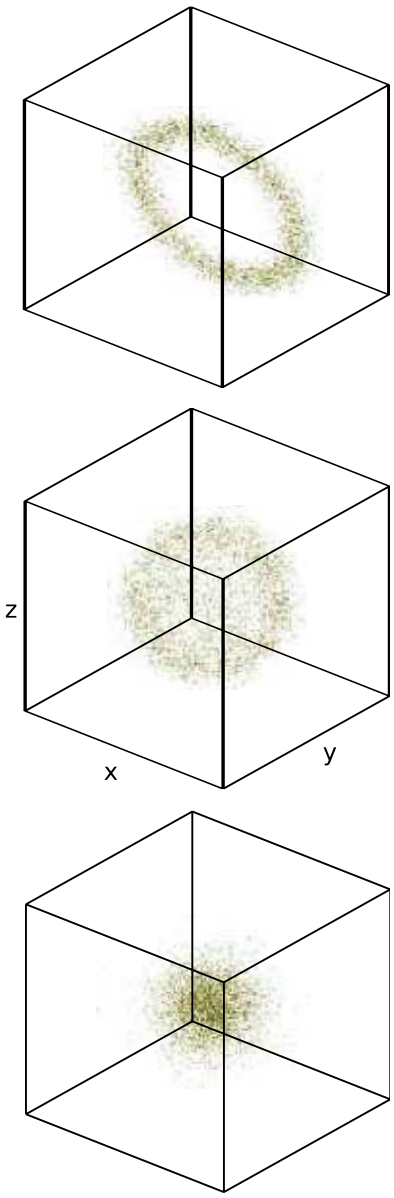

Figure 2.3: Example spatial distributions of the broad line emitting gas that can be recovered by our generic geometric model. They include a ring/disk (top panel), a spherical shell (middle panel), and a spherical gaussian distribution (bottom panel).

the results obtainable by this method of reverberation mapping analysis. Such tests on simulated data also allow us to ascertain the data quality needed to perform inferences regarding increasingly complicated model parameters. We showcase both geometry-only and geometry plus kinematics models, where the latter are the same as the first with the

addition of velocity information given to the BLR gas. We show transfer functions for the geometry models and velocity-resolved transfer functions for the kinematics models.

To ensure that in our method the true parameter values are recovered, we save instances of each model and use them as simulated reverberation mapping data, adding noise and varying the timeseries characteristics to match reverberation mapping campaigns of varying quality. A simulated dataset consists of line flux and continuum flux measurements. Given a BLR model, the continuous continuum light curve is all that we need to create, since the mock line flux measurements can be obtained from the model and continuous continuum light curve. We create continuous continuum light curves by using the hyperparameters of the Gaussian Processes continuum interpolation. The hyperparameters contain information about the timescales and levels of variability in an AGN continuum timeseries. We use values for the hyperparameters from interpolation of the Lick AGN Monitoring Project (LAMP; Walsh et al. 2009; Bentz et al. 2009b) continuum timeseries of Arp 151, one of the most variable AGN in the LAMP sample. The values used for the hyperparameters were $\mu = 75$ (arbitrary units), $\sigma = 30$ (same units as μ), $\tau = 6 \times 10^6$ seconds and $\alpha = 1.5$ (dimensionless).

2.3.1 Geometry model: Ring/disk/shell

Model definition

We use a flexible geometry model of the BLR gas density to test our method when only integrated line flux measurements are used instead of the full spectral shape. The model is that of a spherical shell centered on the central engine with parameters allowing

partial, axisymmetric illumination of the shell and varying inclination of the resulting ring/disk. Examples of possible configurations, ranging from a complete shell to a thin ring/disk, are shown in Figure 2.3. The parameters of the model are the mean radius of the disk, r_0, the thickness of the disk in the radial direction, σ_r, the illumination angle of the shell, and the inclination of the shell. The illumination angle is defined so that values approaching 0 define an increasingly thin ring/disk and a value of $\pi/2$ defines a spherical shell. The inclination angle is defined so that values approaching 0 define a face-on ring/disk and a value of $\pi/2$ is an edge-on ring/disk. We use a normal distribution to define the radial thickness of the shell, so that r_0 and σ_r are the average and 1σ width of a normal distribution. The normal distribution is created in the x, y, and z cartesian coordinates.

It is important to set appropriate prior probability distributions for each model parameter. For parameters where we know the order of magnitude of the parameter value we use a flat prior in the parameter. Examples of parameters with flat priors in the parameter include the inclination angle and the illumination angle, which may only vary between 0 and $\pi/2$. For parameters where we do *not* know the order of magnitude of the parameter value we need a prior that treats many orders of magnitude equally, so we use a flat prior in the log of the parameter. Examples of parameters with flat priors in the log of the parameter include r_0 and σ_r. These choices of prior probability express complete ignorance in the value of a parameter within some reasonable range, but it is necessary to make the distinction between whether or not the order of magnitude of a parameter value is known. In the cases considered in the remainder of this chapter, the posterior is much narrower than the prior, and therefore the inference is dominated by

the likelihood, i.e. the information contained in the data.

The underlying spherical symmetry of these models and the angular dependence of the ring/disk model allow us to use spherical coordinates. In order to sample the gas phase-space density at a finite number of points, we use a grid in $\log(r)$, ϕ, and $\cos(\theta)$. Using equal steps in $\cos(\theta)$ instead of θ means that the volume of each grid point depends only on the radius, r. The density is then multiplied by the volume of the grid point to find the total mass of gas in each grid point. The emissivity of each grid point also depends on the radius r because the continuum ionizing radiation flux falls off as r^{-2}, requiring more gas mass at larger radii to have the same line flux contribution as less gas mass at smaller radii. In general, the illumination parameter allows us to model any axisymmetric ionizing flux.

We test our method to recover the BLR model parameters by creating simulated data, the true parameter values of which are given in Table 2.1. The continous continuum function is obtained using the hyperparameters from the Gaussian Processes interpolation of Arp 151 reverberation mapping data, as described in Section 2.2.1, and evaluated at 120 consecutive "observations" one day apart. The line flux timeseries for each model are generated using this continuous continuum function and a given set of model parameters. The line flux timeseries contain 60 "observations" one day apart, starting 60 days after the start of the continuum flux "observations". These simulated data are meant to represent excellent reverberation mapping data, with an observation campaign of similar length to recent campaigns (see e.g. Bentz et al. 2009b), but without gaps due to difficult weather conditions. Additional noise has also been added to the simulated data. Most simulated datasets have line flux errors of 1.5%, which represents very favorable observing

conditions, but we have also tested simulated data with errors of 5% to reflect the current typical error of reverberation mapping line flux measurements.

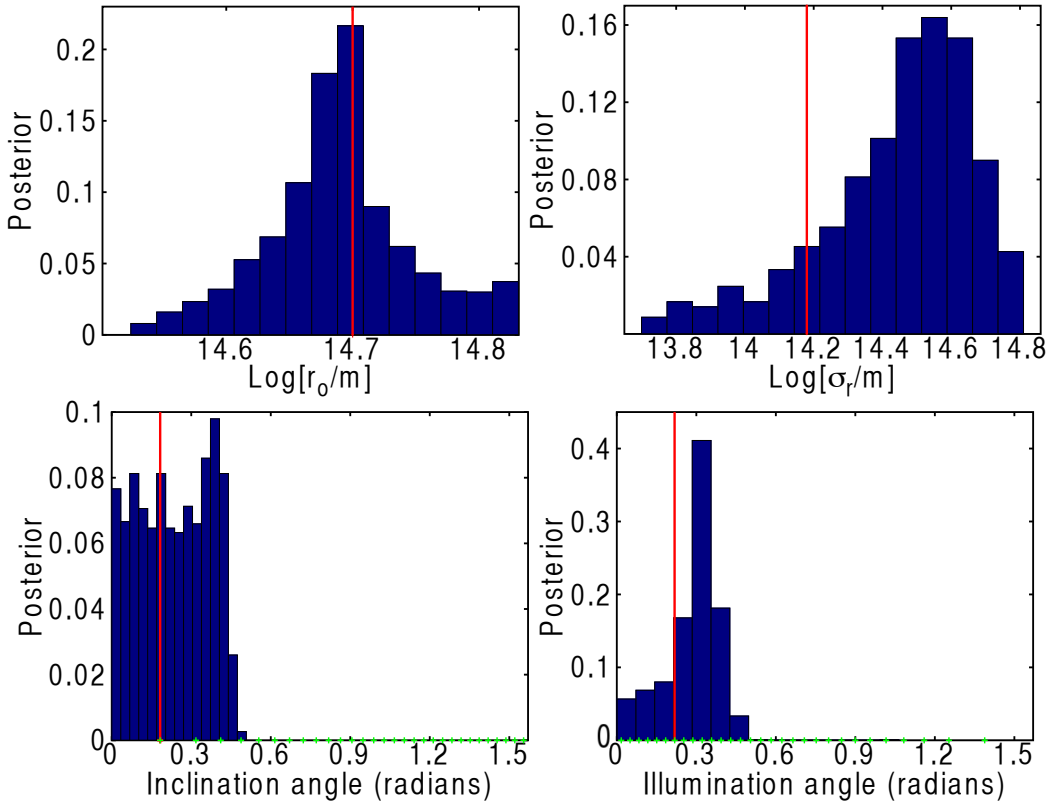

Figure 2.4: Posterior probability distributions for face-on disk geometry model parameters of simulated data 4 (see Table 2.1) with 1.5% line flux uncertainty. Top to bottom: r_0, σ_r, inclination angle, and illumination angle. The inclination angle and illumination angle both have a resolution given by the grid in $\cos\theta$. The true value for each parameter in this model is shown by the vertical red line and the grid in $\cos\theta$ is shown along the x-axis with green crosses for the angular parameters. The grid used to create these posterior distributions is 60 steps in $\log(r)$, 40 steps in ϕ, and 60 steps in $\cos\theta$.

Testing the geometry model

The first test is whether we can recover the parameter values of the simulated data using the MCMC algorithm described in Section 2.2. Since our one flexible geometry model encompasses a number of different geometries, such as a shell, thin or thick ring

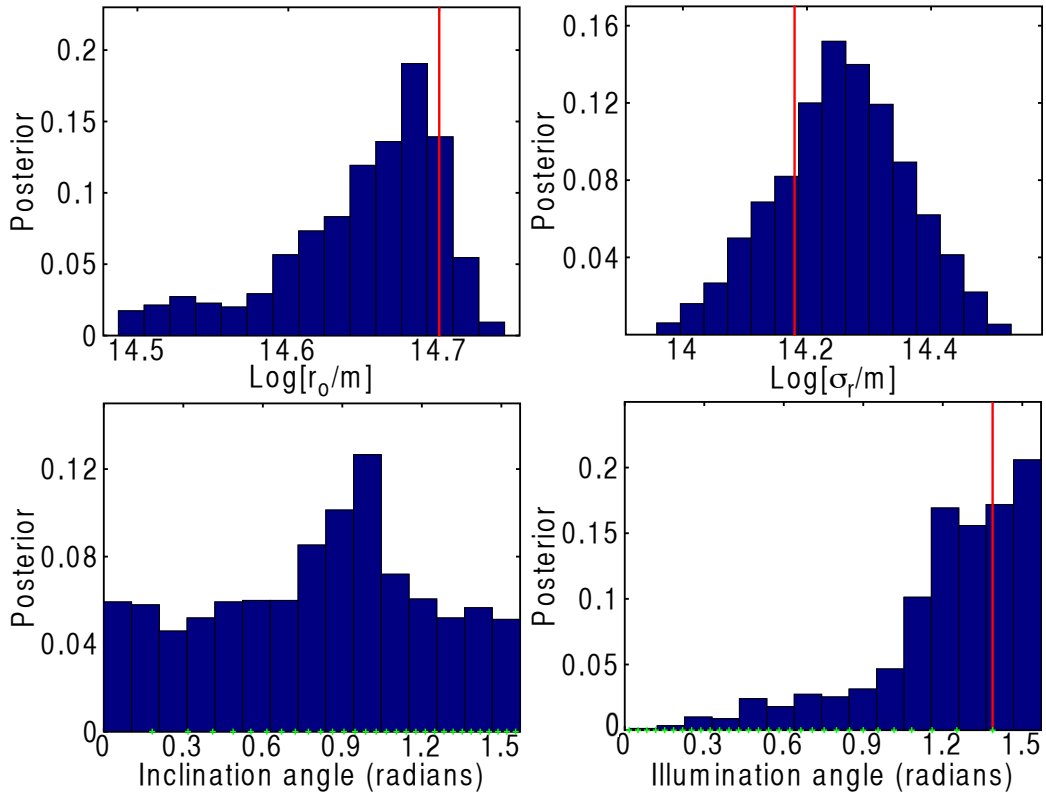

Figure 2.5: Posterior probability distributions for shell geometry model parameters of simulated data 5 (see Table 2.1) with 1.5% line flux uncertainty. Top to bottom: r_0, σ_r, inclination angle, and illumination angle. The true values for the parameters and the grid points are shown as in Figure 2.4. Note that since the simulated data is spherically symmetric, it should not strongly prefer an inclination angle, and thus no true parameter value is shown in the inclination angle pdf.

or disk, we do not have to consider model selection at this point. We test the many possible geometries of this model by creating five simulated datasets, whose true parameter values are given in Table 2.1. The simulated datasets include an inclined disk with line flux errors of 1.5% and 5% and an edge-on disk, a face-on disk, and a shell with line flux errors of 1.5%. The MCMC algorithm is typically run for 150,000 iterations and all parameter values are recovered to within two standard deviations of the posterior probability distributions of the parameters, with 10/13 recovered to within one standard deviation. This is as expected, since we should find the true parameter value to lie within

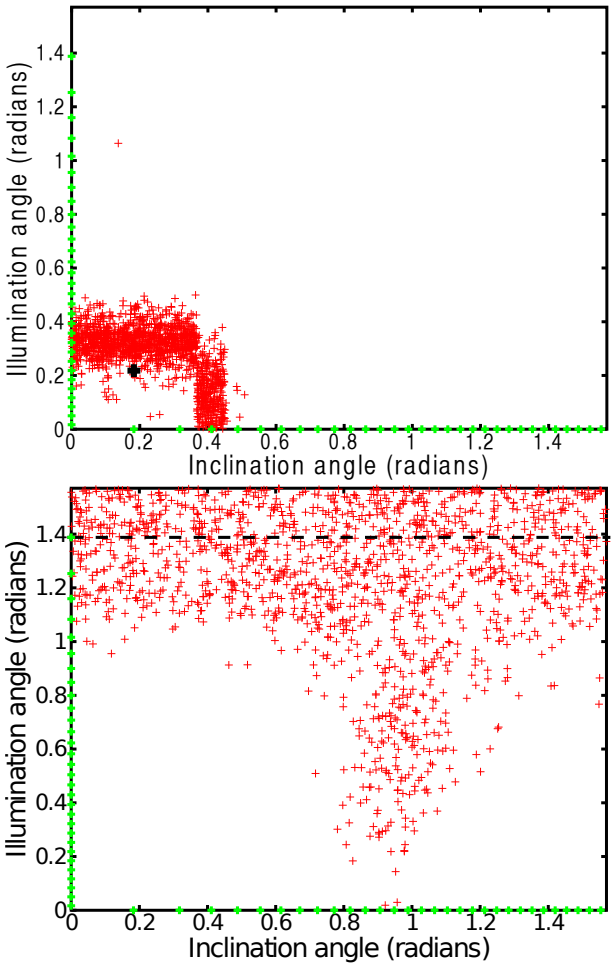

Figure 2.6: Joint posterior probability distributions for inclination and illumination angles for face-on disk with 1.5% line flux uncertainty (simulated data 4) and shell with 1.5% line flux uncertainty (simulated data 5). The true parameter values are shown by (top) the black cross and (bottom) the black dashed line.

1σ about $\sim 68\%$ of the time and to lie within 2σ about $\sim 95\%$ of the time. The mean and standard deviation of the posterior distributions are given in Table 2.2, with the exception of many of the angular parameters, where the quoted 1σ uncertainty does not adequately describe the posterior distribution. Part of the reason for the standard deviation of the angular parameters not describing the posterior is due to the uneven step size in θ, so that values of the illumination angle close to $\pi/2$ and values of the inclination

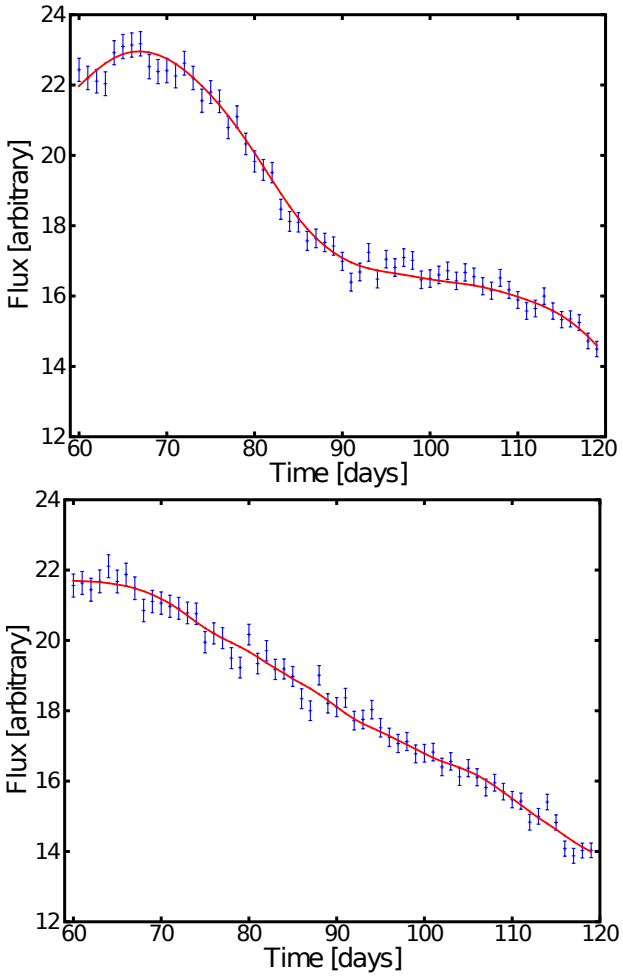

Figure 2.7: Timeseries for face-on disk (simulated data 4, top panel) and shell (simulated data 5, bottom panel), both with 1.5% line flux uncertainty. Simulated data are shown in blue with error bars and the mock data from a random set of parameter values sampled from the posterior is shown in red. The continuum light curve used to create these line light curves is shown in Figure 2.2.

angle close to 0 radians have much poorer angular resolution. This might lead to an angular parameter being quoted as having a mean of 1.22 radians and a 1σ uncertainty of 0.29, as for the illumination angle of the Shell model simulated data, but while this uncertainty may seem large, it corresponds to an uncertainty of only 1-2 grid points in θ. The posterior distributions for the face-on disk and shell simulated data are shown in Figures 2.4 and 2.5. Select joint probability distributions between the inclination and il-

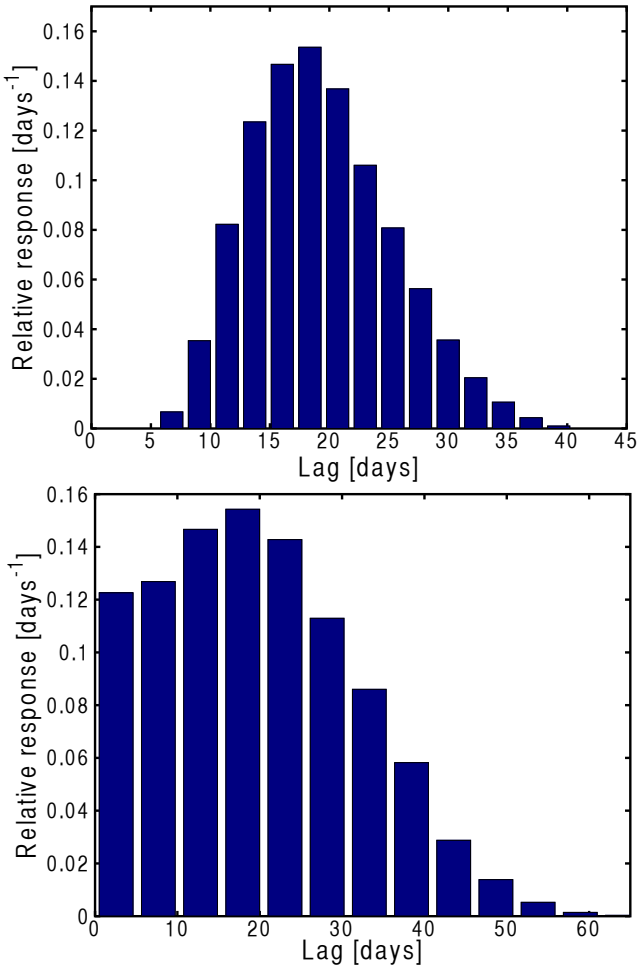

Figure 2.8: Velocity-unresolved transfer functions for face-on disk (simulated data 4) and shell (simulated data 5), both with 1.5% line flux uncertainty. The same grid was used to make these transfer functions as was used to obtain the posterior probability distributions shown in Figures 2.4 and 2.5.

lumination angles are also shown in Figure 2.6 in order to show the degeneracies between different models. In particular, for the shell model, the inclination is not constrained unless the illumination angle is small, or rather, unless the sphere of BLR gas is not entirely illuminated.

The posterior pdfs for the five simulated datasets show that the edge-on disk, face-on disk, and shell geometries allow for excellent recovery of the parameter values with

estimates of the uncertainty. For the two inclined disk simulated datasets, there is some degeneracy in the angular parameters, leading to large uncertainties in their average values. The MCMC algorithm finds a more likely geometry configuration than the true configuration for the inclined disk datasets, although the true configuration is still a valid possibility with posterior local maxima at the true parameter values. With the increased simulated line flux error from 1.5% to 5% however, it becomes increasingly difficult to recover the angular parameters, and only the mean radius is recovered with a small enough uncertainty as to be useful in describing the BLR. This emphasizes the importance of obtaining high quality line flux data in reverberation mapping campaigns.

The timeseries and transfer functions for the face-on disk and shell MCMC geometry model tests are shown in Figures 2.7 and 2.8, respectively. The timeseries show the simulated data overlaid with mock data created with parameters sampled randomly from the posterior probability distributions. The fit of the mock data to the simulated data is excellent for all five models. The variety in the shape of the simulated data timeseries, all well-fit by their respective models, shows that the MCMC algorithm for model parameter value recovery is robust for a wide range of models. The transfer functions also show a variety of shapes. For a thin shell geometry, thinner than the shell of simulated dataset 5, our resulting transfer function agrees with the analytic form of a tophat function (see Peterson 1993).

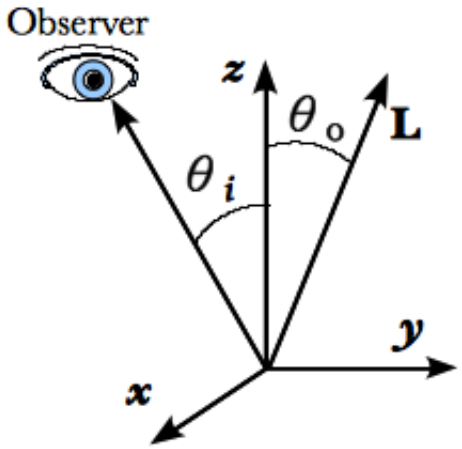

Figure 2.9: Sketch of the dynamical model. The angular momentum vector **L** defines the plane of the orbits. Owing to cylindrical symmetry, for each value of θ_0 we consider the entire family of **L** generated by rotation around the z-axis. The observer is assumed to be in the x-z plane, at angle θ_i from the z-axis.

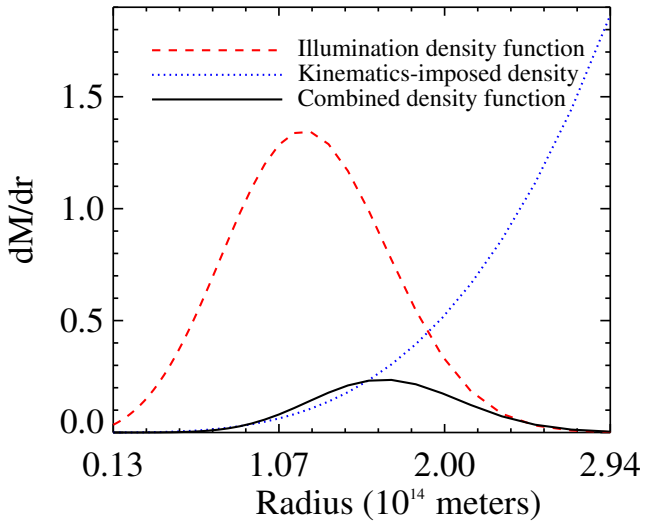

Figure 2.10: Illustration of the combined constraints given by the illumination function and by the dynamical model. The red line shows an example of the distribution of illuminated BLR gas mass assuming a uniform underlying density. The blue line shows the actual underlying mass distribution as constrained by the dynamical model. The resulting effective distribution of illuminated mass, consistent with both the geometry and dynamical constraints is given by the product of the two functions, shown in black.

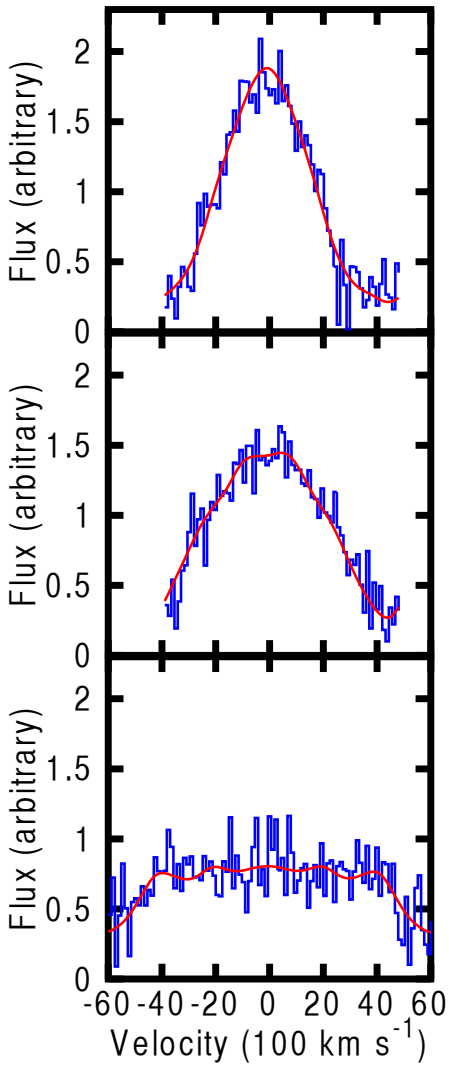

Figure 2.11: Example spectra from three simulated datasets: (top) face-on disk with orbits confined to the disk, (middle) face-on disk with isotropic distribution of orbit orientations, and (bottom) spherical distribution with isotropic distribution of orbit orientations. The instrumental resolution of the simulated spectra is FWHM $\sim 800\,\mathrm{km\,s^{-1}}$. The bottom spectrum for a spherical distribution of orbits is wider than for a face-on disk because the spherical distribution allows for orbits to move directly along the line of sight, while the face-on disk only results in a small component of the BLR gas velocity lying parallel to the line of sight. The width of the spectral line is thus directly connected to both the opening angle of the disk and the inclination angle.

2.3.2 Dynamical model

Model definition

In order to constrain the kinematics of the BLR and the mass of the central black hole, we must model the velocity distribution of the BLR gas in the context of a dy-

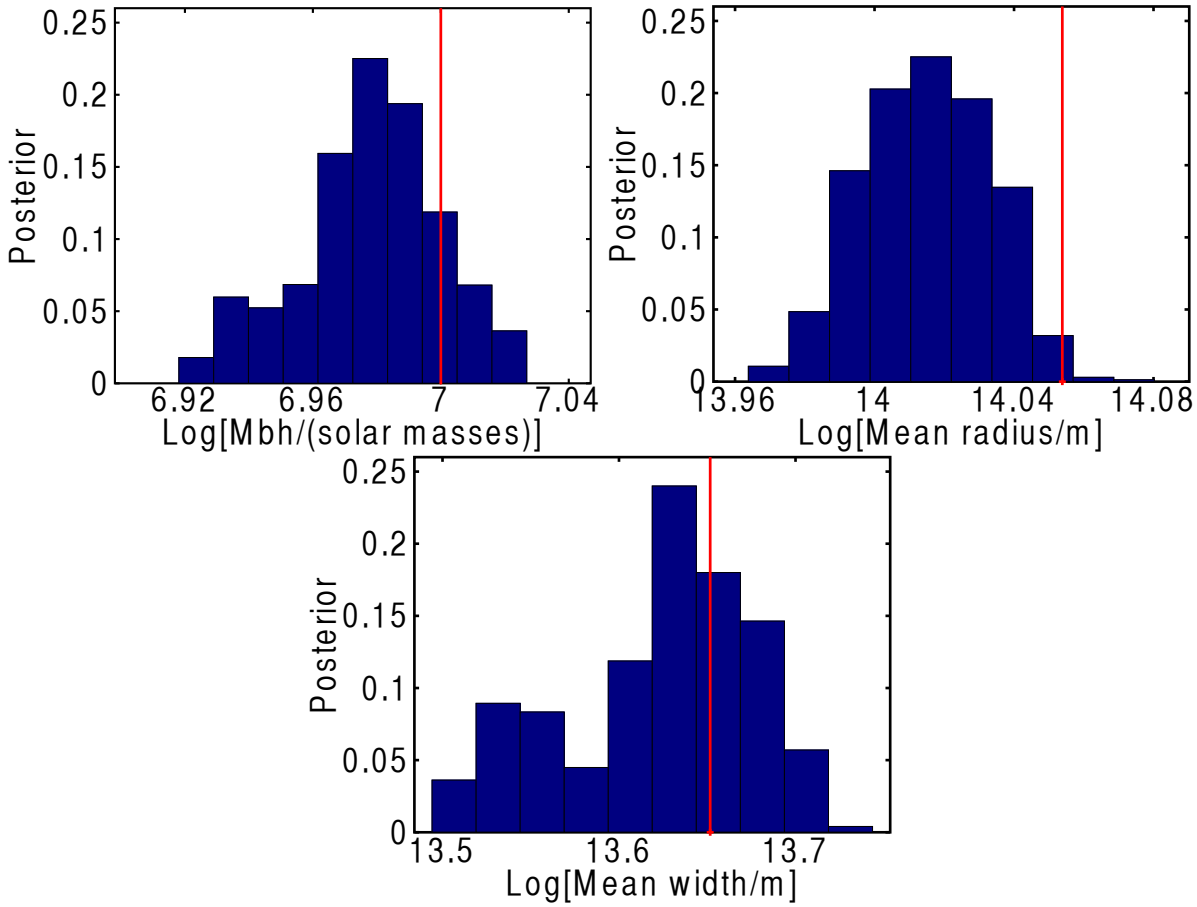

Figure 2.12: Posterior pdfs for the first dynamical simulated dataset: face-on disk with the orbits confined to the disk. (Top) black hole mass, (middle) the average radius of the BLR gas mass, and (bottom) the average width of the BLR gas mass.

namical model. For simplicity of illustration and speed of computation, we consider here a cylindrically symmetric model where the BLR gas is considered to be made of test particles in bound orbits within the spherical Keplerian potential of the black hole. We parameterize the model in terms of energy and angular momentum, constants of the BLR gas motion, so we are guaranteed velocity and geometry distributions that do not evolve in time, and are therefore stationary during the monitoring campaign. In future chapters we will generalize the model to include unbound orbits to describe inflows and outflows, and also other physical mechanisms, such as radiation pressure or winds (Marconi et al.

2008; Netzer & Marziani 2010).

The model is illustrated in Figure 2.9. For any choice of angular momentum $\mathbf{L}$, energy E and black hole mass $M_{\rm BH}$, the motion of the BLR test particles is then described by the standard conservation equation resulting in elliptical orbits in the plane perpendicular to the angular momentum. Given our cylindrical symmetry we will consider families of angular momenta obtained by rotation around the z-axis and defined by the polar angle θ_0 (see Figure 2.9). The spatial density of the BLR is then given by

$$P(r, \theta, \phi | E, L, \theta_0) \propto \frac{1}{v} \times \frac{1}{|\sqrt{\sin^2 \theta_0 - \cos^2 \theta}|}, \tag{2.17}$$

where the angular term comes from integrating over the uniform distribution of azimuthal angle ϕ_0 of the angular momentum vector, and v is the total magnitude of the velocity vector:

$$v = \sqrt{2E + \frac{2GM_{BH}}{r}}. \tag{2.18}$$

Owing to the symmetry of our model we can consider only $\theta_0 < \pi/2$ (i.e. $L_z > 0$), obtaining the following limits on the allowed θ coordinate for the BLR:

$$\frac{\pi}{2} - \theta_0 < \theta < \frac{\pi}{2} + \theta_0. \tag{2.19}$$

As θ_0 approaches zero, the model represents a thin disk, while as θ_0 approaches $\pi/2$ the model covers the whole sphere. Conservation of energy and angular momentum limits the radial coordinate to the range:

$$r > -\frac{GM_{BH}}{2E} - \frac{1}{2}\sqrt{\left(\frac{GM_{BH}}{E}\right)^2 + \frac{2L^2}{E}}, \tag{2.20}$$

$$r < -\frac{GM_{BH}}{2E} + \frac{1}{2}\sqrt{\left(\frac{GM_{BH}}{E}\right)^2 + \frac{2L^2}{E}}. \tag{2.21}$$

Finally, E and L are connected by the usual condition:

$$|L| \leq \frac{GM_{BH}}{\sqrt{-2E}}. \tag{2.22}$$

For every allowed value of r, θ, and ϕ, the component of the velocity vector along the line of sight can be computed in the standard manner, resulting in two solutions per position, in general (outbound and inbound; four if one considers $L_z < 0$ as well). More complex geometries and kinematics can be obtained by superpositions of multiple sets of E, L, and θ_0 values within the same potential given by $M_{\rm BH}$. However, this further increases the dimensionality of parameter space and computing time. Therefore in this example we will only use one such set.

We apply prior probability distributions to the model parameters as described for the geometry model. The priors for the extra parameters in the dynamical model not part of the geometry model are as follows. The parameter θ_0 has a flat prior in the parameter ranging from 0 to $\pi/2$. The parameters $M_{\rm BH}$, E, and L have flat priors in the log of the parameter.

In addition, in order to impose a BLR gas geometry, we model the distribution of *illuminated gas*, as the product of the spatial distribution given by the dynamical model with that imposed by one of our geometrical models, representing in this case the illumination function. This results in a broad range of geometries, giving the model a considerable flexibility (for example, in the future one could think of an anisotropic illumination function to model dust obscuration). The procedure is illustrated in Figure 2.10. Note that the radial distribution of the illuminated gas is not gaussian anymore, as in the ring/disk/shell geometry model. The mean radius then is not the r_0 parameter of

the geometry model, but must be computed numerically for each set of geometric and dynamical parameters. Similarly, the mean width is no longer σ_r and must be computed numerically.

A model spectrum at a given time is obtained by summing all the line of sight velocities, weighted by the spatial density of illuminated gas multiplied by the continuum flux at an epoch corresponding to the appropriate lag-time. In order to compare with real data, the model spectrum is then convolved with a gaussian to represent instrumental broadening. Since we do not expect real data to match our model perfectly, we introduce a relatively large uncertainty in the form of the spectral line by adding gaussian noise with a variance of $\sigma^2(F) = \alpha\, F + \beta$, where $\alpha = 0.00018$ and $\beta = 0.025$. This model for the variance assumes both a dependence on spectral line flux F through the α parameter and a dependence on the continuum uncertainty through the β parameter. The units of α are flux and the units of β are flux^2. The specific values of α and β are related to the arbitrary flux units of our simulated spectra and result in a signal to noise of ~ 4. Conservatively this signal-to-noise ratio is lower than typically achieved in state of the art spectral monitoring campaigns. Examples of synthetic spectra at a resolution of FWHM$=$ 13.1 Å, or $\sim 800\,\mathrm{km\,s^{-1}}$ at the wavelength of Hβ, are shown in Figure 2.11. The face-on disk systems (top and middle panel of Figure 2.11 have velocity bins of $\sim$120 $\mathrm{km\,s^{-1}}$ while the sphere system (bottom panel) has velocity bins of $\sim$20 $\mathrm{km\,s^{-1}}$. Notice how the line shapes are clearly different even for models with the same black hole mass. This is a clear illustration of the power of velocity resolved reverberation mapping as a diagnostic of the BLR geometry as well as kinematics.

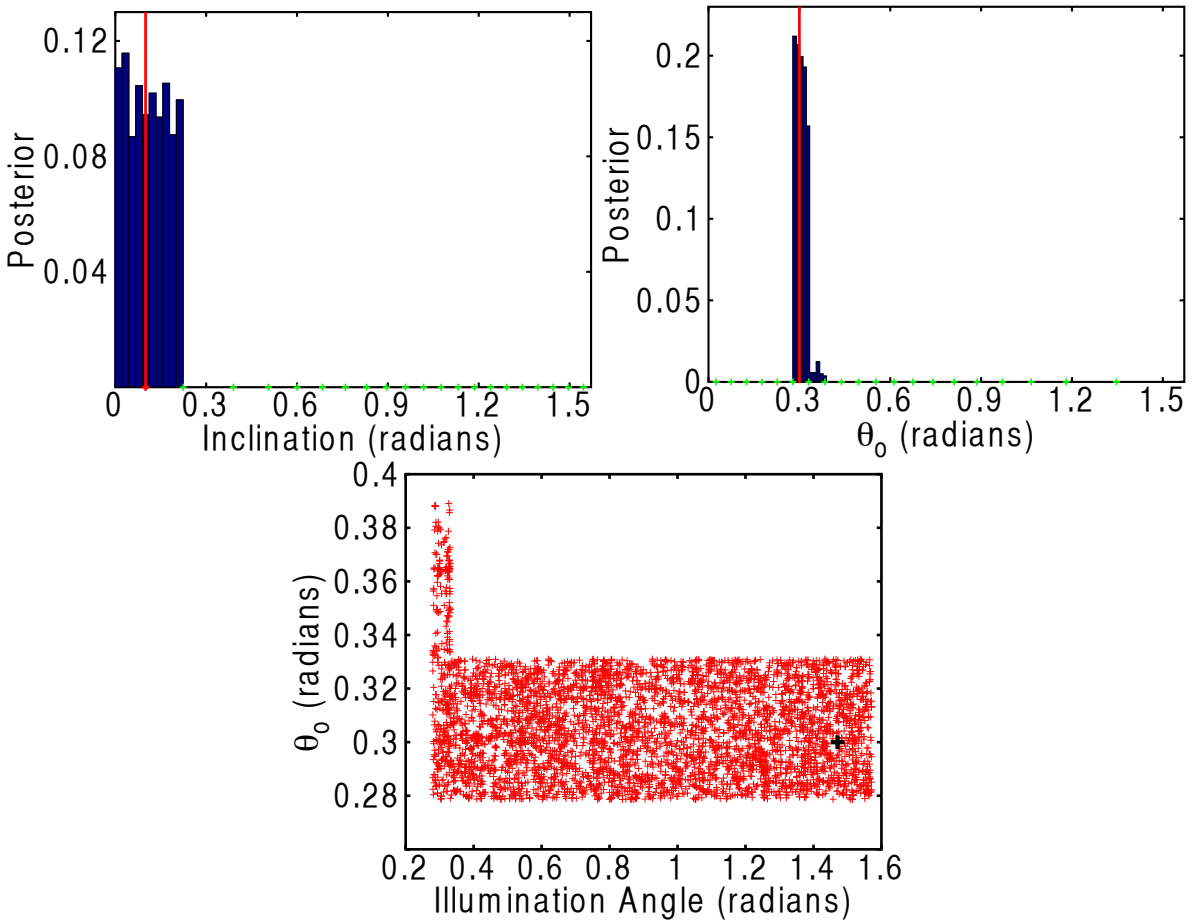

Figure 2.13: Posterior pdfs for the first dynamical simulated dataset: face-on disk with the orbits confined to the disk. (Top) inclination angle, (middle) θ_0, and (bottom) the joint pdf of θ_0 and the illumination angle. Notice in the joint pdf that θ_0 may only be larger than ~ 0.3 radians when the illumination angle is ~ 0.3 radians, so the angular extent of the disk is well determined.

Testing the dynamical model

We test our dynamical model by creating simulated data-sets consisting of timeseries of the continuum flux and of the line profiles of a broad line. The line profiles of the simulated datasets are shown in Figure 2.11. The kinematics parameters E and L are initially chosen to satisfy nearly circular orbits of the BLR gas at the mean radius given by the illumination function. A disk of broad line emitting material can be constrained

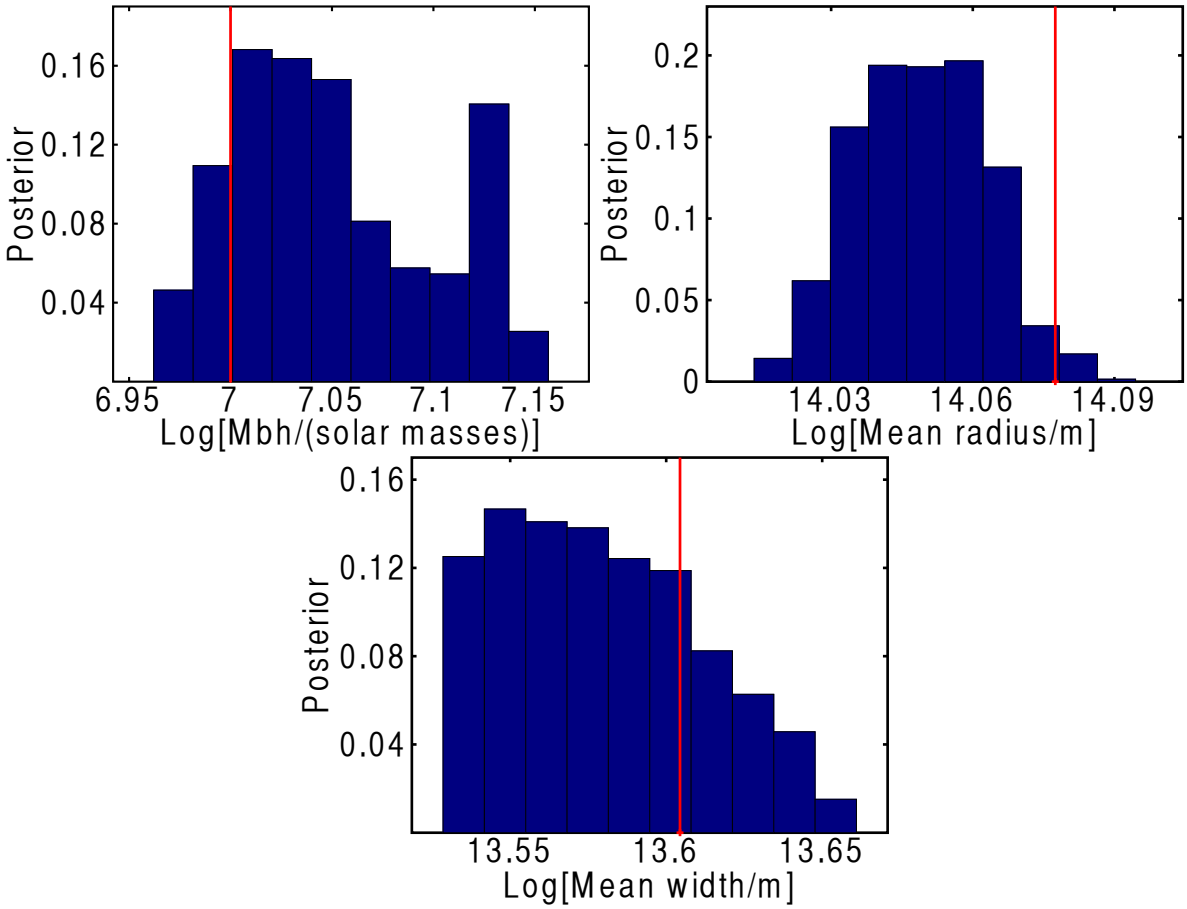

Figure 2.14: Posterior pdfs for the second dynamical simulated dataset: face-on disk with the orbits in the entire sphere. (Top) black hole mass, (middle) the average radius of the BLR gas mass, and (bottom) the average width of the BLR gas mass.

by either the illumination function or the value of θ_0.

The first simulated dataset is a thin disk viewed nearly face-on, with dynamics imposed by a single value of energy and angular momentum. The thin disk is constrained by the value of θ_0, while the illumination function describes the whole sphere being illuminated. This means that all allowed orbits lie in the disk and that the rest of the sphere does not contain broad line emitting gas. The second simulated dataset is also a thin disk viewed nearly face-on with a single value of energy and angular momentum, but for this case the illumination function constrains the disk. We choose a value of θ_0 close

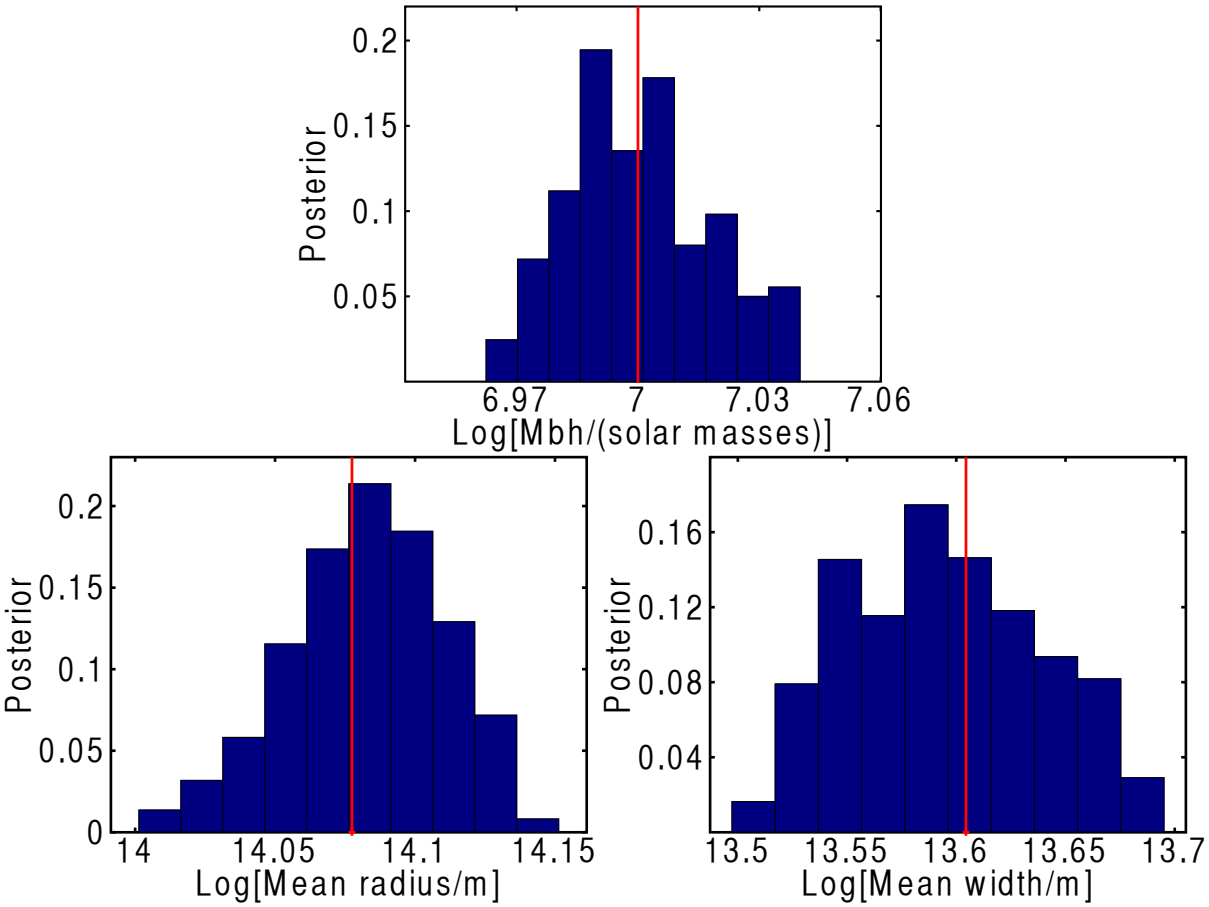

Figure 2.15: Posterior pdfs for the third dynamical simulated dataset: sphere configuration with orbits allowed in the entire sphere. (Top) black hole mass, (middle) the average radius of the BLR gas mass, and (bottom) the average width of the BLR gas mass.

to $\pi/2$ so that orbits are allowed in the entire sphere. The third simulated dataset is a fully illuminated sphere with orbits that are also allowed in the entire sphere, so again θ_0 is close to $\pi/2$. This is still an axisymmetric configuration, as the BLR gas density imposed by the kinematics depends upon the θ-coordinate. The true parameter values of the three simulated datasets used to test the kinematics model are shown in Table 2.3.

We test each of the three simulated datasets assuming only one set of kinematics parameters. The parameter values inferred using our method are shown in Table 2.4, while the full posterior pdfs are shown for all parameters of interest for the first simulated

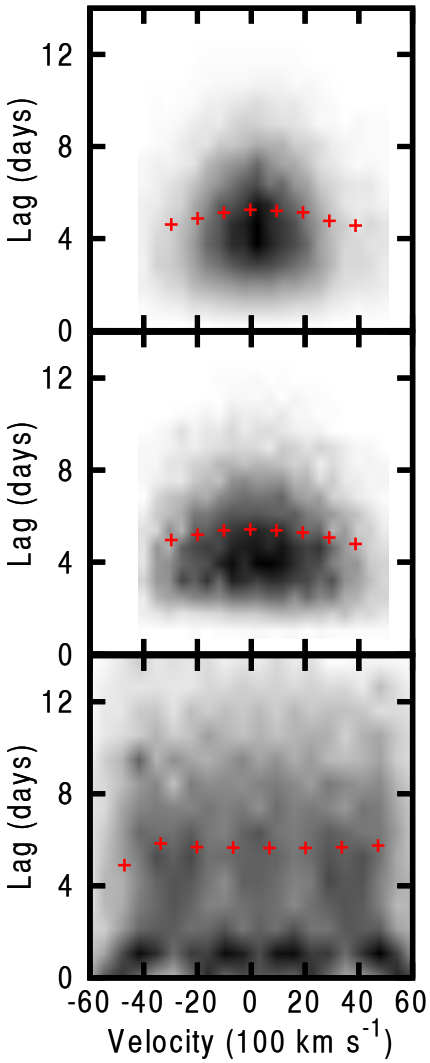

Figure 2.16: Velocity-resolved transfer functions for the three dynamical simulated datasets: (top) face-on disk with orbits confined to the disk, (middle) face-on disk with orbits allowed in entire sphere, and (bottom) sphere configuration with orbits allowed in entire sphere. The red crosses show the response weighted mean lag in 10 velocity bins across the spectra.

dataset in Figures 2.12 and 2.13. The posterior pdfs for the black hole mass, average radius of BLR gas mass, and average width of the BLR gas mass are also shown for the second and third simulated datasets in Figures 2.14 and 2.15. They show that the black hole mass, average radius, and average width of the BLR are well determined for all three simulated datasets. The angular parameters are also well determined when physically

possible. For example, for the first dynamics simulated dataset of a face-on disk with orbits confined to the disk, the inclination angle and θ_0 are determined to within one or two grid points, while the illumination angle is only constrained to be $\gtrsim 0.3$ radians. The illumination angle cannot be determined more accurately because the BLR gas emission only comes from the disk, so as long as the entire disk is illuminated the spectrum is not sensitive to further changes in the illumination angle.

Finally, we also compute the velocity-resolved transfer functions for the three simulated datasets, shown in Figure 2.16. As expected, the transfer functions for the face-on disk configurations show little response at very small lags, while the sphere configuration shows the highest intensity of response at small lags. The transfer functions for the face-on disk configurations are similar, but clearly lead to different line profiles, again illustrating the power of modeling the full dataset rather than just trying to model the transfer function.

2.4 Summary and conclusions

We introduce and test a new method for analyzing reverberation mapping data of AGN by directly modeling the BLR. We illustrate our method by creating simple geometry and dynamical models of the BLR. Using a model of the BLR geometry to reproduce the integrated line flux timeseries from reverberation mapping data allows us to estimate the average radius of the BLR, as well as the mean width, illumination function, and inclination angle to the line of sight. Models of the BLR that include geometry *and* dynamical information allow us to additionally estimate the black hole mass and obtain

an estimate of the extent to which the BLR gas orbits are confined to a disk or the whole sphere.

Our method of analysis provides several advantages over previous methods. First, previous methods rely upon cross-correlation to obtain a mean radius for the BLR and a virial relation with unknown virial coefficient to obtain an estimate of the black hole mass. Our method estimates the black hole mass self-consistently, without the need for a virial coefficient. Second, work modeling reverberation mapping data has previously focused on modeling the velocity-resolved or unresolved transfer function. However the implications for the geometry and kinematics of the BLR are not clear for such analysis, as the transfer function is a function of the lag between the continuum and line emission. Instead of modeling the transfer function and then interpreting the transfer function in terms of a geometrical or dynamical model of the BLR, we focus on modeling the BLR directly. This allows us to extract more information and thus constrain the models more tightly. Finally, our fast method provides estimates of the uncertainty in the model parameter values and can be used with numerical algorithms such as Nested Sampling that allow for model selection. Our main results can be summarized as follows:

1. We create simulated datasets using the geometry model with known true parameter values and find that we can recover these values with uncertainties that depend upon the random uncertainty of the reverberation mapping data. We can recover the mean radius of the BLR to within ~ 0.1 dex and the mean width of the BLR to within ~ 0.2 dex for simulated data with an integrated line flux uncertainty of 1.5%. We can also place constraints on the inclination and illumination with un-

certainties of ~ 0.2 radians for simulated data with face-on and spherical geometry configurations and 1.5% integrated line flux uncertainty. Current integrated line flux uncertainties of about $\sim 5\%$ are on the edge of what would allow for successful recovery of more than just a mean radius for the BLR.

2. We create simulated datasets using the dynamical model that consist of timeseries of a broad line profile and we compare them to mock spectra made using our model. Despite the larger number of free parameters in our dynamical model, we find that we can recover all the parameters physically possible because the line profile is a stronger constraint on the model than the integrated line flux. We can recover the black hole mass and the mean radius of the BLR to within ~ 0.05 dex, for simulated data with a line profile signal to noise ratio of ~ 4 per spectral pixel. We can also recover the mean width of the BLR to within ~ 0.1 dex and the inclination angle and illumination angle to within ~ 2 grid spacings over which the BLR density is defined.

The small random uncertainties obtained in our tests of the simple geometry and dynamical models are partly due to the inherent assumption that our simulated data is drawn directly from the set of possible model configurations. In order to simulate the expected systematic error in applying simple models to complicated real BLR systems, we have added substantial Gaussian noise to instances of the model in order to create our simulated datasets. The timeseries of line profiles, in the case of the dynamical model, is very constraining, and leads to the reduced random uncertainty in the mean radius and mean width of the BLR by a factor of two for the dynamical model, as compared to the

Table 2.1: Simulated geometry data true parameter values. Each simulated dataset consists of 60 line emission datapoints and the same 120 continuum emission datapoints, where the line emission timeseries start half-way through the continuum timeseries. The value of $\sigma_r = 1.5$ corresponds to $0.3\, r_{\rm mean} = 1.5$. *Line flux uncertainty of the simulated dataset.

Data	Model	Uncertainty*	r_o	σ_r	Inclination Angle	Illumination Angle
			[10^{14}m]	[10^{14}m]	[rad]	[rad]
1	Inclined Disk	1.5%	5	1.5	0.79	0.22
2	Inclined Disk	5%	5	1.5	0.79	0.22
3	Edge-On Disk	1.5%	5	1.5	$\pi/2$	0.22
4	Face-On Disk	1.5%	5	1.5	0.0	0.22
5	Shell	1.5%	5	1.5	–	$\pi/2$

geometry model. When applying the method to real data we expect larger uncertainties, owing to modelling errors. The uncertainties quoted here should therefore be considered as lower limits to the overall precision of the method for data of comparable quality. This emphasizes the importance of good quality data *and* increasingly more realistic models, for recovering detailed information about the BLR from reverberation mapping data.

While we have created and tested both simple geometry and dynamical models, our method is more general, allowing for use of any geometry or dynamical model that can be simply parameterized. We plan to expand our library of models to include inflowing or outflowing BLR gas, which may be needed to explain some of the line profile asymmetries of current reverberation mapping data.

Table 2.2: Simulated geometry data recovered parameter values. Results for 150,000 iterations using an MCMC algorithm. See Section 2.3 for a discussion of why average values for the angular parameters are not quoted for most simulated geometry data-sets.

Data	Model	r_o $[10^{14}\text{m}]$	σ_r $[10^{14}\text{m}]$	Inclination Angle [rad]	Illumination Angle [rad]
1	Inclined Disk	4.53 ± 0.47	2.93 ± 0.78	–	–
2	Inclined Disk	4.81 ± 1.10	2.24 ± 1.56	–	–
3	Edge-On Disk	4.76 ± 0.65	1.83 ± 0.60	–	–
4	Face-On Disk	4.93 ± 0.67	3.10 ± 1.31	0.23 ± 0.13	0.29 ± 0.10
5	Shell	4.48 ± 0.52	1.85 ± 0.45	–	1.22 ± 0.29

Table 2.3: Simulated dynamics data true parameter values. *Average signal to noise of the line flux profile. Each simulated dataset consists of 60 line emission profiles and the same 120 continuum emission datapoints, where the line emission timeseries start half-way through the continuum timeseries. The simulated line emission profiles are created by taking the true model and adding gaussian noise with a variance of $v = \alpha \times Flux + \beta$, where $\alpha = 0.00018$ and $\beta = 0.025$.

Data	Model	$\langle \text{S/N} \rangle^*$	M_{BH} $[10^7 M_\odot]$	Mean Radius $[10^{14}\text{m}]$	Mean Width $[10^{14}\text{m}]$	Inclination Angle [rad]	Illumination Angle [rad]	θ_o [rad]
1	Face-on Disk	4.6	1	1.132	4.484	0.1	$\pi/2$	0.3
2	Face-on Disk	4.4	1	1.195	4.022	0.1	0.3	$\pi/2$
3	Sphere	3.5	1	1.195	4.022	0.1	$\pi/2$	$\pi/2$

Table 2.4: Simulated dynamics data recovered parameter values. Results for 470×10^3 (data 1), 330×10^3 (data 2), and 110×10^3 (data 3) iterations using an MCMC algorithm. See Section 2.3 for a discussion of why average values for the angular parameters are not quoted for the illumination angle of data 1.

Data	Model	M_{BH} $[10^7 M_\odot]$	Mean Radius $[10^{14}\text{m}]$	Mean Width $[10^{14}\text{m}]$
1	Face-on Disk	0.95 ± 0.05	1.04 ± 0.04	4.27 ± 0.05
2	Face-on Disk	1.10 ± 0.13	1.12 ± 0.04	3.80 ± 0.03
3	Sphere	1.00 ± 0.04	1.21 ± 0.08	3.95 ± 0.04
Data	Model	Inclination Angle [rad]	Illumination Angle [rad]	θ_o [rad]
1	Face-on Disk	0.11 ± 0.07	–	0.31 ± 0.02
2	Face-on Disk	0.12 ± 0.06	0.31 ± 0.02	1.40 ± 0.13
3	Sphere	0.12 ± 0.07	1.46 ± 0.06	1.50 ± 0.05

Chapter 3

Modeling the broad line region II: Application to Mrk 50

This chapter was published as Pancoast, A. et al. (36 co-authors), "The Lick AGN Monitoring Project 2011: Dynamical Modeling of the Broad-line Region in Mrk 50", The Astrophysical Journal, 754, 49 (2012) and is included here with minor formatting adjustments.

Members of our team have developed a method for determining the geometry and dynamics of the BLR by directly modeling reverberation mapping data (Pancoast et al. 2011; Brewer et al. 2011a, hereafter P11 and B11 respectively), estimating the uncertainties in the framework of Bayesian statistics. Our modeling method constrains M_{BH} without requiring a normalization constant f. We also constrain the geometry of the BLR, its orientation with respect to the line of sight, and the possibility of net inflowing or outflowing gas in the BLR. We have previously demonstrated our method on LAMP 2008 data for Arp 151 and estimated M_{BH} with smaller uncertainties than traditional reverberation mapping analysis (B11).

What is now needed to make further progress is large samples of high quality velocity resolved reverberation mapping data. For this purpose we carried out an 11-week spectro-

scopic observing campaign at Lick Observatory, the Lick AGN Monitoring Project 2011. The project focused on nearby AGNs with bright Hβ lines, which are good candidates for dynamical modeling. Here we present the first results of dynamical modeling for the project, focusing on one of the most variable objects in the sample, Mrk 50. The average time lag and virial M_{BH} estimates from traditional reverberation mapping analysis are presented by Barth et al. (2011b). Here we present an alternative analysis based on our direct modeling technique. The Hβ and V-band continuum light curve data are briefly described in Section 2, the dynamical model for the BLR is described in Section 3, and our results and conclusions are given in Section 4.

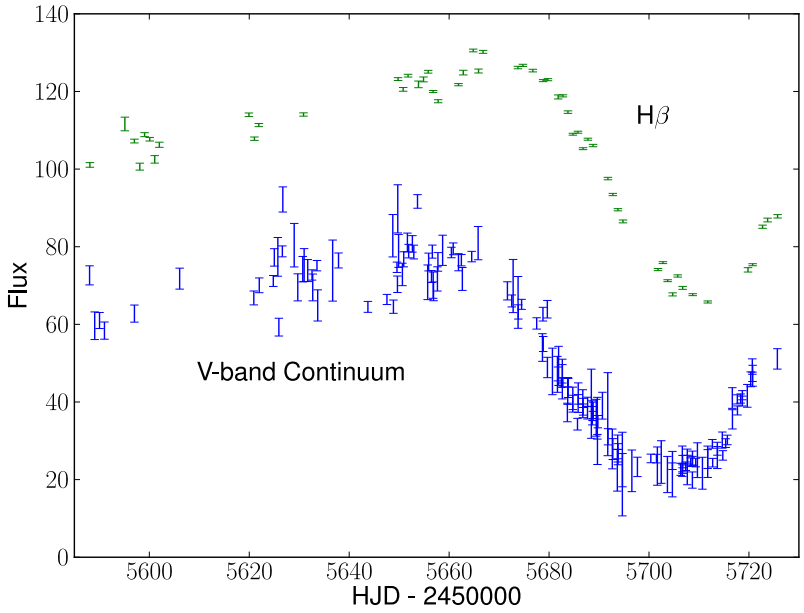

Figure 3.1: The integrated Hβ broad line and V-band continuum light curves. The Hβ light curve has flux units of $10^{-15}\,\mathrm{erg\,cm^{-2}\,s^{-1}}$. The V-band light curve is in arbitrary flux units.

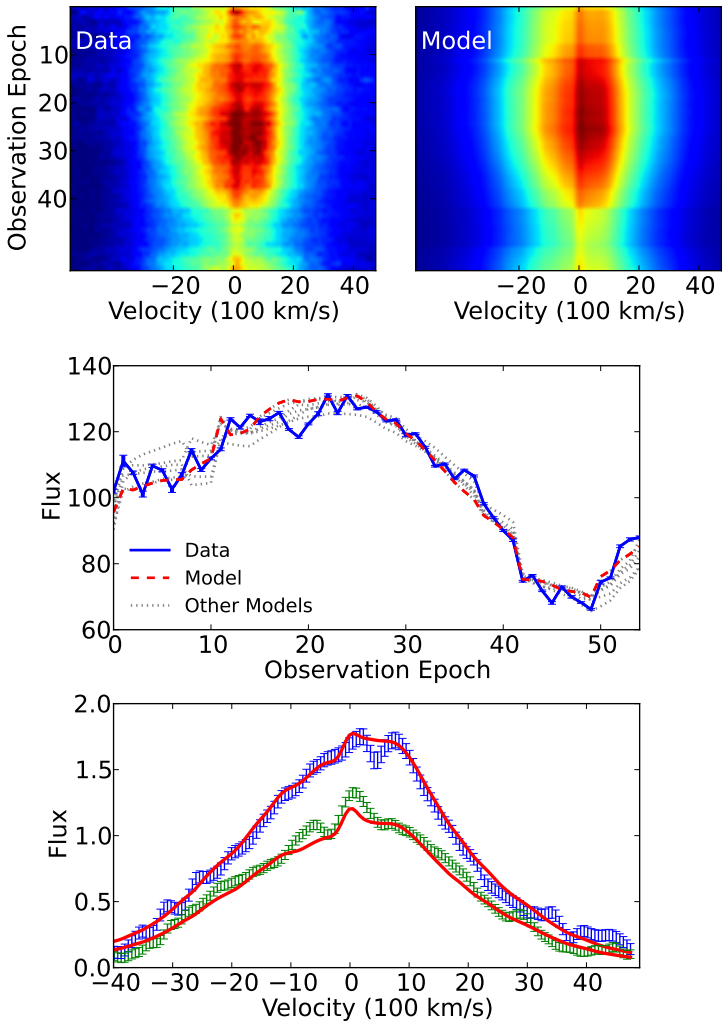

Figure 3.2: Top: Hβ spectra in velocity units for each epoch in the light curve for data, left panel, and model, right panel. Dark red corresponds to the highest levels of flux and dark blue corresponds to the lowest levels, where the same color scale is used for the data and model. Middle: integrated Hβ flux for each epoch in the light curve for the data, blue solid line with errorbars, and model, red dashed line. As an illustration of the range of solutions, we show light curves for five acceptable models as dotted gray lines. For the correct time separation between light curve epochs, see Figure 3.1. The model is able to reproduce the major features of the data. Bottom: two examples of Hβ spectra fit by the model, with data shown by blue and green errorbars and model fits shown by red lines.

3.1 Data

We observed Mrk 50 in Spring 2011. The data, shown in Figure 3.1 and the top left panel of Figure 3.2, include a light curve of V-band continuum flux and a time series of

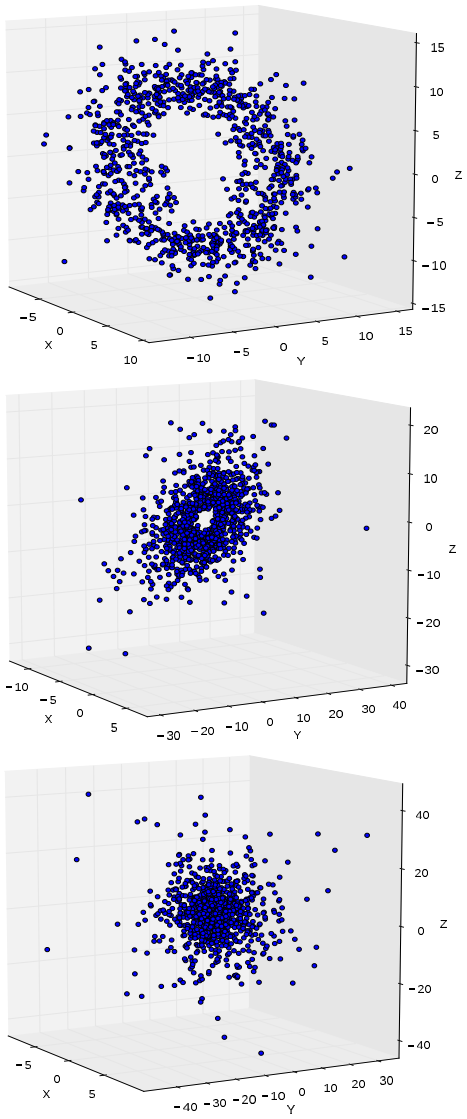

Figure 3.3: Geometry of the BLR for three models, with the x, y, and z axis scales in light days and the observer's line of sight along the x-axis. The top panel BLR distribution is a close to face-on torus of clouds, the middle BLR distribution is a close to face-on disk of clouds similar to the geometry inferred for Mrk 50, and the bottom BLR distribution is a dense sphere of clouds.

the broad Hβ line spectral profile. More observational details, as well as details about the measurement of V-band and Hβ light curves, are described by Barth et al. (2011b). We model all 156 epochs of the V-band light curve and 55 of the 59 epochs of the Hβ line profile, ignoring those epochs with low S/N or other problems. The median S/N for

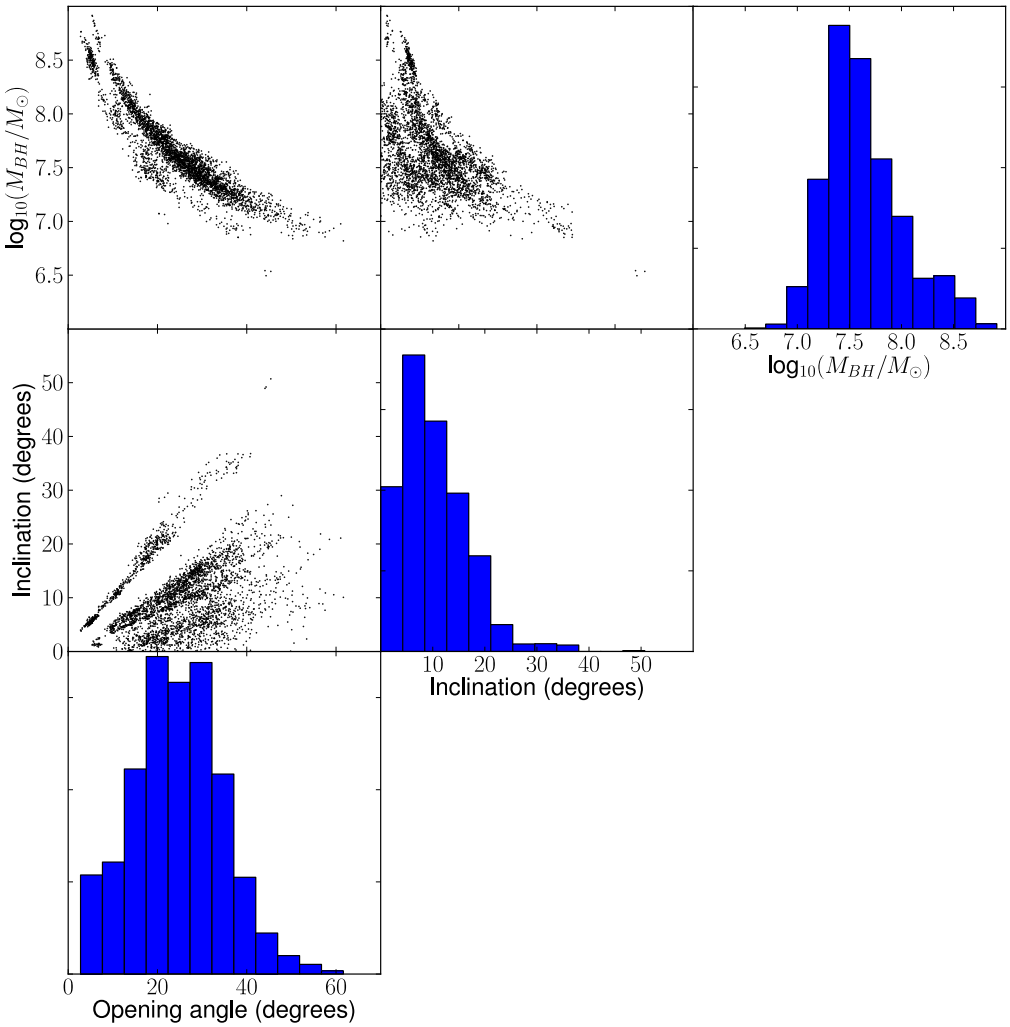

Figure 3.4: Inferred posterior PDFs for model parameters, including M_{BH}, inclination angle (0 degrees is face-on), and opening angle of the BLR disk. Joint posterior PDFs are also shown to illustrate the major degeneracies.

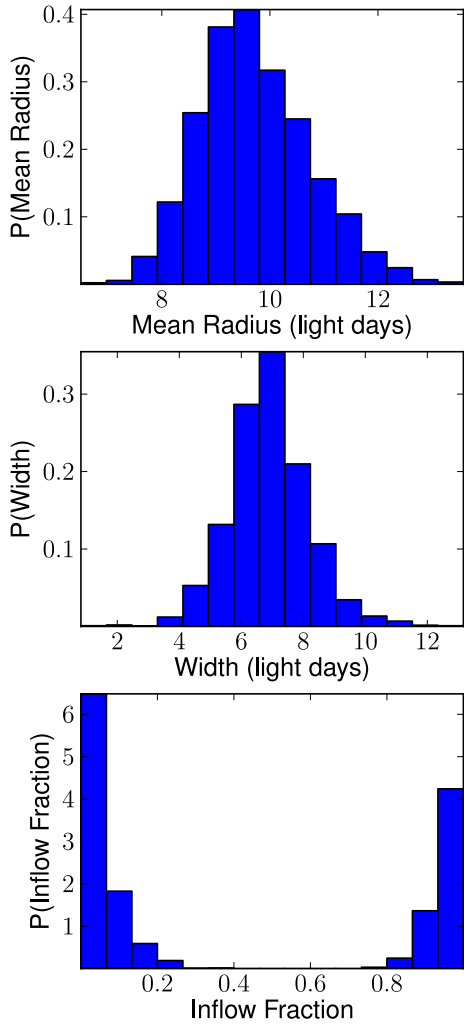

Figure 3.5: Inferred posterior PDFs for model parameters, including the mean radius of the BLR, radial width of the BLR, and the inflow fraction of BLR gas.

the Hβ line profile throughout the campaign is 75 per pixel.

AGN and stellar continuum lines can significantly alter the measured broad line widths in AGNs, affecting single epoch M_{BH} estimates (Denney et al. 2009; Park et al. 2012b). In order to reduce contamination from other lines when modeling the Hβ line profiles, the Mrk 50 spectra have been fit with AGN and stellar continuum components and the He II λ4686 line just blueward of Hβ, and then these components were subtracted

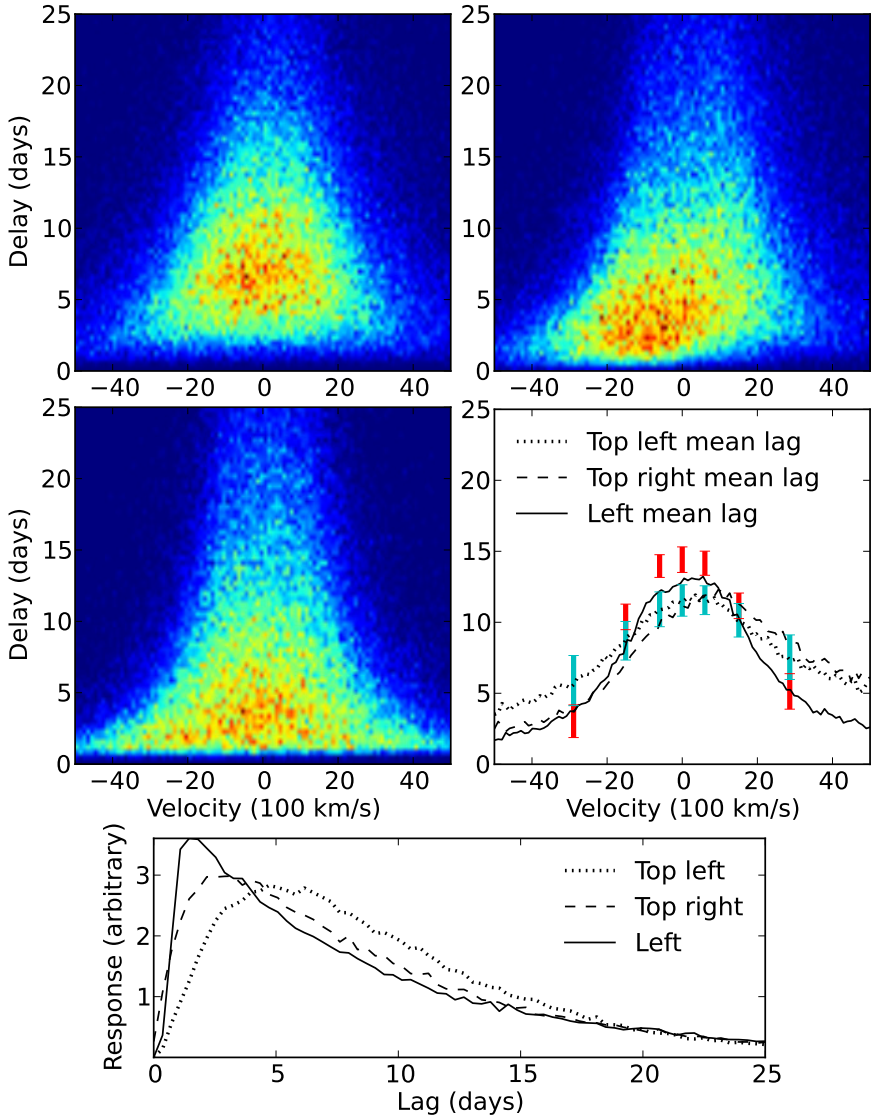

Figure 3.6: Examples of acceptable transfer functions for Mrk 50. The top two and middle left panels show examples of VRTFs drawn from the model parameter posterior PDFs, illustrating the range in inferred transfer function shape. In the color-code of the VRTFs, red corresponds to the highest levels of response and dark blue corresponds to the lowest levels. The middle right panel shows the mean lag for each of the VRTFs. The mean lag in seven velocity bins from Barth et al. (2011b) are shown by red errorbars, which were measured by cross-correlation analysis. We calculate the mean lag in the seven velocity bins of Barth et al. (2011b) for $\sim$ 200 VRTFs made using model parameters drawn randomly from their posterior PDFs, shown in light blue. The bottom panel shows the velocity-integrated transfer functions for the VRTFs shown in the first three panels.

to yield the "pure" Hβ profile (Barth et al. 2011b).

3.2 The dynamical model of the BLR

We now give a brief description of our method for directly modeling reverberation mapping data. The motivation for our approach is developed in P11 and further implementation details are described in B11. We model the BLR as a large number of point-like clouds, each with a given position and velocity. Several parameters describe the overall spatial distribution of the clouds and the prescription for assigning velocities to the clouds, given their positions. Our goal is to estimate these parameters.

The continuum emission from the central ionizing source is absorbed by these clouds and re-emitted as broad line emission, allowing us to predict the line flux and shape as a function of time, i.e. to produce mock data sets of the form shown in Figure 3.2.

The full set of model parameters includes the geometry and dynamics parameters for the BLR clouds corrected to the rest frame of Mrk 50, as well as a continuous version of the continuum light curve, since the continuum light curve must be evaluated at arbitrary times in order to compute mock data for comparison with the actual data. The observed continuum light curve is interpolated using Gaussian Processes to create a continuous light curve and to account for the uncertainty in the interpolation. Gaussian Processes have been found to be a good model for larger samples of AGN light curves (Kelly et al. 2009; Kozłowski et al. 2010; MacLeod et al. 2010; Zu et al. 2011, 2013).

The model for the BLR geometry is simple yet flexible, allowing for disk-like or spherical geometries with asymmetric illumination of the gas. Examples of possible BLR

geometries are shown in Figure 3.3. The model for the spatial distribution of the BLR gas is first generated from an axisymmetric 2-D configuration in the x-y plane, with a parameterized radial profile. The radius r of a cloud from the origin is generated as follows. First, a variable g is drawn from a Gamma distribution with shape parameter α and scale parameter 1:

$$g \sim \Gamma(\alpha, 1) \tag{3.1}$$

Then, the radius r of the cloud is computed by applying the following linear transformation to g:

$$r = F\mu + \frac{\mu(1-F)}{\alpha} g \tag{3.2}$$

The parameters $\{\mu, F, \alpha\}$ control the radial profile of the BLR. μ is the overall mean radius of the BLR (this can be verified by taking the expectation value of r in Equation 3.2). The parameter $F \in [0, 1]$ allows for the possible existence of a hard lower limit $F\mu$ on radius, because there may be some radius interior to which the BLR gas would all be ionized and thus unable to respond to changes in the continuum emission (Korista & Goad 2004). α controls the shape of the gamma distribution: a value of α close to 1 imposes an exponential distribution (allowing for disk or ball configurations) , whereas large values of α create a narrow normal distribution (allowing for shell or ring configurations). In the implementation, and in the description of the same model in B11, we parameterise the shape by $\beta = 1/\sqrt{\alpha}$ instead of α because β has a simple interpretation as the standard deviation of g in units of its mean. The radial width of the BLR can be defined as the standard deviation of r:

$$\sigma_r = \mu\beta(1-F). \tag{3.3}$$

In order to assign velocities to the BLR gas clouds, the model uses probabilistic perturbations about circular orbits. The solution for the radial velocity of a BLR cloud given its position r, energy E, and angular momentum L is:

$$v_r = \pm\sqrt{2\left(E + \frac{GM_{\rm BH}}{r}\right) - \frac{L^2}{r^2}}. \tag{3.4}$$

If we wished to impose circular orbits, the values for E and L would be fully determined by the radius r of the cloud:

$$E_{\rm circ} = -\frac{1}{2}\frac{GM_{\rm BH}}{r} \tag{3.5}$$

$$L_{\rm circ} = \pm r\sqrt{2\left(E + \frac{GM_{\rm BH}}{r}\right)}. \tag{3.6}$$

To obtain elliptical orbits, we generate values for E and L probabilistically, given r. The probability distributions for energy and angular momentum are parameterized by the parameter λ and are given by:

$$E = \left(\frac{1}{1+\exp(-\chi)}\right) E_{\rm circ} \tag{3.7}$$

$$p(L) \propto \exp\left(\frac{|L|}{\lambda}\right) \tag{3.8}$$

where $\chi \sim \mathcal{N}(0, \lambda^2)$ and $|L| < |L_{\rm circ}|$. For $\lambda \to 0$ we recover circular orbits and increasing λ creates more elliptical orbits. Since there are two solutions for the sign of v_r, the model also includes a parameter for the fraction of outflowing vs inflowing gas. The inflowing and outflowing gas is bound to the gravitational potential of the black hole, but an inequality in the fraction of inflowing and outflowing gas has the desired effect of modeling asymmetries in the Hβ spectral line profile as observed in Arp 151 (B11) when an asymmetric illumination model is included.

Once a 2-D configuration of clouds in the x-y plane has been generated, and velocities have been assigned to the clouds, rotations are applied to "puff up" the 2-D configuration into a 3-D configuration. We first rotate the cloud positions about the y axis by a small random angle; the typical size of these angles determines the opening angle of the cloud distribution. The opening angle is defined as the angle above the midplane of the disk or sphere. We then rotate around the z axis by random angles to restore the axisymmetry of the model. Finally, we rotate again about the y axis, by the inclination angle (common to all of the clouds) to model the inclination of the system with respect to the line of sight. The inclination angle is defined so that zero degrees corresponds to a face-on configuration and 90 degrees corresponds to an edge-on configuration.

In order to produce asymmetric broad line profiles, we include a simple prescription for asymmetric illumination of the BLR clouds. We assign a weight w to each cloud, given by $w = 0.5 + \kappa \cos\phi$, where ϕ is the azimuthal position of the cloud in spherical polar coordinates. The parameter κ ranges from 0.5, corresponding to illuminating the near side of the BLR, to -0.5, corresponding to illuminating the far side of the BLR. Physically, the near side of the BLR could be preferentially illuminated if the far side of the BLR were obscured by gas, and the far side of the BLR could be preferentially illuminated if the BLR clouds only reradiate the continuum emission towards the central ionizing source due to self-shielding within the cloud. Inflowing gas with the near side of the BLR illuminated can, in principle, be distinguished from outflowing gas with the far side of the BLR illuminated by the VRTF, since the lags for these two cases are different.

In addition, we allow for a scaling factor to describe the percentage variability of the emission line compared to that of the continuum. While for Arp 151 the variability of

the continuum was approximately equal to that of the Hβ flux, in the case of Mrk 50 we find that the continuum variability is less than that of the line. This is consistent with the amplitude of variability of the ionizing continuum responsible for Hβ being larger than that of the V-band (Meusinger et al. 2011, and references therein).

Once the dynamical model has been defined, we are able to compute simulated data that are then blurred with a Gaussian kernel to model the instrumental resolution. The simulated data are then compared with the actual data. For the likelihood function, we use the standard Gaussian assumption:

$$P(\text{data}|\text{model}) \propto \exp\left[-\frac{1}{2}\chi^2(\text{model}, \text{data})\right] \tag{3.9}$$

With the likelihood function defined, the modeling problem is reduced to computing the inferences on all of the model parameters. The likelihood function, $P(\text{data}|\text{model})$, is combined with the prior distribution for the parameters using Bayes' Theorem:

$$P(\text{model}|\text{data}) \propto P(\text{model}) \times P(\text{data}|\text{model}). \tag{3.10}$$

The posterior probability distribution for the parameters is sampled using the Diffusive Nested Sampling algorithm (Brewer et al. 2011a). Nested Sampling algorithms initially sample the prior distribution, and subsequently create and sample more constrained distributions, climbing higher in likelihood. In the specific case of Diffusive Nested Sampling, uphill and downhill moves are allowed, allowing the exploring particles to return to the prior, take large steps, and then climb the likelihood function again. We assigned uniform priors to most parameters except for the mean radius and M_{BH}, which have log uniform priors to describe initial uncertainty about the order of magnitude of the parameter.

By computational necessity, our model is relatively simple. While it is still rather flexible and can reproduce the large scale features of the reverberation mapping data, it is unable to model every detail of the Hβ light curve. The large scale features of the variability in the Hβ light curve are well-modeled, for example, but the small epoch-to-epoch fluctuations in the light curve are not (see Figure 3.2). In addition, the errorbars reported on the data are very small, and our model is not able to fit the data set to within these small error bars (i.e. we cannot achieve reduced $\chi^2 \sim 1$). If we did not take this into account our uncertainties would be unrealistically small. This issue is a generic feature of the fitting of simply parameterized models to informative data sets, and will be discussed in depth in a forthcoming contribution (Brewer et al, in preparation). In order to account for this effect and to obtain realistic and conservative uncertainties, we explore the effect of inflating the errorbars on the spectrum data by a factor H, or equivalently, choosing to form the posterior distribution from different chunks of the Nested Sampling run (i.e. different ranges of allowed likelihood values). For each value of H tested, we inspect the posterior distribution over simulated data (top right panel in Figure 3.2) to ensure that the major features of the data are reproduced. We find that, as long as H is low enough that the models fit the major features in the data, the resulting posterior distributions on the parameters are insensitive to the exact choice of the value for H.

3.3 Results and conclusions

Our inferred geometry and dynamics parameters of the BLR in Mrk 50 are shown in Figures 3.4 and 3.5. The shape of the BLR gas radial profile is constrained to be closer

to exponential ($\alpha \lesssim 1$), with a mean radius of $\mu = 9.6^{+1.2}_{-0.9}$ light days and a width of $\sigma_r = 6.9^{+1.2}_{-1.1}$ light days (the uncertainties quoted are symmetric 68% confidence limits). Even though the mean radius is not simply c times the mean lag in the general asymmetric case, we expect our mean radius to roughly correspond to the lag measurements using cross-correlation analysis by Barth et al. (2011b), which are $\tau_{\rm peak} = 9.75^{+0.50}_{-1.00}$ and $\tau_{\rm cen} = 10.64^{+0.82}_{-0.93}$ light days. Our mean radius agrees more closely with $\tau_{\rm peak}$, although $\tau_{\rm cen}$ is more commonly used for black hole mass estimation. We infer the inner radius of the BLR distribution to be $F\mu = 2.0^{+1.3}_{-1.1}$ light days. The opening angle of the BLR disk, defined between 0-90 degrees, is 25 ± 10 degrees, closer to a thin disk than to a sphere. The inclination angle of the thick BLR disk with respect to the line of sight is constrained to be 9^{+7}_{-5} degrees, closer to face-on, consistent with the standard model of broad line AGNs (Antonucci 1993; Urry & Padovani 1995).

The dynamical modeling results constrain Mrk 50 to have 39% probability of net inflowing gas and 61% probability of net outflowing gas, with equal amounts of inflowing and outflowing gas ruled out (inflow fraction = 0.5), as shown in Figure 3.5. This result suggests only a slight preference for outflow while the need for either outflow or inflow is quite robust, suggesting that a more physical model for inflow and outflow is needed in order to distinguish between them for the case of Mrk 50. Equal amounts of inflowing and outflowing gas are ruled out because net inflowing or outflowing gas, along with the illumination model, creates the asymmetry in the Hβ line profile observed in the data.

In addition to constraining the geometry of the BLR, our dynamical model also places an independent estimate on $\rm M_{BH}$, inferred to be $\log_{10}(\rm M_{BH}/M_{\odot}) = 7.57^{+0.44}_{-0.27}$. Part of the uncertainty in this estimate comes from the range in possible $\rm M_{BH}$ values at nearly face-on

inclinations (close to zero degrees), as shown in Figure 3.4. Recent cross-correlation reverberation mapping results quote statistical uncertainties of the order of 0.15 dex (Bentz et al. 2009b; Denney et al. 2010; Barth et al. 2011a,b), but this neglects the uncertainty in the normalization factor, f, that is believed to have an object to object scatter of 0.44 dex (Woo et al. 2010; Greene et al. 2010a). Thus, our uncertainty in M_{BH} for Mrk 50 is smaller that achieved by traditional reverberation mapping estimates. Our independent measurement of M_{BH} can be used to estimate the appropriate value of f for Mrk 50 by comparing it to the virial estimate by Barth et al. (2011b), $M_{vir} = f\, v^2\, c\, \tau / G$, where τ and v are obtained from the cross-correlation of the continuum and broad line light curves and from the width of the broad line, respectively. We find $\log_{10} f = 0.78^{+0.44}_{-0.27}$, which agrees to within the errors with the commonly used mean values of $\log_{10} \langle f \rangle = 0.74^{+0.12}_{-0.17}$ from Onken et al. (2004), $\log_{10} \langle f \rangle = 0.72^{+0.09}_{-0.10}$ from Woo et al. (2010), and $\log_{10} \langle f \rangle = 0.45^{+0.09}_{-0.09}$ from Graham et al. (2011). We have used $\langle f \rangle$ to denote a normalization factor derived from large samples of reverberation mapped AGN M_{BH} estimates as distinct from the f value we measure individually for Mrk 50. A sample of 10 independent black hole mass and f measurements with comparable uncertainties to Mrk 50 and Arp 151 would allow us to calculate a mean f value to $\sim 0.3/\sqrt{10} \simeq 0.1$ dex uncertainty and to distinguish between these commonly used mean values.

An additional interesting feature of Figure 3.4 is the complex structure in the joint posterior distribution for the inclination angle and opening angle, a feature that was not seen in Arp 151. The joint posterior appears to have two distinct families of solutions, although one has almost four times as much weight as the other. In an attempt to understand the origin of this structure, we separated the posterior samples in the two

modes in order to test whether they are correlated with any other parameters (such as the inflow fraction), however we were unable to find any such correlations. Future improvements to the flexibility and realism of the model may enable us to rule out one of these modes, and hence constrain the parameters more tightly and further reduce the uncertainties.

While M_{BH} is well constrained, there are many ways to successfully model the large-scale structure of the reverberation mapping data. This is illustrated by the degeneracies in the posterior distributions plotted in Figure 3.4. The quality of the model fits to the data are illustrated in Figure 3.2, including six model integrated Hβ flux light curves, an example of a model dataset of spectra for each epoch in the light curve, and two data spectra with the model spectra overplotted. The smoothness of the models compared to the data is illustrated in the spectral datasets of the data and model shown in the top panels of Figure 3.2. The Mrk 50 Hβ spectral profile did not change in shape drastically over the course of the LAMP 2011 reverberation mapping campaign, and the model spectral profile is likewise very similar for all epochs. Even though the shape of the individual spectral profiles can be well-modeled, more sophisticated models will be required to match the detail of the small-scale variability of the integrated Hβ data light curve.

Note that the uncertainties quoted throughout this chapter are determined from a Monte Carlo method, and are therefore subject to error themselves. As we are interested in reducing the uncertainties on black hole mass estimates from reverberation mapping data, it is important to quantify the uncertainty on the uncertainty. To investigate this, we estimated the effective number of independent samples produced by our Diffusive

Nested Sampling runs, by counting the number of times the exploring particles returned to the prior (allowing large steps to be taken) before climbing the likelihood peak again. Our effective number of independent samples was found to be ~ 180. We then generated samples of size 180 from our full posterior sample, and determined the scatter in the resulting $\log_{10}(M_{\rm BH})$ uncertainties to be 0.02. Thus, the uncertainty on the black hole mass for Mrk50 is $^{+0.44}_{-0.27} \pm 0.02$ dex.

Previous attempts to understand the geometry and dynamics of the BLR have focused on reconstructing the VRTF (Kollatschny & Bischoff 2002; Bentz et al. 2010b; Denney et al. 2010). In the interests of comparing future transfer function studies to our physically motivated model of the BLR, we show three inferred VRTFs for Mrk 50 in Figure 3.6. These three transfer functions were chosen out of the many inferred possible models for Mrk 50 to show some of the variety in allowed transfer function shapes. The top left VRTF has a fairly typical shape and level of asymmetry, while the top right VRTF is more asymmetric than average. One measurement of the VRTF asymmetry is to compare the integral of the mean lag per velocity bin on either side of line center, corresponding to the zero velocity point in the middle right panel of Figure 3.6. By this measurement of asymmetry, 43% of the possible models inferred for Mrk 50 have VRTFs that are less asymmetric than the top left VRTF, while only 8% of the possible models have VRTFs that are more asymmetric than the top right VRTF. The middle left transfer function illustrates the extent to which our inferred model for Mrk 50 can agree with the velocity-resolved cross-correlation measurements by Barth et al. (2011b), shown by red errorbars in the middle right panel of Figure 3.6. This VRTF has the smallest χ^2 distance from the cross-correlation measurements by Barth et al. (2011b) and models with this level

of agreement (or better) have a probability of $\sim 0.3\%$. The average shape of the VRTF is also shown in Figure 3.6, with the same velocity bins as used by Barth et al. (2011b) for their cross-correlation based measurement. This average VRTF is fairly symmetric, but the higher velocity bins have larger errorbars as a result of averaging over transfer functions that have asymmetries from either net inflowing or outflowing gas (see the dashed line in the middle right panel of Figure 3.6).

Note that the average VRTF we infer and the results obtained from cross-correlation measurements by Barth et al. (2011b) do not all agree to within the 1-σ error bars. In order to understand the differences between the time-lags as measured in our dynamical model and those measured through the cross-correlation procedure, we consider the ideal continuous noise-free case. In this case, the cross-correlation function (CCF) between the line and continuum light curves is the transfer function convolved with the autocorrelation function (ACF) of the continuum light curve, which is the CCF of the light curve with itself. While the ACF is symmetric, the transfer function may be asymmetric, as we find for Mrk 50, so the CCF may also be asymmetric. One measurement of the cross-correlation time-lag often used to measure black hole mass is the CCF-weighted mean lag, $\tau_{\rm cen}$, which is by definition affected by the asymmetry in the CCF. Therefore, in the case of asymmetric transfer functions, $\tau_{\rm cen}$ may not correspond to the mean lag of our dynamical model of the BLR. For the non-ideal case, a direct comparison between cross-correlation measurements and the results of our dynamical modeling approach is not straightforward, since the peak (or mean) of the CCF does not measure the true mean lag but only a noisy version of the convolution between the ACF and the transfer function.

We explored this issue by running the cross-correlation technique as implemented by Barth et al. (2011a) on light curves generated by models drawn from the posterior PDF for Mrk 50. For simplicity we considered noise-free light curves sampled in the same way as our data. We find that the peak and CCF-weighted mean ($\tau_{\rm peak}$ and $\tau_{\rm cen}$) of the CCF can be systematically off by $\sim 1-2$ light days with respect to the true mean lag of the model. The amount of the offset varies as a function of the actual shape of the transfer function as well as the details of the implementation of the cross-correlation algorithm. Thus, it is not surprising that we find systematic differences of this order between our estimates of the mean lag and $\tau_{\rm cen}$. Clarifying and quantifying systematically the relationship between these two approaches as a function of BLR structure and data quality is an important topic that goes beyond the scope of this chapter and is left for future work.

In conclusion, the analysis presented here provides new and unique insights into the geometry and kinematics of the BLR, and a $M_{\rm BH}$ estimate that is competitive with the most accurate methods. However, since our modeling uncertainties are greater than data uncertainties, more physical models that take into account the complex processes occurring in the BLR should allow for even better constraints. In the future, we plan to develop such models and apply them to large samples of reverberation mapping data.

Chapter 4

Modeling the broad line region III: Improved method and comparison with cross-correlation

This chapter was published as Pancoast, A.; Brewer, B. J.; Treu, T. "Modeling reverberation mapping data I: improved geometric and dynamical models and comparison with cross-correlation results", Monthly Notices of the Royal Astronomical Society, 445, 3055 (2014) and is included here with minor formatting adjustments.

In this chapter, we introduce an improved and expanded version of our simply parameterized phenomenological model of the BLR to be used with the direct modeling approach. We demonstrate the capabilities of this new model using simulated data and by placing constraints on the uncertainties in traditional cross-correlation function (CCF) analysis. In Chapter 5 of this series (Pancoast et al. 2014b), we apply the improved BLR model to five AGNs in the LAMP 2008 dataset. The additional model flexibility and increased algorithm efficiency of this new implementation are demonstrated by comparing the results for Arp 151 by Brewer et al. (2011a) to the new results described in Chapter 5; in the latter case the uncertainty in black hole mass is decreased by more than 0.1 dex and it is possible to differentiate between inflow and outflow kinematics.

We begin by presenting a detailed description of the improved BLR model in Sec-

tion 5.2. Tests to recover the model parameters using simulated data are presented in Section 4.2. Comparison of direct modeling results to CCF analysis and constraints on CCF lag uncertainties are given in Section 4.3. Finally, we give an overview of the main conclusions in Section 5.4. Throughout this chapter, all BLR model parameter values are given in the rest frame of the AGN.

4.1 The model

In this section we describe our model of the BLR and the numerical methods we use to explore its parameter space. Our model of the BLR can be applied to any broad emission line, although it has so far only been applied to the Hβ broad emission line in six AGNs (Brewer et al. 2011a; Pancoast et al. 2012, 2014b). The basic methodology of our model is also completely generalizable to any model in which the geometry and dynamics of the BLR gas can be computed quickly enough to enable a full exploration of the parameter space when comparing with the data.

4.1.1 Overview

Our goal is to reconstruct the physical structure of the BLR and to measure the mass of the central black hole from reverberation mapping measurements. To achieve this, we describe the possible structure of the BLR by a large number of parameters whose values we infer from the data.

In our model, the BLR is represented by a set of point particles whose positions represent the spatial distribution of broad line emission. If the BLR is really made up of

distinct clouds, then each particle could be associated with emission from a BLR cloud, however if the BLR is made up of a smoother distribution of gas, then the particles are just a Monte Carlo approximation of the density field of emission. Each particle in our model is also associated with a velocity that depends upon the mass of the black hole. Our model parameters for the BLR describe the spatial distribution of the particles as well as their individual positions. Additional parameters describe the rule by which velocities are assigned to the particles, as well as the individual velocities themselves. In the present implementation we ignore gravitational interactions or fluid viscosity between particles, and other non-gravitational forces like radiation pressure.

Given a distribution of particles with associated velocities, we can immediately calculate how the BLR would process an input continuum light curve, resulting in an emitted broad line spectrum (e.g. Hβ) that changes (in both total flux and shape) over time. Apart from the conversion from continuum to line flux, we assume that the particles act as mirrors, reflecting the continuum flux towards the observer, where the velocity of the particle determines how far the emission line flux is shifted in wavelength space away from the systematic emission line wavelength at rest with respect to the black hole.

There are three parts to our model of the BLR, which is formulated as an application of Bayesian inference as described in Section 4.1.2. The first part of the model is the AGN continuum light curve model described in Section 4.1.3. It is necessary to model the AGN continuum light curve because we need to be able to evaluate the continuum light curve at arbitrary times in order to calculate the broad line spectrum variations predicted by the model. The second part is the "geometry model" (spatial distribution) of the BLR described in Section 4.1.4, which describes the spatial distribution of the

particles that make up the BLR emission. The positions of the particles determine their time lags, which tells us how delayed features in the broad emission line light curve are compared to the continuum light curve. The third part is the "dynamical model" of the BLR described in Section 4.1.5. This describes the rule by which velocities are assigned to the particles, and allows for scenarios such as near-circular orbits, inflow, or outflow. The component of a particle's velocity along the line of sight determines which wavelength it affects in the model-predicted broad line spectrum. Once the three parts of our model of the BLR have been specified, we must explore the model parameter space in order to constrain the properties of the BLR given a specific reverberation mapping dataset, as described in Section 4.1.6. Finally, we enumerate the limitations of our current model of the BLR and future improvements in Section 4.1.7.

4.1.2 Bayesian inference framework

We use the formalism of Bayesian statistics to infer the values of our model parameters $\boldsymbol{\theta}$ given a reverberation mapping dataset $\mathbf{D}$. We begin by defining the prior probability distributions of the model parameters, $p(\boldsymbol{\theta}|I)$, which incorporate our initial assumptions about the range of allowed parameter values and depend upon any information I that we have about the problem before we begin. We then assign the probability distribution of the data given a specific set of parameter values $p(\mathbf{D}|\boldsymbol{\theta}, I)$ which tells us how the data and model parameters are related. This term is often called the "sampling distribution", or, once the data is known, the likelihood. Finally, we can combine the prior and likelihood using Bayes' theorem to obtain the posterior distribution of the model parameters given

the data:

$$p(\boldsymbol{\theta}|\mathbf{D}, I) \propto p(\boldsymbol{\theta}|I)\, p(\mathbf{D}|\boldsymbol{\theta}, I). \tag{4.1}$$

The normalization constant of the posterior in Equation 4.1, called the *evidence* or the *marginal likelihood*, is given by

$$p(\mathbf{D}|I) \;\; = \;\; \int p(\boldsymbol{\theta}|I)\, p(\mathbf{D}|\boldsymbol{\theta}, I)\, d^n\theta \tag{4.2}$$

and is useful for model comparison.

For models with many parameters and in which the posterior distribution is not of a known standard form, it is common to calculate properties of the posterior probability density function (PDF) by generating samples using an algorithm such as Markov Chain Monte Carlo (MCMC). As the number of parameters becomes large and the likelihood function potentially multimodal, however, it can be more efficient to use a more complex algorithm such as Diffusive Nested Sampling (DNS), as described in Section 4.1.6. DNS has the added benefit that it computes the marginal likelihood, allowing for model selection, unlike most standard MCMC algorithms that only generate posterior samples.

In our inference problem of modeling the BLR, the data consist of two time series. The first is the AGN continuum light curve $\{\mathcal{Y}_i\}$ and its corresponding timestamps and measurement error variances. The second time series is the spectrum of the broad line measured over time, which we will denote by $\{\mathcal{D}_{ij}\}$ (the index i represents the epoch and j the wavelength bin). The overall dataset that enters into Bayes' theorem is both of these:

$$\mathbf{D} = \{\{\mathcal{Y}_i\}, \{\mathcal{D}_{ij}\}\}. \tag{4.3}$$

We can split the likelihood function into two parts. The likelihood for the continuum

data $\{\mathcal{Y}_i\}$ will be discussed in Section 4.1.3. For the broad line data, we use the model parameters $\boldsymbol{\theta}$ to construct a time series of mock broad emission line spectra $m_{ij}(\boldsymbol{\theta})$ to compare to the data using a Gaussian likelihood function:

$$p(\mathbf{D}|\boldsymbol{\theta}, I) = \prod_{i,j} \frac{1}{\sigma_{ij}\sqrt{2\pi}} \exp\left[-\frac{1}{2\sigma_{ij}^2}\left(\mathcal{D}_{ij} - m_{ij}(\boldsymbol{\theta})\right)^2\right] \tag{4.4}$$

4.1.3 Continuum light curve model

Ground-based reverberation mapping campaigns use optical AGN continuum light curves (e.g. in the V or B bands) to track the variability of photons leading to BLR emission, since the true ionizing photons are in the ultraviolet (UV). While it is expected that the UV photons are created in the accretion disk closer to the black hole than the optical photons, the time lag between variability features in the UV and optical is unresolved (Peterson et al. 1991; Korista et al. 1995) or on the order of a day (Collier et al. 1998). For this reason, we do not distinguish between a UV or optical light curve in our model of the BLR, assuming that either light curve is emitted from a point source at the position of the black hole. While the true UV and optical emitting regions in the accretion disk are certainly not point-like, their distance from the black hole is significantly smaller than that of the BLR compared to the uncertainties in the mean BLR radius (e.g. Morgan et al. 2010), suggesting that detailed modeling of the optical or UV emitting region would not be well-constrained by current reverberation mapping datasets. Since our model of the BLR is many particles each reflecting the continuum light curve to the observer with a time lag given by the particle's distance from the continuum point source, the continuum flux must be computed at arbitrary times within the light curve. Generally, reverberation

mapping AGN continuum light curves are too sparsely sampled to resolve intra-day variability using simple linear interpolation between data points. Linear interpolation also incorrectly assumes that there is no uncertainty associated with the interpolation process or the measurements. For these reasons, we model the AGN continuum light curve using a stochastic model of AGN variability, allowing us to evaluate the light curve at arbitrarily small timescales and also to include the continuum light curve model uncertainty into our inference on the properties of the BLR.

We model the continuous AGN continuum light curve $y(t)$ using Gaussian processes (GPs), which allow us to treat the interpolated and extrapolated light curve points as additional parameters in our model, constrained by the data $\mathbf{D}$. Most of the information about $y(t)$ is, as one would expect, provided by the continuum light curve data $\{\mathcal{Y}_i\}$.

With the GP assumption, the prior distribution for any finite set of interpolated flux values is a multivariate Gaussian:

$$p(\mathbf{y}|\mu_{\rm cont}, \mathbf{C}) \;=\; \frac{1}{\sqrt{(2\pi)^n \det \mathbf{C}}} \exp\left[-\frac{1}{2}(\mathbf{y}-\mu_{\rm cont})^T \mathbf{C}^{-1} (\mathbf{y}-\mu_{\rm cont})\right] \qquad (4.5)$$

where $\mathbf{y}$ are the interpolated continuum light curve points (i.e. evaluations of the function $y(t)$), $\mu_{\rm cont}$ is the long-term mean flux value of the light curve, and $\mathbf{C}$ is the covariance matrix. The covariance between any two points in the interpolated continuum light curve depends on the time difference between them, as given by:

$$C(t_1, t_2) = \sigma^2_{\rm cont} \exp\left[-\left(\frac{|t_2 - t_1|}{\tau_{\rm cont}}\right)^{\alpha_{\rm cont}}\right] \qquad (4.6)$$

where $\sigma_{\rm cont}$ is the long term standard deviation of the continuum light curve, $\tau_{\rm cont}$ is the typical timescale for variations, and $\alpha_{\rm cont}$ is a smoothness parameter between 1 and 2. Larger values of $\alpha_{\rm cont}$ lead to more covariance between points in the continuum light

curve, corresponding to less fluctuations on small timescales. Setting $\alpha_{\rm cont} = 1$ improves the speed with which the densely sampled continuum light curve can be calculated, as well as increasing the performance of the MCMC[1]. For these reasons, we generally set $\alpha_{\rm cont} = 1$, in which case our Gaussian process model is equivalent to a continuous time first-order autoregressive process (CAR(1)). The CAR(1) model has been found to be a good fit to AGN variability data on similar timescales to those probed by reverberation mapping campaigns (Kelly et al. 2009; Kozłowski et al. 2010; MacLeod et al. 2010; Zu et al. 2011, 2013), although a model that further reduces AGN variability on very short timescales provides a better fit to higher-cadence Kepler data (Mushotzky et al. 2011). We interpolate and extrapolate the AGN continuum light curve data using 1000 points, where the range of points starts before the continuum data (usually by 50% the continuum data range) and extends past the end of both the continuum and line data, whichever is later. Points extrapolated past the ends of the continuum data are only constrained by the general behavior of the interpolated points and thus have very high uncertainty.

4.1.4 Geometry model

Once we have a model for the continuum light curve we need a model for the spatial distribution of the particles, which we call the "geometry model". The geometry model has flexibility in the radial distribution of the particles as well as the angular distribution. In particular we include an opening angle parameter that describes whether the BLR is a disk or sphere and an inclination angle parameter that determines from what angle the observer sees any asymmetries of the BLR. Although this is a purely phenomenological

[1]Performance is also increased by parameterising in terms of $\sigma_{\rm cont}/\sqrt{\tau_{\rm cont}}$ rather than $\sigma_{\rm cont}$ itself.

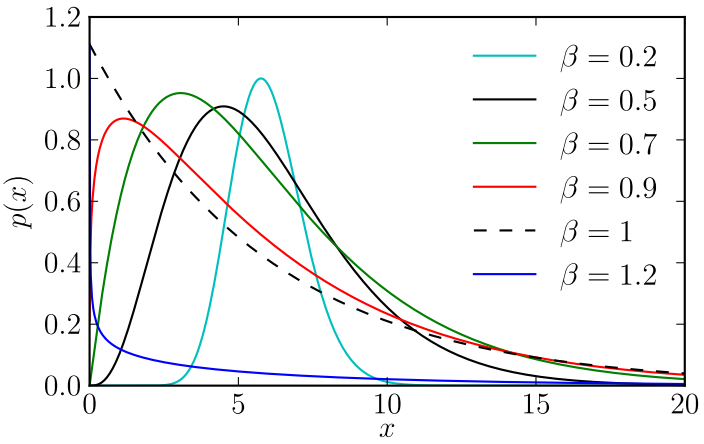

Figure 4.1: Examples of possible radial profiles for the BLR emission given by the Gamma distribution with $\mu = 6$, $F = 0$, and various values for β. The distributions range from a narrow Gaussian ($\beta < 1$) to an exponential profile ($\beta = 1$) or steeper ($\beta > 1$).

model, it is flexible enough that it should allow us to capture a wide variety of realistic geometries with a moderate number of parameters.

We define the geometry model in two stages. First we consider the radial distribution of the particles, and secondly we define the angular structure.

Radial BLR distribution

The radial distribution of BLR emission density is described by a shifted gamma distribution. The gamma distribution for a positive variable x is usually written

$$p(x|\alpha, \theta) \propto x^{\alpha-1} \exp\left(-\frac{x}{\theta}\right) \tag{4.7}$$

where α is the shape parameter and θ is a scale parameter. Our radial distribution is based on a shifted gamma distribution where the lower limit is r_0 instead of zero. Rather than parameterizing the distribution by (α, θ, r_0), whose interpretations are not straightforward (making priors difficult to assign), we use a different parameterisation in

terms of three parameters (μ, β, F), defined as follows.

$$\mu = r_0 + \alpha\theta \tag{4.8}$$

$$\beta = \frac{1}{\sqrt{\alpha}} \tag{4.9}$$

$$F = \frac{r_0}{r_0 + \alpha\theta}. \tag{4.10}$$

The parameter μ is the mean value of the shifted gamma distribution, β is the standard deviation of the gamma distribution in units of the mean μ when $r_0 = 0$, and F is the fraction of μ from the origin at which the gamma distribution begins (i.e. F is r_0 measured in units of μ). For arbitrary r_0, the standard deviation of the shifted gamma distribution is:

$$\sigma_r = \mu\beta(1 - F). \tag{4.11}$$

Finally, we also offset the radial distribution by the Schwarzschild radius, $R_s = 2GM/c^2$, to provide a hard limit to how close a point particle can be to the black hole. For a $10^7 M_\odot$ black hole, $R_s = 0.001$ light days, much smaller than the typical size of the BLR, which is on the order of light days.

The three parameters (μ, β, F) control the radial profile of the particles. To parameterise the actual distances of the particles from the black hole, instead of using the physical distance r, we use a variable g (one for each particle) with a Gamma$(\beta^{-2}, 1)$ prior. Then the actual distance r of the particle is computed by:

$$r = R_s + \mu F + \mu\beta^2(1 - F)g. \tag{4.12}$$

The reason for parameterizing in terms of g rather than F is that Metropolis proposals are simpler. For example, a Metropolis move that changes the parameters (μ, β, F) but

leaves g fixed will automatically move all of the particles appropriately.

Opening and inclination angles

The radial BLR distribution discussed in the previous section is spherically symmetric, however we can break spherical symmetry by introducing a disk opening angle of the BLR. The opening angle is defined as half the angular thickness of the BLR in the angular spherical polar coordinate perpendicular to the plane of the disk. If the BLR is a sphere then the opening angle is $\pi/2$, and if the BLR is a thin disk then the opening angle approaches zero. Once spherical symmetry has been broken, it is necessary to consider at what angle an observer will view the BLR. The inclination angle is defined as the angle between a face-on BLR geometry and the observer's line of sight, so an edge-on disk would have an inclination angle of $\pi/2$ while a face-on disk would have an inclination angle approaching zero.

To construct a specific BLR geometry, we begin by drawing the radial position for each particle in a flat disk in the x-y plane with the observer located at the positive end of the x-axis. In plane polar coordinates, the radial coordinates r of the point particles are calculated using Equation 4.12, and the angular coordinates are drawn from a uniform distribution between 0 and 2π. We then puff up this flat disk by the opening angle, first by rotating each particle around the y-axis by some angle between 0 and the opening angle and then by rotating the particle around the z-axis by some angle between 0 and 2π to restore axisymmetry. Next, we rotate all point particles around the y-axis by 90 degrees minus the inclination angle so that an inclination angle of zero corresponds to a face-on BLR geometry. All of the angles used in this process are extra model parameters.

Angular BLR distribution

We can further add asymmetry by controlling the strength of emission from a given particle using three separate effects:

1. The particles are assigned non-uniform weights, depending upon the angle between the observer's line of sight to the central source and a particle's line of sight to the central source. The strength of this effect is controlled by a parameter κ.

2. The parameter γ controls the extent to which the emission is concentrated near the outer edges of the BLR disk at the opening angle.

3. The parameter ξ determines the transparency of the plane of the BLR disk.

The first effect represents anisotropic emission from the point particles. We use first order spherical harmonics to define a weight, W, for each particle that ranges from 0 to 1 and determines what fraction of the continuum flux is reemitted as line flux in the direction of the observer:

$$W(\phi) = \frac{1}{2} + \kappa \cos \phi. \tag{4.13}$$

The one free parameter is κ, which ranges from -0.5 to 0.5. Negative values of κ correspond to preferential emission from the far side of the BLR from the observer and positive values correspond to preferential emission from the near side of the BLR. Preferential emission from the far side of the BLR could be physically caused by BLR gas only re-emitting continuum emission back towards the central source due to self-shielding, while preferential emission from the near side of the BLR could be physically caused by the closer BLR gas blocking gas farther away. The angle ϕ is defined to be the angle between

the observer's line of sight to the central source and the particle's line of sight to the central source. For $\kappa = -0.5$ and a model where the BLR is made up of spherical balls of gas, this model is equivalent to considering broad line emission from the area of the spheres illuminated by the central source as viewed by the observer, like lunar phases.

The second effect is parameterized by γ and controls the extent to which BLR emission is concentrated near the outer faces of a disk. This could arise for example if the parts of the BLR closer to the plane of the accretion disk are optically thick. The parameter γ controls preferential emission from the outer faces of the BLR disk by affecting how much the particle positions are moved from an initial flat disk to between zero and the opening angle of a thick disk. The angle for a particle's displacement from a flat to thick disk is given by:

$$\theta = \mathrm{acos}\left(\cos\theta_o + (1 - \cos\theta_o) \times U^\gamma\right) \tag{4.14}$$

where θ_o is the opening angle and U is a random number drawn uniformly between 0 and 1. Larger values of U lead to θ values closer to θ_o, so using U^γ with γ between 1 and 5 concentrates more particles close to the opening angle for $\gamma > 1$.

The third effect represents the possibility for an obscuring medium in the plane of the BLR to partly or completely obscure broad line emission from the back side of the BLR and is parameterized by ξ. Unlike the first effect that depends upon the inclination angle at which an observer views the BLR, ξ is roughly defined as the fraction of particles on the far side of the BLR midplane. In the limit of $\xi \to 0$, the entire back half of the BLR is obscured, and the BLR geometry could range from half a disk or sphere when $\gamma \sim 1$ to a single cone when $\gamma \sim 5$. In the limit of $\xi \to 1$, the back half of the BLR is not

obscured. Since it is computationally inefficient to throw out particles on the back side of the BLR, we actually just invert their position with respect to the plane of BLR when $\xi < 1$, making the true definition of ξ be the fraction of particles in the back side of the BLR that have *not* been moved to the front side.

4.1.5 Dynamics models

In order to make a model spectrum from our geometry of the BLR we must also assign velocities to the particles. We consider three different kinematic components, including bound elliptical orbits and a combination of both bound and unbound inflow or outflow.

Elliptical orbits

Consider a particle orbiting a point mass at a distance r with velocity $|v| = \sqrt{v_r^2 + v_\phi^2}$, where v_r is the radial velocity and v_ϕ is the tangential velocity in the plane of the orbit and perpendicular to v_r. The tangential velocity in terms of the angular momentum per unit mass of the particle L is given by $v_\phi = L/r$, and the radial velocity can be obtained by considering the energy per unit mass of the particle:

$$E = \frac{1}{2}\left(v_r^2 + \frac{L^2}{r^2}\right) - \frac{GM_{\rm BH}}{r}. \tag{4.15}$$

Solving for v_r we obtain:

$$v_r = \pm\sqrt{2\left(E + \frac{GM_{\rm BH}}{r}\right) - \frac{L^2}{r^2}}. \tag{4.16}$$

For circular orbits, we have the additional constraint that $v_r = 0$ so that the centripetal force of circular motion must equal the gravitational force, giving $v_\phi^2 = GM_{\rm BH}/r$ or

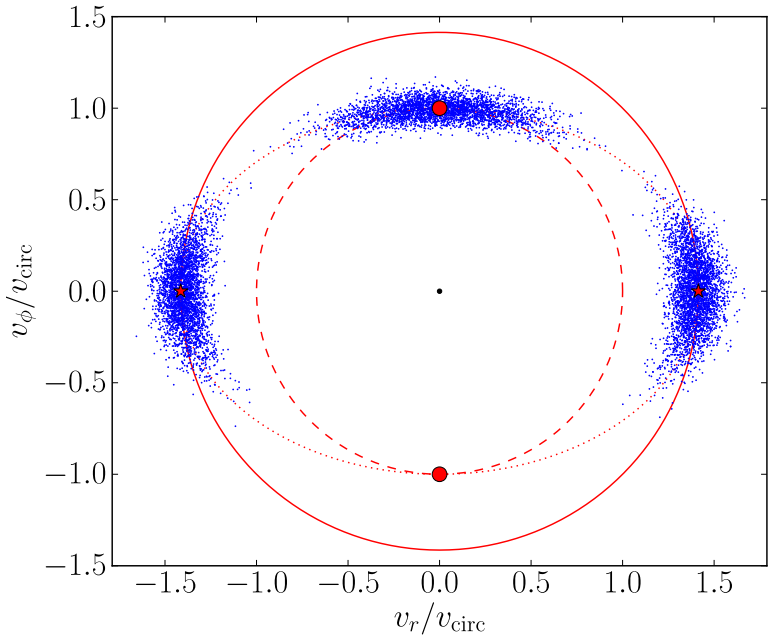

Figure 4.2: Distributions of radial and tangential velocities, v_r and v_ϕ for the dynamical model. Blue points are particle velocities drawn from Gaussian distributions centered around the point for circular orbits $(v_r, v_\phi) = (0, v_{\rm circ})$ shown as the upper filled red circle and centered around the points for outflowing and inflowing escape velocity $(v_r, v_\phi) = (\pm\sqrt{2}\, v_{\rm circ}, 0)$ shown as filled red stars. The red dotted line denotes the ellipse with semi-minor axis $(v_r, v_\phi) = (0,\, v_{\rm circ})$ and semi-major axis $(v_r, v_\phi) = (\sqrt{2}\, v_{\rm circ}, 0)$ along which the radial and tangential velocities are drawn. The outer solid red circle at a radius of $|v| = \sqrt{2GM_{\rm BH}/r}$ denotes the velocity beyond which orbits are unbound. The red dashed circle at a radius of $|v| = \sqrt{GM_{\rm BH}/r}$ denotes velocities with magnitude of the circular velocity.

$v_{\rm circ} = \sqrt{GM_{\rm BH}/r}$. Thus, the circular orbit solutions are two special points in the $v_r - v_\phi$ plane at $(v_r, v_\phi) = (0, \pm v_{\rm circ})$.

We consider generalizations of circular orbits to elliptical orbits by considering distributions in v_r and v_ϕ centered around the circular orbit solutions. Such a model allows us to recover circular orbits when the distributions are narrow, but also allows for highly elliptical orbits when the distributions are on the order of $v_{\rm circ}$. We draw the velocities of the particles from the ellipse in the v_r and v_ϕ plane that has semi-minor axis $v_{\rm circ}$ at $v_r = 0$ and semi-major axis equal to the escape velocity $\sqrt{2}v_{\rm circ}$ at $v_\phi = 0$, as shown in Figure 4.2. The reason for drawing velocities from around this ellipse instead of a circle with radius $v_{\rm circ}$ is that the parameter space naturally includes the points at $v_r = \pm\sqrt{2}v_{\rm circ}$ that correspond to the radial outflowing and inflowing escape velocities. We will discuss these inflowing and outflowing velocity solutions in more detail in Section 4.1.5. Since reverberation mapping measurements cannot distinguish between rotations of the BLR around the line of sight axis, it is only necessary to define the positive v_ϕ side of the $v_r - v_\phi$ plane. The radial and tangential velocities are thus drawn from Gaussian distributions centered at $(v_r, v_\phi) = (0, v_{\rm circ})$ with standard deviations given by $\sigma_{\rho,\,\rm circ}$ and $\sigma_{\Theta,\,\rm circ}$, where ρ is the radial coordinate in the $v_r - v_\phi$ plane and Θ is the angular coordinate. Circular orbits are recovered when $\sigma_{\rho,\,\rm circ} \to 0$ and $\sigma_{\Theta,\,\rm circ} \to 0$, whereas highly elliptical orbits approaching the escape velocity $|v| = \sqrt{2}v_{\rm circ}$ are obtained when $\sigma_{\rho,\,\rm circ} \to 0.1$ and $\sigma_{\Theta,\,\rm circ} \to 1.0$, the upper limits of their priors.

Inflow and outflow

In order to include the possibility of substantial unbound outflowing or inflowing gas in the BLR, we allow a variable fraction of the point particles to have elliptical, inflowing, and outflowing orbits. Since we do not expect to find both inflowing and outflowing gas in the BLR in the same spatial location, especially at the velocities assumed by our model, we only allow for inflowing or outflowing particles in addition to elliptical orbits for a specific instance of our model. The fraction of particles with elliptical orbits is given by $f_{\rm ellip}$, where $1 - f_{\rm ellip}$ is thus the fraction of particles in either inflowing or outflowing orbits. Whether the orbits are inflowing or outflowing is given by $f_{\rm flow}$, where values between 0 and 1 and less than 0.5 denote inflow and values greater than 0.5 denote outflow. Inflowing orbits are obtained around values of $(v_r, v_\phi) = (-\sqrt{2}\, v_{\rm circ}, 0)$ while outflowing orbits are obtained around values of $(v_r, v_\phi) = (\sqrt{2}\, v_{\rm circ}, 0)$.

As for elliptical orbits, we draw the radial and tangential velocities of inflowing or outflowing particles from Gaussian distributions for ρ and Θ, the radial and angular coordinates of the $v_r - v_\phi$ plane. The width of the Gaussian distributions is similarly given by $\sigma_{\rho,\,\rm radial}$ and $\sigma_{\Theta,\,\rm radial}$, where the widths are the same for both inflowing and outflowing orbits. Since the Gaussian distributions are centered on the points $v_r = \pm\sqrt{2}\, v_{\rm circ}$, about half of the inflowing and outflowing particles will actually have bound orbits. In order to allow for completely bound inflowing and outflowing trajectories, we also allow the distributions centered around $v_r = \pm\sqrt{2}\, v_{\rm circ}$ to be rotated by an angle θ_e along the ellipse connecting $v_r = \pm\sqrt{2}\, v_{\rm circ}$ to the circular orbit velocities $v_\phi = \pm v_{\rm circ}$. When $\theta_e = 0$, the inflowing or outflowing orbits are centered around the escape velocities at $v_r = \pm\sqrt{2}\, v_{\rm circ}$,

while $\theta_e \to \pi/2$ recovers bound elliptical orbits centered around circular orbits. When $\theta_e \sim \pi/4$, we obtain mostly bound inflowing or outflowing gas.

Macroturbulent velocities

We also consider macroturbulent velocities of the particles in addition to the velocities from elliptical, inflowing, or outflowing orbits. For each particle, we calculate the magnitude of the turbulent velocity along the observer's line of sight, given by:

$$v_{\rm turb} = \mathcal{N}(0, \sigma_{\rm turb})|v_{\rm circ}| \tag{4.17}$$

where $\mathcal{N}(0, \sigma_{\rm turb})$ is a normal distribution centered on zero and with standard deviation $\sigma_{\rm turb}$. The magnitude of the turbulent velocity is relative to the magnitude of the velocity of the particle's circular orbit described in Section 4.1.5, given by $v_{\rm circ}$. We can recover the case with no additional turbulent velocities when $\sigma_{\rm turb} \to 0$. We apply the additional macroturbulent velocity to a point particle first by calculating the elliptical, inflowing, or outflowing velocity and then adding $v_{\rm turb}$. This model for macroturbulent velocities is similar to the one presented by Goad et al. (2012) for the case of a disk with constant opening angle.

Relativistic effects

As highlighted in Goad et al. (2012), relativistic effects can have a strong influence on the shape of emission line profiles if the BLR gas is sufficiently close to the black hole. We include two simple relativistic effects in the calculation of particle velocities. The first effect is the full relativistic expression for the doppler shift of the broad emission

line due to the line of sight velocity of the emitting BLR gas. The second relativistic effect is that of gravitational redshift, which is caused by a photon being emitted from deeper in a gravitational potential well than the observer of the photon. The wavelength shift caused by gravitational redshift depends upon the ratio of the Schwarzschild radius, $R_s = 2GM/c^2$, to the radial distance of the emitting source. Together, the full relativistic expression for doppler shift and the expression for gravitational redshift act to shift the emitted wavelength $\lambda_{\rm emit}$ of line emission from a particle to the observed wavelength $\lambda_{\rm obs}$ given by:

$$\lambda_{\rm obs} = \lambda_{\rm emit} \frac{\sqrt{\frac{1+\frac{v}{c}}{1-\frac{v}{c}}}}{\sqrt{1-\frac{R_s}{r}}} \tag{4.18}$$

where the particle has velocity v and radial distance from the black hole r. Since we compare our model broad emission line spectra to the data in wavelength space, we can include the relativistic doppler shift and gravitational redshift in the simulated data by converting the simulated data from velocity to wavelength space using Equation 4.18.

Narrow line emission

In addition to a model of the broad emission line, we must also consider the superimposed narrow emission line from the narrow line region (NLR). Since the NLR is farther from the black hole, the narrow emission line is not expected to reverberate on timescales as short as those for the BLR (e.g. Peterson et al. 2013). We therefore assume that the narrow emission line flux is constant over the duration of a reverberation mapping dataset. We model the narrow emission line component using a Gaussian with line dispersion given by another more isolated narrow emission line profile. For example, to model the narrow component of the Hβ emission line we use the line dispersion of the nar-

row [O III]λ5007 emission line, just red-ward of Hβ. Since the width of [O III]λ5007 in a given reverberation mapping dataset is due to both intrinsic line width and instrumental resolution, we use measurements of the intrinsic line width to calculate the instrumental resolution, which is needed to smooth the model spectra. Differences in observing conditions can also change the instrumental resolution as a function of time, so we calculate the line dispersion of the narrow [O III]λ5007 line for each spectrum individually and include the measurements of the line dispersion as free parameters with Gaussian priors given by the line width measurement uncertainties. The intrinsic narrow line width of [O III]λ5007 is also treated as a free parameter with a Gaussian prior given by the line width measurement uncertainties. For objects where the NLR is not resolved and thus there is no intrinsic line width to the narrow line profile, the width of the narrow emission line directly gives a measurement of the instrumental resolution. Since subtracting narrow emission lines from broad emission lines can introduce significant uncertainty into the spectrum, we model spectra that have not had the narrow emission line subtracted and we include the total flux of the narrow line as an additional free parameter to be constrained by the data.

4.1.6 Exploring parameter space

Once our model of the BLR has been defined, we can explore this high-dimensional parameter space to constrain which parameter values best fit a specific reverberation mapping dataset by measuring the posterior PDFs and correlations between parameters. The full list of all parameters in our BLR model is given in Table 4.1 along with all of the

Table 4.1: BLR model parameters and their prior probability distributions. Equation numbers refer to the first equation in which the parameter is used and section numbers refer to those subsections where the parameter is defined. $\Delta t_{\rm data}$ is the time span between the first and last data point in the reverberation mapping dataset. The prior is designated by the scale in which a parameter is sampled uniformly and by the range (minimum value, maximum value). Uniform$(0, 1)$ denotes a uniform prior distribution between 0 and 1. LogUniform$(1, 100)$ denotes a uniform prior for the log of the parameter, or alternatively, a prior density $p(x) \propto 1/x$, between the parameter values 1 and 100. A log-uniform prior is used for positive parameters whose order of magnitude is unknown.

Parameter	Definition	Prior
μ	Mean radius of the BLR radial profile Eq. 5.3	LogUniform$(1.02 \times 10^{-3}$, $\Delta t_{\rm data}$ light days)
β	Unit standard deviation of BLR radial profile Eq. 5.4	Uniform$(0, 2)$
F	Beginning radius in units of μ of BLR radial profile Eq. 5.5	Uniform$(0, 1)$
θ_i	Inclination angle § 4.1.4	Uniform$(\cos\theta_i(0, \pi/2))$
θ_o	Opening angle § 4.1.4	Uniform$(0, \pi/2)$
κ	Cosine illumination function parameter Eq. 5.6	Uniform$(-0.5, 0.5)$
γ	Disk edge illumination parameter Eq. 5.7	Uniform$(1, 5)$
ξ	Plane transparency fraction § 4.1.4	Uniform$(0, 1)$
$M_{\rm BH}$	Black hole mass Eq. 4.15	LogUniform$(2.78 \times 10^4$, $1.67 \times 10^9 M_\odot)$
$f_{\rm ellip}$	Fraction of elliptical orbits § 4.1.5	Uniform$(0, 1)$
$f_{\rm flow}$	Flag determining inflowing or outflowing orbits § 4.1.5	Uniform$(0, 1)$
$\sigma_{\rho,\,\rm circ}$	Radial standard deviation around circular orbits § 4.1.5	LogUniform$(0.001, 0.1)$
$\sigma_{\Theta,\,\rm circ}$	Angular standard deviation around circular orbits § 4.1.5	LogUniform$(0.001, 1.0)$
$\sigma_{\rho,\,\rm radial}$	Radial standard deviation around radial orbits § 4.1.5	LogUniform$(0.001, 0.1)$
$\sigma_{\Theta,\,\rm radial}$	Angular standard deviation around radial orbits § 4.1.5	LogUniform$(0.001, 1.0)$
$\sigma_{\rm turb}$	Standard deviation of turbulent velocities § 4.1.5	LogUniform$(0.001, 0.1)$
θ_e	Angle in the $v_\phi - v_r$ plane § 4.1.5	Uniform$(0, \pi/2)$

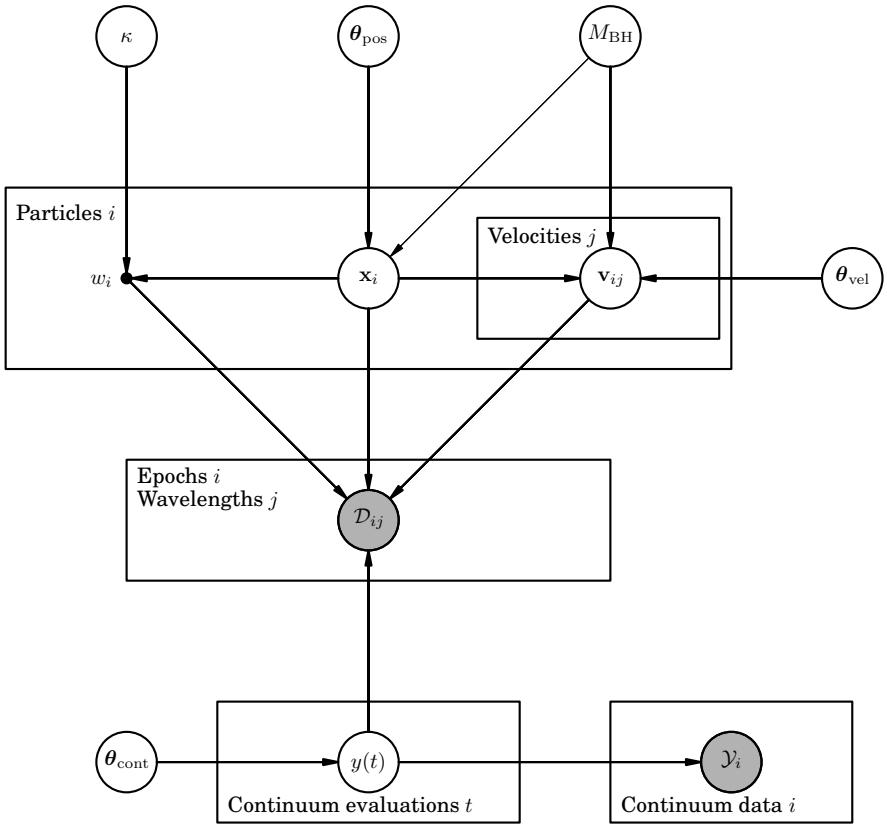

Figure 4.3: A probabilistic graphical model of the parameters and their influence on simulated reverberation data created by the BLR model. Each unshaded node represents a parameter (e.g. M_{BH}) or continuum hyperparameter (e.g. $\boldsymbol{\theta}_{\text{cont}}$) in the model and each shaded node represents a data value (e.g. $\mathcal{D}_{ij}$). Arrays of parameters are represented with a box, which can be thought of as a for loop. The arrows represent dependence between two nodes, where the arrow between M_{BH} and $\mathbf{x}_i$ corresponds to a weak dependency due to the minimum BLR radius being set by the Schwarzschild radius. The geometry model parameters, which determine the positions of the particles $\mathbf{x}_i$, include κ and $\boldsymbol{\theta}_{\text{pos}}$, a vector of the remaining geometry model parameters given in Table 4.1: μ, β, F, θ_i, θ_o, γ, and ξ. The dynamics model parameters, which determine the velocities of the particles $\mathbf{v}_{ij}$, include M_{BH} and $\boldsymbol{\theta}_{\text{vel}}$, a vector of the remaining dynamics model parameters given in Table 4.1: f_{ellip}, f_{flow}, $\sigma_{\rho,\,\text{circ}}$, $\sigma_{\Theta,\,\text{circ}}$, $\sigma_{\rho,\,\text{radial}}$, $\sigma_{\Theta,\,\text{radial}}$, σ_{turb}, and θ_e. The continuum hyperparameters in vector $\boldsymbol{\theta}_{\text{cont}}$ include μ_{cont}, σ_{cont}, τ_{cont}, and α_{cont}. This figure was made using daft-pgm.org.

random numbers used to assign the point particle positions and velocities in Section 5.2. A probalistic graphical model (PGM) of the interdependence of the parameters is shown in Figure 4.3. One way to interpret Figure 4.3 is as a recipe for making simulated reverberation mapping data:

1. Generate a model continuum light curve using Gaussian processes and then
2. sample it to create a realistic continuum light curve.
3. Use BLR geometry and dynamics parameters to generate the positions and velocities of all the particles in the BLR.
4. Finally, use those positions and velocities along with the model continuum light curve to make a simulated time series of broad emission line spectra or integrated broad line fluxes.

As described in Section 4.1.2, we can explore high-dimensional parameter spaces using an MCMC algorithm. We use the diffusive nested sampling code DNest (Brewer et al. 2011b) due to its ability to explore correlations between parameters efficiently in high dimensional spaces, and because it calculates the Bayesian evidence and thus allows for model selection. DNest works by using multiple walkers to explore parameter space, starting from the prior and gradually adding hard likelihood constraints.

One of the inherent difficulties of fitting real data with a simplified model is that the model is unlikely to match the data perfectly, especially if the error bars on the data are very small. In practice, one often obtains unrealistically precise inferences of the model parameters because the model contains simplifications. However we still expect

the model to capture the main features of the structure of the BLR. We account for the systematic uncertainty from using a simple model by inflating the errorbars of the data until only the macroscopic fluctuations in the data are fit by the model. Since we use a Gaussian likelihood function, as discussed in Section 4.1.2, we can rephrase the inflation of errorbars as an increased weighting of the prior probability compared to the likelihood when calculating the posterior probability. The weighting term is called a "temperature" T, such that $\log(\text{posterior}) \propto \log(\text{prior}) + \log(\text{likelihood})/T$ and hence the inflated errorbars are $\sqrt{T}$ larger than the original errorbars for a Gaussian likelihood function. Generally higher quality datasets require larger values of T. Another advantage of using nested sampling for the computation is that we can vary the temperature and check the sensitivity of the results without having to repeat the MCMC run.

4.1.7 Limitations of the model and future improvements

Finally, we discuss some of the limitations of our model of the BLR and discuss improvements to be made in the future. One of the main limitations of our model is the simplified dynamics of the point particles. We ignore the effects of radiation pressure, a force that has a $1/r^2$ dependence like gravity, making it difficult to disentangle from the black hole mass. Unfortunately, this degeneracy of radiation pressure with black hole mass means that black hole masses could be significantly underestimated, and that the degeneracy can only be broken by including external information about the BLR gas density in the model (Marconi et al. 2008, 2009; Netzer 2009; Netzer & Marziani 2010). We also ignore the self-gravity and viscosity of the BLR gas and any interaction it has

with the gas in the accretion disk. Finally, we assume that the gas in elliptical orbits is the same gas that could be inflowing or outflowing, when in reality the BLR could have multiple components with different geometries and dynamics.

Another limitation to our model of the BLR is the simplified treatment of radiative transfer, both for the ionizing and broad line photons. We ignore any asymmetry of the ionizing photons except for an optional preference for photons away from the BLR midplane. We also ignore detailed radiative transfer of line photons within the BLR gas, both locally and globally. While we have included two additional obscuration effects in this new version of the BLR model, transparency of the disk midplane to line photons (ξ) and asymmetry of the ionizing photons away from the disk midplane (γ), these are simplifications of what is most likely an inherently complicated problem.

Some of these limitations can be at least partially solved in future models of the BLR. For example, CLOUDY models constrain the direction in which line photons are emitted from individual clouds of BLR gas, as well as the emissivity and responsivity of line emission as a function of radius (e.g. Ferland et al. 1998, 2013). Using a table of pre-computed values from CLOUDY would not only provide a more physically-detailed local opacity to our model, but would also constrain the radial distribution of broad line emitting gas. By modeling the BLR using multiple broad emission lines simultaneously, we can also start to place constraints on the underlying distribution of gas density.

Recently Li et al. (2013) developed an independent code to model reverberation mapping data using a geometry model of the BLR based on the model of Pancoast et al. (2011). They include additional flexibility in their model by allowing for non-linear response of the broad emission lines to incident continuum radiation. While the average

emission line response of their sample is close to linear, they find that individual AGNs can have non-linear response, suggesting that this effect may be important to include in future implementations of our modeling code.

Another improvement that could be made to our model is better treatment of the dynamics. One option could be to include separate geometries for each dynamical component, for example a thin disk of gas in elliptical orbits with a cone of outflowing gas. We could also improve our treatment of outflows to include the detailed dynamics found in simulations of disk winds or complex models of outflows. For example, instead of assuming that outflowing gas has mainly radial trajectories at or near the escape velocity of its present position, we could consider the more complicated case where the gas is accelerated to velocities on the order of the escape velocity and where the escape velocity is defined at an initial wind launching radius instead of the current position of the gas (e.g. Castor et al. 1975; Proga 1999).

Finally, breathing of the BLR may play an important role in determining the response of emission line flux as a function of time (see Korista & Goad 2004, and references therein). Breathing of the BLR is where BLR emission comes from gas farther from or closer to the central engine based on increases or decreases in the ionizing luminosity, respectively. If the mean radius of the BLR changes substantially over the course of a reverberation mapping campaign, then this could have a noticeable effect on the measured time lag and the results from direct modeling analysis.

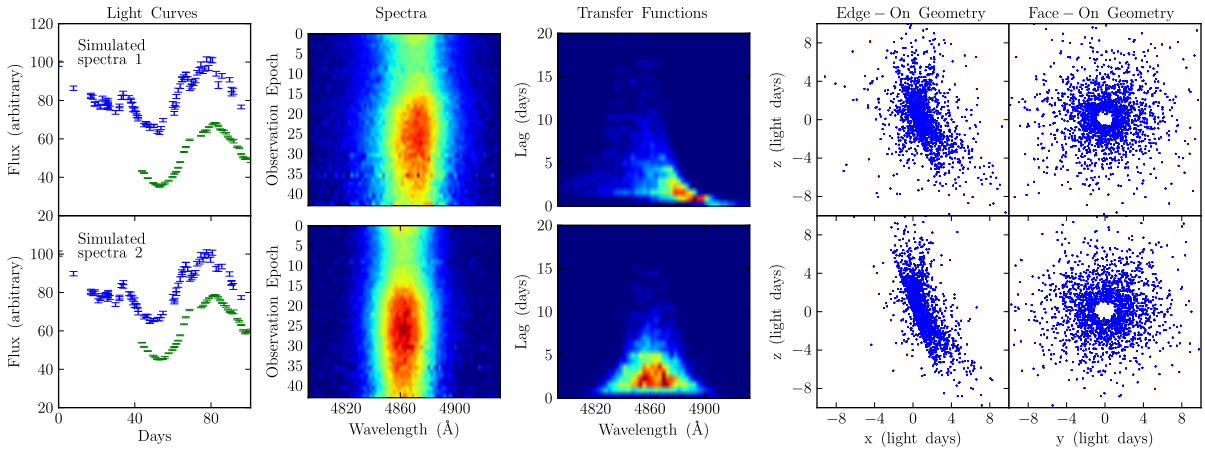

Figure 4.4: Simulated spectral time series 1 (top row) and 2 (bottom row). First (left-most) column shows the integrated line light curve in green and the continuum light curve in blue. Second column shows the spectral time series over the wavelength range of the emission line as a function of time series epoch. Third column shows the transfer function as a function of time lag and wavelength. Fourth and fifth columns show the edge-on and face-on views, respectively, of the BLR geometries for each simulated dataset (the observer views the origin from the positive x-axis).

4.2 Tests with simulated data and Arp 151

We demonstrate the capabilities of our improved model of the BLR and direct modeling code by recovering the model parameters for two simulated reverberation mapping datasets. By modeling the time series of emission line profiles using a geometry and dynamical model of the BLR as well as modeling the integrated emission line light curve using a geometry model of the BLR, we illustrate the benefits of a full spectroscopic dataset.

4.2.1 The simulated datasets

In order to generate realistic simulated reverberation mapping datasets, we use the LAMP 2008 dataset of Hβ emission for Arp 151 (Walsh et al. 2009; Bentz et al. 2009b) to

Table 4.2: Geometry and dynamics true parameter values of simulated spectral datasets and inferred geometry and dynamics posterior median parameter values and 68% confidence intervals. The columns with (True) give the true parameter values for the simulated datasets and the columns with (Inf) give the inferred parameter values and their uncertainties. True parameter values with – are unimportant for that specific simulated dataset.

Geometry Model Parameter	Simulated Data 1 (True)	Simulated Data 1 (Inf)	Simulated Data 2 (True)	Simulated Data 2 (Inf)
$r_{\rm mean}$ (light days)	4.0	$4.19^{+0.21}_{-0.21}$	4.0	$3.54^{+0.44}_{-0.35}$
$r_{\rm min}$ (light days)	1.0	$0.85^{+0.18}_{-0.26}$	1.0	$0.89^{+0.22}_{-0.19}$
σ_r (light days)	3.0	$3.23^{+0.30}_{-0.25}$	2.4	$2.39^{+0.40}_{-0.24}$
$\tau_{\rm mean}$ (days)	3.62	$3.59^{+0.15}_{-0.15}$	3.39	$3.30^{+0.18}_{-0.15}$
β	1.0	$0.97^{+0.09}_{-0.09}$	0.8	$0.92^{+0.09}_{-0.11}$
θ_o (degrees)	40	$49.0^{+8.4}_{-7.6}$	30	$27.3^{+11.0}_{-8.6}$
θ_i (degrees)	20	$20.2^{+2.7}_{-3.3}$	20	$22.8^{+10.0}_{-6.7}$
κ	-0.4	$-0.31^{+0.09}_{-0.09}$	-0.4	$-0.16^{+0.31}_{-0.24}$
γ	5.0	$2.73^{+1.29}_{-1.19}$	5.0	$3.50^{+1.02}_{-1.86}$
ξ	0.3	$0.31^{+0.10}_{-0.08}$	0.1	$0.53^{+0.37}_{-0.32}$
Dynamical Model Parameter	**Simulated Data 1 (True)**	**Simulated Data 1 (Inf)**	**Simulated Data 2 (True)**	**Simulated Data 2 (Inf)**
$\log_{10}(M_{\rm BH}/M_\odot)$	6.5	$6.42^{+0.06}_{-0.05}$	6.5	$6.48^{+0.08}_{-0.26}$
$f_{\rm ellip}$	0.0	$0.07^{+0.05}_{-0.04}$	1.0	$0.84^{+0.12}_{-0.50}$
$f_{\rm flow}$	0.0	$0.25^{+0.18}_{-0.17}$	–	$0.32^{+0.28}_{-0.22}$
θ_e (degrees)	0.0	$7.9^{+7.1}_{-5.0}$	–	$70.2^{+16.7}_{-38.6}$
$\sigma_{\rm turb}$	0.0	$0.024^{+0.055}_{-0.021}$	0.0	$0.009^{+0.026}_{-0.007}$

determine the sampling cadence, flux errors, instrumental smoothing, and approximate scale of the BLR. The Arp 151 dataset includes a *B*-band continuum light curve and a time series of Hβ emission line profiles, where the broad and narrow Hβ flux is isolated from the spectrum using spectral decomposition techniques as described by Park et al. (2012b). As described in Section 4.1.6, the simulated datasets are created by first generating a model of the Arp 151 continuum light curve using Gaussian processes and sampling that model continuum light curve with the same cadence as for Arp 151. We then add Gaussian noise to the continuum light curve using the error vector of the Arp 151 light curve. Next we set fixed the BLR geometry and dynamics model parameters to the values found in Table 4.2 and sample the Hβ emission line profile at the times given by the Arp 151 spectral dataset. Finally, we add Gaussian noise to the model spectra based on the spectral errors in the Arp 151 dataset. In order to account for the fact that real reverberation mapping datasets are likely more complicated than our model of the BLR assumes, we inflate the spectral errors and added Gaussian noise on the simulated dataset by a factor of three compared to the Arp 151 dataset, to obtain more realistic uncertainties on the inferred model parameters. To reduce numerical noise in the simulated spectra to less than the uncertainty in the spectral fluxes, we use 2000 particles and assign each one ten independent velocity values. The width of the narrow line component of Hβ is modeled using the line dispersion of the narrow [O III]λ5007 emission line from the Arp 151 dataset, calculated for each epoch of spectroscopy. The instrumental resolution is then measured by comparing the measured line dispersion for [O III]λ5007 with its intrinsic line width as calculated by Whittle (1992).

The simulated datasets are based on the geometry and dynamics inferred for the

LAMP 2008 dataset in Chapter 5 as shown in Table 4.2, with small mean radii for the BLR of 4 light days, close to exponential radial profiles with $\beta \sim 1$, substantial width to the BLR of $\sim 2-3$ light days, thick disks with opening angles of $30-40$ degrees, close to face-on inclination angles of 20 degrees, preferential emission from the far side of the BLR ($\kappa = -0.4$) and the edges of the disk ($\gamma = 5$), and mostly opaque mid-planes ($\xi = 0.1 - 0.3$). The black hole masses are also chosen to be similar to the LAMP 2008 sample with $M_{\rm BH} = 10^{6.5} M_{\odot}$ and each of the simulated datasets is dominated by either elliptical orbits or inflowing orbits. The differences between the simulated datasets can also be easily seen in Figure 4.4, which shows not only the continuum, line, and spectral timeseries, but also the transfer functions and geometries of the BLR. The simulated spectral datasets consist of the following:

1. A thick, wide disk with an exponential profile and dynamics dominated by inflowing orbits.

2. A thinner, narrower disk, with a radial profile between a Gaussian and exponential and dynamics dominated by elliptical orbits.

The continuum light curve interpolation using Gaussian processes is also held constant for all three simulated datasets, although the random noise added to each realistically sampled continuum light curve is different.

While not an issue for simulated emission line profiles, real reverberation mapping data must contend with ambiguity in multiple spectral components overlying the broad emission line profile. For example, with Hβ we not only have possible overlap of the red wing with the narrow [O III] emission lines and the blue wing with He II, but there may

also be substantial overlap with Fe II broad line emission. Blending between multiple broad components is especially important to disentangle because the different broad emission lines will be generated in BLR gas at different radii from the black hole and blending could confuse the dynamical modeling results. In order to isolate any single broad emission line profile, it is necessary to apply a method of spectral decomposition that will remove most of the ambiguity in overlapping spectral components.

4.2.2 Recovery of model parameters: spectral datasets

As a first test of our direct modeling code and BLR model, we attempt to recover the true parameter values of the two simulated spectral datasets described in Section 4.2.1. We assume the same instrumental resolutions as a function of time that are used to generate the simulated datasets and use 2000 particles and assign ten independent velocities to each one. Since we add Gaussian noise to the simulated datasets, we do not expect to recover every parameter of the BLR exactly. In addition, certain BLR geometries and dynamics make it difficult to constrain certain parameters. For example, when the majority of particles are in elliptical orbits, the fraction of particles in inflowing or outflowing orbits may not be well constrained. Or, a nearly face-on very thin disk will make it difficult to constrain the parameters κ, γ, and ξ since these parameters affect the relative line emission throughout the height of the very thin disk in this case.

The inferred posterior PDFs for the BLR geometry and dynamics model parameters are shown in Figures 4.5 and 4.6 for simulated datasets 1 and 2, respectively. The true parameter values for the simulated datasets are shown by vertical red dashed lines for

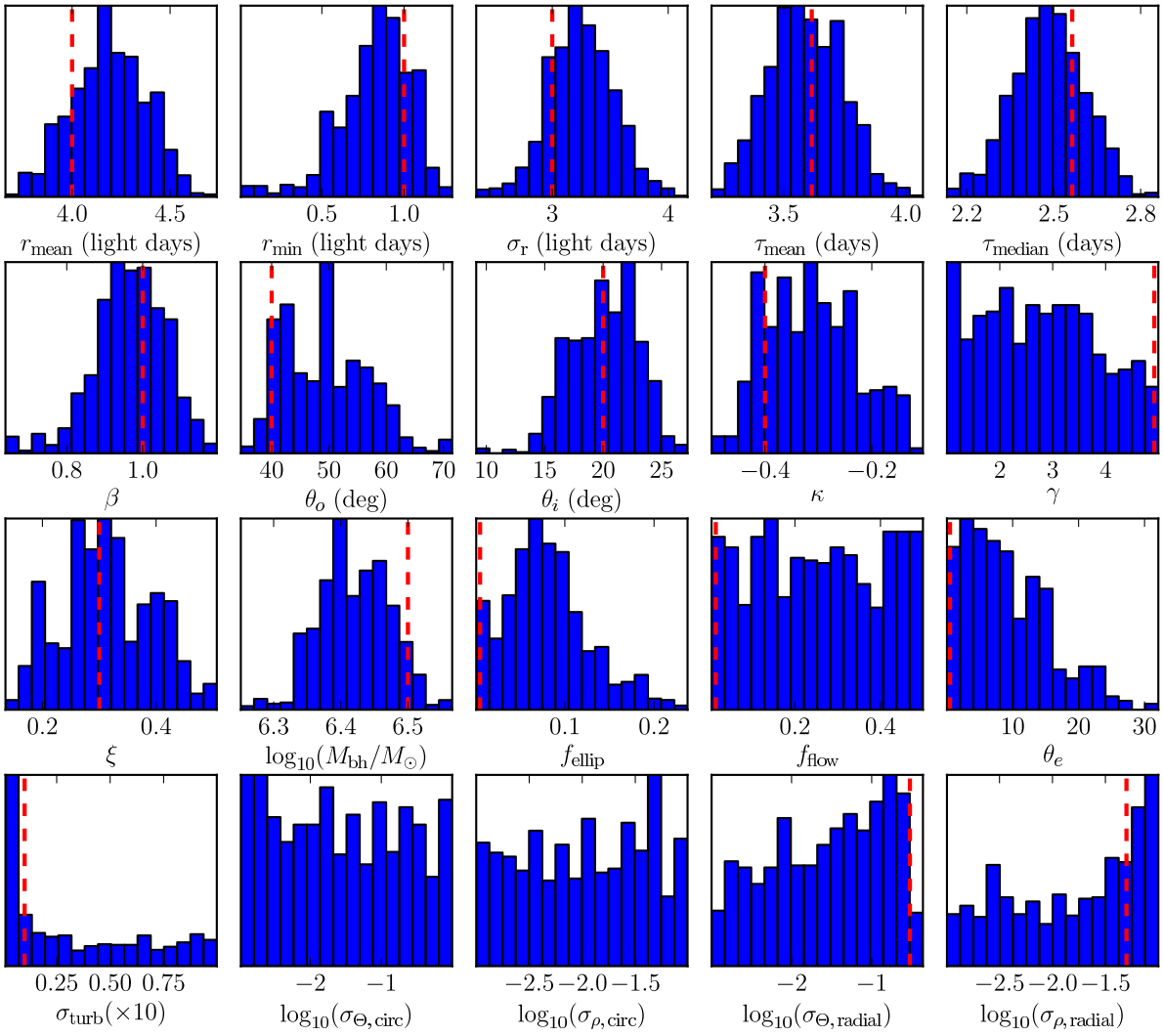

Figure 4.5: Inferred model parameters for simulated spectral dataset 1. The true parameter values are given by the vertical dashed red lines for those cases where the true value affects the shape of the simulated spectral dataset.

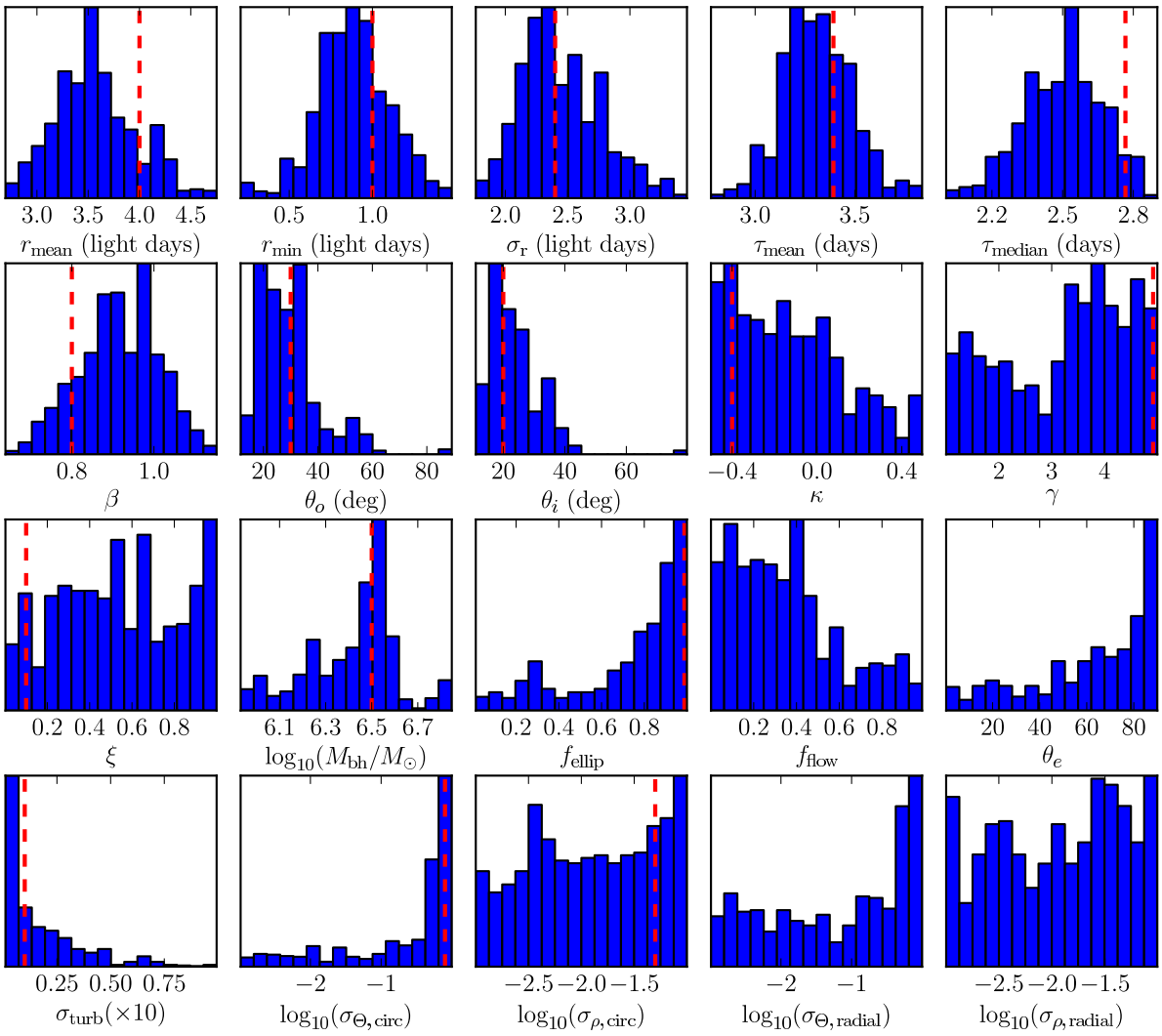

Figure 4.6: The same as Figure 4.5 for simulated spectral dataset 2.

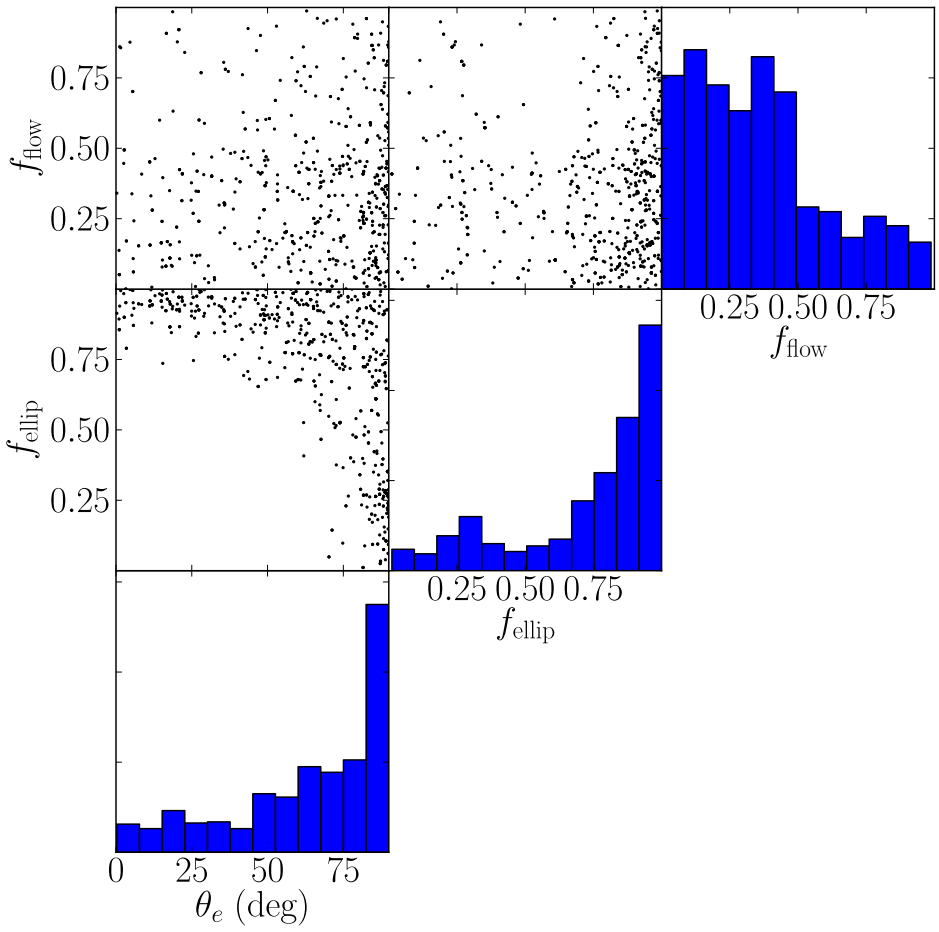

Figure 4.7: Marginal posterior PDFs and correlations between parameters for simulated dataset 2, including the fraction of elliptical orbits ($f_{\rm ellip}$), the flag determining inflowing or outflowing orbits ($f_{\rm flow}$), and the angle in the $v_\phi - v_r$ plane (θ_e).

comparison, and in the cases where the true parameter value does not matter (e.g. when the dynamics are entirely dominated by elliptical orbits so there is no true value of $f_{\rm flow}$) no red line is given. Overall, the modeling code is able to recover the true parameter values to within reasonable uncertainties, as listed in Table 4.2. Specifically, we constrain the mean radius of the BLR to within 0.5 light days uncertainty, the mean time lag to within 0.2 days uncertainty, and the inclination and opening angles to within $\sim$ 10 degrees. The geometry parameters that add asymmetry to the BLR are more difficult to constrain, with κ and ξ well constrained for simulated dataset 1 while neither κ, γ, nor ξ are well-determined for simulated dataset 2.

We also constrain $\log_{10}(M_{\rm BH}/M_{\odot})$ to $0.05 - 0.25$ dex uncertainty, where the variation comes mainly from larger correlated uncertainties with the inclination and opening angles for simulated dataset 2. The dynamics are also well-recovered for both simulated datasets, with a clear preference for inflow in simulated dataset 1 and for elliptical orbits centered around the circular orbit values in simulated dataset 2. A clearer picture of the preference for elliptical orbits for simulated dataset 2 can be seen in Figure 4.7, which shows the correlations between $f_{\rm ellip}$, $f_{\rm flow}$, and θ_e. Specifically, for values of θ_e approaching 90 degrees, the distribution of inflowing or outflowing orbits becomes identical to the distribution for elliptical orbits centered around the circular orbit value in the $v_\phi - v_r$ plane. This means that when $\theta_e \sim 90$ degrees, although $f_{\rm ellip}$ and $f_{\rm flow}$ are mostly unconstrained, the velocity distribution for the particles is very similar to that of $f_{\rm ellip} \sim 1$.

In general, these two simulated spectral datasets show that we can expect to obtain substantial constraints on the geometry and dynamics of the BLR for reverberation

mapping datasets similar in quality to LAMP 2008. The potential constraints on the black hole mass are also promising, although they depend upon the geometry of the BLR, specifically the precision with which we can measure the inclination and opening angles.

4.2.3 Recovery of model parameters: integrated line datasets

For those cases where a full spectroscopic reverberation mapping dataset is not available, we can apply a geometry-only model of the BLR and reproduce integrated emission line flux light curves. We test whether this approach provides constraints on the geometry of the BLR that are comparable to the full geometry plus dynamical modeling problem using the simulated datasets described in Section 4.2.1 and shown in the left panel of Figure 4.4.

We find that the mean time lag and mean radius are well constrained with geometry-only modeling. The mean and median time lag inferred for each simulated dataset are given in Table 4.3, along with the true mean and median lag values and the value measured by CCF analysis. The inferred mean time lag is not only accurate, but the inferred uncertainty in the mean time lag through geometry-only modeling of ~ 0.25 days is almost half as large as for the CCF time lag. This shows that geometry-only modeling is a promising tool for measuring time lags. The mean radius is inferred with slightly larger uncertainties to be $3.58^{+1.18}_{-0.97}$ light days for simulated dataset 1 and $2.90^{+0.97}_{-0.24}$ for simulated dataset 2, while the true mean radius is 4 light days.

Unfortunately the other geometry model parameters are not as well constrained. The

Table 4.3: Comparison of BLR geometry modeling, JAVELIN, and CCF lag measurements. $\tau_{\rm mean}$ and $\tau_{\rm median}$ are the mean and median time lags inferred from BLR geometry modeling, $\tau_{\rm JAVELIN}$ is the time lag measured by JAVELIN, and $\tau_{\rm cen}$ is the center-of-mass lag measured from the CCF.

Lag (days)	Sim Data 1	Sim Data 2
True mean lag	3.62	3.39
True median lag	2.56	2.77
$\tau_{\rm mean}$	$3.36^{+0.20}_{-0.15}$	$3.29^{+0.23}_{-0.17}$
$\tau_{\rm median}$	$2.61^{+0.25}_{-0.21}$	$3.10^{+0.17}_{-0.18}$
$\tau_{\rm JAVELIN}$	$2.94^{+0.13}_{-0.12}$	$3.21^{+0.13}_{-0.14}$
$\tau_{\rm cen}$	$3.70^{+0.50}_{-0.48}$	$3.62^{+0.56}_{-0.40}$

parameters γ and ξ are completely unconstrained for both of the simulated datasets, and θ_o, θ_i, β, F, and κ are mostly unconstrained. Generally there is a slight preference for a specific value of θ_o, θ_i, β, F, and κ, but none or almost none of the parameter space is ruled out. These results for geometry-only modeling suggest that a full spectroscopic reverberation mapping dataset is needed to constrain the geometry of the BLR, since otherwise there are too many degeneracies between model parameters to infer anything other than the mean time lag and mean radius consistently.

4.2.4 Comparison with JAVELIN

Recently another method has been developed for measuring the time lag in reverberation mapping data using integrated emission line light curves by Zu et al. (2011). This method has been implemented in an open-source code called JAVELIN written in Python.[2] JAVELIN works by using a top-hat transfer function with two parameters, a mean lag and a width of the top hat. The continuum light curve in JAVELN is interpolated using a CAR(1) model, which is equivalent to the continuum model implemented

[2]Download JAVELIN here: https://bitbucket.org/nye17/javelin

here. The parameter space of the continuum light curve and transfer function models is sampled using MCMC, providing posterior PDFs for the model parameter values.

We can compare recovery of the time lag using BLR geometry modeling of integrated emission line light curves to the results from JAVELIN. For simulated dataset 1, we measure a mean lag of $\tau_{\rm JAVELIN} = 2.94^{+0.13}_{-0.12}$ days and a mean width of the top-hat transfer function of $w = 7.33^{+0.26}_{-0.30}$ days using JAVELIN. This can be compared to the true mean lag of 3.62 days and the true median lag of 2.56 days for simulated dataset 1 to see that the mean lag measured by JAVELIN is between the true mean and median lags. For simulated dataset 2, we measure $\tau_{\rm JAVELIN} = 3.21^{+0.13}_{-0.14}$ days and $w = 5.26^{+0.82}_{-0.63}$ days. Again, the mean lag measured by JAVELIN is between the true mean lag of 3.39 days and the true median time lag of 2.77 days, although closer to the mean lag. The tendency for the time lag measured by JAVELIN to fall closer to the true mean or median lag is due to the shape of the transfer function; in very asymmetric transfer functions, the mean and median time lag are increasingly discrepant, with JAVELIN more sensitive to the true median time lag for very asymmetric transfer functions.

While the tendency of JAVELIN to measure a time lag ranging between the true mean and median time lags may appear to complicate its interpretation, an uncertainty of ~ 1 day from the difference between the true mean and median lags is comparable to the uncertainty introduced by additional assumptions, as discussed in Section 4.3, when using time lag measurements to estimate the mean radius of the BLR or to measure the black hole mass. These comparisons suggests that JAVELIN is a excellent resource for measuring the time lag even if the JAVELIN lag uncertainties do not reflect the uncertainty introduced by asymmetric transfer functions. However, to constrain more

than the time lag, more flexible modeling of the transfer function must be done.

In comparison, the CCF lag measurements for the two simulated datasets agree with the true mean lag values due to larger uncertainties. The CCF lag measurements do not agree more closely with the true median lag values than with the true mean lag values for more asymmetric transfer functions, as for JAVELIN lags. The quoted error bars on the CCF lag values, $\tau_{\rm cen}$, in Table 4.3 are calculated by drawing a random subset of the line and continuum light curves points, with the same number of random draws as the original light curves. For points in the light curves that are drawn N times, the flux error is reduced by $\sqrt{N}$. Finally, the randomly drawn light curve fluxes are modified by adding random Gaussian noise given by the flux errors. This is similar to the "flux randomization"/"random subset selection" (FR/RSS) approach described in Peterson et al. (1998) except the FR/RSS approach throws out any redundant points in the light curve instead of reducing the flux errors by $\sqrt{N}$, resulting in slightly larger uncertainties in the CCF lag. The CCF time lag is measured for 1000 iterations of this sequence and we quote the median and 68% confidence intervals of the CCF time lag distributions. For the two simulated datasets tested here with data quality comparable to the LAMP 2008 dataset for Arp 151 (Bentz et al. 2009b), the error bars are ~ 0.5 days, or $\sim 14\%$ the value of $\tau_{\rm cen}$. This comparison suggests that while CCF analysis may not give the most precise measurement of the mean or median time lag, the CCF lag uncertainties likely include much of the systematic uncertainties from an unknown transfer function.

Finally, we also consider the effects of detrending the light curves before calculating the CCF lag. Detrending can improve the shape of the CCF when there are strong long-term trends that can be removed by subtracting a linear fit to the light curves (Welsh

1999). Since our simulated data do not contain strong long-term trends, detrending the light curves should have minimal impact on the measured CCF lags. We confirm this by subtracting a linear fit to the simulated continuum light curves from both the continuum and line light curves. Due to the difference in length between the continuum and line light curves, fitting the continuum and line light curves with linear fits separately destroys the correlation between the light curves. When we use a linear fit to the continuum light curve to detrend both light curves we obtain CCF lag measurements for simulated dataset 1 of $\tau_{\rm cen} = 3.37^{+0.48}_{-0.37}$ days and for simulated dataset 2 of $\tau_{\rm cen} = 3.38^{+0.47}_{-0.37}$ days, which agree to within the uncertainties with the un-detrended CCF lag values.

4.2.5 Dynamical modeling without a full spectral dataset

As shown in Section 4.2.3, a spectroscopic dataset offers substantially more information about the BLR for direct modeling. Here we explore an intermediate case, where the available data consist of the usual continuum light curve, an integrated emission line light curve, and a mean spectrum. Since the mean spectrum contains some information about the kinematics of the BLR, we can model this dataset using the fully dynamical model of the BLR. However, with only the mean spectrum, this dataset cannot constrain the time lag as a function of velocity or wavelength, as possible for a full spectroscopic dataset.

In order to provide a test of this intermediate dataset case that is as realistic as possible, we use the LAMP 2008 dataset for Arp 151. A description of the dataset can be found in Chapter 5. In the analysis of this test, we focus on the differences in inferred

parameter values between this test and the full dynamical modeling results presented in Chapter 5. In general, the modeling results for the full spectroscopic dataset and for the intermediate dataset are fully consistent, but the uncertainty on the inferred model parameter values is much larger for the intermediate dataset. For example, the black hole mass is inferred to have a posterior PDF with a long tail at high masses, giving $\log_{10}(M_{\rm BH}/M_{\odot}) = 6.74^{+0.66}_{-0.13}$ compared to the value from Chapter 5 of $\log_{10}(M_{\rm BH}/M_{\odot}) = 6.62^{+0.10}_{-0.13}$. Similarly, the uncertainty in θ_i, θ_o, and κ is larger by at least a factor of 3, the uncertainty in ξ is larger by at least a factor of two, and γ is completely undetermined for the intermediate dataset. The two marginally consistent results are the mean radius and mean lag, which are both substantially larger for the intermediate dataset and have uncertainties at least 10 times larger than for the full spectroscopic dataset. This is due to a preference for $\beta \rightarrow 2$, corresponding to heavy-tailed radial distributions where the median radius and median lag are more consistent measurements of the characteristic size of the BLR. Overall, this test suggests that considerable information about the BLR can be inferred from the mean line profile, but the constraints on BLR geometry and dynamics parameters are significantly better when the full spectroscopic dataset is used. Finally, while this intermediate dataset allows for measurement of the black hole mass, it cannot be constrained to less than the ~ 0.4 dex scatter in the f factor due to a tail in the posterior PDF at high masses.

4.3 Comparison with cross-correlation analysis

We can compare the results of direct modeling to the standard reverberation mapping analysis of using the cross-correlation function (CCF) to measure time lags and the dispersion or FWHM of the broad emission line to measure a characteristic velocity of the BLR. In addition to providing a sanity check on our direct modeling results, such a comparison allows us to explore some of the uncertainties involved in standard reverberation mapping analysis. First, we consider the time lag traditionally measured using the CCF, how it compares to a measurement of the mean radius and how sampling of the line light curve and variability of the continuum light curve affect its measurement. Second, we consider the combination of the CCF lag with measurements of the emission line width to explore the uncertainty in black hole masses measured using the virial product.

4.3.1 Comparing the time lag and mean radius

One of the main assumptions in the traditional analysis is that the time lag measured from CCF analysis is related to some characteristic radius of the BLR. We explore the validity of this assumption by comparing the mean radius and the mean time lag in our geometry model of the BLR. We hold the mean radius fixed at $\mu = 4$ light days and allow the other geometry model parameter values to sample their priors as listed in Table 4.1, with the exception of the inclination angle, which we constrain to vary between zero (face-on) and 45 degrees. The results of this comparison are shown in Figure 4.8 for 200,000 samples. The difference between the mean radius, $r_{\rm mean}$, and the mean lag, τ, is

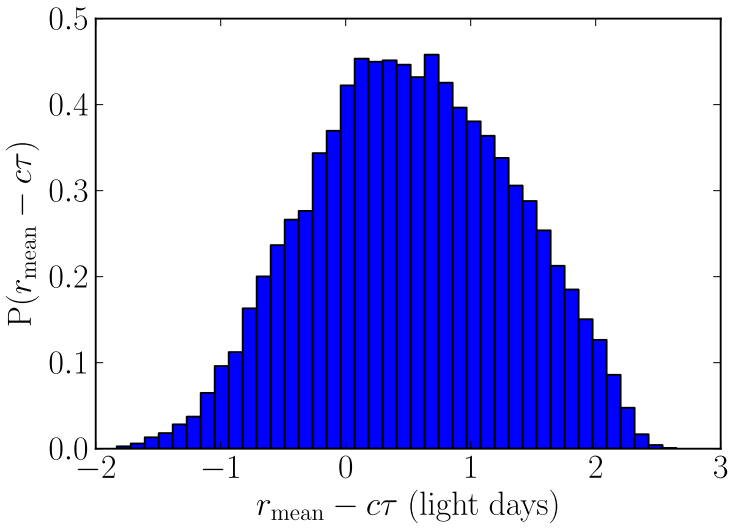

Figure 4.8: Difference between the mean radius and mean lag for BLR models drawn randomly from the prior with $\mu = 4$ light days. The distribution is asymmetric because the parameter ξ, the BLR plane transparency fraction, only shortens the mean lag compared to the mean radius, creating an excess of models where the mean radius is larger than the mean lag.

generally greater than one, meaning that the mean lag (in days) is usually shorter than the mean radius (in light days). This is due to the geometry parameter ξ that allows the midplane of the BLR to be transparent or opaque, since a BLR midplane that is not transparent will result in fewer particles with longer lags and hence a tendency for the mean lag to be smaller than the mean radius. The mean of $r_{\mathrm{mean}} - \tau$ is 0.53 light days and the standard deviation of the distribution is 0.80 light days. This suggests that the uncertainty in using the time lag as a measurement of the mean radius is relatively small, on the order of the CCF time lag uncertainty typically quoted for high-quality reverberation mapping data of ~ 1 day.

Table 4.4: Geometry model parameter values of simulated emission line light curves used in the comparison of direct modeling with the cross-correlation analysis approach. All simulated datasets were created with a mean radius, μ, of 4 light days and with $\gamma = 1$.

Mock Line	$\tau_{\rm mean}$ (days)	θ_i (deg)	θ_o (deg)	κ	β	F	ξ
1	3.69	10	25	-0.25	1.0	0.2	0.5
2	3.77	10	25	0.5	0.11	0.5	1
3	4.01	10	90	0.0	0.11	0.99	1
4	5.34	10	90	-0.5	0.11	0.99	1
5	4.00	0	0.5	0.0	0.11	0.99	1

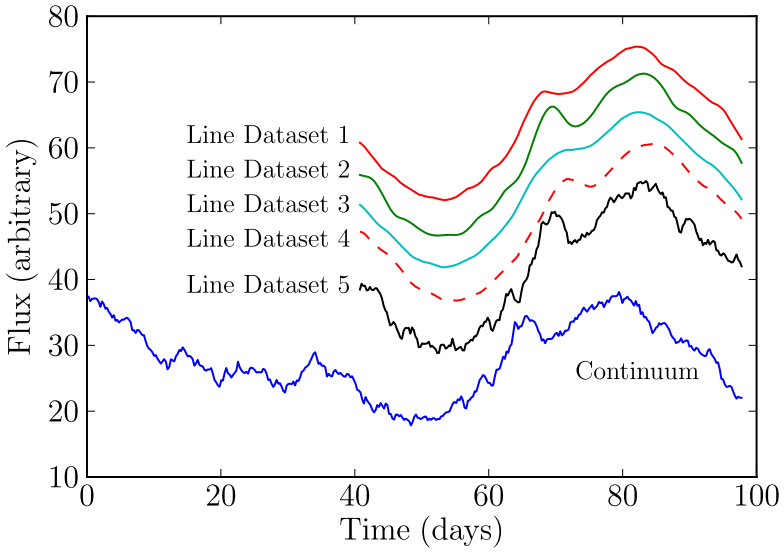

Figure 4.9: Simulated integrated emission line datasets including the AGN continuum light curve in solid blue and integrated Hβ line light curves in solid red, green, cyan, black, and dashed red. The continuum light curve is based on the LAMP 2008 light curve of Arp 151 (Walsh et al. 2009). The simulated Hβ line light curves correspond to five different BLR geometries, as shown in Figure 4.10.

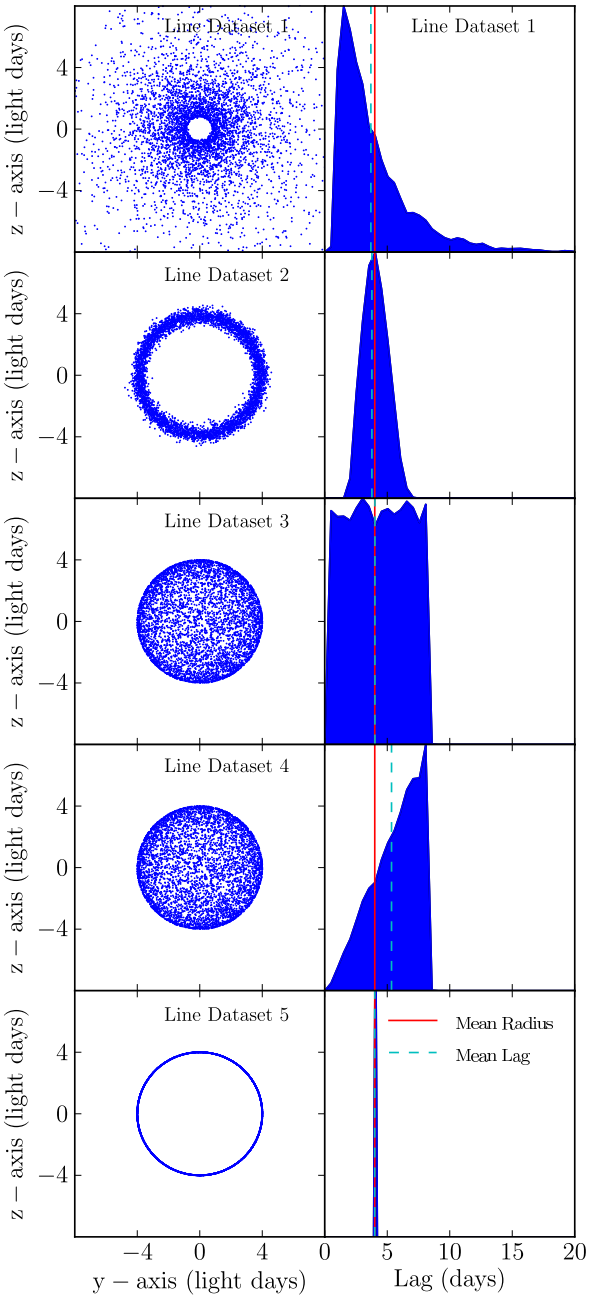

Figure 4.10: Geometries of the BLR (left panels) and corresponding transfer functions (right panels) of the simulated reverberation mapping datasets shown in Figure 4.9. Top to bottom BLR geometries: face-on wide disk, face-on donut, spherical shell, spherical shell with preferential emission from the back of the sphere, and a face-on thin ring.

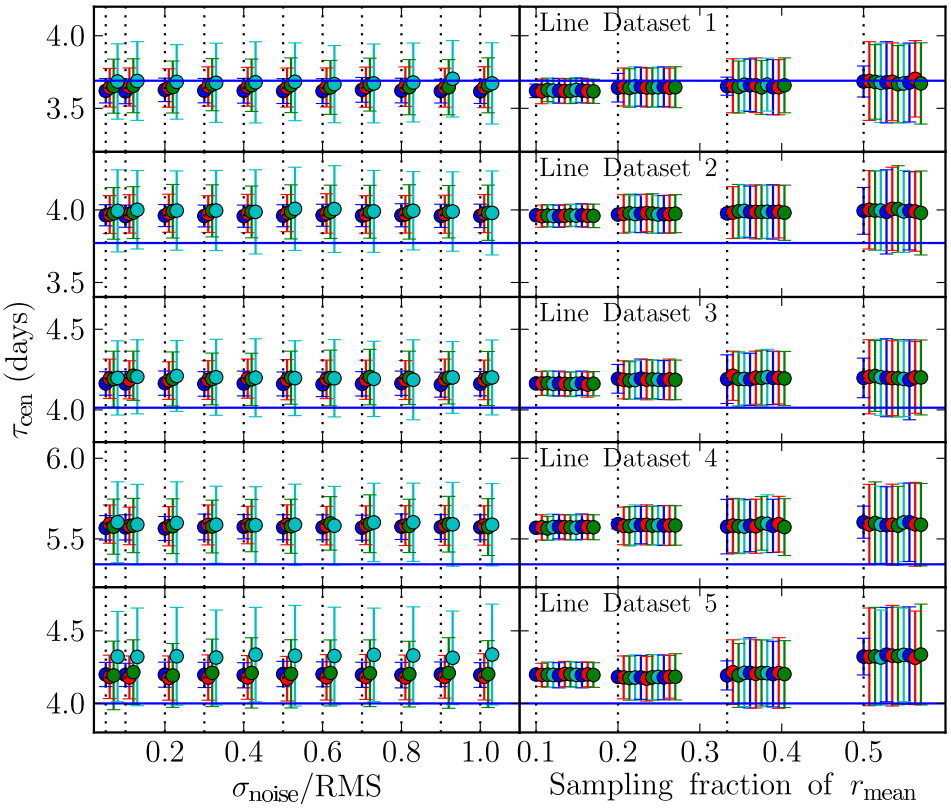

Figure 4.11: The CCF lag $\tau_{\rm cen}$ as a function of the ratio of $\sigma_{\rm noise}$ to the RMS variability of the line light curve and versus the cadence as given by the sampling fraction of the mean radius. Top to bottom: simulated line dataset 1, 2, 3, 4, and 5. The horizontal blue lines show the true mean time lags for each simulated line dataset. The vertical dotted lines show the values of the x-axis for which each cluster of points correspond, where the clusters of points are spread out along the x-axis to show their spread. These results are for the case where 3/4 of the epochs are not lost to weather.

4.3.2 The effects of line light curve sampling

Next we explore the dependence of the measured CCF lag on the geometry of the BLR and on the sampling characteristics of the emission line light curve. We focus on four very simple BLR geometries and one more realistic one, as shown in Figure 4.10, including

1. A nearly face-on wide disk with preferential emission from the far side and a disk midplane that is more than half opaque.

2. A nearly face-on ring with preferential emission from the near side.

3. A spherical shell (making a top-hat transfer function).

4. A spherical shell with preferential emission from the far side.

5. A perfectly face-on thin ring (making a δ-function transfer function).

We use these five geometries of the BLR to create simulated emission line light curves, as shown in Figure 4.9 using the same input continuum light curve and with very fine sampling of 0.1 days for both the line and continuum light curves. The geometry model parameter values are given in Table 4.4. In order to test how the quality of integrated emission line light curves affects measurement of the CCF lag, we degraded the quality of the simulated data by adding random Gaussian noise to the line light curve and by reducing the sampling cadence. For each simulated dataset degraded by adding $\sigma_{\rm noise}$ of random Gaussian noise, by sampling the line light curve at some fraction of the true mean radius of the BLR, and by losing a fraction of that sampled line light curve to weather, we computed the CCF lags $\tau_{\rm cen}$ and $\tau_{\rm peak}$ for 1000 realizations of assigning the

random noise and losing a fraction of the light curve to weather. The simulated line light curves were degraded by:

1. Reducing the sampling cadence to 1/10, 1/5, 1/3, or 1/2 of the true mean radius value of the geometry model of 4 light days. This means that the highest cadence is about half a day.

2. Adding random Gaussian noise, $\sigma_{\rm noise}$, at the level of 0.05, 0.1, 0.2, 0.3, 0.4, 0.5, 0.6, 0.7, 0.8, 0.9, or 1.0 times the RMS variability of the simulated line light curve.

3. Including only a fraction of the total number of line light curve data points randomly from the light curve to simulate observations lost to weather. The fractions are 1, 3/4, 2/3, and 1/2.

Some illustrative results of this comparison are shown in Figure 4.11, with the lefthand column showing the CCF lag $\tau_{\rm cen}$ versus the ratio of $\sigma_{\rm noise}$ over the RMS variability and with the righthand column showing the CCF lag $\tau_{\rm cen}$ versus the cadence as a sampling fraction of $r_{\rm mean}$. Figure 4.11 shows the results for when 3/4 of the line light curve is not lost to weather. The trend continues for larger fractions of the light curve lost to weather: the uncertainties on the measured CCF lag $\tau_{\rm cen}$ increase while the mean lag measurement stays the same. For the case where no observations are lost to weather, the error bars become comparable to the size of the points in Figure 4.11. Overall, these results suggest that for different geometries of the BLR $\tau_{\rm cen}$ can be offset from the true lag value by as much as a quarter of a light day (for a true mean lag of ~ 4 light days, see Table 4.4 for the exact values), which is well within typical uncertainties on CCF time lags quoted in the literature. For light curves with larger flux errors and lower cadence,

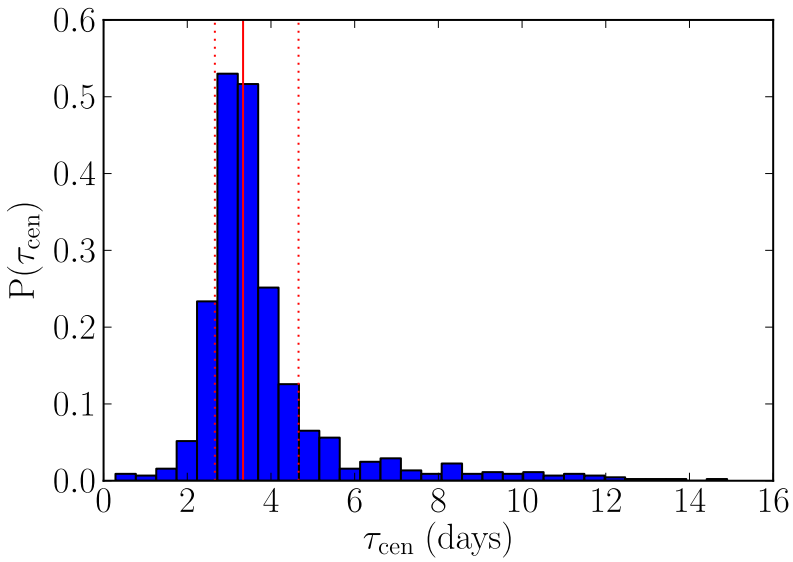

Figure 4.12: Histogram of the CCF center-of-mass time lag $\tau_{\rm cen}$ for 1000 random continuum light curve model realizations. The true mean lag is 3.74 days. The vertical solid red line denotes the median value of 3.33 days and the dotted vertical red lines give the 68% confidence interval around the median at 2.66 and 4.66 days.

this offset is easily within the error bars. In addition to a possible offset from the true lag values, these results show the importance of sampling the light curve at smaller fractions of the mean lag, even when the signal to noise quality of the light curve is high. As the fraction of the light curve lost to weather increases, this effect becomes more important. Detrending of the simulated light curves does not change these results.

4.3.3 The effects of continuum variability

In addition to light curve sampling effects, there is also the possibility that variability features in the AGN continuum light curve could affect measurement of CCF lags. We explore this source of uncertainty by generating 1000 random realizations of AGN continuum light curves, keeping the continuum hyper-parameters fixed to values similar to

those inferred for Arp 151 and the BLR geometry model fixed to the values for simulated integrated line dataset 1 given in Table 4.4. Given each realization of the AGN continuum light curve and the fixed BLR geometry model, we generate an integrated emission line light curve. We use the sampling cadence of the LAMP 2008 dataset for Arp 151, described in Section 4.2.1, for each realization of the continuum and line light curves. We then calculate the CCF center-of-mass lag $\tau_{\rm cen}$ for each of the 1000 realizations, obtaining successful CCF lag measurements for over 90% of the random continuum realizations.

The results are shown in Figure 4.12 as a histogram of $\tau_{\rm cen}$ values, where we have truncated the histogram to between zero and fifteen days for clarity. The median and 68% confidence interval for all measurements of $\tau_{\rm cen}$ is $3.33^{+1.33}_{-0.67}$ days, and considering only values of $\tau_{\rm cen}$ between zero and fifteen days reduces the uncertainties by less than 0.1 days. Detrending of the simulated light curves results in a similar median value for $\tau_{\rm cen}$ of $3.23^{+0.97}_{-0.61}$ days. These inferred median values for $\tau_{\rm cen}$ agree to within the uncertainties with each other and the true value of the mean lag of 3.74 days. This test demonstrates that the main consequence of continuum variability is to add additional scatter to measurements of $\tau_{\rm cen}$ on the order of $\sim$ 1 day, without shifting the median measurement of $\tau_{\rm cen}$ away from the true value.

4.3.4 Comparing the black hole mass and virial product

Other than the mean lag from CCF analysis, the black hole mass measured from the virial product is the key measurement of reverberation mapping studies. However the use of the virial product, $M_{\rm vir} = c\tau\Delta v^2/G$, to measure black hole mass involves making many

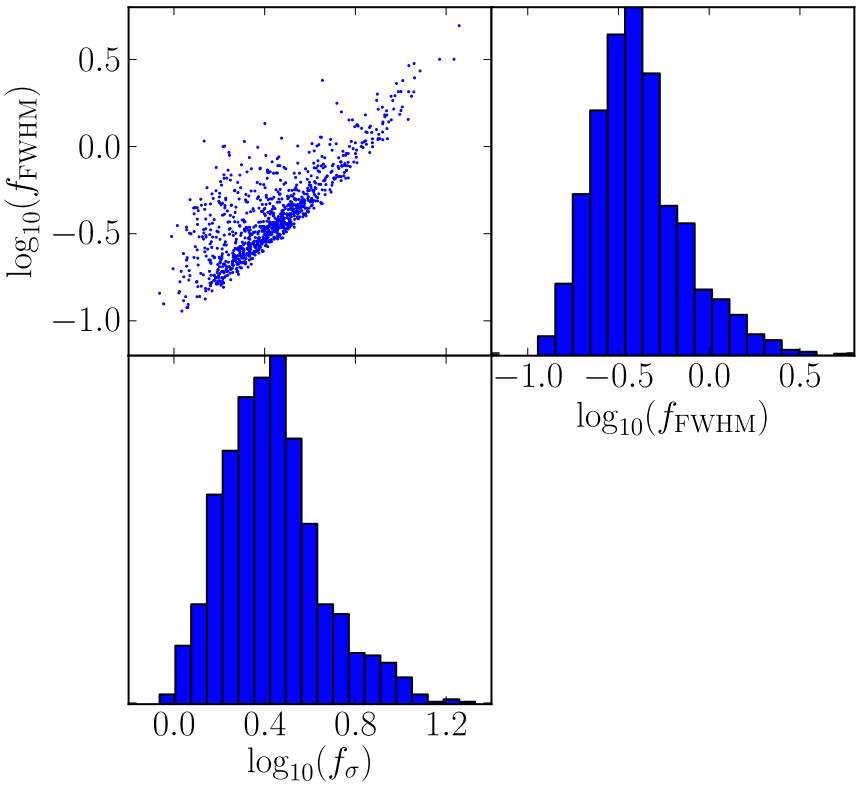

Figure 4.13: Distributions of f factor values for a fixed value of black hole mass and mean radius, with the other BLR model parameters allowed to vary. f_σ and $f_{\rm FWHM}$ are calculated using the CCF lag $\tau_{\rm cen}$ and the line dispersion of the RMS emission line profile or the FWHM of the mean emission line profile respectively. The top left panel shows the correlation between f_σ and $f_{\rm FWHM}$.

assumptions, including that the mean lag is a good measure of the physical scale of the BLR and that the width of the broad emission line is a good measure of the velocity field of the BLR. We attempt to quantify the uncertainty introduced by these assumptions by calculating the virial product from instances of our geometry and dynamics BLR model. We hold the black hole mass fixed at $M = 10^{6.5} M_{\odot}$ and the mean radius fixed at $\mu = 4$ light days while allowing all other geometry and dynamics model parameters to vary within their prior bounds, except for the inclination angle, which is limited to within zero (face-on) and 45 degrees. For each sample of a BLR model, we calculate the CCF lag $\tau_{\rm cen}$, the line dispersion of the RMS emission line profile, and the full width at half maximum (FWHM) of the mean line profile. Using these three values we can calculate the virial product either using the line dispersion or FWHM line width measurement. By further dividing the true black hole mass by the virial product we can work in terms of the virial coefficient f, where f_{σ} is calculated from the virial product using the line dispersion and $f_{\rm FWHM}$ is calculated from the virial product using the FWHM.

The results for the comparison of true black hole mass to virial product are shown in Figure 4.13 for 1000 samples of the BLR model parameters (other than M and μ, which are held fixed). The cadence of the continuum light curve and spectral time series were based on the cadence of the LAMP 2008 dataset for Arp 151, as described by Bentz et al. (2009b). The values of $\log_{10}(f_{\sigma})$ and $\log_{10}(f_{\rm FWHM})$ are clearly correlated, but there is significant scatter in the relation. More importantly, the dispersion in the f factors is encouragingly small: the mean value of $\log_{10}(f_{\sigma})$ is 0.43, with a standard deviation of 0.22, and the mean value of $\log_{10}(f_{\rm FWHM})$ is -0.39 with a standard deviation of 0.26, where the dispersion in the f factors does not depend on whether the light curves have

been detrended. This means that if the BLR is well described by our phenomenological model, we should not be surprised that the $M_{\rm BH} - \sigma_*$ relation based on reverberation mapping black hole mass measurements does not have much larger scatter than the canonical ~ 0.4 dex found for galaxies with dynamical mass measurements.

4.4 Conclusions

In this chapter we present an improved and expanded simply parameterized phenomenological model of the BLR for direct modeling of reverberation mapping data. In addition to describing the model in detail, we test the performance of the direct modeling approach using simulated reverberation mapping datasets with and without full spectral information. We also use this model of the BLR to explore sources of uncertainty in the traditional cross-correlation analysis used to measure time lags in reverberation mapped AGNs as well as sources of uncertainty in traditional measurements of the black hole mass using the virial product. Our main conclusions are as follows:

1. For simulated data with the same properties as the LAMP 2008 spectroscopic dataset for Arp 151, we can recover the black hole mass to within 0.05-0.25 dex uncertainty and distinguish between elliptical orbits and inflow. We recover the mean radius and mean lag with $5-12\%$ uncertainties and the opening angle of the disk and inclination angle to within $5-10$ degrees.

2. For the same simulated datasets, but where integrated emission line fluxes are used instead of the full spectroscopic information, we can use a BLR geometry model to constrain the mean radius and mean lag with $5-35\%$ uncertainties and obtain

only minimal constraints on the geometry of the BLR.

3. Using a combination of an integrated emission line light curve and a mean emission line profile for direct modeling allows for some constraints on the geometry of the BLR, but with greater uncertainty than from using the full spectroscopic dataset. The uncertainty in $\log_{10}(M_{\rm BH}/M_{\odot})$ is also greater compared to using the full spectroscopic dataset.

4. Comparison of BLR geometry modeling results to those from JAVELIN (Zu et al. 2011) and CCF analysis shows that JAVELIN recovers a time lag between the true mean and median lag, while CCF analysis recovers a time lag closer to the true mean lag. While the larger lag uncertainties from CCF analysis may reflect the unknown shape of the transfer function, the lag uncertainties from JAVELIN are smaller than the difference between the true mean and median time lag.

5. By considering the range in possible BLR geometries of our model, we estimate the uncertainty in converting a mean lag into a mean radius to be $\sim 25\%$.

6. The CCF lag $\tau_{\rm cen}$ can be offset from the true lag of a BLR model depending on the geometry. Both signal-to-noise of the flux light curve and sampling rate affect the dispersion in how far the CCF lag is relative to the true lag. Gaps in the light curve due to weather also introduce more uncertainty in the CCF lag.

7. For a given BLR geometry, changes in the variability features of the AGN continuum light curve introduces an uncertainty of $\sim 25\%$ into measurements of the CCF lag $\tau_{\rm cen}$.

8. By considering the range in possible BLR geometries and dynamics of our model, we estimate the uncertainty in measuring the black hole mass using the virial product to be smaller than the spread in the $M_{\rm BH} - \sigma_*$ relation. We find that the standard deviation of $f = M_{\rm BH}/M_{\rm vir}$ is only ~ 0.25 dex, i.e. smaller than the uncertainty typically quoted for virial mass estimates.

The tests presented here demonstrate the unique capabilities of dynamical modeling of reverberation mapping data to constrain the geometric and kinematic properties of the BLR. While we can use hybrid datasets consisting of integrated line flux measurements and a mean emission line profile, considerably more information is available from modeling the reverberations across the emission line profile. The improvements we have made to this simply parameterized phenomenological model of the BLR have increased the flexibility of the method to fit a wider variety of emission line profiles. Future improvements will add a deeper connection to photoionization physics, relating the distribution of broad line emission to the distribution of underlying gas, and explore the effects of non-gravitational forces, important for inferring the correct black hole mass.

These tests also confirm that the uncertainties inherent in the traditional analysis of measuring lags using the cross-correlation function and black hole masses using the virial product are relatively small, although larger than the formal uncertainties. The simplified problem of modeling integrated emission line light curves using a geometry-only model for the BLR presents an alternative approach for measuring time lags and mean radii of the BLR compared to the traditional analysis. One advantage to measuring time lags and mean radii with geometry modeling of the BLR is that the final uncertainties reflect

the unknown underlying transfer function.

4.5 Appendix: Comparison of dynamics model to previous work

In previous versions of our geometric and dynamical model of the BLR, we used a less general dynamical model in which point particle velocities were drawn from distributions of energy E and angular momentum L centered around the circular orbit energy and angular momentum values $E_{\rm circ}$ and $L_{\rm circ}$ (e.g. Pancoast et al. 2011; Brewer et al. 2011a; Pancoast et al. 2012). We can solve for $E_{\rm circ}$ by evaluating Equation 4.15 when $v_r = 0$ and $v_\phi = v_{\rm circ}$:

$$E_{\rm circ} = -\frac{1}{2}\frac{GM}{r}. \tag{4.19}$$

Similarly, we can solve Equation 4.15 for L, setting $v_r = 0$ and plugging in $E_{\rm circ}$ to find an expression for the angular momentum of a particle in a circular orbit:

$$L_{\rm circ} = \sqrt{rGM}. \tag{4.20}$$

This previous E/L model incorporated inflow and outflow in the BLR gas through the fraction of elliptical orbits with positive or negative radial velocity component solutions. The inflowing and outflowing gas in the E/L model is thus always bound to the black hole.

For comparison to the current more general dynamical model in Figure 4.14, we show the distributions of energy and angular momentum in the $v_r - v_\phi$ plane for direct comparison with Figure 4.2. The radial and tangential velocity distributions for the

E/L model are centered around the red dashed ring of radius $v_{\rm circ}$ and constrained to lie within the solid red circle, corresponding to orbits that are bound to the black hole. The velocity at which a particle becomes unbound is given by setting $E = 0$ and solving for $|v| = \sqrt{v_r^2 + v_\phi^2} = \sqrt{2GM/r}$, which is $\sqrt{2}v_{\rm circ}$. Unfortunately, while the distributions of E and L are centered around their circular orbit values, the chance of having a particle draw a close to circular orbit is vanishingly small, as shown by the lack of points in Figure 4.14 at $(v_r, v_\phi) = (0, v_{\rm circ})$. This suggests a better way of including the circular orbit solution: draw point particle velocities directly from distributions in radial and tangential velocity space instead of in E and L space.

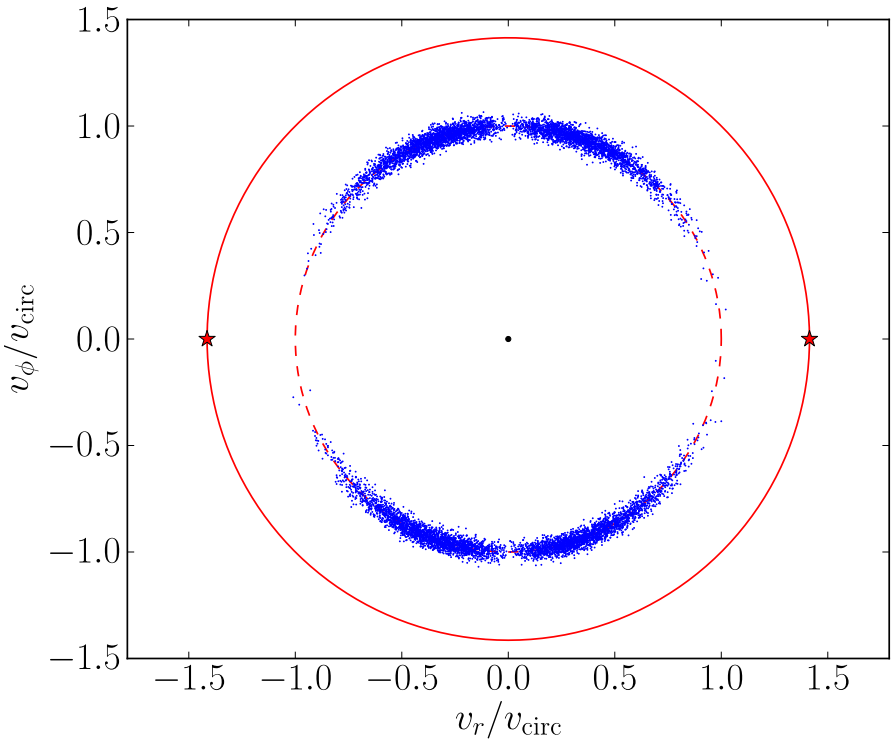

Figure 4.14: Distributions of radial and tangential velocities, v_r and v_ϕ for the previous E/L model. Blue points are particle velocities drawn from distributions in energy and angular momentum centered around the point for circular orbits $(v_r, v_\phi) = (0, v_{\rm circ})$. Outflow corresponds to positive v_r. The outer solid red circle at a radius of $|v| = \sqrt{2GM/r}$ denotes the velocity beyond which orbits are unbound. The red dashed circle at a radius of $|v| = \sqrt{GM/r}$ denotes velocities with magnitude of the circular velocity and the circle around which bound elliptical orbits were distributed in the E/L model.

Chapter 5

Modeling the broad line region IV: Application to LAMP 2008

This chapter was published as Pancoast, A.; Brewer, B. J.; Treu, T.; Park, D.; Barth, A. J.; Bentz, M. C.; Woo, J.-H. "Modeling reverberation mapping data II: dynamical modeling of the Lick AGN Monitoring Project 2008 dataset", Monthly Notices of the Royal Astronomical Society, 445, 3073 (2014) and is included here with minor formatting adjustments.

In this chapter we apply the direct modeling method to the Lick AGN Monitoring Project (LAMP) 2008 reverberation mapping dataset (Walsh et al. 2009; Bentz et al. 2009b).[1] The LAMP 2008 campaign observed 13 AGNs using spectroscopy from the Shane Telescope at Lick Observatory and Johnson V and B broad-band photometry from a number of ground-based telescopes. We focused our direct modeling on the Hβ line of the 9 objects with measurable time lags, using the broad and narrow Hβ emission line components isolated from the stellar continuum and Fe II lines using spectral decomposition techniques by Park et al. (2012b). Out of the 9 objects to which we

[1]The LAMP 2008 spectroscopic dataset is available for download here: http://www.physics.uci.edu/∼barth/lamp.html

applied our direct modeling method, only 5 objects showed sufficient continuum and line variability to allow for constraints on the geometry and dynamics of the BLR. Of the five objects with successful direct modeling of the Hβ line presented here, one of the objects, Arp 151, has previous direct modeling results as described by Brewer et al. (2011a). There are two main differences between the direct modeling of Brewer et al. (2011a) and this work: the first is that we use the spectral decompositions from Park et al. (2012b) instead of Bentz et al. (2009b), and the second is that the model of the BLR has since been substantially improved. Improvements to the BLR model include a new dynamics model and two additional geometry model parameters that add flexibility to the shape of the BLR. In addition, we now model the narrow emission line component of Hβ using the width of the [O III]λ5007 narrow emission line and calculate the instrumental resolution for each epoch of spectroscopy separately.

Our focus in this chapter is to apply the direct modeling method to the remainder of the LAMP 2008 sample, including reanalysis of Arp 151. In Section 5.1 we describe the LAMP 2008 data used in our analysis. In Section 5.2 we briefly review our model for the BLR with further details to be found in Chapter 4 (Pancoast et al. 2014a). In Section 6.4 we present the results of our analysis for the five successfully modeled AGNs in the LAMP 2008 sample. Finally, in Section 5.4 we summarize our results and discuss their implications for future direct modeling work. All quantities related to properties of the BLR are given in the rest frame of the system.

5.1 Data

Our sample of AGNs was observed in the LAMP reverberation mapping campaign in 2008. The first part of the data consists of Johnson B and V broad-band AGN continuum light curves measured using standard aperture photometry techniques, as described by Walsh et al. (2009). The B and V band images were taken at a number of telescopes, including the 30-inch Katzman Automatic Imaging Telescope (KAIT), the 2-m Multicolor Active Galactic Nuclei Monitoring telescope, the Palomar 60-inch telescope, and the 32-inch Tenagra II telescope. For direct modeling of each AGN, we choose to use either the B or V band light curve depending on which has more data points, better sampling of variability features, and higher overall variability. In general, the choice of B or V-band AGN continuum light curve does not change our results.

The second part of the data comprises light curves of broad and narrow Hβ line profiles. Measurement of the Hβ line profiles was done in two ways: Bentz et al. (2009b) isolated the Hβ flux by fitting a local linear continuum underneath the Hβ and O III lines, while Park et al. (2012b) applied a multi-component fit to isolate the Hβ line from the AGN continuum, stellar continuum, and Fe II emission lines. Due to the non-negligible contribution of the stellar continuum and Fe emission lines to the five LAMP 2008 objects considered here, we performed direct modeling on the Hβ emission line profiles as measured by Park et al. (2012b). The final spectra we use here for modeling include the broad and narrow Hβ line profiles, as well as the spectral decomposition residuals, equivalent to subtracting off all other components from the original spectrum. The details of the final spectra, including wavelength range used for direct modeling, are

given in Table 5.1.

One other important parameter of the spectral dataset is the instrumental resolution, which is used to smooth the simulated emission line profiles. The instrumental resolution was measured by Bentz et al. (2009b, see their Table 11) for four of the five objects by comparing the [O III]λ5007 line widths to the values measured by Whittle (1992). However, there were variations in the [O III]λ5007 line width over the duration of the reverberation mapping campaign due to small changes in the observing and instrumental conditions. For this reason, we calculate the instrumental resolution, $\Delta\lambda_{\rm dis}$, for each night independently using the width of the [O III]λ5007 line from the spectral decomposition by Park et al. (2012b), $\Delta\lambda_{\rm obs}$, and the intrinsic line width as measured by Whittle (1992), $\Delta\lambda_{\rm true}$, by subtracting them in quadrature:

$$\Delta\lambda_{\rm dis}^2 \approx \Delta\lambda_{\rm obs}^2 - \Delta\lambda_{\rm true}^2. \tag{5.1}$$

In order to include the uncertainties in these line width measurements, we consider both the measured and intrinsic widths of the [O III]λ5007 line to be free parameters with Gaussian priors centered on the measured values and with dispersions given by the quoted measurement uncertainties. For the one object, SBS 1116+583A, without a comparison line width by Whittle (1992), we use a value in the middle of the range of the values of the other four objects. The values of the intrinsic [O III]λ5007 line width used in this analysis are given in the last column of Table 5.1 as the line dispersion in Å, converted from the FWHM of the line widths in units of km s^{-1} listed in Whittle (1992) assuming the Gaussian conversion of 2.35, for all objects except SBS 1116+583A.

Table 5.1: Properties of the LAMP 2008 spectra and photometry. Band is the Johnson broad-band filter. N_c is the number of data points in the AGN continuum light curve in the band given by column 2. N_s is the number of spectra in the broad emission line time series. N_p is the number of pixels in the Hβ spectrum between the wavelength ranges given in the next column. Wavelengths are in the rest frame. Intrinsic [O III]λ5007 Width is the intrinsic line dispersion σ of the narrow [O III]λ5007 emission line used for calculating the instrumental resolution. [a] These values are converted from measurements by Whittle (1992) assuming an uncertainty of 10 km/s.

Object	Band	N_c	N_s	N_p	Wavelength Range (Å)	Intrinsic [O III]λ5007 Width (Å)
Arp 151	*B*	84	43	73	4792.3 – 4933.4	1.562 ± 0.071^a
Mrk 1310	*B*	50	47	51	4815.5 – 4913.6	0.852 ± 0.071^a
NGC 5548	*V*	57	51	171	4706.5 – 5040.9	2.910 ± 0.071^a
NGC 6814	*V*	46	45	81	4776.7 – 4935.8	0.888 ± 0.071^a
SBS 1116+583A	*B*	56	50	67	4797.3 – 4925.7	1.4 ± 0.3

5.2 The dynamical model of the broad line region

In this section we give a brief overview of our simply parameterized phenomenological model of the BLR geometry and dynamics, with full model details given in Chapter 4. We model the distribution of broad line flux emission by the density of many point particles that instantaneously and linearly reprocess the AGN continuum flux and reemit some fraction of it back towards the observer with time lags that depend upon the point particles' positions. The velocities of the point particles then determine how redshifted or blueshifted the broad line flux from the point particles is relative to the systemic velocity of the BLR system. This means that in addition to a model describing the distribution of point particles in position and velocity space, we must also model the AGN continuum flux in order to evaluate it at arbitrary times.

For our model of the AGN continuum light curve we use Gaussian processes, which allows us to sample the AGN continuum variability on scales much smaller than the

typical one day cadence between datapoints. This AGN continuum variability model allows us to include the uncertainty from interpolation in our final uncertainties in the BLR model parameters, as well as allowing us to extrapolate beyond the ends of the light curve in order to evaluate long time lags (for an illustration see Pancoast et al. 2011).

We model the BLR geometry by defining the physical distribution of point particles. The radial distribution is given by a shifted Gamma distribution, which can reproduce Gaussian, exponential or heavy-tailed radial distributions depending on the value of its shape parameter. The point particles are also constrained to be within an (unknown) opening angle, which allows for spherical geometries ranging to thin disk geometries. The BLR is then viewed by an observer with an inclination angle ranging from face-on to edge-on. Finally, there are a number of non-axisymmetric effects that allow for more flexibility in the BLR geometry. These include preferential emission of the point particles from the near or far side of the BLR along the observer's line of sight, a transparent to opaque mid-plane, and the possibility of increased emission from the edges of the BLR disk, relative to the inner portion.

Similarly, we model the BLR dynamics by defining the velocity distribution of point particles as a function of position and black hole mass. We draw the point particles' velocities from distributions in the space of radial and tangential velocities, centered around the circular orbit values or from around the radial escape velocity values for inflowing or outflowing orbits. We allow for a combination of elliptical orbits centered around the circular orbit values plus either inflow or outflow centered around their respective radial escape velocities. To allow for mostly bound inflowing or outflowing orbits, we also allow the distributions of inflowing and outflowing orbits to be centered anywhere along

an ellipse between the radial escape velocity and the circular orbit velocity. In order to add more flexibility, we also allow for additional macroturbulent velocities. Finally, we include gravitational redshift and the full expression for doppler shift when moving between the velocities of the point particles and the wavelengths of broad line flux emission. The exact definitions of the geometry and dynamics model parameters are given in Appendix 5.5, with more detailed descriptions given in Chapter 4.

In addition to modeling the broad emission line component using a model for the BLR, we also model the narrow emission line component using the width of the [O III]λ5007 narrow emission line. Since the width of the [O III]λ5007 line is a combination of intrinsic line width and instrumental resolution, we use measurements of the intrinsic line width to constrain the instrumental resolution for smoothing of the broad emission line component.

We explore the parameter space of the BLR model and AGN continuum variability model using Diffusive Nested Sampling (Brewer et al. 2011b). This algorithm samples the posterior distribution for the parameters, and provides the "evidence" value which can be used to compare distinct models. We use a Gaussian likelihood function that compares the time series of broad emission line profiles of the data to the simulated versions generated by our BLR model. Since the model is of finite flexibility and the spectral data have high signal to noise and a large number of data points, it is necessary to soften the likelihood function. We do this by defining a temperature T by which the log of the likelihood is divided, where $T \geq 1$. Temperatures greater than one can be thought of as an additional source of uncertainty in the likelihood due to the model not providing a perfect fit to the data, either because the error bars of the data are underestimated or because the model does not contain enough complexity to reproduce all features of

the data. The use of a temperature can be thought of as a computationally inexpensive approximation to a correlated noise model. Since we use Nested Sampling, the choice of temperature T can be made in post-processing and does not require multiple runs.

5.3 Results

We now present the results of direct modeling of five AGNs in the LAMP 2008 sample, including Arp 151, Mrk 1310, NGC 5548, NGC 6814, and SBS 1116+583A. First, the modeling results are presented in detail for each AGN, including key posterior PDFs and correlations, the model fit to the data, and the transfer function. Examples of the inferred geometry of the BLR for each AGN are also shown in Figure 5.1 and the AGN continuum light curves with Gaussian process interpolations drawn from the posterior are shown in Figure 5.2. The posterior median and central 68% credible intervals for the main BLR model parameters are given in Table 5.2. Second, we present an overview of the BLR modeling results to emphasize the similarities and differences in the sample. Finally, we calculate the mean f factor for this sample of five AGNs.

5.3.1 Individual modeling results

Arp 151 (Mrk 40)

Both the AGN continuum and broad Hβ line showed strong variability over the duration of the LAMP 2008 campaign, leading to the clearest velocity-resolved lag measurements of the LAMP 2008 sample (Bentz et al. 2009b) and the most detailed transfer function recovered at the time using MEMECHO (Bentz et al. 2010b). It is therefore

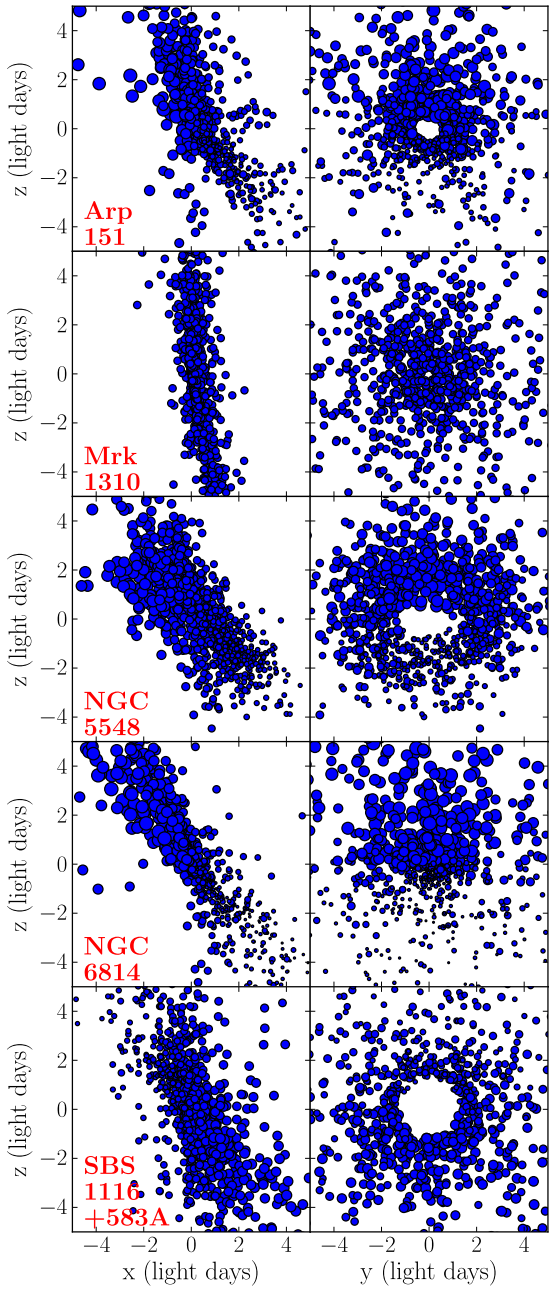

Figure 5.1: Geometries of the BLR for the five objects in our sample. The left panels show the BLR from along the y axis (the edge-on view), while the right panels show the BLR from along the positive x axis (the observer's point of view). Top to bottom: Arp 151, Mrk 1310, NGC 5548, NGC 6814, and SBS 1116+583A. Each point corresponds to a point particle in our BLR model and the size of the points is proportional to the relative amount of Hβ emission coming from each point particle, given the same incident continuum flux.

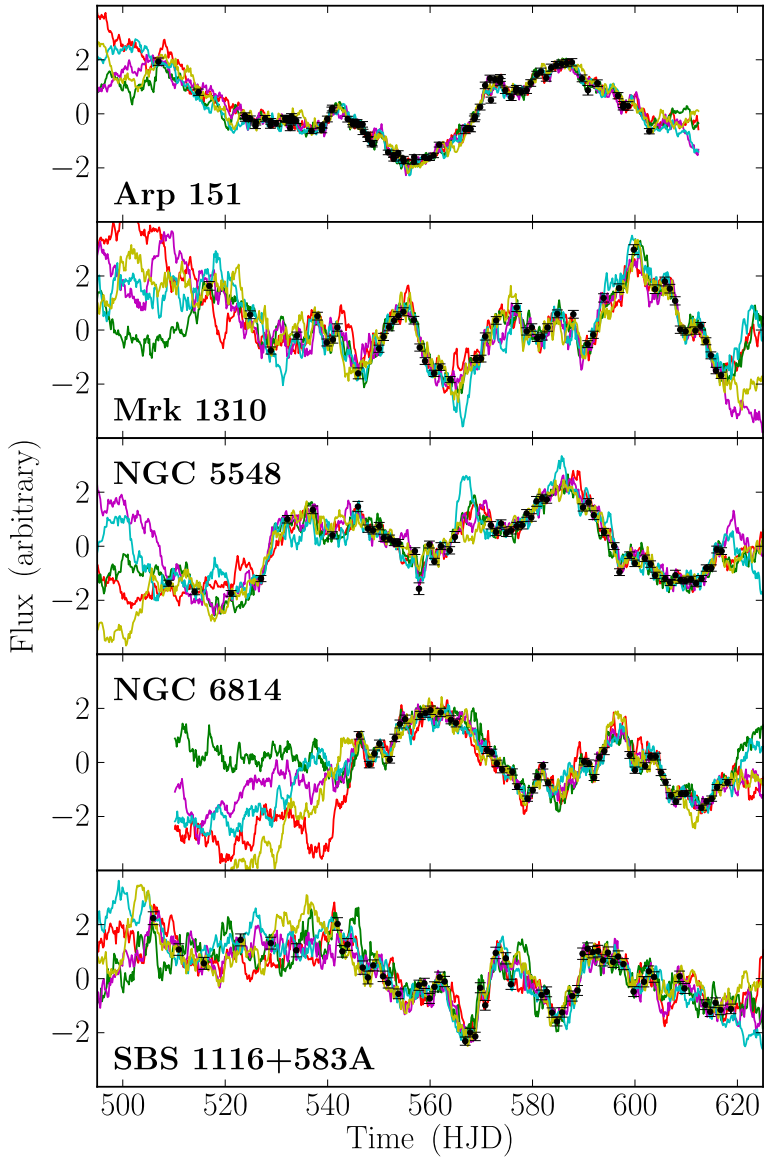

Figure 5.2: AGN continuum light curves for the five objects in our sample. The data are shown by black points with error bars and the Gaussian process interpolations drawn from the posterior PDF are shown by the colored lines. Top to bottom: Arp 151, Mrk 1310, NGC 5548, NGC 6814, and SBS 1116+583A.

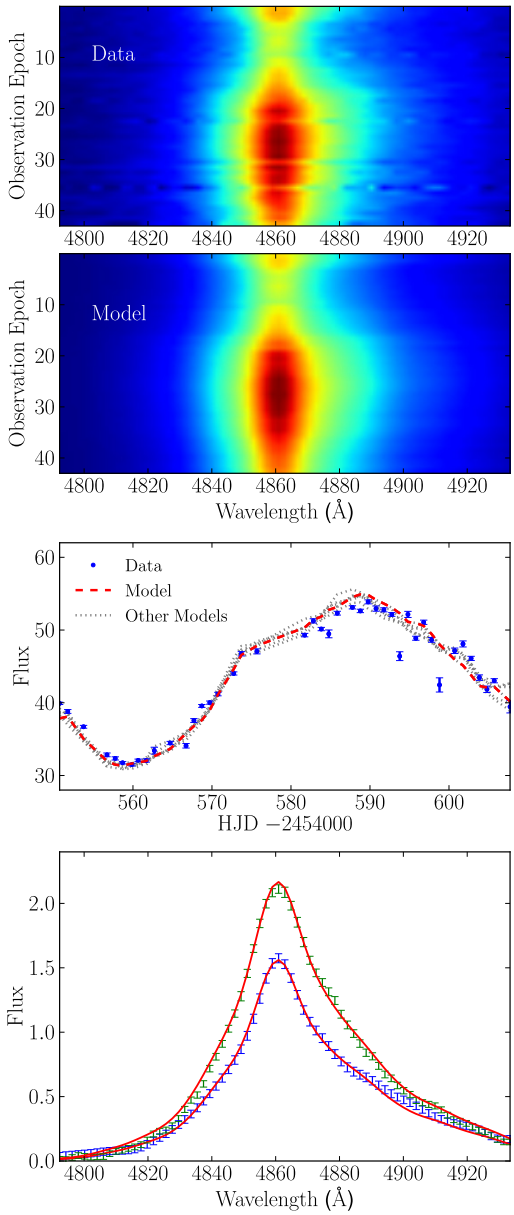

Figure 5.3: Model fit to the broad and narrow Hβ line dataset for Arp 151. Top panel: the Hβ spectral time series of data from Park et al. (2012b). Top middle panel: an example of a simulated Hβ spectral time series for a model drawn randomly from the posterior PDF. Bottom middle panel: the integrated Hβ line light curve with data from Park et al. (2012b) given by the blue points with error bars, the model in the top middle panel shown with the red dashed line, and additional models drawn from the posterior shown with the dotted grey lines. Bottom panel: two examples of the Hβ line profile shown with blue and green error bars with the model fits over-plotted with red lines.

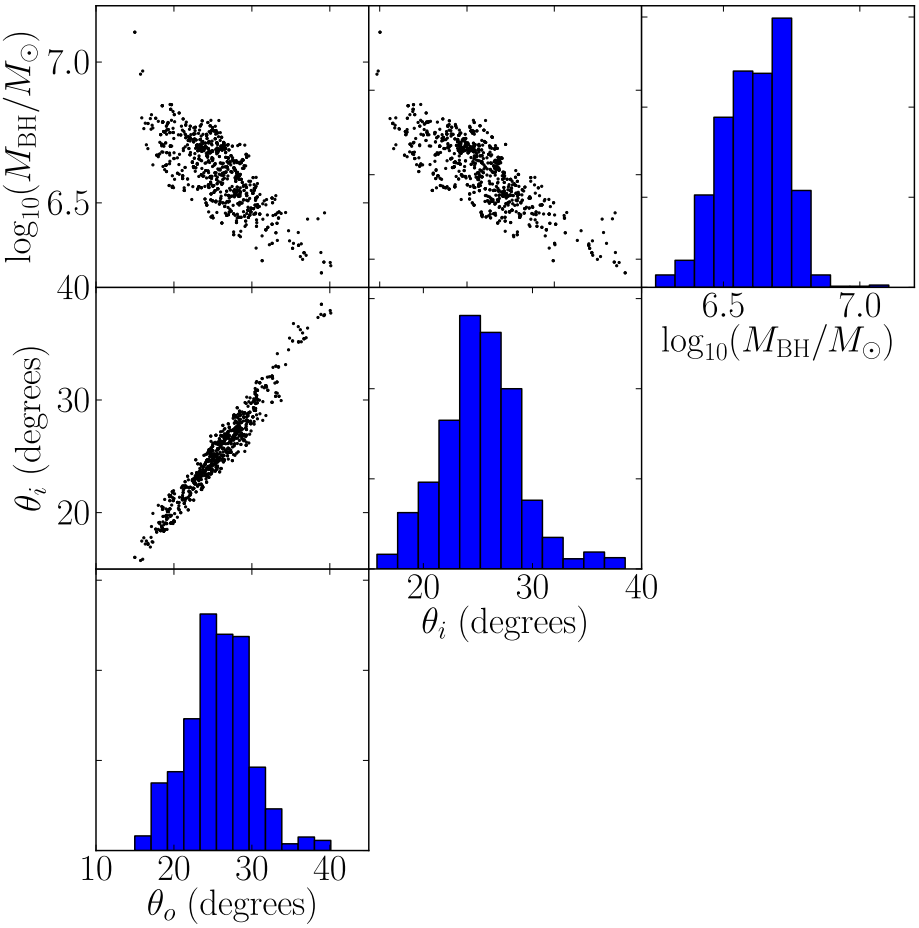

Figure 5.4: Marginal posterior PDFs and correlations between parameters for Arp 151, including black hole mass ($M_{\rm BH}$), inclination angle (θ_i), and opening angle (θ_o).

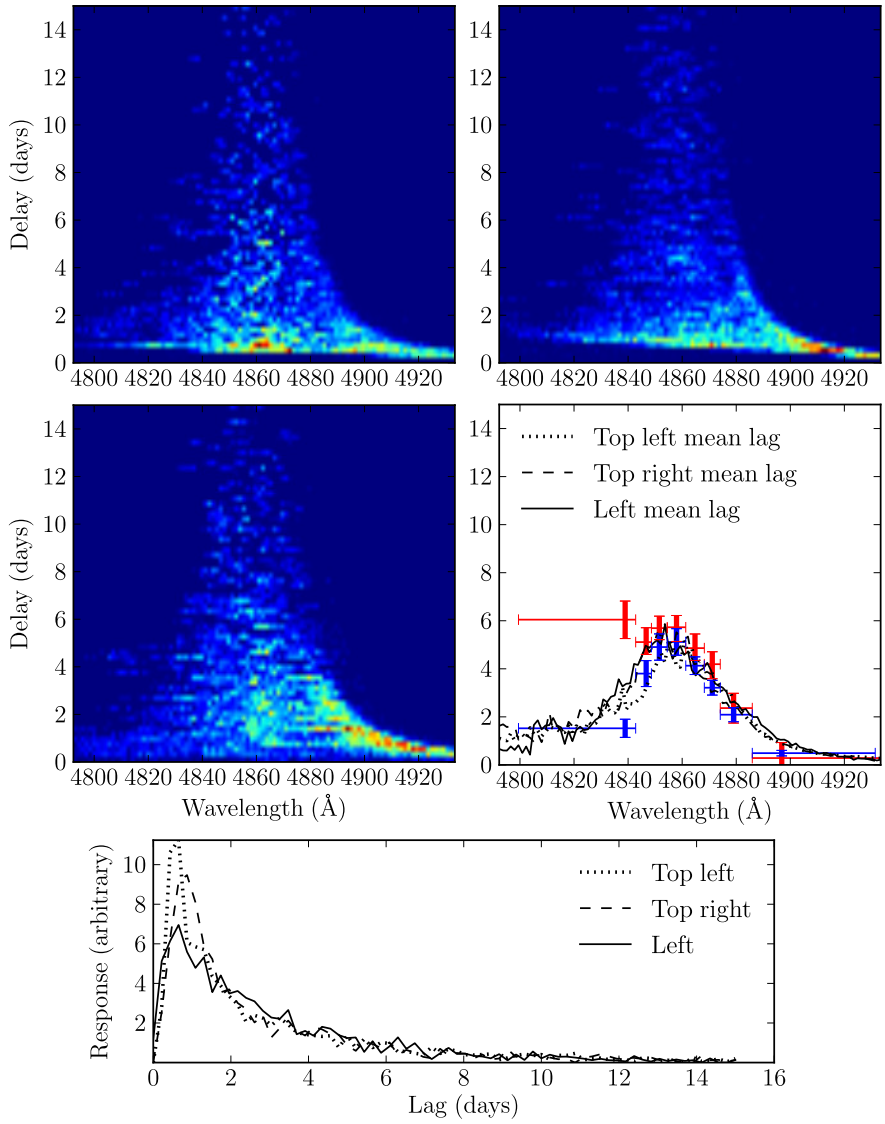

Figure 5.5: Transfer functions for Arp 151. The top two panels and the middle left panel are all examples of transfer functions drawn from the posterior PDF of the model fit. The middle right panel shows the mean lag as a function of velocity for each of the three transfer functions from the posterior. Also shown in this panel are the velocity-resolved cross-correlation lag measurements from Bentz et al. (2009b) as red error bars, where the horizontal error bars show the wavelength ranges used in the integrated light curves. Our mean lag values in these same bins are shown by the blue error bars, except for the longest wavelength bin which does not extend as far to the red as the one by Bentz et al. (2009b). The bottom panel shows the velocity-integrated transfer function for each of the three transfer functions from the posterior.

unsurprising that the direct modeling results for Arp 151 also have the highest quality of the LAMP 2008 sample.

Comparison of the spectral time series and time series of simulated spectra, as illustrated in Figure 5.3, suggests that the model is able to fit the overall variability structure of the Hβ line profile very well. In addition, the integrated model Hβ emission line and individual model spectra show excellent agreement. The model is unable to capture very short timescale variations that are either due to noise or processes with much faster response times than the overall variability of the BLR would suggest. Fortunately, such short timescale variations are infrequent and do not appear to substantially affect inference of the model parameters.

The geometry of the BLR in Arp 151 as traced by Hβ emission is inferred to be a wide thick disk, inclined by $\theta_i = 25.2^{+3.3}_{-3.4}$ degrees relative to the observer (0 = face-on). The radial distribution of Hβ emission has heavier tails than an exponential profile, with a Gamma distribution shape parameter of $\beta = 1.25^{+0.15}_{-0.16}$, mean radius $r_{\rm mean} = 3.44^{+0.26}_{-0.24}$ light days, and dispersion or radial width of $\sigma_r = 3.72^{+0.45}_{-0.43}$ light days. The radial distribution is offset from the origin, the source of the ionizing photons and visible continuum emission, by $r_{\rm min} = 0.44^{+0.13}_{-0.20}$ light days. The mean radius equals to within the uncertainties the mean lag of $\tau_{\rm mean} = 3.07^{+0.25}_{-0.20}$ days, which in turn is consistent with the cross-correlation measured central lag of $\tau_{\rm cent} = 3.99^{+0.49}_{-0.68}$ days by Bentz et al. (2009b) to within the uncertainties. Due to the heavy tails of the radial profile, the median lag of $\tau_{\rm median} = 1.75^{+0.28}_{-0.23}$ days is significantly shorter. The opening angle of the disk is well constrained to be $\theta_o = 25.6^{+3.7}_{-4.0}$ degrees, however more emission is found to come from the outer faces of the disk ($\gamma = 4.27^{+0.54}_{-0.80}$), making the geometry closer to a cone. There is

also preferential emission from the far side of the BLR from the observer ($\kappa = -0.36^{+0.08}_{-0.08}$) and the mid-plane of the BLR disk is found to be mostly opaque ($\xi = 0.09^{+0.08}_{-0.05}$). An example of the BLR geometry in Arp 151 for a set of model parameters drawn from the posterior is shown in Figure 5.1.

The dynamics of the BLR in Arp 151 are inferred to be dominated by inflowing orbits, with the fraction of point particles in elliptical orbits only $f_{\rm ellip} = 0.06^{+0.09}_{-0.05}$, or $1 - 15\%$. The majority of the point particles are in inflowing orbits as given by the inflow/outflow parameter $f_{\rm flow} = 0.24^{+0.20}_{-0.17}$, where values of $f_{\rm flow}$ between 0 and 0.5 indicate inflow and values between 0.5 and 1 indicate outflow. Comparing the probability for values of $f_{\rm flow}$ between 0 and 0.5 with the probability for values between 0.5 and 1 indicates a 100% preference for inflow compared to outflow. Furthermore, the inferred inflowing orbits are not strictly radial or drawn from a velocity distribution centered on the radial escape velocity, but can be distributed closer to the circular orbit value, leading to more bound inflowing orbits. The value of $\theta_e = 12.0^{+10.7}_{-8.3}$ that we infer for Arp 151 indicates that the inflow orbit velocity distribution is rotated about a seventh of the way towards the circular-orbit-centered distribution and that more than half of the inflowing orbits are bound. Finally, we find a negligible contribution to the dynamics of the BLR from macroturbulent velocities, with the dispersion of additional macroturbulent velocities drawn from a Gaussian distribution of only $\sigma_{\rm turb} = 0.008^{+0.028}_{-0.007}$ times the circular orbit velocity.

We measure a black hole mass for Arp 151 of $\log_{10}(M_{\rm BH}/M_\odot) = 6.62^{+0.10}_{-0.13}$. As illustrated in Figure 5.4, there is strong degeneracy between the black hole mass, inclination angle, and opening angle, preventing us from measuring the black hole mass with greater

precision. The correlation between these parameters is easy to understand if one considers that the BLR model parameters are constrained such that the line-of-sight velocity matches the width of the emission line: for thin disks, the more face-on the BLR, the higher the black hole mass must be to produce the same line-of-sight velocities. The opening angle is also strongly correlated, since a thicker disk allows for larger line-of-sight velocities for a given black hole mass.

With an independent measurement of the black hole mass we can use the virial product $M_{\rm vir}$ from traditional reverberation mapping analysis to measure the f factor for Arp 151. We use the time lags $\tau_{\rm cent}$ from cross-correlation analysis from Bentz et al. (2009b) and measurements of the Hβ line width after spectral decomposition from Park et al. (2012b) to construct two sets of virial products. The first type of virial product uses the line dispersion measured from the RMS line profile as the Hβ line width and the second uses the FWHM of the mean line profile as the Hβ line width. Values of the f factor calculated using the first type of virial product will be referred to as f_σ, while values calculated using the second type of virial product will be referred to as $f_{\rm FWHM}$. We obtain the distribution of f for each AGN by subtracting the virial product from the normalized posterior PDF of black hole mass. The inferred f factors for the five AGNs in our sample are listed in Table 5.3. For Arp 151, we measure f factors of $\log_{10}(f_\sigma) = 0.51^{+0.10}_{-0.13}$ and $\log_{10}(f_{\rm FWHM}) = -0.24^{+0.10}_{-0.13}$.

Previous direct modeling results for Arp 151 constrained the black hole mass to be $10^{6.51\pm0.28}\,M_\odot$ and the geometry to be a wide thick disk with an opening angle of $\theta_o = 34.5^{+10.7}_{-8.6}$ degrees, inclined with respect to the observer by $\theta_i = 22.2 \pm 7.8$ degrees (Brewer et al. 2011a). Our improved modeling results for Arp 151 are completely consistent to

within the uncertainties with these previous modeling results, and clarify the previous ambiguity in whether the dynamics of Hβ in Arp 151 are dominated by inflow or outflow.

For comparison with work focused on recovering the velocity-resolved transfer function, we show three transfer functions created from models drawn randomly from the multi-dimensional posterior PDF in Figure 5.5. While the three transfer functions show slightly different detailed structure, the mean lag as a function of velocity is very similar for all three, as is the velocity-integrated transfer function. In addition, all three velocity-resolved transfer functions show at least some preference for prompt response on the red side of the line profile, indicative of inflow kinematics. The same inflow signatures were found in the transfer function recovered using MEMECHO (Bentz et al. 2010b), as well as the velocity-resolved lag measurements, shown in red in the middle right panel of Figure 5.5. The discrepancy in the blue wing of the line between the velocity-resolved lag measurements from CCF analysis (in red in Figure 5.5) and dynamical modeling (in blue) is due to a combination of data preprocessing and systematics from measurement of the time lag. Recalculating the velocity-resolved time lags from CCF analysis using the same datasets as in the dynamical modeling decreased the discrepancy in the bluest lag bin by ~ 1.5 days while remaining consistent with the values from Bentz et al. (2009b). The remaining discrepancy is due to the difference between the true mean time delay and the time delay proxy estimated by CCF analysis. We confirm this by creating velocity-resolved light curves using the inferred models of the BLR for Arp 151, calculating and showing that the CCF time lag from those model light curves and the time lags from dynamical modeling are consistent with the values from Bentz et al. (2009b). However there are residual differences between the transfer functions from direct modeling and

MEMECHO, including response in the blue wing of the line, where direct modeling finds significantly shorter lags, and prompt response of the line emission at line center, where the MEMECHO solution finds no prompt response.

Mrk 1310

With the narrowest Hβ line profile in our sample, the dataset for Mrk 1310 provides fewer constraints on the BLR model due to a smaller number of pixels per spectrum and reduced variability compared to Arp 151. Despite these issues, the model is able to match the overall variability of the emission line profile, as well as the detailed line profile shape, as shown in Figure 5.6.

The geometry of the Hβ BLR for Mrk 1310 is constrained to be a thick disk, inclined by $\theta_i = 6.6^{+5.0}_{-2.5}$ degrees with respect to the observer, although inclination angles up to 35 degrees are not completely ruled out. The radial distribution of Hβ emission is constrained to be between exponential and Gaussian ($\beta = 0.89^{+0.10}_{-0.10}$), with a mean radius of $r_{\rm mean} = 3.13^{+0.42}_{-0.40}$ light days, a minimum radius away from the central source of ionizing photons of $r_{\rm min} = 0.12^{+0.19}_{-0.08}$ light days, and a radial dispersion or width of $\sigma_r = 2.59^{+0.42}_{-0.35}$ light days. The mean time lag of $\tau_{\rm mean} = 2.96^{+0.42}_{-0.35}$ days is very similar to the mean radius and median time lag of $\tau_{\rm median} = 2.26^{+0.35}_{-0.31}$, and agrees to within the uncertainties with the cross-correlation lag of $\tau_{\rm cent} = 3.66^{+0.59}_{-0.61}$ days measured by Bentz et al. (2009b). The opening angle of the disk is inferred to be $\theta_o = 8.6^{+3.5}_{-2.1}$ degrees, although opening angles up to 35 degrees are not completely ruled out. There is no preference for Hβ emission from the outer faces of the BLR disk ($\gamma = 2.97^{+1.38}_{-1.43}$), for emission from the far or near side of the BLR ($\kappa = -0.04^{+0.38}_{-0.35}$) or for the transparency of the BLR midplane

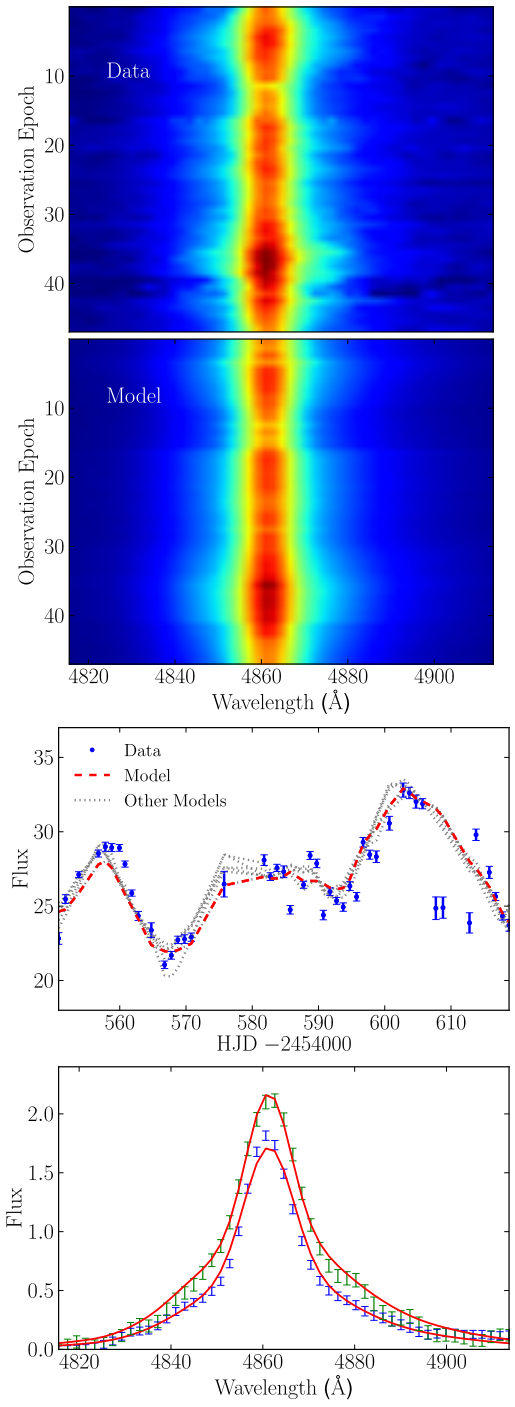

Figure 5.6: Same as Figure 5.3, but for Mrk 1310.

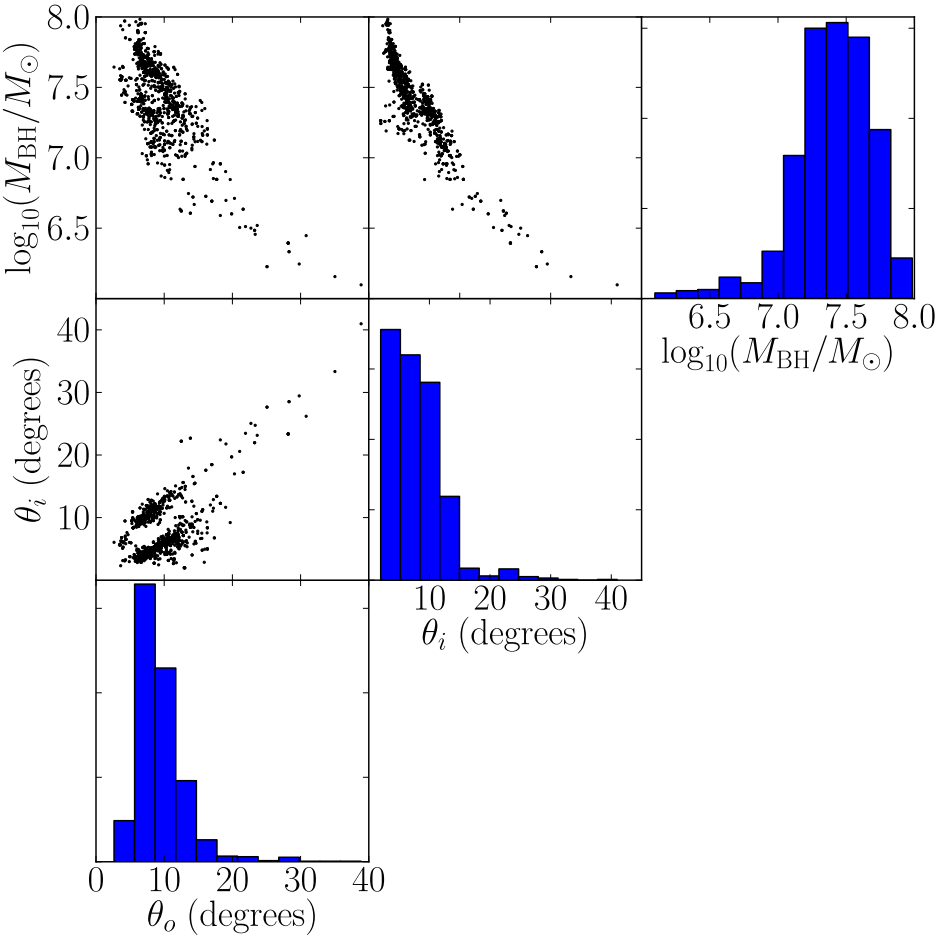

Figure 5.7: Same as Figure 5.4, but for Mrk 1310.

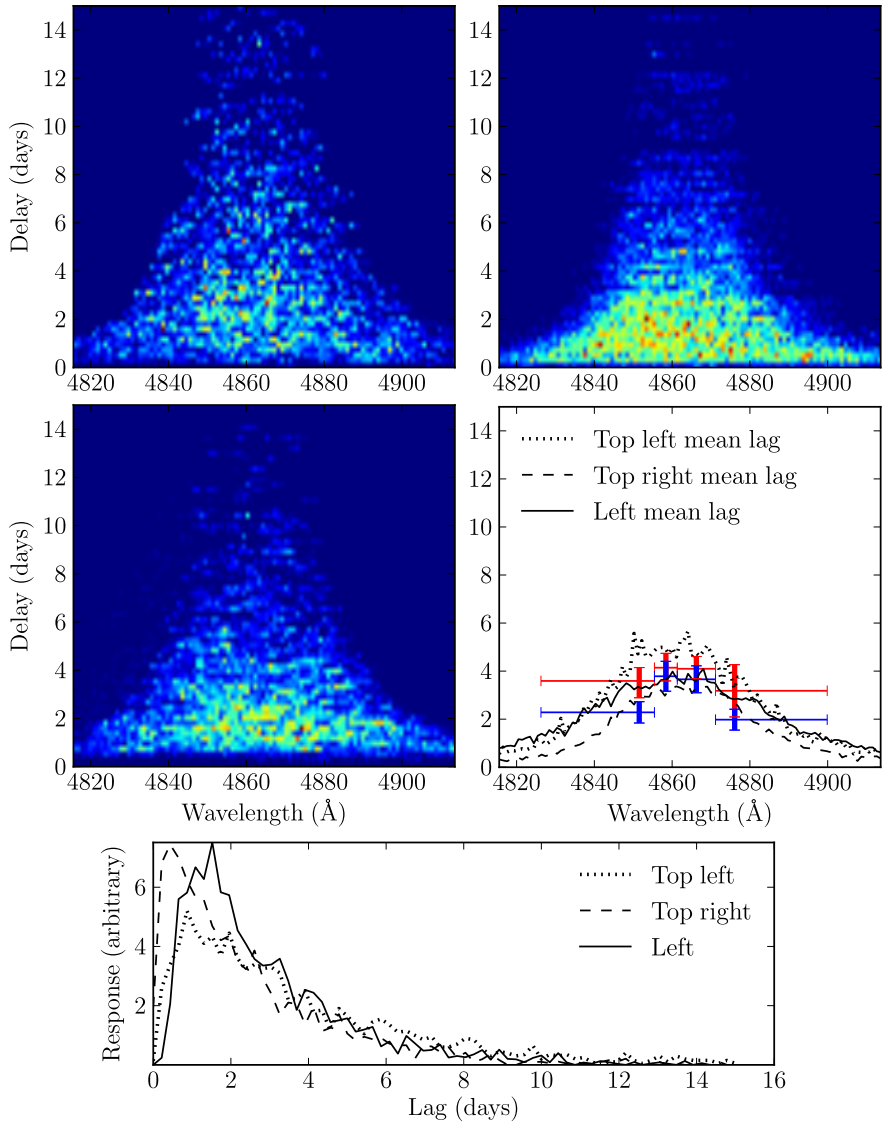

Figure 5.8: Same as Figure 5.5, but for Mrk 1310.

($\xi = 0.40^{+0.38}_{-0.29}$). An illustration of the BLR geometry for Mrk 1310 is shown in Figure 5.1 for one sample from the posterior PDF.

The dynamics of the BLR for Mrk 1310 are unclear. There is a slight preference for elliptical orbits ($f_{\rm ellip} = 0.56^{+0.34}_{-0.39}$) and placement of the inflowing/outflowing velocity distribution closer to the distribution centered on the circular orbit value ($\theta_e = 57.2^{+24.9}_{-41.0}$ degrees), but also a preference for the remaining orbits to be outflowing when $\theta_e \rightarrow 90$ degrees ($f_{\rm flow} = 0.65^{+0.24}_{-0.38}$, probability of inflow/outflow is 31%/69%). This shows that radial outflowing orbits are not actually strongly preferred compared to radial inflowing orbits and the dynamics of the BLR are not well-constrained in this case. We also find no preference for substantial macroturbulent velocities ($\sigma_{\rm turb} = 0.004^{+0.010}_{-0.003}$).

The black hole mass for Mrk 1310 is inferred to be $\log_{10}(M_{\rm BH}/M_{\odot}) = 7.42^{+0.26}_{-0.27}$. The uncertainty in the black hole mass is due in large part to degeneracy with the inclination angle and opening angle, as shown in Figure 5.7, since at very small inclination and opening angles large changes in black hole mass are needed to maintain the line-of-sight velocity of the point particles for even small changes in inclination or opening angle. Comparing our measurement of the black hole mass to the virial products calculated from cross-correlation time lags from Bentz et al. (2009b) and line widths from Park et al. (2012b), we measure the f factors for Mrk 1310 to be $\log_{10}(f_{\sigma}) = 1.63^{+0.26}_{-0.27}$ and $\log_{10}(f_{\rm FWHM}) = 0.79^{+0.26}_{-0.27}$ (see Section 5.3.1).

The velocity-resolved transfer functions for Mrk 1310, drawn randomly from the posterior PDF, show very similar structure as illustrated in Figure 5.8, despite ambiguity in the dynamics of the BLR. The mean velocity-resolved transfer functions and the velocity-integrated transfer functions also show very similar features, and agree to within the

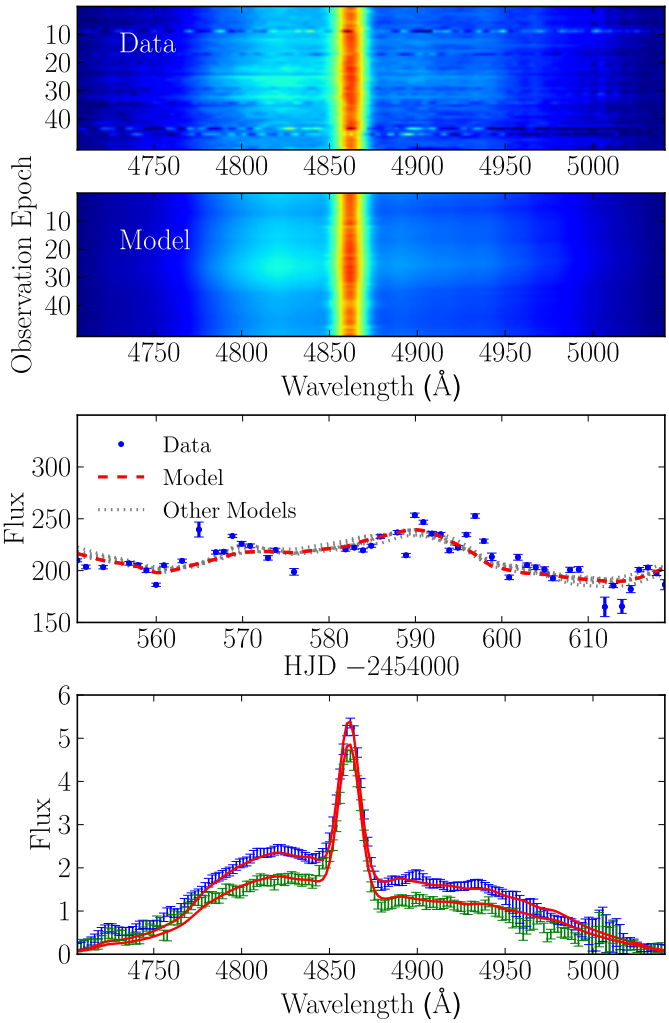

Figure 5.9: Same as Figure 5.3, but for NGC 5548.

uncertainties with the cross-correlation velocity-resolved lag measurements from Bentz et al. (2009b).

NGC 5548

While not as variable as Arp 151 over the duration of the LAMP 2008 campaign, the NGC 5548 Hβ line profile is the widest in the sample, providing an informative dataset

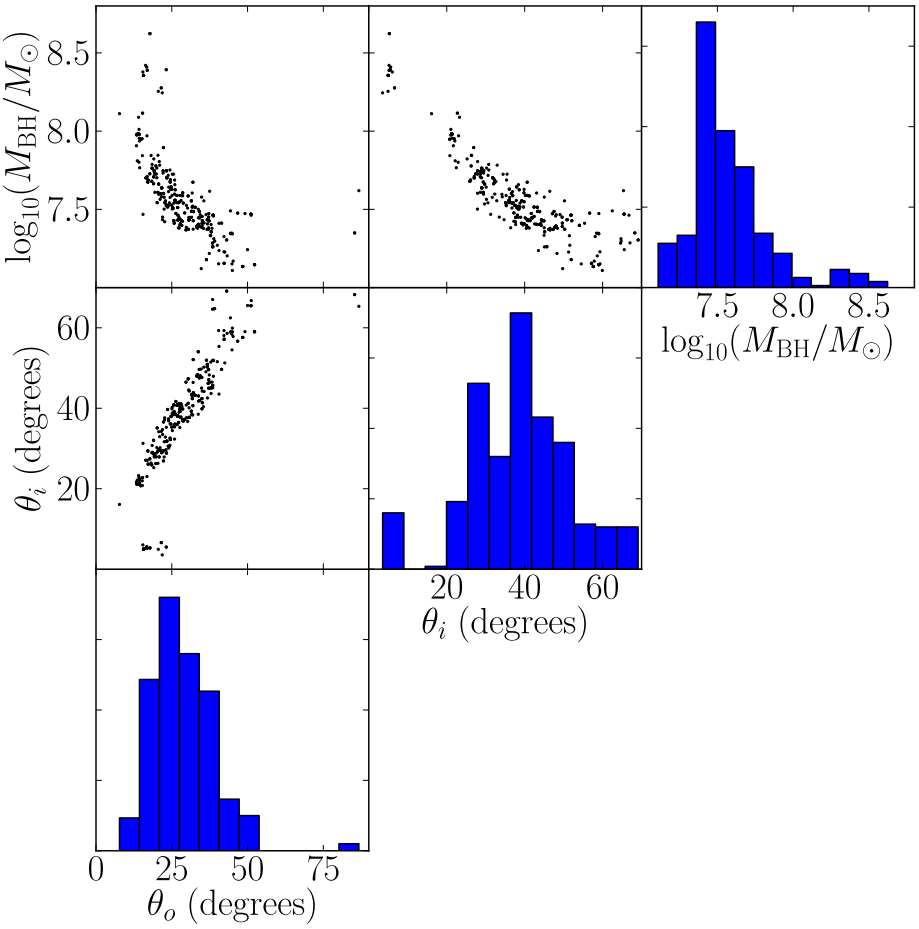

Figure 5.10: Same as Figure 5.4, but for NGC 5548.

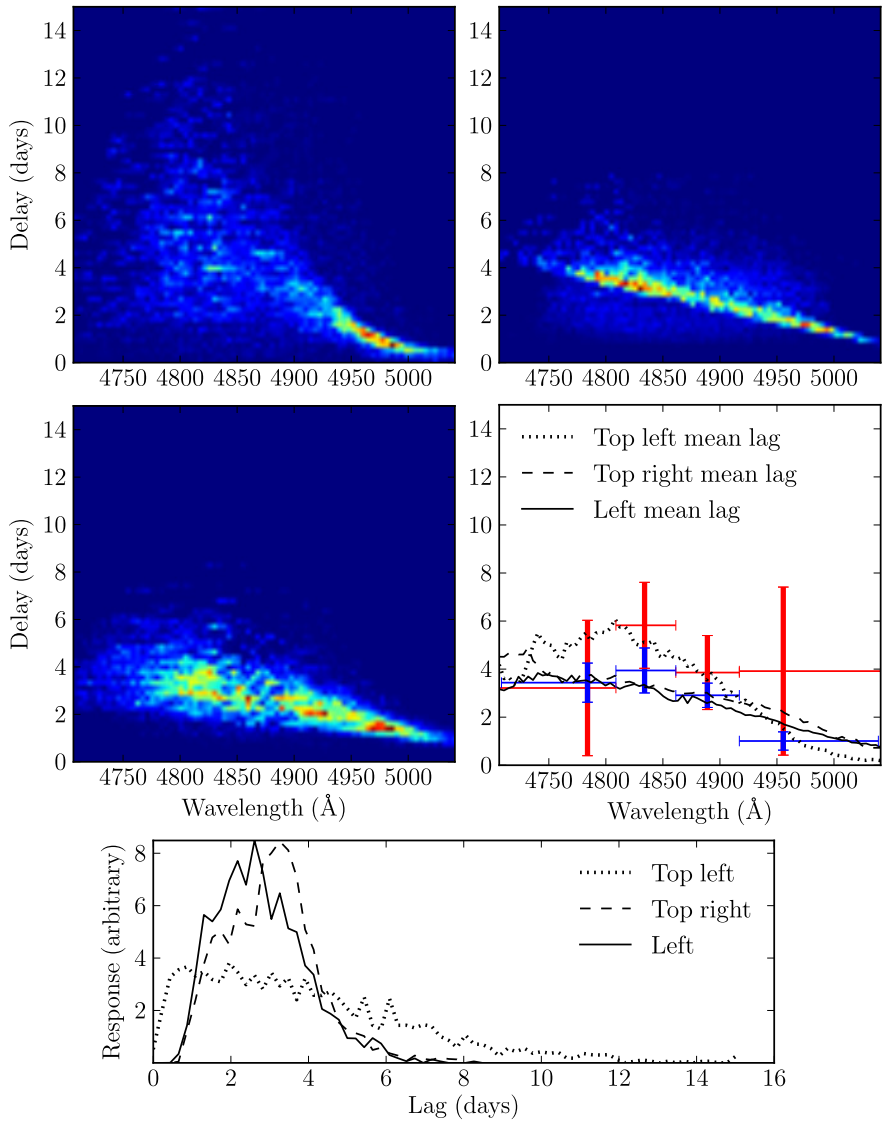

Figure 5.11: Same as Figure 5.5, but for NGC 5548.

with which to constrain the BLR model. The model is able to fit the overall variability of the Hβ line profile as well as the detailed emission line shape, as shown in Figure 5.9.

The geometry of the Hβ BLR in NGC 5548 is constrained to be a narrow thick disk, with an inclination angle of $\theta_i = 38.8^{+12.1}_{-11.4}$ degrees. The radial distribution of Hβ emission is between exponential and Gaussian ($\beta = 0.80^{+0.60}_{-0.31}$), with a mean radius of $r_{\rm mean} = 3.31^{+0.66}_{-0.61}$ light days, a minimum radius from the central ionizing source of $r_{\rm min} = 1.39^{+0.80}_{-1.01}$ light days, and a dispersion or width of the BLR of $\sigma_r = 1.50^{+0.73}_{-0.60}$ light days. The mean lag is very similar to the mean radius, with $\tau_{\rm mean} = 3.22^{+0.66}_{-0.54}$ days, and consistent to within the uncertainties with the cross-correlation lag measurement of $\tau_{\rm cent} = 4.17^{+0.90}_{-1.33}$ by Bentz et al. (2009b). The median lag is smaller with $\tau_{\rm median} = 2.77^{+0.63}_{-0.42}$ days. The opening angle of the disk is inferred to be $\theta_o = 27.4^{+10.6}_{-8.4}$ degrees with opening angles near 90 degrees not completely ruled out and with a slight preference for emission equally concentrated throughout the disk ($\gamma = 2.01^{+1.78}_{-0.71}$). The H$\beta$ emission is also found to preferentially emit from the far side of the BLR ($\kappa = -0.24^{+0.06}_{-0.13}$) and the midplane of the BLR is found to be not fully transparent ($\xi = 0.34^{+0.11}_{-0.18}$). An example of the BLR geometry in NGC 5548 is shown in Figure 5.1 for a single posterior sample.

The dynamics of the BLR in NGC 5548 are found to be mostly inflow. The fraction of point particles with elliptical orbits is $\sim 10-40\%$ ($f_{\rm ellip} = 0.23^{+0.15}_{-0.15}$), with the rest of the point particles favoring inflowing orbits ($f_{\rm flow} = 0.25^{+0.21}_{-0.16}$, probability of inflow/outflow is 94%/6%). Like in the case of Arp 151, the inferred inflowing orbits are mostly bound, with the inflow velocity distribution rotated towards the elliptical orbit distribution by $\theta_e = 21.3^{+21.4}_{-14.7}$ degrees in the radial and tangential velocities plane. There is also minimal contribution from additional macroturbulent velocities ($\sigma_{\rm turb} = 0.016^{+0.044}_{-0.013}$).

We measure the black hole mass in NGC 5548 to be $\log_{10}(M_{\rm BH}/M_{\odot}) = 7.51^{+0.23}_{-0.14}$. Similar to Arp 151 and Mrk 1310, there are strong correlations between the black hole mass, inclination angle, and opening angle that contribute to the uncertainty in black hole mass, as shown in Figure 5.10. By comparing our measurement of the black hole mass to the virial products calculated from cross-correlation time lags from Bentz et al. (2009b) and line widths from Park et al. (2012b), we measure the f factors for NGC 5548 to be $\log_{10}(f_{\sigma}) = 0.42^{+0.23}_{-0.14}$ and $\log_{10}(f_{\rm FWHM}) = -0.58^{+0.23}_{-0.14}$ (see Section 5.3.1).

The velocity-resolved transfer functions randomly chosen from the posterior show a variety of structures consistent with inflow, as shown in Figure 5.11. However, the mean lags for the velocity-resolved transfer functions and the velocity-integrated transfer functions are not completely consistent. Despite this, the velocity-resolved lag measurements by Bentz et al. (2009b) are consistent to within the uncertainties with our mean lag estimates, suggesting that we are able to constrain the general shape of the transfer function if not the detailed structure.

NGC 6814

While the model is able to capture the detailed line profile shape for NGC 6814, it has more difficulty matching the overall variability of the Hβ emission, as illustrated in Figure 5.12. The integrated Hβ light curves show some discrepancy, especially at early times, and the second bright peak in the spectra is not as strong in the model.

For this object, the BLR as traced by Hβ emission is constrained to be a wide thick disk, inclined by $\theta_i = 49.4^{+20.4}_{-22.2}$ degrees with respect to the line of sight, where inclination angles approaching 90 degrees are not ruled out. The radial distribution of Hβ emission

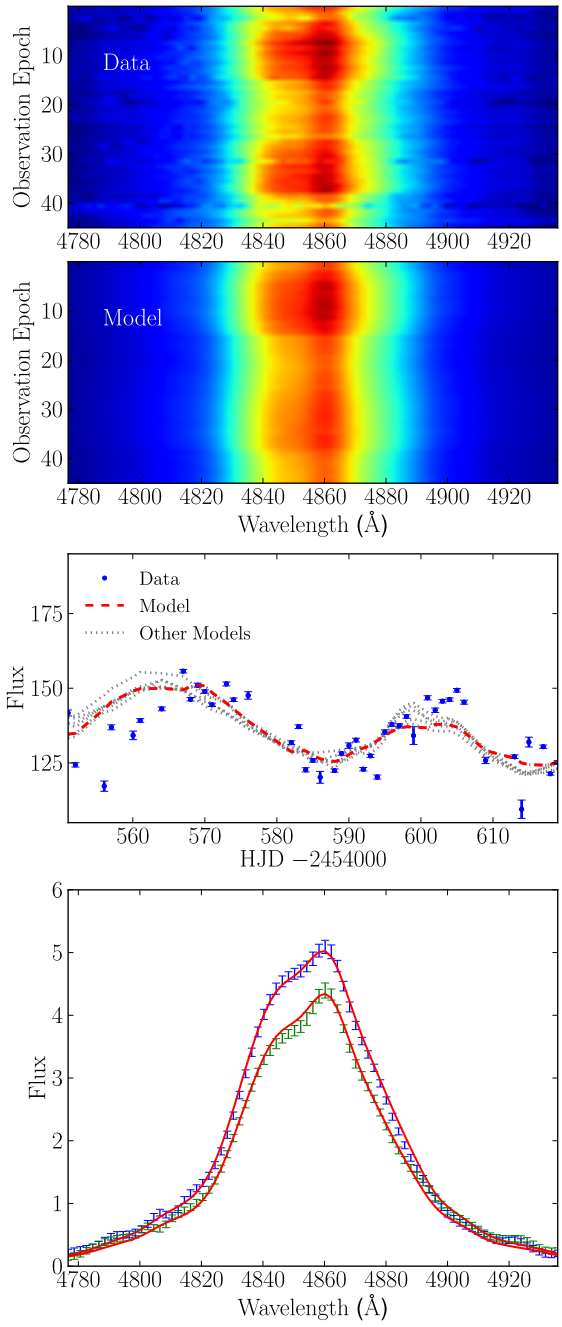

Figure 5.12: Same as Figure 5.3, but for NGC 6814.

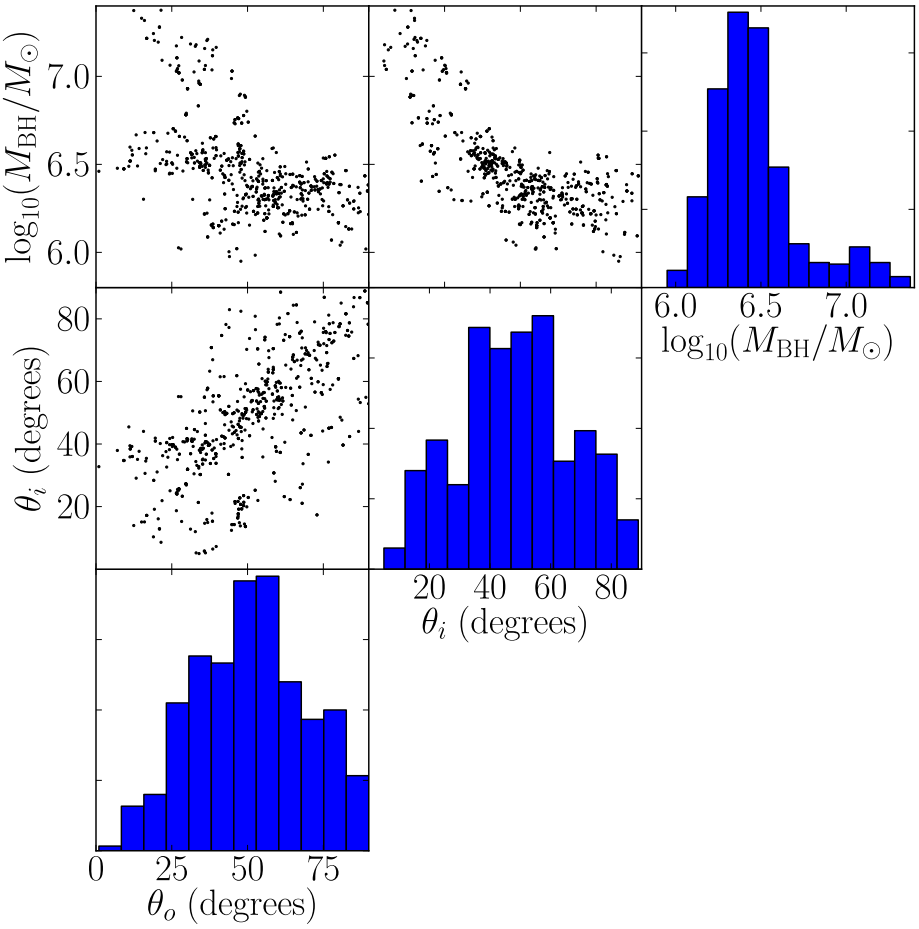

Figure 5.13: Same as Figure 5.4, but for NGC 6814.

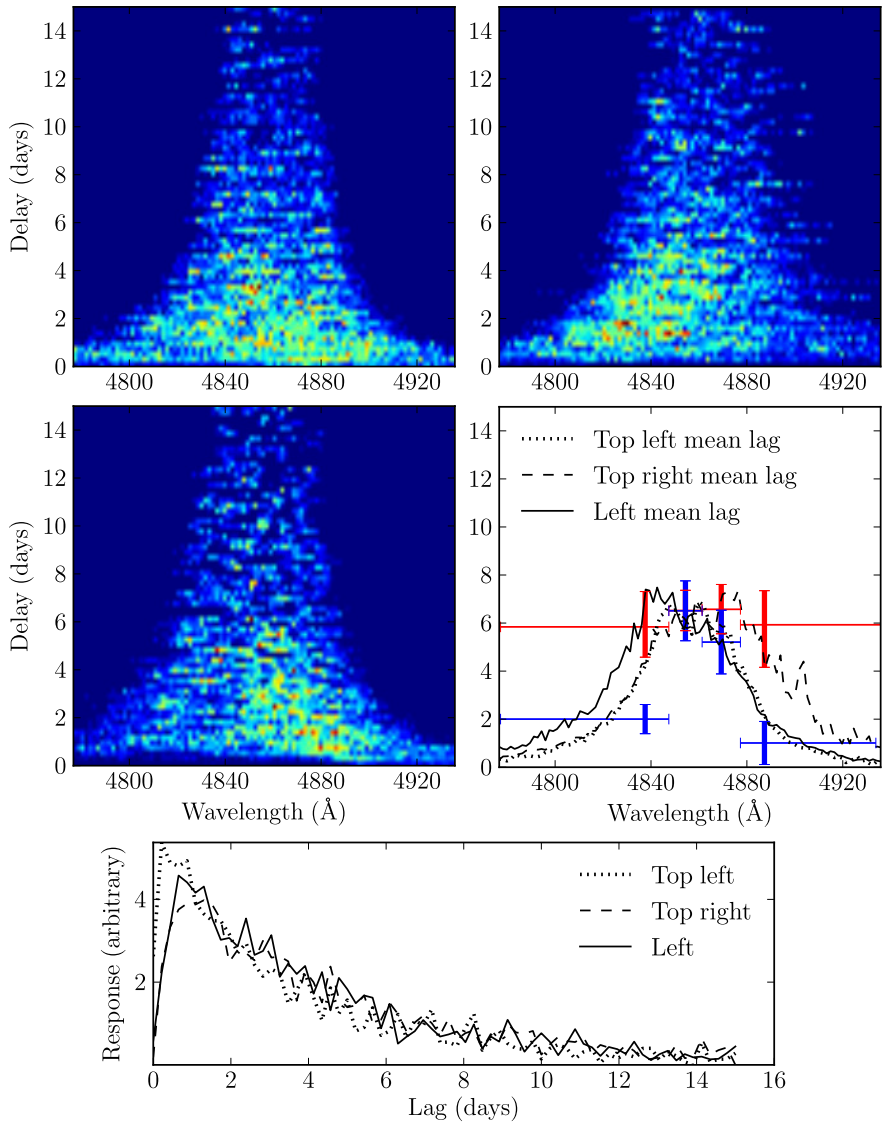

Figure 5.14: Same as Figure 5.5, but for NGC 6814.

is close to exponential ($\beta = 1.07^{+0.08}_{-0.09}$), with a mean radius of $r_{\rm mean} = 3.76^{+1.15}_{-0.77}$ light days, a minimum radius from the central ionizing source of $r_{\rm min} = 0.15^{+0.19}_{-0.11}$ light days, and a dispersion or width of the BLR of $\sigma_r = 3.75^{+1.05}_{-0.69}$ light days. The mean radius is close to the mean time lag of $\tau_{\rm mean} = 4.43^{+0.72}_{-0.83}$ days, which is marginally consistent with the cross-correlation lag of $\tau_{\rm cent} = 6.46^{+0.94}_{-0.96}$ by Bentz et al. (2009b). The median lag is considerably shorter, with $\tau_{\rm median} = 2.67^{+0.60}_{-0.61}$. The opening angle of the disk is inferred to be $\theta_o = 50.2^{+22.0}_{-18.6}$ degrees, and a spherical geometry is not ruled out. While there is no preference for concentrated Hβ emission from the edges of the disk ($\gamma = 2.91^{+1.37}_{-1.31}$), there is a slight preference for the disk midplane to be transparent ($\xi = 0.71^{+0.22}_{-0.33}$) and a strong preference for concentration of Hβ emission from the far side of the BLR ($\kappa = -0.44^{+0.10}_{-0.05}$), although more emission from the near side is not completely ruled out. The BLR geometry for NGC 6814 from one posterior sample is illustrated in Figure 5.1.

The dynamics of the BLR for NGC 6814 are inferred to be a combination of elliptical and inflowing orbits. The fraction of elliptical orbits ranges between $0 - 70\%$ ($f_{\rm ellip} = 0.32^{+0.17}_{-0.22}$), with the remainder of the orbits mostly inflowing ($f_{\rm flow} = 0.29^{+0.25}_{-0.19}$, probability for inflow/outflow is 83%/17%). For the inflowing/outflowing orbits where the fraction of elliptical orbits is small, the distribution of inflowing/outflowing velocities is rotated by ~ 60 degrees towards the elliptical orbit distribution in the radial and tangential velocity plane ($\theta_e \sim 60$). This means that in the majority of inferred model solutions with low fractions of elliptical orbits, the inflowing orbits are bound and more similar to circular orbits in terms of tangential versus radial velocity component magnitudes. For the full set of posterior model solutions, $\theta_e = 47.0^{+16.7}_{-26.5}$. Finally, there is minimal contribution from additional macroturbulent velocities ($\sigma_{\rm turb} = 0.013^{+0.036}_{-0.011}$).

We measure the black hole mass in NGC 6814 to be $\log_{10}(M_{\rm BH}/M_{\odot}) = 6.42^{+0.24}_{-0.18}$. The correlations of inclination angle and opening angle with black hole mass are not as tight for this object, adding less uncertainty to the inference of black hole mass, as shown in Figure 5.13. By comparing our measurement of the black hole mass to the virial products calculated from cross-correlation time lags from Bentz et al. (2009b) and line widths from Park et al. (2012b), we measure the f factors for NGC 6814 to be $\log_{10}(f_{\sigma}) = -0.14^{+0.24}_{-0.18}$ and $\log_{10}(f_{\rm FWHM}) = -0.68^{+0.24}_{-0.18}$ (see Section 5.3.1).

The velocity-resolved transfer functions drawn randomly from the posterior show similar overall structure, as shown in Figure 5.14, although an excess of response in the blue wing, red wing, or center of the line changes between samples. The line wings also generally have shorter lags than suggested by the velocity-resolved lag measurements by Bentz et al. (2009b). As for Arp 151, this discrepancy is due to the method of measuring the time lag. Again, we confirm this by creating velocity-resolved light curves using the inferred models of the BLR for NGC 6814 and comparing the CCF time lag measured from these model light curves to the CCF time lags from Bentz et al. (2009b). In this case, the comparison is not conclusive. Owing to the low signal-to-noise ratio of the data in the wings of the line, the cross-correlation results are very uncertain, and depend significantly upon the details of the CCF calculation, such as the interval over which the CCF is calculated. Despite this, the velocity-integrated transfer functions are consistent, suggesting that the general shape of the velocity resolved transfer function is well constrained.

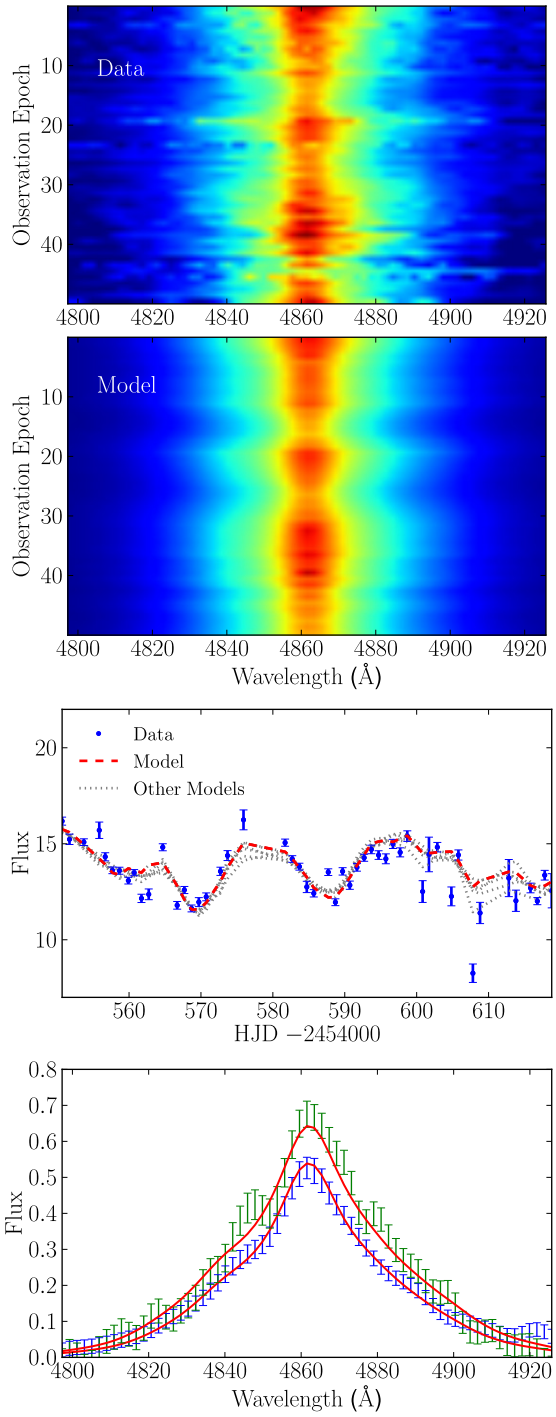

Figure 5.15: Same as Figure 5.3, but for SBS 1116+583A.

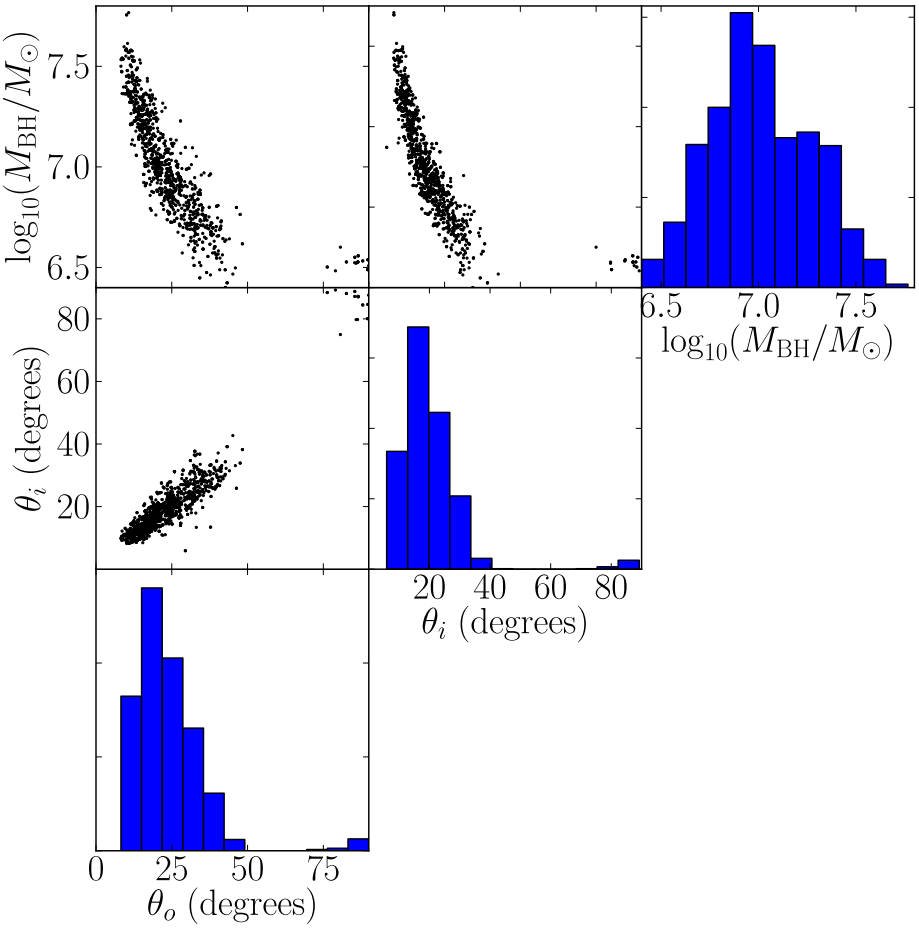

Figure 5.16: Same as Figure 5.4, but for SBS 1116+583A.

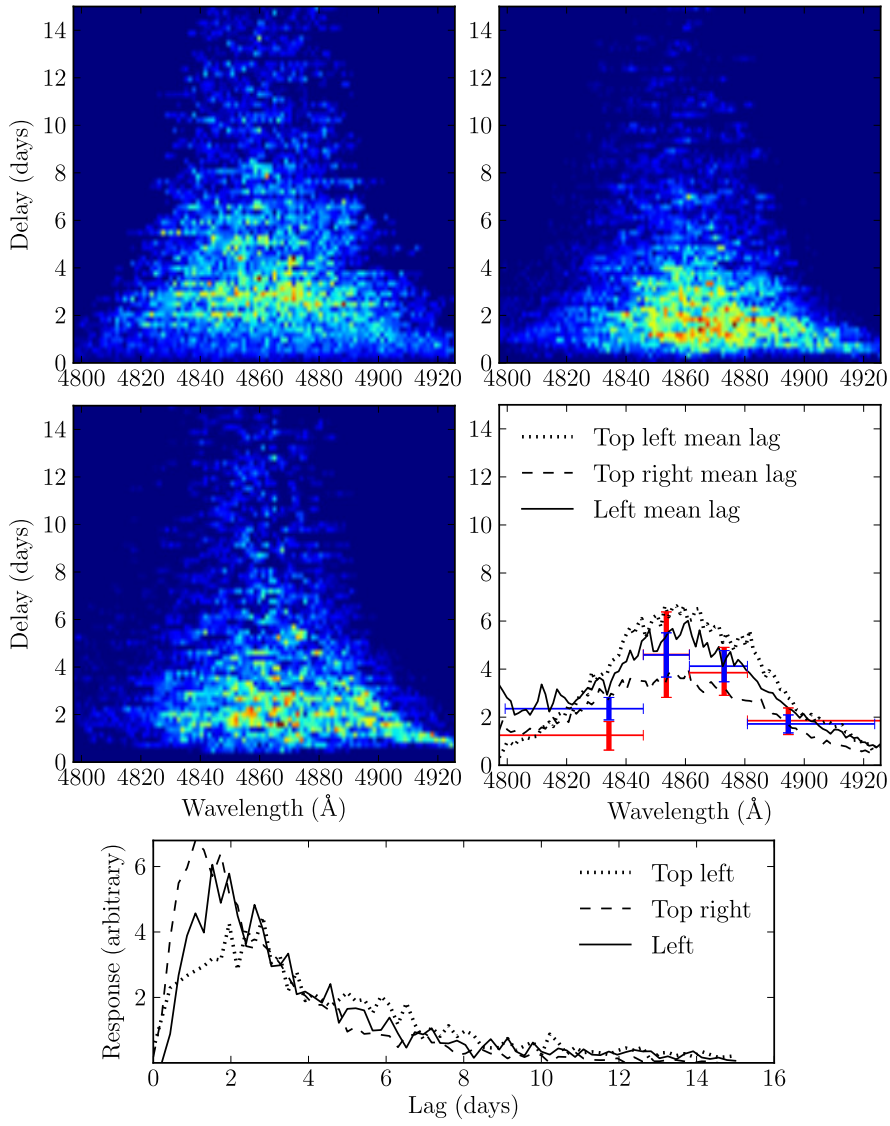

Figure 5.17: Same as Figure 5.5, but for SBS 1116+583A.

SBS 1116+583A

The model fits to SBS 1116+583A capture the overall variability of the data and successfully match the Hβ line profile shape, as shown in Figure 5.15. We infer the geometry for the BLR in this object to be a wide, thick disk inclined by $\theta_i = 18.2^{+8.4}_{-5.9}$ degrees with respect to the line of sight, although inclination angles approaching 90 degrees are not ruled out. The radial distribution of Hβ emission is constrained to be close to exponential ($\beta = 1.00^{+0.27}_{-0.21}$). The mean radius is $r_{\rm mean} = 4.07^{+0.79}_{-0.65}$ light days, the minimum radius from the central ionizing source is $r_{\rm min} = 0.93^{+0.50}_{-0.49}$ light days, and the radial dispersion or width of the BLR is $\sigma_r = 3.14^{+0.81}_{-0.66}$ light days. The mean radius agrees well with the mean lag of $\tau_{\rm mean} = 3.78^{+0.57}_{-0.52}$ days, which is marginally consistent to within the uncertainties with the cross-correlation lag of $\tau_{\rm cent} = 2.31^{+0.62}_{-0.49}$ days (Bentz et al. 2009b). In this case the cross-correlation lag is closer to the median time lag of $\tau_{\rm median} = 2.71^{+0.40}_{-0.37}$ days. The opening angle of the disk is inferred to be $\theta_o = 21.7^{+11.0}_{-7.5}$ degrees, and opening angles approaching 90 degrees, corresponding to spherical geometries, are not ruled out. The other parameters of the BLR geometry model are unconstrained, including emission from the front or back side of the BLR ($\kappa = -0.03^{+0.31}_{-0.34}$), preferential emission from the faces of the disk ($\gamma = 3.19^{+1.21}_{-1.37}$), and the transparency of the disk mid-plane ($\xi = 0.61^{+0.28}_{-0.37}$).

The dynamics of the BLR are inferred to be dominated by elliptical orbits. The elliptical orbit fraction is $f_{\rm ellip} = 0.66^{+0.21}_{-0.27}$. The remaining orbits are mostly inflowing ($f_{\rm flow} = 0.31^{+0.31}_{-0.22}$, probability of inflow/outflow is 79%/21%). When the elliptical orbit fraction drops below $\sim 50\%$ then the majority of inflow or outflow solutions have $\theta_e > 50$

degrees, so the inflow or outflow velocity distributions are rotated in the radial and tangential velocity plane towards the elliptical orbit distribution. This is compared to $\theta_e = 49.7^{+28.8}_{-32.1}$ degrees for the full posterior. This means that even posterior samples with a majority of point particle velocities drawn from the inflow or outflow velocity distributions have mainly elliptical-like orbits. Finally, the dynamics in SBS 1116+583A is inferred to have minimal contribution from macroturbulent velocities with $\sigma_{\rm turb} = 0.011^{+0.033}_{-0.009}$ in units of the circular velocity.

We measure the black hole mass in SBS 1116+583A to be $\log_{10}(M_{\rm BH}/M_\odot) = 6.99^{+0.32}_{-0.25}$. There is a strong correlation between black hole mass and inclination angle and opening angle, as shown in Figure 5.16. Comparing our measurement of the black hole mass to the virial products calculated from cross-correlation time lags from Bentz et al. (2009b) and line widths from Park et al. (2012b), we measure the f factors for SBS 1116+583A to be $\log_{10}(f_\sigma) = 0.96^{+0.32}_{-0.25}$ and $\log_{10}(f_{\rm FWHM}) = 0.34^{+0.32}_{-0.25}$ (see Section 5.3.1).

Three velocity-resolved transfer functions drawn randomly from the posterior and shown in Figure 5.17 show similar detailed structure. However, the strength of the prompt emission in the red wing varies between the velocity-resolved transfer functions, most prominent in the middle left panel of Figure 5.17 and least prominent in the top left panel. This is due to the variation in $f_{\rm ellip}$ and a preference for the remaining orbits to be inflowing. The velocity-integrated transfer functions also show consistent results, although the peakiness of the transfer function at lags of ~ 1 day varies.

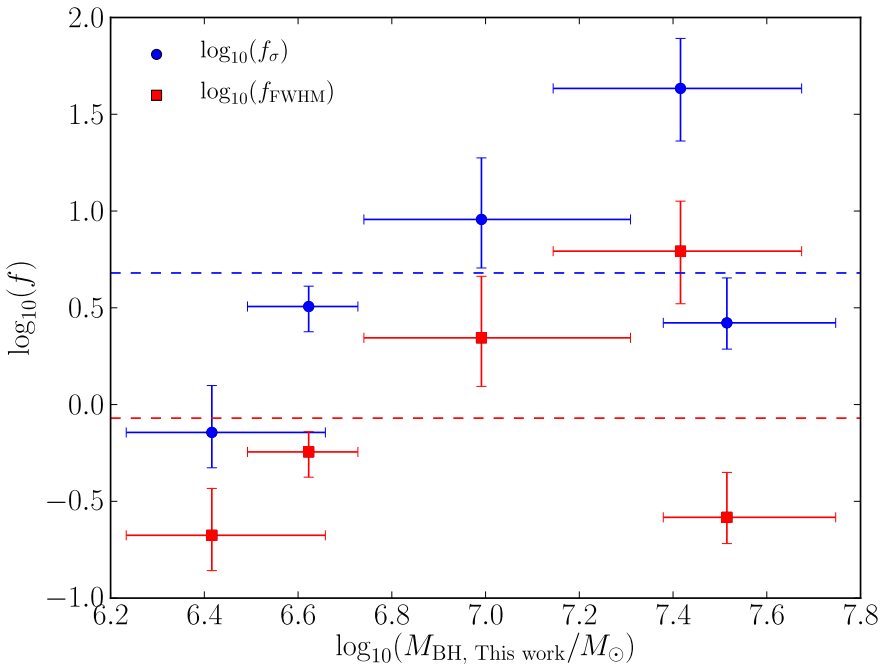

Figure 5.18: Individual f factors versus black hole mass as inferred by direct modeling. The blue circles show the values of $\log_{10}(f_{\sigma})$, while the red squares show the values of $\log_{10}(f_{\mathrm{FWHM}})$. The values of $\langle \log_{10}(f_{\sigma}) \rangle$ and $\langle \log_{10}(f_{\mathrm{FWHM}}) \rangle$ for the sample are shown by the top blue and bottom red dashed lines, respectively.

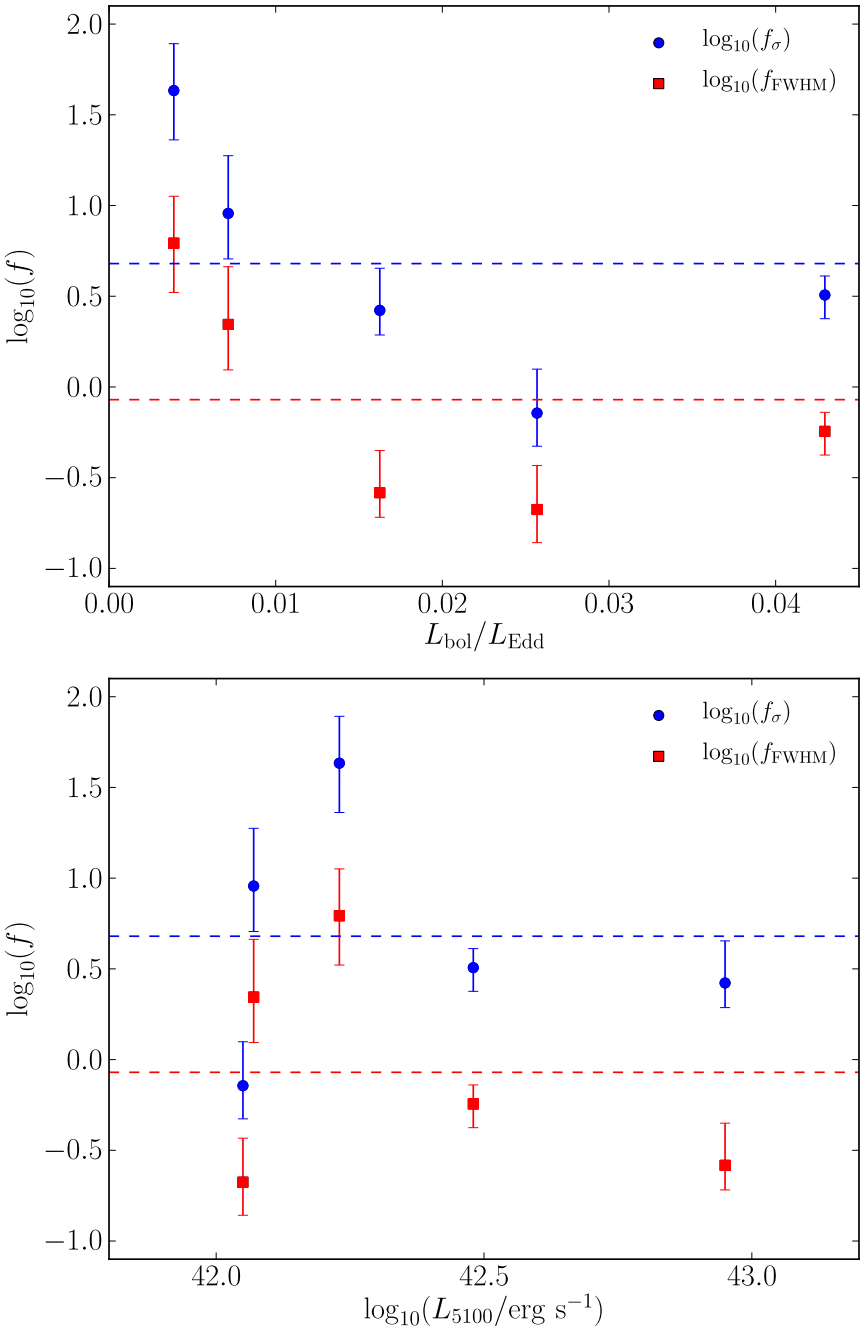

Figure 5.19: Individual f factors versus Eddington ratio (top panel) and AGN continuum luminosity, L_{5100} (bottom panel). The AGN luminosities at 5100Å are corrected for host galaxy contamination as described by Bentz et al. (2013) and the bolometric luminosities are calculated using a bolometric correction factor of nine. The blue circles show the values of $\log_{10}(f_\sigma)$, while the red squares show the values of $\log_{10}(f_{\rm FWHM})$. The values of $\langle\log_{10}(f_\sigma)\rangle$ and $\langle\log_{10}(f_{\rm FWHM})\rangle$ for the sample are shown by the top blue and bottom red dashed lines, respectively.

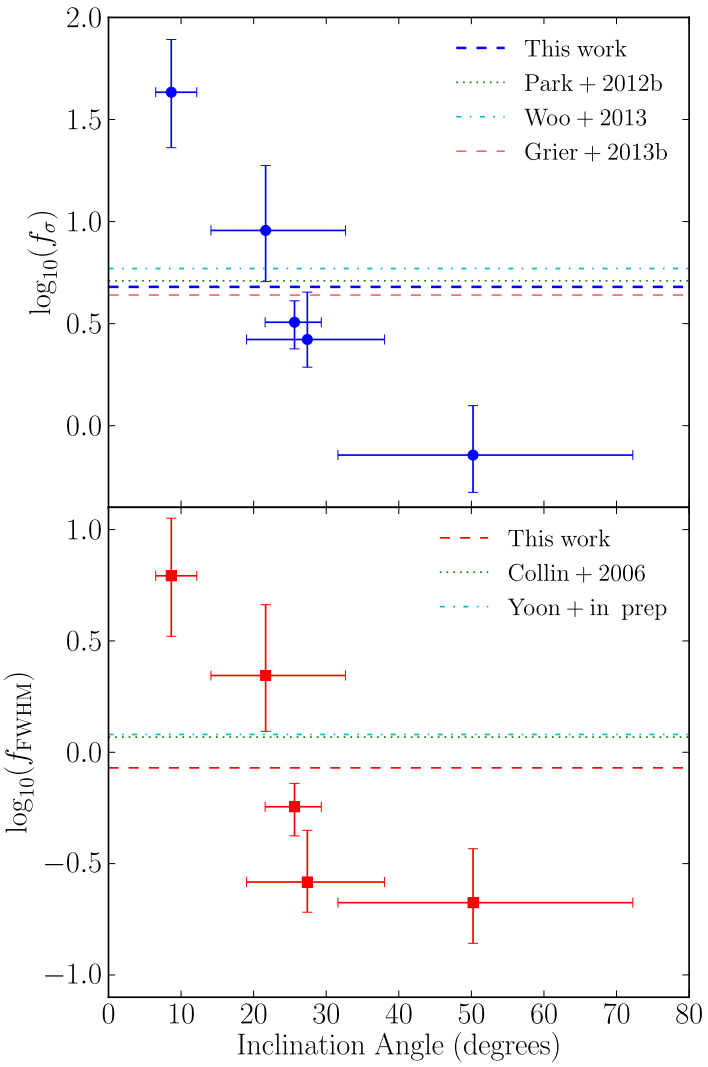

Figure 5.20: Individual f factors versus inclination angle as inferred by direct modeling. The values of $\langle \log_{10}(f_\sigma) \rangle$ and $\langle \log_{10}(f_{\rm FWHM}) \rangle$ for the sample are shown by the blue dashed line in the top panel and the red dashed line in the bottom panel, respectively. Also shown as horizontal dotted, dot-dashed, and dashed lines are the mean f values by Park et al. (2012b), Woo et al. (2013), and Grier et al. (2013a) in the top panel, and values by Collin et al. (2006) and Yoon et al. (in preparation) in the bottom panel.

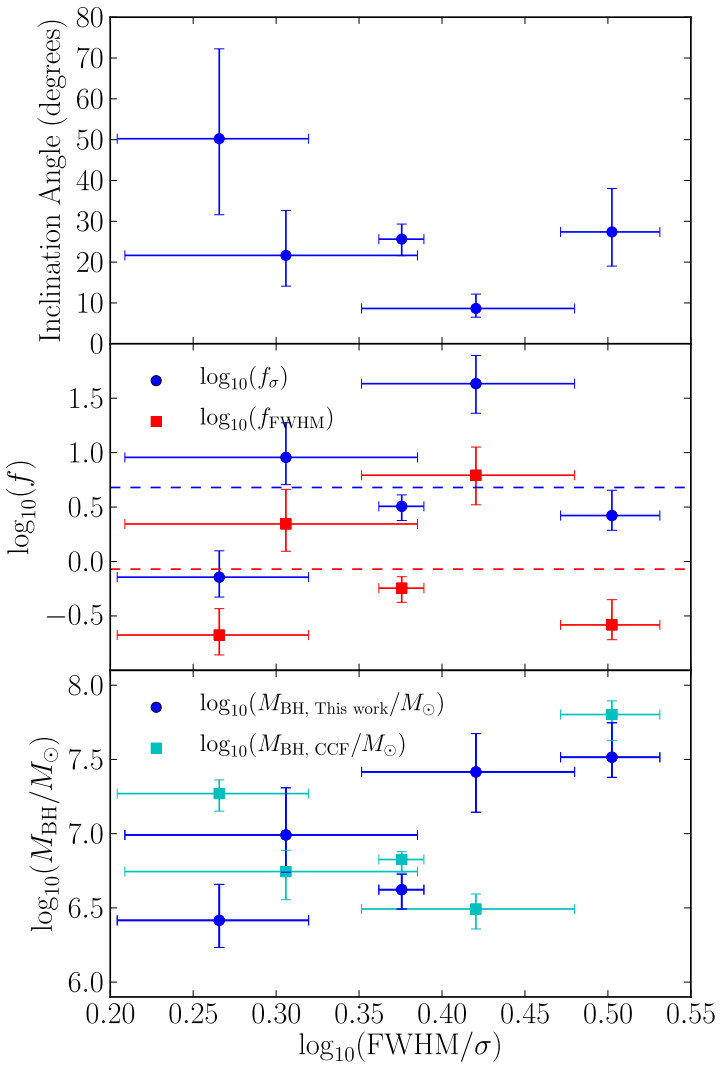

Figure 5.21: Inclination angle, f, and black hole mass as a function of the ratio of the FWHM to the line dispersion σ of the Hβ line. Line width measurements are from Park et al. (2012b). For a Gaussian distribution, $\log_{10}({\rm FWHM}/\sigma) = 0.37$. In the middle panel, the values of $\langle\log_{10}(f_\sigma)\rangle$ and $\langle\log_{10}(f_{\rm FWHM})\rangle$ for the sample are shown by the top blue and bottom red dashed lines, respectively. In the bottom panel the black hole masses from cross-correlation function analysis and assuming $\log_{10}\langle f_\sigma\rangle = 0.71$ are plotted as light blue squares for comparison.

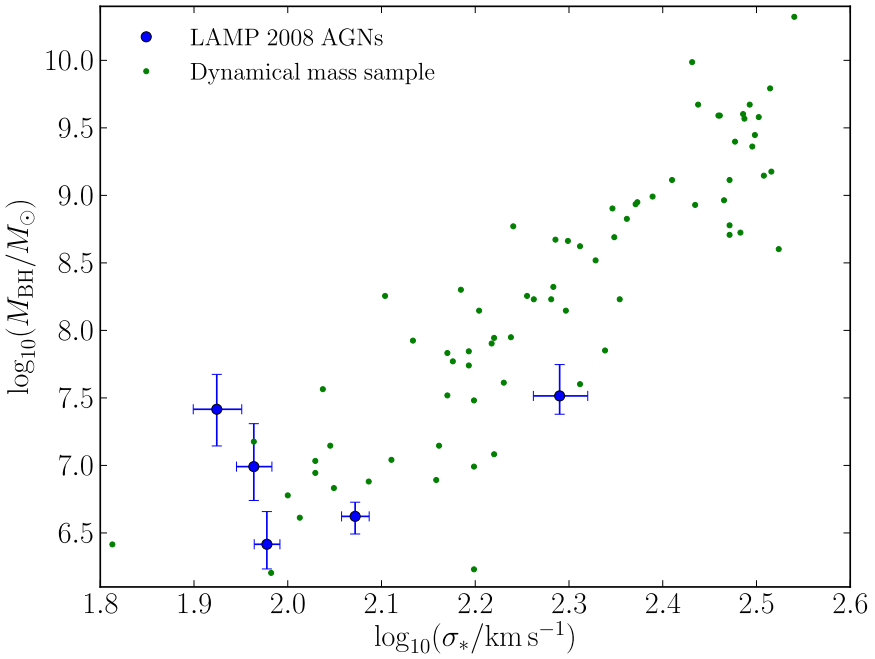

Figure 5.22: Black hole masses from our direct modeling approach and their host-galaxy stellar velocity dispersions, compared to the $M_{\rm BH} - \sigma_*$ relationship for black holes with masses from spatially-resolved stellar and gas dynamical modeling (as compiled by Woo et al. 2013). Measurements of the host-galaxy velocity dispersion for our sample of five LAMP 2008 objects are by Woo et al. (2010). Our sample is shown by the large blue circles with error bars. The dynamical mass sample is shown by the small green points.

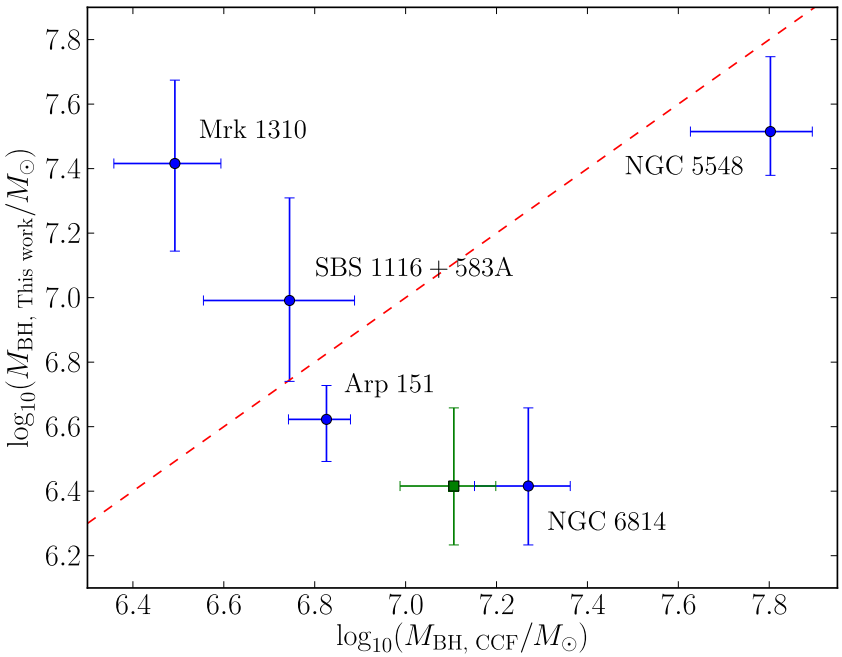

Figure 5.23: Comparison of the black hole mass estimates from our direct modeling approach on the y-axis versus the values measured using cross-correlation function analysis. The blue circles denote the sample using cross-correlation masses assuming $\log_{10}\langle f_\sigma \rangle = 0.71$, where the points corresponding to individual AGNs have been labeled. The single green square is for NGC 6814 for the case where the cross-correlation mass has been calculated using the time lag from our dynamical modeling instead of the time lag from cross-correlation. The red dashed line shows a slope of unity through the origin.

5.3.2 Overview of modeling results

We will now give an overview of the similarities between the inferred BLR model parameters for the five objects in our sample. To begin with, the Hβ BLR geometry is consistent with a thick disk with preferential emission from the far side. While the minimum radius of the BLR from the central ionizing source and the dispersion or width of the BLR vary within our sample, the radial distribution shape is generally inferred to be exponential or between Gaussian and exponential.

For the dynamics, we generally infer either elliptical orbits, inflowing orbits, or a combination of the two. Both Arp 151 and NGC 5548 show clear signatures of inflow, while SBS 1116+583A shows clear signatures of elliptical orbits and NGC 6814 shows evidence for both inflow and elliptical orbits. In addition, both Arp 151 and NGC 5548 prefer bound inflowing orbits, a solution that is closer to the elliptical orbit solution. The absence of strong outflow dynamics in our sample is reassuring, since reverberation mapping relies on BLR gas dynamics being dominated by the gravitational potential of the black hole, although this is unsurprising given the low Eddington ratios of the objects in our sample.

We can also examine whether there are common degeneracies between the model parameters. The correlations between black hole mass, inclination angle, and opening angle are typically quite pronounced in our sample (see Figures 5.4, 5.7, 5.10, 5.13, and 5.16), and often the correlation between black hole mass and inclination angle is the strongest. This degeneracy is very important for BLRs viewed close to face-on, where the uncertainty in black hole mass becomes larger as the inclination angle approaches

zero. Smaller opening angles accentuate the degeneracy, leading to strong correlations as for Mrk 1310 (see Figure 5.7). An interesting consequence of these degeneracies is what they predict for correlations of model parameters with individual values of the f factor.

As shown in Figure 5.18, there is no strong correlation between the f factor and black hole mass, as one might expect if the BLR geometry and dynamics are somehow correlated with the size of the black hole. There is also no strong correlation between the f factor and the Eddington ratio, $L_{\rm bol}/L_{\rm Edd}$, or the AGN continuum luminosity at 5100Å, L_{5100}, as shown in Figure 5.19. The AGN luminosities are corrected for host galaxy contamination by Bentz et al. (2013) and the Eddington ratios are calculated assuming a bolometric correction factor for $L(5100\text{Å})$ of nine. A correlation between f and the Eddington ratio might be expected if the BLR geometry or dynamics changed substantially with accretion rate, for example with contributions to the dynamics from radiation pressure. Since both f and the Eddington ratio are calculated using the values of $M_{\rm BH}$ inferred from dynamical modeling, the errors are correlated. For this reason we also plot f versus L_{5100}, as shown in the bottom panel of Figure 5.19, which does not have correlated errors, although it is not as closely related to accretion rate as the Eddington ratio since it has not been normalized by $M_{\rm BH}$. However, there does appear to be a correlation between the f factor and inclination angle, as illustrated in Figure 5.20. Such a correlation was predicted by Goad et al. (2012) for a general class of BLR models similar to the ones used in our direct modeling analysis. Since the errors in black hole mass and f are the same, and since black hole mass correlates so strongly with inclination angle, one might expect to see at least a small trend between the f factor and inclination angle based only on correlated errors. Direct modeling on a larger sample of AGNs will

allow us to quantify the contribution of correlated errors to the strength of the correlation between inclination angle and f.

On a related note, it has been suggested that the ratio of the FWHM to the line dispersion of broad emission lines is related to the inclination angle of the BLR to our line of sight (Collin et al. 2006; Goad et al. 2012). We use the FWHM and line dispersion measurements for the objects in our sample from Park et al. (2012b) to investigate the possibility of such trends, as shown in Figure 5.21. We find no strong correlation between $\log_{10}(\mathrm{FWHM}/\sigma)$ and the inclination angle or the f factors for individual AGNs, but we do find a tentative correlation between $\log_{10}(\mathrm{FWHM}/\sigma)$ and black hole mass. The trend of $\log_{10}(\mathrm{FWHM}/\sigma)$ with black hole mass is not seen for the virial product. A larger sample of AGNs with direct modeling analysis could clarify the strength of these correlations.

There are few independently measured quantities to compare with our direct modeling results. One of these is measurements of the time lag from cross-correlation function analysis, where we find good agreement within the uncertainties. Recently, Li et al. (2013) used our direct modeling formalism to develop an independent code to model the geometry of the BLR. Their geometry model includes a Gamma distribution for the radial profile of gas, as well as an opening angle and inclination angle. In addition, their model includes non-linear response of the broad emission lines to changes in the continuum light curve. They measure the mean radius of the BLR for our sample of five AGNs using their geometry modeling code and obtain results that are mostly consistent with the results presented here. The one object for which our values of mean radius are inconsistent is NGC 6814, for which we measure a smaller value than both the mean lag by Bentz et al. (2009b) of $\tau_{\mathrm{cent}} = 6.46^{+0.94}_{-0.96}$ days and the mean radius by Li et al. (2013) of

$r_{\rm mean} = 6.9 \pm 0.7$ light days. The inconsistency between direct modeling results for NGC 6814 for the geometry model of Li et al. (2013) and the dynamical model implemented here could be caused by using the integrated line profiles versus the full spectral dataset, since for the full spectral dataset the model must fit not only the mean time lag but also the response as a function of velocity, placing more stringent constraints on the value of the mean radius. There are also a number of differences between the geometry model used here and the one used by Li et al. (2013), the most important being that we do not include non-linear response of the emission line flux, while Li et al. (2013) do not include asymmetry parameters such as κ, γ, or ξ in their model.

We can also compare our independent measurements of the black hole mass to those of quiescent and active galaxies with dynamical mass estimates. Using host galaxy velocity dispersion measurements by Woo et al. (2010), we overlay our five AGNs onto the dynamical mass sample from Woo et al. (2013) on the $M_{\rm BH} - \sigma_*$ relation, as shown in Figure 5.22. The five objects in our sample are consistent with the distribution of masses and stellar velocity dispersions in the dynamical sample, confirming that Seyfert 1 galaxies appear to lie on the same $M_{\rm BH} - \sigma_*$ as Seyfert 2 galaxies with black hole mass measurements from maser kinematics. With a larger sample of Seyfert 1 galaxies with direct modeling, we can test whether the agreement holds across the entire relation.

Another independently measured quantity is the mean f factor, $\langle f \rangle$, measured by aligning the $M_{\rm BH} - \sigma_*$ relations for quiescent and active galaxies. We will denote mean f factors that have been calculated using the dispersion of the RMS emission line profile by $\langle f_\sigma \rangle$ and those that have been calculated using the FWHM of the mean emission line profile by $\langle f_{\rm FWHM} \rangle$. Values of $\langle f_\sigma \rangle$ from the literature include $\log_{10}\langle f_\sigma \rangle = 0.74^{+0.12}_{-0.17}$

(Onken et al. 2004), $\log_{10}\langle f_\sigma \rangle = 0.72^{+0.09}_{-0.10}$ (Woo et al. 2010), $\log_{10}\langle f_\sigma \rangle = 0.45 \pm 0.09$ (Graham et al. 2011), $\log_{10}\langle f_\sigma \rangle = 0.71 \pm 0.11$ (Park et al. 2012a), $\log_{10}\langle f_\sigma \rangle = 0.77 \pm 0.13$ (Woo et al. 2013), and $\log_{10}\langle f_\sigma \rangle = 0.64^{+0.10}_{-0.12}$ (Grier et al. 2013a). These values agree to within the uncertainties except for the value by Graham et al. (2011), for which the discrepancy is explained by sample selection and choice of the independent variable when fitting for f. We choose to adopt the Park et al. (2012a) value of $\log_{10}\langle f_\sigma \rangle = 0.71$ for calculations of the black hole mass using the virial product, since it is midway between the two most recent values of $\log_{10}\langle f_\sigma \rangle$ by Woo et al. (2013) and Grier et al. (2013a) and the difference between either measurement and the Park et al. (2012a) value is within the quoted error bars.

The f_σ factors measured individually for the five objects in our sample and listed in Table 5.3 are generally consistent to within the uncertainties with all of these values, although the low value of f_σ for NGC 6814 is only marginally consistent with the higher $\langle f_\sigma \rangle$ values (Onken et al. 2004; Woo et al. 2010; Park et al. 2012a; Woo et al. 2013; Grier et al. 2013a). Part of the discrepancy for NGC 6814 may be due to the difference in time lags between the value measured from the cross-correlation function of $\tau_{\rm cent} = 6.46^{+0.94}_{-0.96}$ days (Bentz et al. 2009b) and the value we infer from direct modeling of $\tau_{\rm mean} = 4.43^{+0.72}_{-0.83}$ days. Using our measurement of the time lag to calculate the virial mass increases the value of f_σ by 0.16 dex to $\log_{10}(f_\sigma) = 0.02^{+0.24}_{-0.18}$ for NGC 6814. To better illustrate this issue, a comparison of our independent measurements of black hole mass to those measured using cross-correlation function analysis and assuming $\log_{10}\langle f_\sigma \rangle = 0.71$ (Park et al. 2012a) is shown in Figure 5.23. NGC 6814 has one of the most discrepant measurements of the black hole mass, and the discrepancy is reduced when the cross-correlation

mass is calculated using the smaller time lag we infer from direct modeling. However, since the posterior PDF for the black hole mass in NGC 6814 extends up to values of $\log_{10}(M_{\rm BH}/M_{\odot}) \sim 7.3$, this means the posterior PDF for f_{σ} also extends up to values consistent with the higher $\langle f_{\sigma} \rangle$ values. While the high posterior median value of f_{σ} for Mrk 1310 is also only marginally consistent with the higher $\langle f_{\sigma} \rangle$ values, the posterior PDF for black hole mass for Mrk 1310 extends down to values below $\log_{10}(M_{\rm BH}/M_{\odot}) \sim 6.5$ and hence the posterior PDF for f_{σ} also extends down to values consistent with the higher $\langle f_{\sigma} \rangle$ values.

There are fewer measurements of $f_{\rm FWHM}$ in the literature. Collin et al. (2006) find $\log_{10}\langle f_{\rm FWHM} \rangle = 0.07^{+0.15}_{-0.24}$, in good agreement with the more recently calculated value of $\log_{10}\langle f_{\rm FWHM} \rangle = 0.08 \pm 0.12$ from Yoon et al. (in preparation). While three of the AGNs in our sample have values of $f_{\rm FWHM}$ consistent with the mean value of Yoon et al., Mrk 1310 and NGC 6814 have values that are only marginally consistent.

5.3.3 The mean f factor for LAMP 2008

With five independent black hole mass measurements we can now calculate the mean f factors for our AGN sample, called $\langle f_{\sigma} \rangle$ and $\langle f_{\rm FWHM} \rangle$. We use the full posterior distributions of f for each AGN to measure the mean and the dispersion of the distribution of f factors for the whole sample, as described in Appendix 5.6. We measure a value for $\langle \log_{10}(f_{\sigma}) \rangle$ of 0.68 ± 0.40 and a dispersion for $\log_{10}(f_{\sigma})$ of 0.75 ± 0.40, while we measure a value for $\langle \log_{10} f_{\rm FWHM}) \rangle$ of -0.07 ± 0.40 and a dispersion for $\log_{10}(f_{\rm FWHM})$ of 0.77 ± 0.38. The posterior distributions for $\langle \log_{10}(f_{\sigma}) \rangle$ and $\langle \log_{10}(f_{\rm FWHM}) \rangle$ and the

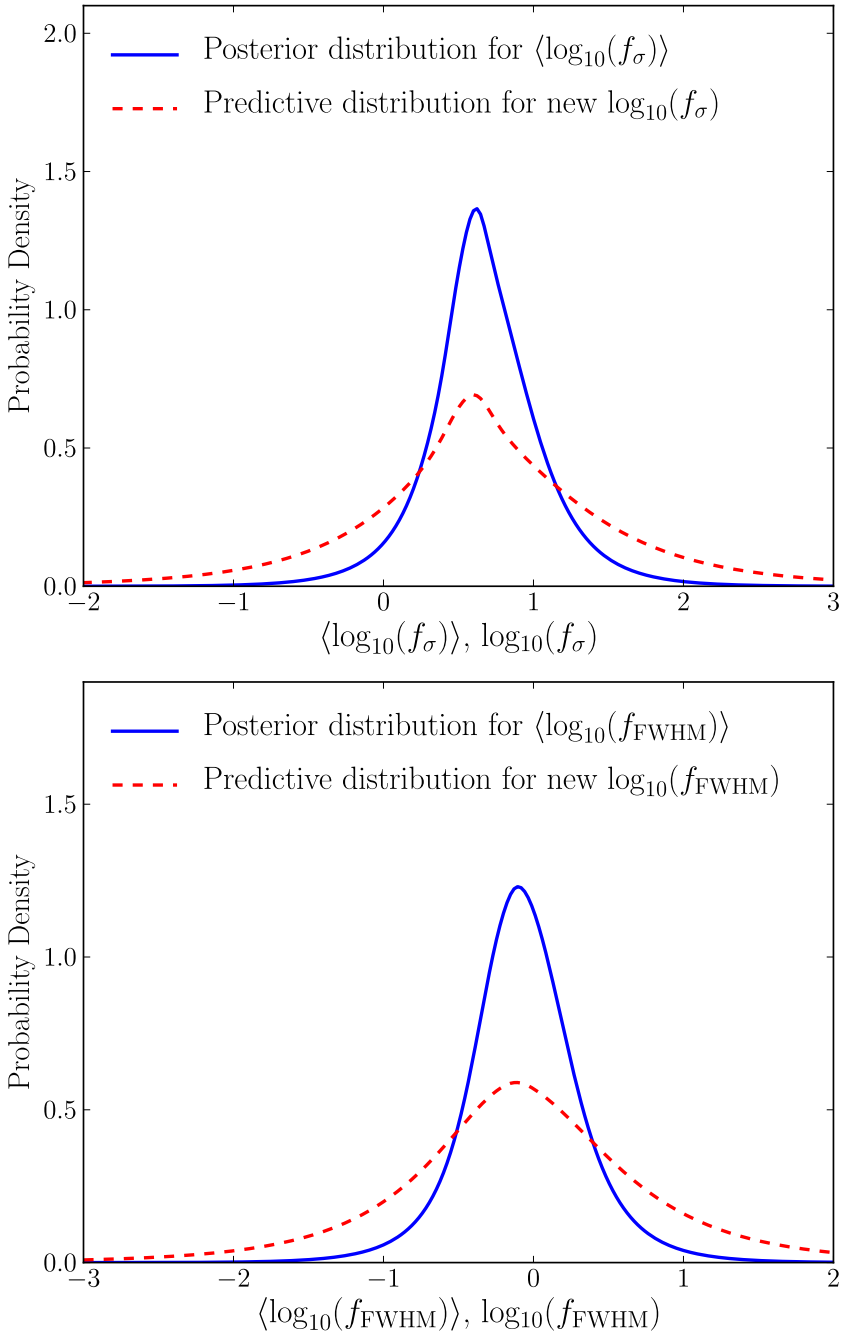

Figure 5.24: Top: The posterior distribution for $\langle \log_{10}(f_\sigma) \rangle$, the mean of the f_σ factor distribution for our sample of five AGNs, is shown by the solid blue line. The predictive distribution for new measurements of $\log_{10}(f_\sigma)$ is shown by the dashed red line. Bottom: The posterior distribution for $\langle \log_{10}(f_{\rm FWHM}) \rangle$, the mean of the $f_{\rm FWHM}$ factor distribution for our sample of five AGNs, is shown by the solid blue line. The predictive distribution for new measurements of $\log_{10}(f_{\rm FWHM})$ is shown by the dashed red line.

predictive distributions for new measurements of $\log_{10}(f_\sigma)$ and $\log_{10}(f_{\rm FWHM})$ are illustrated in Figure 5.24. The predictive distribution is the distribution from which new measurements of f are drawn and is wider than the posterior for the mean value due to the large scatter in individual f posterior distributions. Both our values of $\langle f_\sigma \rangle$ and its dispersion are consistent to within the uncertainties with the values for $\langle f_\sigma \rangle$ measured by aligning the $M_{\rm BH} - \sigma_*$ relation for active galaxies with the relation for galaxies with dynamical mass estimates (e.g. Onken et al. 2004; Woo et al. 2010; Graham et al. 2011; Park et al. 2012a; Woo et al. 2013; Grier et al. 2013a). Similarly, our values of $\langle f_{\rm FWHM} \rangle$ and its dispersion are consistent to within the uncertainties with the values measured by Collin et al. (2006) and Yoon et al. (in preparation). The mean f factors derived here are meant to illustrate the capabilities of the direct modeling approach and should not be used to normalize the black hole masses of reverberation mapped AGNs until the direct modeling sample is both larger and more representative of the overall AGN population.

5.4 Conclusions

We have applied direct modeling techniques to a sample of five AGNs from the LAMP 2008 reverberation mapping campaign in order to constrain the geometry and dynamics of the Hβ BLR. Direct modeling also allows us to measure the black hole mass independently and, by comparison with the virial product from traditional reverberation mapping analysis, to measure the virial coefficient or f factor for individual AGNs. We have also measured the mean f factor for our sample, a number that determines the absolute mass scaling for the whole reverberation mapping sample. Our main results are as follows:

Table 5.2: Inferred posterior median parameter values and central 68% credible intervals for direct modeling of five LAMP 2008 AGNs. The definitions of the geometry and dynamical model parameters can be found in Appendix 5.5.

Geometry Model Parameter	Arp 151	Mrk 1310	NGC 5548	NGC 6814	SBS 1116+583A
$r_{\rm mean}$ (light days)	$3.44^{+0.26}_{-0.24}$	$3.13^{+0.42}_{-0.40}$	$3.31^{+0.66}_{-0.61}$	$3.76^{+1.15}_{-0.77}$	$4.07^{+0.79}_{-0.65}$
$r_{\rm min}$ (light days)	$0.44^{+0.13}_{-0.20}$	$0.12^{+0.19}_{-0.08}$	$1.39^{+0.80}_{-1.01}$	$0.15^{+0.19}_{-0.11}$	$0.93^{+0.50}_{-0.49}$
σ_r (light days)	$3.72^{+0.45}_{-0.43}$	$2.59^{+0.42}_{-0.35}$	$1.50^{+0.73}_{-0.60}$	$3.75^{+1.05}_{-0.69}$	$3.14^{+0.81}_{-0.66}$
$\tau_{\rm mean}$ (days)	$3.07^{+0.25}_{-0.20}$	$2.96^{+0.42}_{-0.35}$	$3.22^{+0.66}_{-0.54}$	$4.43^{+0.72}_{-0.83}$	$3.78^{+0.57}_{-0.52}$
$\tau_{\rm median}$ (days)	$1.75^{+0.28}_{-0.23}$	$2.26^{+0.35}_{-0.31}$	$2.77^{+0.63}_{-0.42}$	$2.67^{+0.60}_{-0.61}$	$2.71^{+0.40}_{-0.37}$
β	$1.25^{+0.15}_{-0.16}$	$0.89^{+0.10}_{-0.10}$	$0.80^{+0.60}_{-0.31}$	$1.07^{+0.08}_{-0.09}$	$1.00^{+0.27}_{-0.21}$
θ_o (degrees)	$25.6^{+3.7}_{-4.0}$	$8.6^{+3.5}_{-2.1}$	$27.4^{+10.6}_{-8.4}$	$50.2^{+22.0}_{-18.6}$	$21.7^{+11.0}_{-7.5}$
θ_i (degrees)	$25.2^{+3.3}_{-3.4}$	$6.6^{+5.0}_{-2.5}$	$38.8^{+12.1}_{-11.4}$	$49.4^{+20.4}_{-22.2}$	$18.2^{+8.4}_{-5.9}$
κ	$-0.36^{+0.08}_{-0.08}$	$-0.04^{+0.38}_{-0.35}$	$-0.24^{+0.06}_{-0.13}$	$-0.44^{+0.10}_{-0.05}$	$-0.03^{+0.31}_{-0.34}$
γ	$4.27^{+0.54}_{-0.80}$	$2.97^{+1.38}_{-1.43}$	$2.01^{+1.78}_{-0.71}$	$2.91^{+1.37}_{-1.31}$	$3.19^{+1.21}_{-1.37}$
ξ	$0.09^{+0.08}_{-0.05}$	$0.40^{+0.38}_{-0.29}$	$0.34^{+0.11}_{-0.18}$	$0.71^{+0.22}_{-0.33}$	$0.61^{+0.28}_{-0.37}$
Dynamical Model Parameter	Arp 151	Mrk 1310	NGC 5548	NGC 6814	SBS 1116+583A
$\log_{10}(M_{\rm BH}/M_\odot)$	$6.62^{+0.10}_{-0.13}$	$7.42^{+0.26}_{-0.27}$	$7.51^{+0.23}_{-0.14}$	$6.42^{+0.24}_{-0.18}$	$6.99^{+0.32}_{-0.25}$
$f_{\rm ellip}$	$0.06^{+0.09}_{-0.05}$	$0.56^{+0.34}_{-0.39}$	$0.23^{+0.15}_{-0.15}$	$0.32^{+0.17}_{-0.22}$	$0.66^{+0.21}_{-0.27}$
$f_{\rm flow}$	$0.24^{+0.20}_{-0.17}$	$0.65^{+0.24}_{-0.38}$	$0.25^{+0.21}_{-0.16}$	$0.29^{+0.25}_{-0.19}$	$0.31^{+0.31}_{-0.22}$
θ_e (degrees)	$12.0^{+10.7}_{-8.3}$	$57.2^{+24.9}_{-41.0}$	$21.3^{+21.4}_{-14.7}$	$47.0^{+16.7}_{-26.5}$	$49.7^{+28.8}_{-32.1}$
$\sigma_{\rm turb}$	$0.008^{+0.028}_{-0.007}$	$0.004^{+0.010}_{-0.003}$	$0.016^{+0.044}_{-0.013}$	$0.013^{+0.036}_{-0.011}$	$0.011^{+0.033}_{-0.009}$

Table 5.3: Inferred posterior median parameter values and central 68% credible intervals for f factors of five LAMP 2008 AGNs. The f factor corresponding to the difference between black hole mass and the virial product measured using the dispersion of the RMS line profile is given as f_σ, while the one corresponding to a virial product measured using the FWHM of the mean line profile is given as $f_{\rm FWHM}$.

Object	$\log_{10}(f_\sigma)$	$\log_{10}(f_{\rm FWHM})$
Arp 151	$0.51^{+0.10}_{-0.13}$	$-0.24^{+0.10}_{-0.13}$
Mrk 1310	$1.63^{+0.26}_{-0.27}$	$0.79^{+0.26}_{-0.27}$
NGC 5548	$0.42^{+0.23}_{-0.14}$	$-0.58^{+0.23}_{-0.14}$
NGC 6814	$-0.14^{+0.24}_{-0.18}$	$-0.68^{+0.24}_{-0.18}$
SBS 1116+583A	$0.96^{+0.32}_{-0.25}$	$0.34^{+0.32}_{-0.25}$

1. The geometry of the BLR is consistent with a thick disk. The radial distribution of Hβ emitting gas is closer to exponential than Gaussian and is viewed closer to face-on than edge-on. For Arp 151 we find a more detailed geometry of a half-cone, where the Hβ emission is concentrated towards the outer faces of the disk and the disk mid-plane is mostly opaque, similar to the bowl BLR geometry proposed by Goad et al. (2012).

2. There is preferential Hβ emission from the far side of the BLR with respect to the observer, consistent with models where the BLR gas is self-shielding.

3. The dynamics of the BLR are consistent with inflowing motions, elliptical orbits, or a combination of both. Specifically, the dynamics of Arp 151 are inferred to be inflowing motions, in agreement with velocity-resolved cross-correlation lag measurements (Bentz et al. 2009b) and reconstruction of the transfer function using maximum entropy techniques (Bentz et al. 2010b).

4. The black hole masses for the five objects in our sample are $\log_{10}(M_{\rm BH}/M_{\odot}) = 6.62^{+0.10}_{-0.13}$ for Arp 151, $7.42^{+0.26}_{-0.27}$ for Mrk 1310, $7.51^{+0.23}_{-0.14}$ for NGC 5548, $6.42^{+0.24}_{-0.18}$ for NGC 6814, and $6.99^{+0.32}_{-0.25}$ for SBS 1116+583A.

5. Using our measurements of the black hole mass and virial products based on the dispersion of the RMS line profile, we measure the f factors for the AGNs in our sample to be $\log_{10}(f_{\sigma}) = 0.51^{+0.10}_{-0.13}$ for Arp 151, $1.63^{+0.26}_{-0.27}$ for Mrk 1310, $0.42^{+0.23}_{-0.14}$ for NGC 5548, $-0.14^{+0.24}_{-0.18}$ for NGC 6814, and $0.96^{+0.32}_{-0.25}$ for SBS 1116+583A. Using instead the virial products based on the FWHM of the mean line profile, we find

that $\log_{10}(f_{\rm FWHM}) = -0.24^{+0.10}_{-0.13}$ for Arp 151, $0.79^{+0.26}_{-0.27}$ for Mrk 1310, $-0.58^{+0.23}_{-0.14}$ for NGC 5548, $-0.68^{+0.24}_{-0.18}$ for NGC 6814, and $0.34^{+0.32}_{-0.25}$ for SBS 1116+583A.

6. The f factors for individual AGNs are correlated with inclination angle, but not with black hole mass, AGN optical luminosity, or Eddington ratio.

7. Neither the f factors nor the inclination angles for individual AGNs are strongly correlated with the ratio of the FWHM to the line dispersion in the mean Hβ spectrum, as would be expected if line shape correlated strongly with viewing angle of the BLR. However, we do find a tentative correlation between the ratio of the FWHM to the line dispersion and black hole mass.

8. By combining the posterior distributions of f for each AGN, we measure mean values of f for the sample. With virial products based on the dispersion of the RMS line profile, we measure a mean value of $\log_{10}(f_\sigma)$ of 0.68 ± 0.40 with a dispersion in $\log_{10}(f_\sigma)$ of 0.75 ± 0.40, and using virial products based on the FWHM of the mean line profile we measure a mean $\log_{10}(f_{\rm FWHM})$ value of -0.07 ± 0.40 with a dispersion in $\log_{10}(f_{\rm FWHM})$ of 0.77 ± 0.38. These values of the mean f factor are meant to illustrate the capabilities of the direct modeling approach and should not be used to calibrate black hole masses from reverberation mapping until the sample size is larger and more representative of the overall AGN population.

The modeling results presented here demonstrate the capabilities of the direct modeling approach and show that significant information about the BLR geometry and dynamics is encoded in high-quality reverberation mapping datasets. We find that the five AGNs in our sample have similar geometric and kinematic features, suggesting that the

BLR may also be similar in other Seyfert 1 galaxies with low luminosities, black hole masses of $10^{6.5-7.5} M_{\odot}$, and small Eddington ratios. By applying the direct modeling approach to a larger sample of AGNs, we can determine if and how the properties of the BLR might change with increasing luminosity, accretion rate, and black hole mass.

Our results also demonstrate the feasibility of measuring black hole masses independently of the f factor in Seyfert 1 galaxies. For the reverberation mapping datasets shown here, black hole masses can be constrained to $0.15 - 0.3$ dex uncertainty depending upon data quality and degeneracy of the black hole mass with the geometrical properties of the BLR, such as inclination angle of the observer and opening angle of the disk. In addition, the BLR kinematics inferred for our sample are consistent with bound orbits, suggesting that the Hβ-emitting BLR is not significantly affected by disk winds or outflows. This is an important consistency check for reverberation mapped black hole masses because they are measured by assuming the BLR gas orbits are dominated by the gravity of the black hole. Future versions of our BLR model will explore the issue of non-gravitational forces further and relate broad line emission to the properties of the emitting gas by incorporating the results of photoionization physics.

5.5 Appendix: Definition of model parameters

5.5.1 Geometry model parameters

We use a Gamma distribution to model the radial distribution of point particles in the BLR:

$$p(x|\alpha,\theta) \propto x^{\alpha-1} \exp\left(-\frac{x}{\theta}\right). \tag{5.2}$$

We then allow the Gamma distribution to be offset from the origin by an amount $r_{\rm min}$ plus the Schwarzschild radius, $R_s = 2GM/c^2$, and perform a change of variables between (α, θ) and (μ, β, F) such that

$$\mu = R_s + r_{\rm min} + \alpha\theta \tag{5.3}$$

$$\beta = \frac{1}{\sqrt{\alpha}} \tag{5.4}$$

$$F = \frac{r_{\rm min}}{r_{\rm min} + \alpha\theta} \tag{5.5}$$

where μ is the mean radius, β determines the shape of the Gamma distribution, and F is the fraction of μ corresponding to $r_{\rm min}$. The prior on μ is uniform in the log of the parameter between 1.02×10^{-3} light days and the time span between the first and last measurement of the continuum or line flux, while the prior on β is uniform between 0 and 2 and the prior on F is uniform between 0 and 1. The standard deviation for the radial distribution is given by $\sigma_r = \mu\beta(1-F)$. We can also calculate the numerical mean radius $r_{\rm mean}$, the numerical mean time lag $\tau_{\rm mean}$, and the numerical median time lag $\tau_{\rm median}$ for a specific realization of point particle positions. The direct modeling results in Table 5.2 include values for $r_{\rm mean}$, $r_{\rm min}$, σ_r, τ, and β. The geometry of the BLR is further defined

by θ_o, the half-opening angle of the BLR disk. Values of $\theta_o \to 0$ (90) degrees correspond to thin disk (spherical) geometries and the prior is uniform between 0 and 90 degrees. The inclination angle, θ_i, is the angle by which an observer views the BLR. Values of $\theta_i \to 0$ (90) degrees correspond to face-on (edge-on) geometries and the prior is uniform in the cosine of the inclination angle between 0 and 90 degrees. We weight the emission from each point particle by a cosine function:

$$W(\phi) = \frac{1}{2} + \kappa \cos \phi. \tag{5.6}$$

where W is the weight (between 0 and 1) given to each point particle, ϕ is the angle between the observer's line of sight to the central source and the point particle's line of sight to the central source, and κ is a parameter with uniform prior between -0.5 and 0.5. Values of $\kappa \to -0.5$ (0.5) correspond to the far (near) side of the BLR producing more line emission. We also include the option for preferential emission from the faces of the BLR disk by changing the angle θ for a point particle's displacement from a flat to thick disk, given by

$$\theta = \mathrm{acos}\left(\cos \theta_o + (1 - \cos \theta_o) \times U^{\gamma}\right) \tag{5.7}$$

where U is a random number drawn uniformly between the values of 0 and 1. Values of $\gamma \to 1$ (5) correspond to uniform concentrations of point particles in the disk (more point particles along the faces of the disk), where γ has a uniform prior between 1 and 5. Finally, we allow the midplane of the BLR to range between opaque and transparent, where ξ is the fraction of the point particles below the midplane that are not moved to the top half. For $\xi \to 1$ (0) the midplane is transparent (opaque), where ξ has a uniform prior between 0 and 1.

5.5.2 Dynamical model parameters

The dynamics of the BLR are determined by the black hole mass, $M_{\rm BH}$, which has a uniform prior in the log of the parameter between 2.78×10^4 and $1.67 \times 10^9 M_\odot$. We draw the velocities for the point particles from two distributions in the plane of radial and tangential velocities. The fraction of point particles with velocities drawn from the distribution centered around the circular orbit value is given by $f_{\rm ellip}$, which has a uniform prior between 0 and 1. The remaining point particles have velocities drawn from the distribution centered around either the radial inflowing or outflowing escape velocity values, where $0 < f_{\rm flow} < 0.5$ corresponds to the inflowing distribution and $0.5 < f_{\rm flow} < 1$ corresponds to the outflowing distribution, and where $f_{\rm flow}$ has a uniform prior between 0 and 1. The inflow/outflow-centered distributions can also be rotated by an angle θ_e towards the circular orbit-centered distribution, where θ_e has a uniform prior between 0 and 90 degrees. Finally, we include additional macroturbulent velocities given by:

$$v_{\rm turb} = \mathcal{N}(0, \sigma_{\rm turb})|v_{\rm circ}| \tag{5.8}$$

where $v_{\rm circ}$ is the circular orbit velocity and $\sigma_{\rm turb}$ is the standard deviation of the Gaussian distribution from which a random macroturbulent velocity component is drawn. $\sigma_{\rm turb}$ has a uniform prior in the log of the parameter between 0.001 and 0.1.

5.6 Appendix: Calculating the mean f factor

For each of the five AGNs in our sample, we can compute the posterior distribution for the f factor that relates the black hole mass to either the velocity dispersion or the

FWHM of the broad emission line. Here we describe the method used to constrain the distribution of f values from the modelling results (see Hogg et al. 2010; Brewer & Elliott 2014, for examples using the same approach). Consider a collection of N objects, each of which has a property θ which we infer from data D. Modelling each object yields a posterior distribution

$$p(\theta_i|D_i) \propto \pi(\theta_i)p(D_i|\theta_i) \tag{5.9}$$

where $\pi(\theta_i)$ is the prior used in the modelling, which is the same for each object. In practice, since we are using MCMC, the posterior distributions $p(\theta_i|D_i)$ are represented computationally by samples. In our particular application, $\theta \equiv \log_{10}(f)$.

Unfortunately, the use of the $\pi(\theta_i)$ prior for each object implies we do not expect the objects to be clustered around a typical θ value. If we did expect such clustering, we should have used a different prior for the $\{\theta_i\}$, such as a normal distribution:

$$p(\{\theta_i\}|\mu_\theta, \sigma_\theta) \;=\; \prod_{i=1}^{N} \frac{1}{\sigma_\theta\sqrt{2\pi}} \exp\left[-\frac{1}{2\sigma_\theta^2}\left(\theta_i - \mu_\theta\right)^2\right] \tag{5.10}$$

This is the prior, conditional on two new hyperparameters describing the typical value μ_θ that the objects are clustered around, and the scatter σ_θ. To complete the inference we also need to assign a prior to μ_θ and σ_θ, which we take to be vague. Using this model, we can summarise our uncertainty about the properties of the sample by calculating the posterior distribution for μ_θ and σ_θ. Alternatively the posterior distribution for the *actual* mean $\frac{1}{N}\sum_{i=1}^{N}\theta_i$ could be calculated, but the former approach allows for generalisation beyond the current sample.

The posterior distribution for the hyperparameters is

$$
\begin{aligned}
p(\mu_\theta, \sigma_\theta|\{D_i\}) &\propto p(\mu_\theta, \sigma_\theta) p(\{D_i\}|\mu_\theta, \sigma_\theta) && (5.11)\\
&\propto p(\mu_\theta, \sigma_\theta) \int \prod_{i=1}^{N} p(\theta_i, D_i|\mu_\theta, \sigma_\theta)\, d^N\theta_i && (5.12)\\
&\propto p(\mu_\theta, \sigma_\theta) \int \prod_{i=1}^{N} p(\theta_i|\mu_\theta, \sigma_\theta) p(D_i|\theta_i, \mu_\theta, \sigma_\theta)\, d^N\theta_i && (5.13)\\
&\propto p(\mu_\theta, \sigma_\theta) \int \prod_{i=1}^{N} p(\theta_i|\mu_\theta, \sigma_\theta) p(D_i|\theta_i)\, d^N\theta_i && (5.14)\\
&\propto p(\mu_\theta, \sigma_\theta) \int \prod_{i=1}^{N} p(\theta_i|\mu_\theta, \sigma_\theta) \frac{\pi(\theta_i)}{\pi(\theta_i)} p(D_i|\theta_i)\, d^N\theta_i && (5.15)\\
&\propto p(\mu_\theta, \sigma_\theta) \prod_{i=1}^{N} \left\langle \frac{p(\theta_i|\mu_\theta, \sigma_\theta)}{\pi(\theta_i)} \right\rangle . && (5.16)
\end{aligned}
$$

where the expectation is taken with respect to the posterior distributions we have actually sampled, and can be computed straightforwardly. Essentially, Eq 5.16 favors $(\mu_\theta, \sigma_\theta)$ values that place a lot of probability in regions that overlap with the posteriors that we found.

Chapter 6

Photometric light curves for the LAMP 2011 reverberation mapping dataset

This chapter is taken from Pancoast, A. et al. (37 co-authors), "The Lick AGN Monitoring Project 2011: Photometric Light Curves", in preparation, and is included here with minor formatting adjustments and a section on future work.

The Lick AGN Monitoring Project 2008 (LAMP; Walsh et al. 2009; Bentz et al. 2009b), a reverberation mapping campaign with spectroscopy taken at Lick Observatory and V and B-band imaging taken at a number of ground-based observatories, provided a sample with sufficient quality to develop the direct modeling approach to constrain the geometry and dynamics of the BLR (Pancoast et al. 2011, 2014a). The LAMP 2008 sample was chosen to measure black hole masses of $\sim 10^6 - 10^7\,\mathrm{M}_\odot$, filling in the lower-mass regime of the $M_{\mathrm{BH}} - \sigma_*$ relation and providing a measurement of the average value of the f factor (Woo et al. 2010), allowing for improved constraints on the BLR size-luminosity relation (Greene et al. 2010b), and providing a recalibration of single-epoch AGN black hole masses (Park et al. 2012b). For the most variable object in the sample, Arp 151, the data allowed for reverberation mapping of multiple Balmer lines (Bentz et al. 2010a), constraints on the form of the velocity-resolved transfer function

using the maximum-entropy MEMECHO software (Bentz et al. 2010b), and, along with four other LAMP 2008 targets, dynamical modeling of the BLR to obtain independent measurements of the black hole mass and f factor (Brewer et al. 2011a; Pancoast et al. 2014b).

In order to obtain additional high-quality reverberation mapping data using spectroscopy from Lick Observatory, the LAMP team undertook a second reverberation mapping campaign in the Spring of 2011, the Lick AGN Monitoring Project 2011. In addition to spectroscopy in the optical covering Hα through Hδ taken with the Kast Spectrograph on the Shane Telescope at Lick Observatory, V-band AGN continuum images were taken by six different telescopes: the West Mountain Observatory, the Faulks telescopes North and South, the Katzman Automatic Imaging Telescope, Super-LOTIS at Kitt Peak, and the Palomar 60 inch telescope. The resulting reverberation mapping dataset from the LAMP 2011 campaign provides an ideal target for detailed analysis such as spectral decomposition to isolate broad lines with lower fluxes and constraints on the geometry and dynamics of the BLR through recovery of the transfer function or dynamical modeling of the BLR. Preliminary results for LAMP 2011 focused on the most variable AGN in the sample, Mrk 50, including both a black hole mass measurement using cross-correlation (Barth et al. 2011a) and a black hole mass measurement from dynamical modeling of the BLR (Pancoast et al. 2012). Additional preliminary results for NGC 4593 and Mrk 1511 focused on reverberation of the Fe II broad line complexes close to Hβ (Barth et al. 2013). Here we analyze the V-band AGN continuum light curves for the entire LAMP 2011 sample. The Hβ light curves are analyzed in a companion paper by Barth et al. (2015).

In this chapter, we describe the analysis of V-band AGN continuum images for reverberation mapping. The resulting V-band light curves are measured using image subtraction software for the higher-quality targets and traditional aperture photometry techniques for those showing less V-band or broad emission line variability. We align the light curves for each telescope by modeling the AGN continuum variability using Gaussian processes. In Section 6.1 we describe the LAMP 2011 sample of AGNs and in Section 6.2 we list the observations from the six telescopes. In Section 6.3 we describe the data reduction and photometry, including the Gaussian process model for aligning the different telescope light curves. In Section 6.4 we present the V-band continuum light curves and in Section 6.5 we discuss future work.

6.1 Sample selection

The sample selection for this project was motivated by recent advances in measuring high quality AGN light curves and analyzing velocity-resolved reverberation mapping data (Bentz et al. 2009b; Denney et al. 2010; Pancoast et al. 2011; Brewer et al. 2011a) to obtain constraints on the geometry and dynamics of the BLR. Since velocity-resolved reverberation mapping data requires a high signal-to-noise ratio (SNR) across the broad emission line profile, this sample focused on AGN with $V \lesssim 17$ so that exposure times would not exceed 40 minutes. The LAMP 2011 sample includes 15 Seyfert 1 galaxies within $z < 0.042$, listed in Table 6.1. These objects were chosen from the Sloan Digital Sky Survey (SDSS) Data Release 7 archive (Abazajian et al. 2009) and other AGN catalogs for strong broad Hβ emission. The time lag between the continuum and Hβ line

Table 6.1: Details of the AGN sample. Coordinates are given in hours, minutes, seconds for right ascension (α) and degrees, arcminutes, and arcseconds for declination (δ). Redshifts are from the NASA Extragalactic Database (NED). Galactic extinctions (A_V) are taken from NED values from Schlafly & Finkbeiner (2011) with $R_V = 3.1$.

Object	α(J2000.0)	δ(J2000.0)	z	A_V (mag)	Alternate Name
Mrk 40	11 25 36.2	+54 22 57	0.0211	0.039	Arp 151
Mrk 50	12 23 24.1	+02 40 45	0.0234	0.044	
Mrk 141	10 19 12.5	+63 58 03	0.0417	0.028	
Mrk 279	13 53 03.4	+69 18 30	0.0305	0.044	PG 1351+695
Mrk 486	15 36 38.3	+54 33 33	0.0389	0.040	PG 1535+547
Mrk 493	15 59 09.6	+35 01 47	0.0313	0.068	
Mrk 504	17 01 07.7	+29 24 25	0.0359	0.135	PG 1659+294
Mrk 704	09 18 26.0	+16 18 19	0.0292	0.079	
Mrk 817	14 36 22.1	+58 47 39	0.0315	0.019	PG 1434+590
Mrk 841	15 04 01.2	+10 26 16	0.0364	0.082	PG 1501+106
Mrk 1392	15 05 56.5	+03 42 26	0.0361	0.125	
Mrk 1511	15 31 18.1	+07 27 28	0.0339	0.112	NGC 5940
NGC 4593	12 39 39.4	-05 20 39	0.0090	0.068	Mrk 1330
PG 1310-108	13 13 05.8	-11 07 42	0.0343	0.143	II SZ 10
Zw229-015	19 05 25.9	+42 27 40	0.0279	0.198	

flux was chosen to be < 25 light days from the radius-luminosity relation by Bentz et al. (2009a) or previous reverberation mapping studies, ensuring that the campaign cadence would be smaller than the time lag for all objects and that the longest time lag could still be well-constrained within the duration of the campaign. The full details of the LAMP 2011 sample selection are given in Barth et al. (2015).

6.2 Observations

We obtained V-band images of our sample of AGNs using six telescopes including the West Mountain Observatory (WMO), the Faulks Telescopes North and South (FTN/S), the Katzman Automatic Imaging Telescope (KAIT), Super-LOTIS at Kitt Peak, and the Palomar 60 inch telescope (P60). Telescope details are listed in Table 6.2. All AGNs in

Table 6.2: Telescope properties. FOV is field of view. The gain and read noise are parameters in the IRAF photometry procedure.

Telescope	Mirror diameter (m)	FOV	Pixel scale ″/pixel	Gain e^-/ADU	Read noise e^-
WMO	0.91	$25'.2 \times 25'.2$	0.49	1.53	13.2
FTN	2	$10'.5 \times 10'.5$	0.304	8.09	11.31
FTS	2	$10'.5 \times 10'.5$	0.304	5.2	8.2
KAIT	0.76	$6'.7 \times 6'.7$	0.8	4.5	12.0
Super-LOTIS	0.6	$17' \times 17'$	0.5	3.93	11.59
P60	1.5	$12'.9 \times 12'.9$	0.378	2.2	5.72

the sample were observed with WMO, FTN or FTS, and P60, while most AGNs were also observed with KAIT and Super-LOTIS. The AGNs were monitored from early March through mid-June, 2011. The exceptions were Mrk 50, for which spectroscopy was taken before the main observing campaign, and Mrk 817 and Zw 229, for which Spitzer data was taken during and after the campaign. Exposure times were generally 180-300 s.

6.2.1 West Mountain Observatory

The 0.91 m telescope at West Mountain Observatory (WMO) is the largest of five telescopes operated by Brigham Young University. The telescope uses a 3056×3056 pixel Finger Lakes PL-09000 CCD with a pixel scale of $0.''49$/pixel and field of view of $25'.2 \times 25'.2$. All AGNs in our sample were observed with WMO and photometric observations of each AGN will be calibrated using Landolt fields.

6.2.2 Faulks Telescopes North and South

The 2 m Faulkes Telescope North (FTN) and Faulkes Telescope South (FTS) are part of the Los Cumbres Observatory Global Telescope Network (LCOGT). FTN is at Mt.

Haleakala Hawaii and FTS is at Siding Spring Australia, providing coverage of both the northern and southern hemispheres. For both telescopes we used the 4097×4096 pixel Spectral cameras with Fairchild CCD486 BI CCDs. The pixel scale of the Spectral cameras is $0.''304$/pixel, providing a field of view of $10'.5 \times 10'.5$. We used FTN to observe Mrk 704, Mrk 141, Mrk 279, Mrk 817, Mrk 486, Mrk 504, Mrk 493, and Arp 151 and used FTS to observe Mrk 50, NGC 4593, IISZ10, Mrk 841, Mrk 1392, and Mrk 1511.

6.2.3 Katzman Automatic Imaging Telescope

The 0.76 m Katzman Automatic Imaging Telescope (KAIT) is a robotic telescope at Lick Observatory (Filippenko et al. 2001). The telescope uses a 500×500 pixel Apogee Instruments Peltier cooled CCD with a pixel scale of $0.''8$/pixel giving a field of view of $6'.7 \times 6'.7$. KAIT was used to observe all objects in the sample except Arp 151, NGC 4593, IISZ10, Mrk 841, and Mrk 486.

6.2.4 Super-LOTIS

The 0.6 m Super-LOTIS telescope is a robotic telescope at the Steward Observatory, Kitt Peak. The telescope uses a 2048×2048 pixel SpectralInst. 800 Series CCD Camera with a pixel scale of $0.''5$/pixel giving a field of view of $17' \times 17'$. Super-LOTIS was used to observe all objects in the sample except for Zw229-015. Due to a filter wheel problem, images before March 26 were excluded from the light curve analysis.

6.2.5 P60

The 1.5 m Palomar 60 inch (P60) telescope is a robotic telescope at the Palomar Observatory operated by the California Institute of Technology (Cenko et al. 2006). The telescope has a 2048×2048 pixel SITe CCD with a pixel scale of $0.''378$/pixel giving a field of view of $12'.9 \times 12'.9$. All objects in the sample were observed nightly.

6.3 Data reduction and photometry

Initial reduction of the data was performed by the automated pipeline for each telescope. The data then underwent additional reductions to ensure that the images from each telescope were flat-fielded, bias subtracted, and cosmic-ray cleaned using the LACOSMIC routine (van Dokkum 2001). The preprocessed data for the nine AGN targets with significant Hβ variability were then analyzed using image subtraction software in order to isolate the variable AGN flux from the constant flux of the host galaxy. We performed photometry on the data with the constant flux sources removed using point-source IRAF photometry routines. The details of the photometry and image subtraction process are described in Section 6.3.1. Since we created separate light curves for each telescope for a given AGN, we had to align the multiple light curves for each AGN as described in Section 6.3.2. For the remaining six AGN targets without image subtraction photometry, we performed standard aperture photometry techniques as described in Section 6.3.4. Finally, a discussion of how the photometry flux errors are calculated is given in Section 6.3.3.

6.3.1 Image subtraction photometry

The goal of the V-band imaging campaign is to measure differential photometry light curves for each AGN in the LAMP 2011 sample. Without a flux calibration, the differential photometry light curves have units of relative flux, which is sufficient for reverberation mapping analysis. What is crucial, however, is isolation of the variable AGN flux from the constant host galaxy flux. The added constant host galaxy flux has the effect of diluting the AGN variability, leading to less stringent constraints on the black hole mass and lag measurements.

The traditional approach of creating differential photometry light curves for reverberation mapping involves doing photometry on extended source images of the host galaxy plus AGN. In the traditional approach, a single aperture size is required for the photometry in each image of the light curve in order to minimize the effect of including a variable amount of host galaxy light. However, variable seeing conditions over the course of the observing campaign can lead to more or less host galaxy light being inside the fixed-size aperture. Choosing the best aperture size to use is then an optimization problem of including as small a fraction of host galaxy light as possible in order to not dilute the AGN signal while using an aperture wide enough to not suffer from the effects of variable seeing conditions.

One way to circumvent these problems is to subtract the constant flux sources in an image before photometry. Image subtraction software is made especially for this purpose and is what we use to create relative flux light curves for the majority of AGNs in the LAMP 2011 sample. Once the variable AGN continuum has been isolated, we create

V-band light curves using point-source photometry of the AGN. Since most of the AGNs in the LAMP 2011 sample have extended host galaxies, isolating the point-source AGN continuum is crucial for creating light curves whose variability is not diluted with the constant host galaxy light. Isolating the AGN point-source also solves the problem of aperture effects on extended sources.

Applying image subtraction to a set of images is done by: 1) astrometrically aligning the images, 2) creating a template image that has the best seeing and lowest background and is typically a combination of the best couple of images, 3) creating individualized templates for each image by solving for the space-varying convolution kernal that matches the point-spread-functions of the image and template, and 4) subtracting the template from each image. After subtracting the template from an image, only the variable components are left, including the AGN point-source. Non-variable comparison stars in the field of view are used to properly combine the different images into a light curve.

We use the HOTPANTS image subtraction package by A. Becker[1] based on the algorithm by Alard (2000) and a version of the ISIS image subtraction code (Alard & Lupton 1998) modified by the High-z Supernova Search Team (Tonry et al. 2003) and W. Li. For the highest quality images, the HOTPANTS and Highz software packages provide consistent results. However, for lower quality images, one software package may provide a better image subtraction than the other, in which case only one software package is used for that light curve or individual image. Once the image subtraction has been completed, we perform point-source photometry on the image-subtracted images using the IRAF task PHOT in the DAOPHOT package to calculate the flux and flux uncertainty of the

[1]http://www.astro.washington.edu/users/becker/v2.0/hotpants.html

AGN and comparison stars. The photometry analysis consists of measuring the flux in a circular aperture centered on an object (AGN or comparison star) and then using a circular ring of flux outside the aperture to measure and subtract the background flux. After point-source photometry, the light curve is in relative flux units.

We use a different template image for each telescope for a given AGN so that there are multiple light curves for each AGN, one from each telescope. The comparison stars for a given AGN field do not have to be the same for the different telescopes, making it easier to deal with fields of view of varying size. In order to combine the different telescope light curves for an AGN, we model the light curves using Gaussian Processes, as described in Section 6.3.2.

6.3.2 Image subtraction light curve alignment

After applying image subtraction and point-source photometry techniques to the V-band images, we are left with multiple relative flux light curves for each AGN, one for each telescope. In order to align the different light curves for each AGN, we model the light curve using Gaussian Processes (MacKay 2003; Rasmussen & Williams 2006), which has been found to be a good model for AGN variability for large samples of AGN (Kelly et al. 2009; Kozłowski et al. 2010; MacLeod et al. 2010; Zu et al. 2013). The model takes an arbitrary number of light curves and aligns them to a primary light curve. We use the WMO light curves as the primary light curves for our sample, since the WMO light curves will be flux-calibrated, as described in Section 6.5.

The model we use for the AGN light curves has a probability distribution for the

fluxes f in the light curve given by a multivariate Gaussian:

$$p(\mathbf{f}|\mu, C) = \frac{1}{\sqrt{(2\pi)^n \det\mathbf{C}}} \times \exp\left(-\frac{1}{2}(\mathbf{f}-\boldsymbol{\mu})^T\mathbf{C}^{-1}(\mathbf{f}-\boldsymbol{\mu})\right) \tag{6.1}$$

where $\mu(t)$ is the mean function, and $C(t_1, t_2)$ is the covariance function. The covariance function is parametrized by four hyperparameters: μ (the long-term mean), σ (the long-term standard deviation), τ (typical timescale of variations) and α (a smoothness parameter between 1 and 2), so that the mean function is a constant $\mu(t) = \mu$ and the covariance function is given by:

$$C(t_1, t_2) = \sigma^2 \exp\left[-\left(\frac{|t_2 - t_1|}{\tau}\right)^{\alpha}\right] \tag{6.2}$$

We illustrate the light curve alignment model using two light curves (true, complete, and noise-free), $y_1(t)$ and $y_2(t)$. There is a scaling A and a shift B that relates the two light curves, given by:

$$y_2(t) = Ay_1(t) + B \tag{6.3}$$

Suppose our knowledge of $y_1(t)$ is a Gaussian Process (GP) with mean μ_1 (a constant, for our purposes) and covariance function $C_1(\tau)$. By the linearity of Equation 6.3, our knowledge of $y_2(t)$ is also a GP, and indeed so is our joint knowledge of $y_1(t)$ and $y_2(t)$. The expectation value of $y_2(t)$ is:

$$\mu_2 = \langle y_2(t)\rangle = A\langle y_1(t)\rangle + B \tag{6.4}$$

$$= A\mu_1 + B \tag{6.5}$$

and the covariance function for $y_2(t)$ is:

$$\begin{aligned} C_2(\tau) &= \langle (y_2(t) - \mu_2)\,(y_2(t+\tau) - \mu_2)\rangle && (6.6)\\ &= \langle (Ay_1(t) + B - (A\mu_1 + B)) && (6.7)\\ &\quad \times (Ay_1(t+\tau) + B - (A\mu_1 + B))\rangle \\ &= \langle (Ay_1(t) - A\mu_1)\,(Ay_1(t+\tau) - A\mu_1)\rangle && (6.8)\\ &= A^2 C_1(\tau). && (6.9) \end{aligned}$$

We also need the "cross-terms", the covariance between $y_1(t_1)$ and $y_2(t_2)$. This is given by:

$$\begin{aligned} \mathrm{Cov}(y_1(t_1), y_2(t_2)) &= \langle (y_1(t_1) - \mu_1)\,(y_2(t_2) - \mu_2)\rangle && (6.10)\\ &= \langle (y_1(t_1) - \mu_1)\,(Ay_1(t_2) \\ &\quad + B - (A\mu_1 + B))\rangle && (6.11)\\ &= A\,\langle (y_1(t_1) - \mu_1) \\ &\quad \times (y_1(t_2) - \mu_1)\rangle && (6.12)\\ &= AC_1(t_2 - t_1). && (6.13) \end{aligned}$$

We use a Metropolis-Hastings Markov Chain Monte Carlo (MCMC) algorithm to explore the parameter space of A, B, and the parameters of the GP that include τ, σ, α, and μ. The MCMC algorithm returns an inference on the parameter values in the form of the posterior probability density function (PDF);we use the mean values of the posterior PDFs for A and B for the final alignment of the light curves. Since there is some uncertainty in the inferred values for the A and B alignment constants, one could use the uncertainty values to explore the range in allowed light curve alignments.

6.3.3 Image subtraction light curve error estimation

The relative flux uncertainties from image subtraction analysis are measured from the IRAF photometry procedure PHOT in the DAOPHOT package. In many cases the flux uncertainties are very low for the high-quality images, due to the image subtraction process isolating only the variable AGN point source from the extended host galaxy.

In order to obtain reasonable errorbars on photometry measurements after image subtraction, there are two steps that must be taken. First, in order to properly account for the level of background flux in an image when using image subtraction and performing subsequent photometry, the background flux is not removed prior to performing image subtraction. Second, the aperture size for point-source photometry is only slightly larger than the typical point-spread-function width of the light curve. This second steps ensures that the AGN variability is not diluted by the noise of the background in the image subtraction-processed image.

The telescope quality also has an effect on the final flux uncertainties through the quality of the camera, observing conditions, and integration time of the exposure or number of exposures. These affects lead to each of the individual telescope light curves for an AGN having different typical flux uncertainties.

We tested whether an example of the Super-LOTIS light curve having significantly larger errorbars than the WMO and LCOGT datapoints was also true when doing photometry on the images before image subtraction. We used data for PG 1310-108 and performed extended source photometry on the AGN and three comparison stars for two images in the Super-LOTIS light curve for which the flux difference should be greatest

based on higher signal-to-noise data. We found that the difference in flux, ΔF, between these two points F_1 and F_2 divided by the error in this difference measurement $\left(\sigma_{\Delta \mathrm{F}} = \sqrt{\sigma_{\mathrm{F}_1}^2 + \sigma_{\mathrm{F}_2}^2}\right)$ was greater for image subtraction than for the extended source photometry. This shows that image subtraction is able to isolate the variable AGN flux with greater precision than extended source photometry. As a final test, we checked that the value $\Delta \mathrm{F}/\sigma_{\Delta \mathrm{F}}$ is conserved during realignment of each telescope light curve to that of WMO.

One source of systematic uncertainty that is not accounted for in the final light curve fluxes is the uncertainty from aligning the light curves from different telescopes. As described in Section 6.3.2, we use an MCMC algorithm to constrain the values and uncertainties of the additive and multiplicative constants that align each telescope light curve to the WMO light curve. The uncertainty in the light curve alignment is difficult to incorporate into the final light curve values because it is a correlated error for all points in each telescope light curve. For analysis that easily works with a sample of light curves instead of a single light curve, such as cross-correlation analysis, it is possible to use the posterior sample of light curve alignments instead.

6.3.4 Standard aperture photometry

For objects that were comparatively less variable, we chose to use aperture photometry instead of image subtraction to construct the AGN light curves. After the images were reduced, we used the *Astrometry.net* software (Lang et al. 2010) to register celestial coordinates onto the images. We then performed aperture photometry in IDL using

an aperture radius of 4″and sky annulus radii of 10″−20″and obtained instrumental magnitudes for all AGNs and several comparison stars in each field. The comparison stars were chosen to have similar or slightly brighter instrumental magnitudes compared to the AGN in the field. For nights where multiple exposures were taken at the same telescope, the magnitude measurements for each object were averaged into a single value.

For each AGN, employing the comparison stars as constant-flux references, we obtained a separate light curve for images from each telescope. The uncertainties from aperture photometry photon counting errors underestimate the true photometric error budget. Additional sources of error include inconsistencies in flat-field corrections and poor comparison-star magnitude measurements due to imperfections on the detector. We estimated the magnitude of these errors by calculating the excess variance, defined as

$$\sigma_{\rm x}^2 = \frac{1}{N}\sum_{i=1}^{N}[(X_i - \mu)^2 - \sigma_i^2], \tag{6.14}$$

of the scaled comparison-star light curves. Here, N is the number of measurements in the sample, μ is the mean magnitude, and X_i and σ_i are the individual measurements and their associated uncertainties, respectively. We took the mean scatter of all comparison stars in each field and added this in quadrature to the uncertainties from aperture photometry to produce the final AGN light curve for each telescope. Finally, to combine the different telescope light curves, we scaled each light curve so that the mean comparison-star magnitudes for each telescope matched those from WMO, which had the highest SNR.

6.4 Results

The AGN V-band continuum light curves from image subtraction and standard aperture photometry are shown in Figures 6.1 and 6.2, respectively. As expected for reverberation mapping datasets, there is a range in variability within the sample. In addition, variability can be observed on a variety of timescales, as illustrated by the low-frequency variations for Mrk 50 compared to the high-frequency variations for NGC 4593. These differences demonstrate why a reverberation mapping campaign with high cadence over a long period of time is necessary to characterize the variability of an AGN sample.

The light curves for each telescope are indicated with different colors in Figures 6.1 and 6.2 to show the range in data quality. Generally, the WMO and FTN/FTS (labeled as LCOGT) light curves are of the highest quality, but suffer from uneven or sparse sampling in the case of FTN/FTS or a delay in the start of observations for WMO with respect to the beginning of the monitoring campaign. The KAIT and Super-LOTIS data are required to fill in many gaps, especially before the start of WMO monitoring. On the other hand, the P60 data suffer from rows of bad pixels, making it challenging to find comparison stars that do not fall on a bad row in any of the images. The P60 data typically have the largest errors and have only been included for the Mrk 50 light curve, since it has the densest sampling of any of the AGNs, ensuring that the P60 data agree with the other data. There is less agreement between P60 data and data from other telescopes in the other objects. Finally, at this time we include datapoints with very large errors that have no obvious reason to be discarded based on image quality; once the light curves have been flux calibrated, we will make a cut based on absolute flux

uncertainty, discarding many of the points with the largest errors.

While the light curves from image subtraction for different telescopes agree very well, there is some discrepancy between telescopes for the standard aperture photometry light curves, most noticeably for Mrk 817. These light curves are not aligned using the Gaussian process model for AGN variability used for the image subtraction light curves, so the difference may be due to variations in telescope or filter properties. Despite this issue, the standard aperture photometry procedure has two main advantages compared to the image subtraction procedure. First, the standard aperture photometry is fast, requiring less parameter fine-tuning and inspection of images at different stages of the analysis. Second, because the light curves for different telescopes are aligned independently, they do not need to have datapoints that overlap, as is required for the Gaussian process model used with the image subtraction procedure. The dataset for Mrk 486 is a good example of one for which the Gaussian process alignment would not be well-constrained. For these reasons, standard aperture photometry is an ideal method for measuring light curves for AGN that will not undergo detailed analysis such as dynamical modeling of the BLR.

6.5 Summary and future work

In this chapter, we present V-band continuum light curves in relative-flux units for the fifteen AGN in the LAMP 2011 reverberation mapping dataset. For the AGNs with high levels of Hβ variability (see Barth et al. 2015), the AGN continuum light curves were measured using image subtraction software in order to create high-quality reverberation

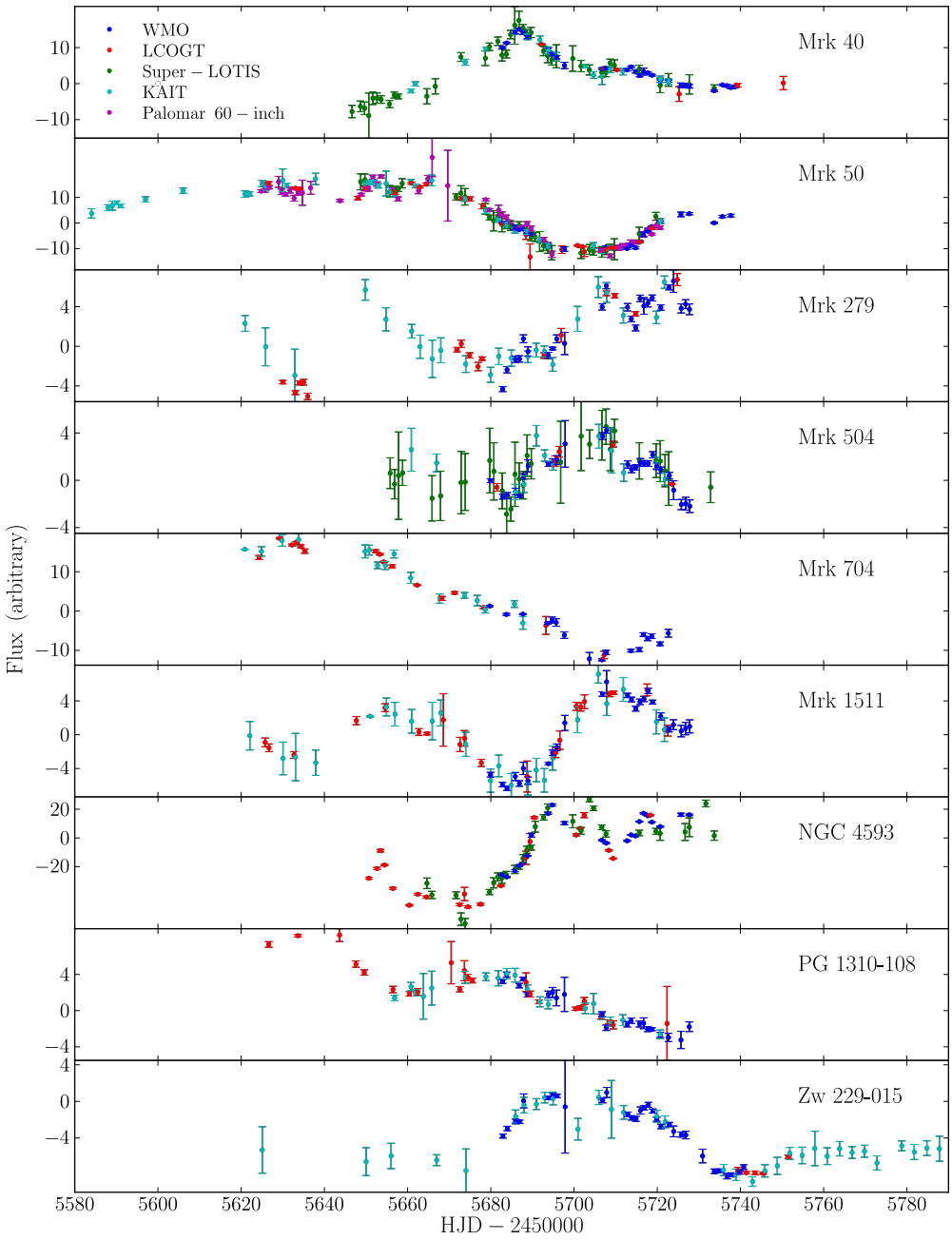

Figure 6.1: Image subtraction light curves for LAMP 2011. The different colors correspond to data from different telescopes, as indicated in the legend. LCOGT data consists of either FTN or FTS. Mrk 50 has additional monitoring before the beginning of the main LAMP 2011 campaign and Zw 229-015 has additional monitoring at the end of the main campaign.

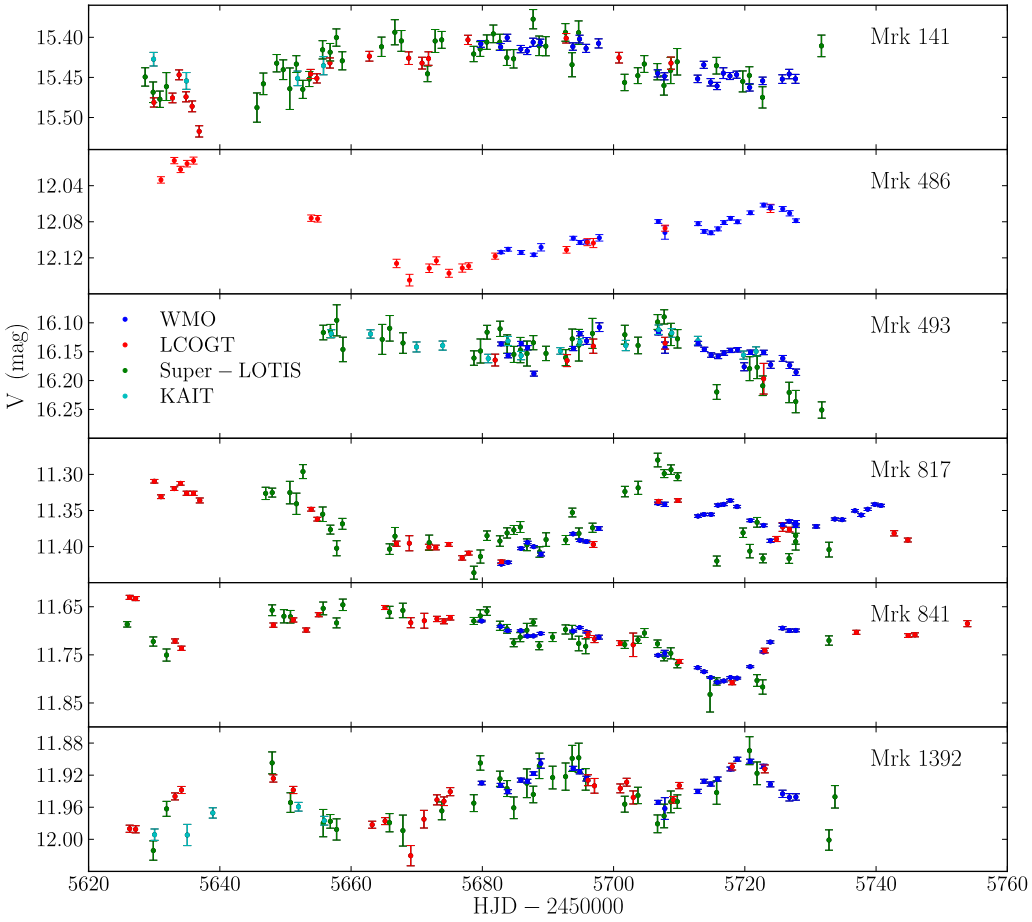

Figure 6.2: Same as for Figure 6.1, but for standard aperture photometry light curves.

mapping data for dynamical modeling of the BLR (e.g. Brewer et al. 2011a; Pancoast et al. 2012, 2014b). For the AGNs with lower levels of Hβ variability, the AGN continuum light curves were measured using standard aperture photometry techniques.

While AGN continuum light curves in relative-flux units are sufficient for reverberation mapping analysis such as calculation of the cross-correlation function or BLR modeling, future work with this dataset will include flux calibration of the AGN continuum light curves using Landolt (1992) standard stars observed at WMO. Since we only have data

for the V band, we will not attempt to perform color-dependent Landolt calibrations. Flux calibration will allow us to probe the variability characteristics of the light curves, measure the AGN V-band luminosity, and measure absolute light curve flux errors.

Chapter 7

Conclusions and future directions

This thesis develops a new method to analyze reverberation mapping data that provides an independent measurement of the black hole mass and constraints on the geometry and dynamics of the broad line region (BLR) in active galactic nuclei (AGN). In Chapter 2, we present the formalism of this method and demonstrate its utility using simulated reverberation mapping datasets, including promising predictions for reduced uncertainties in reverberation mapped black hole mass measurements. In Chapter 3, we apply this method to the highest-quality dataset from the Lick AGN Monitoring Project (LAMP) 2011 reverberation mapping campaign for the AGN Mrk 50, constraining the BLR geometry to be a nearly face-on thick disk. In Chapter 4, we present major improvements to the method and BLR model and compare the results for simulated data from the BLR modeling approach to the standard cross-correlation function analysis. In Chapter 5, we apply the improved BLR models to five AGN from the LAMP 2008 campaign, measuring the black holes masses more precisely than the standard analysis and providing detailed constraints on the geometry and dynamics of the BLR. Finally, in Chapter 6, we present the measurement of AGN continuum light curves using image subtraction as part of the LAMP 2011 dataset.

The results of this thesis demonstrate the unique constraining power of high-quality reverberation mapping data in studies of AGN structure and the measurement of black hole masses. While standard reverberation mapping analysis provides black hole mass measurements using an average value of the normalization factor f and uncertainties on the order of ~ 0.4 dex, analysis for the six AGN from LAMP 2008 and 2011 using BLR modeling provides black hole masses with uncertainties of only $0.15 - 0.35$ dex. This is possible because, instead of assuming an average value of f, the BLR modeling approach provides the first direct measurements of f for individual AGN from constraints on BLR structure. The individual values of f are consistent to within the uncertainties with the average f value measured using the $M_{\rm BH} - \sigma_*$ relation and are found to be a function of inclination angle of the BLR. Since the BLR cannot be spatially resolved with even the largest current telescopes, BLR modeling is the only method capable of simultaneously constraining the shape, inclination, and dynamics of the BLR. For the six AGN in the LAMP 2008 and 2011 sample, we find that the Hβ-emitting BLR geometry is generally a thick disk viewed close to face-on, with preferential emission from the far side, while the BLR dynamics range from near-circular to inflowing orbits. Preferential emission from the far side of the BLR is consistent with models where the BLR gas is self-shielding. The constraints on the inclination angle provide the first verification of the AGN standard model for the BLR, where AGN with broad emission lines should be observed close to face-on (Antonucci 1993; Urry & Padovani 1995). As a whole, these results represent the most comprehensive information about BLR structure and the smallest uncertainties in reverberation mapped black hole mass measurements to date.

Having demonstrated the unique contributions made by the BLR modeling approach,

the next steps in this work involve 1) applying BLR modeling to a larger sample of AGN with high-quality reverberation mapping data and 2) developing more physical models of the BLR to use in the analysis. We discuss these future directions in the remainder of this chapter.

7.1 Increasing the sample of AGN with broad line region modeling

While the BLR modeling approach has provided the first detailed contraints on the geometry and dynamics of BLR emission in a small handful of reverberation mapped AGN, many important questions remain unanswered, including: 1) What is the range in BLR geometries and dynamics in the larger reverberation mapped AGN sample and do the properties depend upon black hole mass, accretion rate, or AGN luminosity? 2) How is the BLR structure related to that of the accretion disk, jet, or dusty torus? and 3) How can constraints on BLR structure reduce black hole mass measurement uncertainties for AGN without BLR modeling of reverberation mapping data? The key to answering these questions is to apply the BLR modeling technique to a larger sample of reverberation mapped AGN that 1) span a range of black hole mass, accretion rate, and AGN luminosity, 2) have constraints on the structure of the accretion disk, jet, or dusty torus from other studies, and 3) span the range of possible BLR structure found at both low and high redshifts.

The BLR modeling approach has been applied to six AGN so far, including the

five highest-quality datasets from LAMP 2008 (Walsh et al. 2009; Bentz et al. 2009b) and the highest-quality dataset from LAMP 2011 (Barth et al. 2015). Analysis is also underway for four AGN from the 2010 reverberation mapping campaign by the Ohio State University (OSU) collaboration (Grier et al. 2012, Grier et al. in preparation). In addition, there are ~ 5 more high-quality datasets from LAMP 2011 as well as a handful of promising candidates from the 2012 and 2014 OSU campaign datasets that can be analysed using the BLR modeling technique. Analysis of these data will quadruple the number of AGN with BLR modeling and allow us to begin answering the important questions outlined above.

In addition, there are now multiple reverberation mapping campaigns aimed at higher redshift AGN using mainly the Mg II λ2798 and C IV λ1549 broad emission lines (e.g. Shen et al. 2015; King et al. 2015). With sufficient data quality, these datasets will allow us to constrain the properties of the BLR outside the local Universe, expanding the range of AGN luminosity, black hole mass, and accretion rate in the BLR modeling sample.

7.2 Photoionization modeling

As the data quality of reverberation mapping campaigns continues to increase, it will be possible to constrain additional information about BLR physics through the BLR modeling approach. Photoionization modeling codes (e.g. CLOUDY, Ferland et al. 2013) relate the BLR emission to the underlying BLR gas properties and give predictions for the response of different broad emission lines to changes in the ionizing photon flux from the accretion disk. Most importantly, including the results from photoionization modeling

in the BLR modeling approach will allow us to move from modeling the geometry of BLR emission to modeling the geometry of BLR gas. Also, for a select few AGN with reverberation mapping data for multiple broad emission lines, we can model the lines simultaneously using their different response functions from photoionization modeling, making it possible to constrain the distribution of BLR gas densities and test the 'locally optimally emitting cloud' model (Baldwin et al. 1995).

Recently, an intensive reverberation mapping campaign has been carried out for one of the best studied reverberation mapping targets, NGC 5548, with data spanning the x-rays through infrared and including UV spectroscopy with *HST* (De Rosa et al. 2015; Edelson et al. 2015). While only for a single AGN, this is the highest-quality reverberation mapping dataset currently in existence and the first to provide a good candidate for detailed BLR modeling using photoionization physics.

7.3 Outflows in the broad line region

While the culprit driving feedback between black holes and their host galaxies is most likely AGN outflows, the launching radius and driving mechanism of the outflows remain unknown. This is due, in part, to the challenging nature of outflow simulations; detailed models of radiation-driven outflows (e.g. Proga & Kallman 2004) are highly sensitive to radiative transfer calculations that determine where the gas is ionized (Higginbottom et al. 2014) and that provide predictions for observational outflow signatures such as blue-shifted emission or absorption features. The outflow driving mechanism may be line opacity (Castor et al. 1975), dust opacity (Dorodnitsyn & Kallman 2012), or magnetic

fields (Blandford & Payne 1982), each of which provides predictions for the dynamics of outflowing gas.

One way to constrain the properties of AGN outflows is to look for their influence in the BLR. We can constrain whether outflow dynamics are at work at the radii probed by reverberation mapping by testing different models for AGN outflows within a dynamics model of the BLR. If evidence for outflows is found, it could provide the first robust constraints on the launching radius and driving mechanism. Considering the full range of AGN outflow models is critical, however, since degeneracies between geometry, orientation, and dynamics can generate similar features in the data (e.g. Bottorff et al. 1997).

Bibliography

Abazajian, K. N., Adelman-McCarthy, J. K., Agüeros, M. A., et al. 2009, ApJS, 182, 543

Alard, C. 2000, A&AS, 144, 363

Alard, C., & Lupton, R. H. 1998, ApJ, 503, 325

Antonucci, R. 1993, ARA&A, 31, 473

Baldwin, J., Ferland, G., Korista, K., & Verner, D. 1995, ApJL, 455, L119

Barth, A. J., Nguyen, M. L., Malkan, M. A., et al. 2011a, ApJ, 732, 121

Barth, A. J., Pancoast, A., Thorman, S. J., et al. 2011b, ApJL, 743, L4

Barth, A. J., Pancoast, A., Bennert, V. N., et al. 2013, ApJ, 769, 128

Barth, A. J., Bennert, V. N., Canalizo, G., et al. 2015, ApJS, 217, 26

Bentz, M. C., & Katz, S. 2015, PASP, 127, 67

Bentz, M. C., Peterson, B. M., Netzer, H., Pogge, R. W., & Vestergaard, M. 2009a, ApJ, 697, 160

Bentz, M. C., Peterson, B. M., Pogge, R. W., Vestergaard, M., & Onken, C. A. 2006, ApJ, 644, 133

Bentz, M. C., Walsh, J. L., Barth, A. J., et al. 2009b, ApJ, 705, 199

—. 2010a, ApJ, 716, 993

Bentz, M. C., Horne, K., Barth, A. J., et al. 2010b, ApJL, 720, L46

Bentz, M. C., Denney, K. D., Grier, C. J., et al. 2013, ApJ, 767, 149

Blandford, R. D., & McKee, C. F. 1982, ApJ, 255, 419

Blandford, R. D., & Payne, D. G. 1982, MNRAS, 199, 883

Bottorff, M., Korista, K. T., Shlosman, I., & Blandford, R. D. 1997, ApJ, 479, 200

Brandt, W. N., & Alexander, D. M. 2015, A&ARv, 23, 1

Brewer, B. J., & Elliott, T. M. 2014, MNRAS, 439, L31

Brewer, B. J., Pártay, L. B., & Csányi, G. 2011a, Statistics and Computing, 21, 649, astrophysics Source Code Library

Brewer, B. J., Treu, T., Pancoast, A., et al. 2011b, ApJL, 733, L33

Carini, M. T., & Ryle, W. T. 2012, ApJ, 749, 70

Castor, J. I., Abbott, D. C., & Klein, R. I. 1975, ApJ, 195, 157

Cenko, S. B., Fox, D. B., Moon, D.-S., et al. 2006, PASP, 118, 1396

Collier, S. J., Horne, K., Kaspi, S., et al. 1998, ApJ, 500, 162

Collin, S., Kawaguchi, T., Peterson, B. M., & Vestergaard, M. 2006, A&A, 456, 75

Davies, R. I., Thomas, J., Genzel, R., et al. 2006, ApJ, 646, 754

De Rosa, G., Venemans, B. P., Decarli, R., et al. 2014, ApJ, 790, 145

De Rosa, G., Peterson, B. M., Ely, J., et al. 2015, ArXiv e-prints, arXiv:1501.05954

Denney, K. D., Peterson, B. M., Dietrich, M., Vestergaard, M., & Bentz, M. C. 2009, ApJ, 692, 246

Denney, K. D., Pogge, R. W., Assef, R. J., et al. 2013, ApJ, 775, 60

Denney, K. D., Peterson, B. M., Pogge, R. W., et al. 2010, ApJ, 721, 715

Done, C., & Krolik, J. H. 1996, ApJ, 463, 144

Dorodnitsyn, A., & Kallman, T. 2012, ApJ, 761, 70

Edelson, R., Vaughan, S., Malkan, M., et al. 2014, ApJ, 795, 2

Edelson, R., Gelbord, J. M., Horne, K., et al. 2015, ArXiv e-prints, arXiv:1501.05951

Fabian, A. C. 2012, ARA&A, 50, 455

Ferland, G. J., Korista, K. T., Verner, D. A., et al. 1998, PASP, 110, 761

Ferland, G. J., Porter, R. L., van Hoof, P. A. M., et al. 2013, RMXAA, 49, 137

Ferrarese, L., & Ford, H. 2005, SSRv, 116, 523

Ferrarese, L., & Merritt, D. 2000, ApJL, 539, L9

Filippenko, A. V., Li, W. D., Treffers, R. R., & Modjaz, M. 2001, in Astronomical Society of the Pacific Conference Series, Vol. 246, IAU Colloq. 183: Small Telescope Astronomy on Global Scales, ed. B. Paczynski, W.-P. Chen, & C. Lemme, 121

Gebhardt, K., Bender, R., Bower, G., et al. 2000, ApJL, 539, L13

Genzel, R., Eisenhauer, F., & Gillessen, S. 2010, Reviews of Modern Physics, 82, 3121

Goad, M. R., Korista, K. T., & Ruff, A. J. 2012, MNRAS, 426, 3086

Graham, A. W., Onken, C. A., Athanassoula, E., & Combes, F. 2011, MNRAS, 412, 2211

Greene, J. E., Peng, C. Y., Kim, M., et al. 2010a, ApJ, 721, 26

Greene, J. E., Hood, C. E., Barth, A. J., et al. 2010b, ApJ, 723, 409

Grier, C. J., Peterson, B. M., Pogge, R. W., et al. 2012, ApJ, 755, 60

Grier, C. J., Martini, P., Watson, L. C., et al. 2013a, ApJ, 773, 90

Grier, C. J., Peterson, B. M., Horne, K., et al. 2013b, ApJ, 764, 47

Hicks, E. K. S., & Malkan, M. A. 2008, ApJS, 174, 31

Higginbottom, N., Proga, D., Knigge, C., et al. 2014, ApJ, 789, 19

Hogg, D. W., Myers, A. D., & Bovy, J. 2010, ApJ, 725, 2166

Horne, K. 1994, in Astronomical Society of the Pacific Conference Series, Vol. 69, Reverberation Mapping of the Broad-Line Region in Active Galactic Nuclei, ed. P. M. Gondhalekar, K. Horne, & B. M. Peterson, 23–25

Horne, K., Welsh, W. F., & Peterson, B. M. 1991, ApJL, 367, L5

Kasliwal, V. P., Vogeley, M. S., & Richards, G. T. 2015, ArXiv e-prints, arXiv:1505.00360

Kaspi, S., Smith, P. S., Netzer, H., et al. 2000, ApJ, 533, 631

Kelly, B. C., Bechtold, J., & Siemiginowska, A. 2009, ApJ, 698, 895

Kelly, B. C., & Shen, Y. 2013, ApJ, 764, 45

Kelly, B. C., Vestergaard, M., Fan, X., et al. 2010, ApJ, 719, 1315

King, A. L., Martini, P., Davis, T. M., et al. 2015, ArXiv e-prints, arXiv:1504.03031

Kollatschny, W., & Bischoff, K. 2002, A&A, 386, L19

Kollatschny, W., Bischoff, K., Robinson, E. L., Welsh, W. F., & Hill, G. J. 2001, A&A, 379, 125

Korista, K. T., & Goad, M. R. 2004, ApJ, 606, 749

Korista, K. T., Alloin, D., Barr, P., et al. 1995, ApJS, 97, 285

Kormendy, J., & Ho, L. C. 2013, ARA&A, 51, 511

Kormendy, J., & Richstone, D. 1995, ARA&A, 33, 581

Kozłowski, S., Kochanek, C. S., Udalski, A., et al. 2010, ApJ, 708, 927

Krolik, J. H., & Done, C. 1995, ApJ, 440, 166

Krolik, J. H., Horne, K., Kallman, T. R., et al. 1991, ApJ, 371, 541

Landolt, A. U. 1992, AJ, 104, 340

Lang, D., Hogg, D. W., Mierle, K., Blanton, M., & Roweis, S. 2010, AJ, 139, 1782

Laor, A., Barth, A. J., Ho, L. C., & Filippenko, A. V. 2006, ApJ, 636, 83

Li, Y.-R., Wang, J.-M., Ho, L. C., Du, P., & Bai, J.-M. 2013, ApJ, 779, 110

Lynden-Bell, D. 1969, Nature, 223, 690

Lynden-Bell, D., & Rees, M. J. 1971, MNRAS, 152, 461

MacKay, D. J. C. 2003, Information Theory, Inference and Learning Algorithms. Cambridge University Press.

MacLeod, C. L., Ivezić, Ž., Kochanek, C. S., et al. 2010, ApJ, 721, 1014

Marconi, A., Axon, D. J., Maiolino, R., et al. 2008, ApJ, 678, 693

—. 2009, ApJL, 698, L103

Meusinger, H., Hinze, A., & de Hoon, A. 2011, A&A, 525, A37

Morgan, C. W., Kochanek, C. S., Morgan, N. D., & Falco, E. E. 2010, ApJ, 712, 1129

Mushotzky, R. F., Edelson, R., Baumgartner, W., & Gandhi, P. 2011, ApJL, 743, L12

Netzer, H. 2009, ApJ, 695, 793

—. 2015, ArXiv e-prints, arXiv:1505.00811

Netzer, H., & Marziani, P. 2010, ApJ, 724, 318

Onken, C. A., Ferrarese, L., Merritt, D., et al. 2004, ApJ, 615, 645

Onken, C. A., Valluri, M., Brown, J. S., et al. 2014, ApJ, 791, 37

Pancoast, A., Brewer, B. J., & Treu, T. 2011, ApJ, 730, 139

—. 2014a, MNRAS, 445, 3055

Pancoast, A., Brewer, B. J., Treu, T., et al. 2014b, MNRAS, 445, 3073

—. 2012, ApJ, 754, 49

Park, D., Kelly, B. C., Woo, J.-H., & Treu, T. 2012a, ApJS, 203, 6

Park, D., Woo, J.-H., Treu, T., et al. 2012b, ApJ, 747, 30

Peterson, B. M. 1993, PASP, 105, 247

Peterson, B. M. 2006, in Lecture Notes in Physics, Berlin Springer Verlag, Vol. 693, Physics of Active Galactic Nuclei at all Scales, ed. D. Alloin, 77

—. 2014, SSRv, 183, 253

Peterson, B. M., & Wandel, A. 2000, ApJL, 540, L13

Peterson, B. M., Wanders, I., Horne, K., et al. 1998, PASP, 110, 660

Peterson, B. M., Balonek, T. J., Barker, E. S., et al. 1991, ApJ, 368, 119

Peterson, B. M., Ferrarese, L., Gilbert, K. M., et al. 2004, ApJ, 613, 682

Peterson, B. M., Denney, K. D., De Rosa, G., et al. 2013, ApJ, 779, 109

Proga, D. 1999, MNRAS, 304, 938

Proga, D., & Kallman, T. R. 2004, ApJ, 616, 688

Rasmussen, C. E., & Williams, C. K. I. 2006, Gaussian Processes for Machine Learning (Cambridge, MA: MIT Press)

Richards, G. T., Kruczek, N. E., Gallagher, S. C., et al. 2011, AJ, 141, 167

Salpeter, E. E. 1964, ApJ, 140, 796

Schlafly, E. F., & Finkbeiner, D. P. 2011, ApJ, 737, 103

Schwarzschild, K. 1916, Abh. Konigl. Preuss. Akad. Wissenschaften Jahre 1906,92, Berlin,1907, 1916, 189

Shen, Y., & Liu, X. 2012, ApJ, 753, 125

Shen, Y., Brandt, W. N., Dawson, K. S., et al. 2015, ApJS, 216, 4

Sivia, D. S., & Skilling, J. 2006, Data Analysis: A Bayesian Tutorial. 2nd Edition. Oxford University Press.

Skielboe, A., Pancoast, A., Treu, T., et al. 2015, ArXiv e-prints, arXiv:1502.02031

Skilling, J., & Bryan, R. K. 1984, MNRAS, 211, 111

Tonry, J. L., Schmidt, B. P., Barris, B., et al. 2003, ApJ, 594, 1

Urry, C. M., & Padovani, P. 1995, PASP, 107, 803

van Dokkum, P. G. 2001, PASP, 113, 1420

Vestergaard, M., & Peterson, B. M. 2006, ApJ, 641, 689

Vio, R., Horne, K., & Wamsteker, W. 1994, PASP, 106, 1091

Volonteri, M., & Bellovary, J. 2012, Reports on Progress in Physics, 75, 124901

Walsh, J. L., Minezaki, T., Bentz, M. C., et al. 2009, ApJS, 185, 156

Wandel, A., Peterson, B. M., & Malkan, M. A. 1999, ApJ, 526, 579

Welsh, W. F. 1999, PASP, 111, 1347

Whittle, M. 1992, ApJS, 79, 49

Woo, J.-H., Schulze, A., Park, D., et al. 2013, ApJ, 772, 49

Woo, J.-H., Treu, T., Barth, A. J., et al. 2010, ApJ, 716, 269

Zu, Y., Kochanek, C. S., Kozłowski, S., & Udalski, A. 2013, ApJ, 765, 106

Zu, Y., Kochanek, C. S., & Peterson, B. M. 2011, ApJ, 735, 80